Terahertz (THz), Mid Infrared (MIR) and Near Infrared (NIR) Technologies for Protection of Critical Infrastructures Against Explosives and CBRN

Edited by
Mauro Fernandes Pereira
Apostolos Apostolakis

Springer

Terahertz (THz), Mid Infrared (MIR) and Near Infrared (NIR) Technologies for Protection of Critical Infrastructures Against Explosives and CBRN

NATO Science for Peace and Security Series

This Series presents the results of scientific activities supported through the framework of the NATO Science for Peace and Security (SPS) Programme.

The NATO SPS Programme enhances security-related civil science and technology to address emerging security challenges and their impacts on international security. It connects scientists, experts and officials from Alliance and Partner nations to work together to address common challenges. The SPS Programme provides funding and expert advice for security-relevant activities in the form of Multi-Year Projects (MYP), Advanced Research Workshops (ARW), Advanced Training Courses (ATC), and Advanced Study Institutes (ASI). The NATO SPS Series collects the results of practical activities and meetings, including:

Multi-Year Projects (MYP): Grants to collaborate on multi-year R&D and capacity building projects that result in new civil science advancements with practical application in the security and defence fields.

Advanced Research Workshops: Advanced-level workshops that provide a platform for experts and scientists to share their experience and knowledge of security-related topics in order to promote follow-on activities like Multi-Year Projects.

Advanced Training Courses: Designed to enable specialists in NATO countries to share their security-related expertise in one of the SPS Key Priority areas. An ATC is not intended to be lecture-driven, but to be intensive and interactive in nature.

Advanced Study Institutes: High-level tutorial courses that communicate the latest developments in subjects relevant to NATO to an advanced-level audience.

The observations and recommendations made at the meetings, as well as the contents of the volumes in the Series reflect the views of participants and contributors only, and do not necessarily reflect NATO views or policy.

The series is published by IOS Press, Amsterdam, and Springer, Dordrecht, in partnership with the NATO SPS Programme.

Sub-Series

A.	Chemistry and Biology	Springer
B.	Physics and Biophysics	Springer
C.	Environmental Security	Springer
D.	Information and Communication Security	IOS Press
E.	Human and Societal Dynamics	IOS Press

- http://www.nato.int/science
- http://www.springer.com
- http://www.iospress.nl

Series B: Physics and Biophysics

Terahertz (THz), Mid Infrared (MIR) and Near Infrared (NIR) Technologies for Protection of Critical Infrastructures Against Explosives and CBRN

edited by

Mauro Fernandes Pereira

Department of Physics
Khalifa University of Science and
Technology
Abu Dhabi, United Arab Emirates

and

Apostolos Apostolakis

Institute of Physics
Czech Academy of Sciences
Prague, Czech Republic

Springer

Preface

The NATO Advanced Research Workshop (ARW) -Terahertz (THz), Mid Infrared (MIR) and Near Infrared (NIR) Technologies for Protection of Critical Infrastructures against Explosives and CBRN, took place at Liblice Castle, in Czech Republic, 5–9 November 2018. The underlying reasons that inspired this activity and the accomplishments of the ARW are summarized below.

Exposure of citizens to potential disasters has led to vulnerable societies that require risk reduction measures. The size and complexity of our society has led governments to identify Critical Infrastructures, which are assets that play an essential role for the functioning of a society and economy; such as the water supply, electricity, transportation and telecommunications.

Critical infrastructures are targets for terrorism and deliver a valuable vector through which the proliferation of Chemical, Bacteriological, Radiological, or Nuclear (CBRN) threats and explosive precursors can be detected, notably waste water and air quality providers. Recent technological breakthroughs, especially in the field of near infrared (NIR), mid infrared (MIR), Terahertz (THz) and Gigahertz (GHz) sources and detectors, have led to rugged commercial devices, capable of standoff sensing a range of these dangerous substances. However, at the same time criminal and terrorist organizations have also benefited from the availability of technologies to increase the threat they pose to the security of citizens and a concerted effort is needed to improve early detection measures to identify activities, such as the production of homemade explosives or CBRN that can be potentially dangerous to society. The key global technological bottleneck to be overcome is the current lack of integration and networking of mature detection technology into early warning systems for critical infrastructures. Thus, this ARW brought together leading teams working on critical Infrastructure protection with academic developers and industrial producers of state of the art sensors.

Why GHz-THz-MIR?

The answer is that many substances exhibit rotational and vibrational transitions in this region, hence giving access to a spectroscopic analysis of a large variety of molecules which play a key role in security as well as various other areas, e.g. air pollution, climate research, industrial process control, agriculture, food industry, workplace safety and medical diagnostics can be monitored by sensing and identifying them via THz and mid infrared (MIR-15 THz to 120 THz) absorption "finger prints". Most plastics, textiles and paper are nearly transparent for THz radiation.

Therefore, the main physical threats to Critical Infrastructures namely CBRN agents, explosives, illegal drugs can be detected by their characteristic absorption spectra at THz frequencies with high selectivity and resolution in applications fields as industrial quality inspection control, customs inspection and security screening. Moreover, THz and MIR radiation has no endangering effects on human beings and enables higher contrast for "soft matter" than x-rays. In comparison to standard optical technologies for wavelengths up to about 2 μm, sources and detectors for THz and MIR have not yet reached this level of maturity and there is still a large gap for features like wavelength tunability, spectral purity, high power and room temperature operation, which all are necessary for commercial applications.

Plastic or ceramics are detected by X-rays very poorly especially against a background of human body. Unlike X-rays, THz (or T-wave) is not a dangerous radiation, and in some cases T-wave sensors can reveal not only the shape of a hidden object but also its chemical composition. This unique combination of traits make T-waves perfect for effective applications like explosive detection, and security applications. Besides, T-rays have high resolution in 3D space in case of THz ultra-short pulses. The possibility to analyse chemical composition of substances by spectroscopic methods is of big interest. Even in case if the substance is in the plastic tank or under the cloth. However, there are many open problems on the path to practical and routine use of THz and also GHz sources.

Note that heavier threats, such as biological have resonances at smaller frequencies and thus the addition of "GHz" our previous THz and MIR focus. Furthermore, this adds another signature to fully distinguish certain targets that have similar absorption spectra in the NIR, MIR and THz.

In order to achieve the goals of informing the different techno/scientific communities about the current state of the art and to express what each currently need to improve the protection of critical infrastructures, the following general topics were covered during the Advanced Research Workshop (ARW):

State of the Art in sensors for the protection of critical infrastructures, where data fusion from different sources including UAVs and airborne threats were discussed, helping the sensor development identify new directions on their development. In parallel, both direct technological developments and the underlying fundamental science behind a new generation of sources and detectors to create new sensors were discussed. Since we need real time detection that can generate input for the global algorithms constantly monitoring possible targets,

we have focused on the most promising devices such as: Quantum Cascade Lasers (QCLs), Interband Cascade Lasers (ICLs), Semiconductor Superlattices (SSLs) as well as promising alternatives beyond ICLs and QCLs. Expensive, ultra-high precision sensors were discussed hand in hand with less precise, but rather inexpensive approaches, such as point contact sensors, looking for ways into which high precision devices can be integrated with less expensive ones for both calibration and expansion of detection networks for a wide range of detection.

This was the fourth "TERA-MIR" workshop and details of our networking activities can be found at http://www.tera-mir.org. These meetings have been taking place every 3 years and have already led to joint fundamental and applied research as well as successful funding bids. Continuing this successful approach, the last part of the ARW was dedicated to a round table, in which the academic and industrial teams discussed ideas for further joint cooperation and for the submission of new proposals, exploiting both National and International mechanisms, such the NATO Science for Peace and Security Program and Horizon 2020 (H2020).

The event promoted a very efficient update on science and technology of GHz-THz-MIR and optical fibre Technologies that can be used at MIR and NIR with potential for Protection of Critical Infrastructures against Explosives & CBRN as well as the state of the art in applications. As in the previous NATO sponsored "TERA-MIR" ARW's, this event led to a strong impact on attendees, who can re-design some of their activities to integrate in networked effort. Some of the new results presented in this workshop are a consequence of networking from the previous events. Regarding spin-off and follow-on activities, it is very important to note that bringing together colleagues working on data fusion and directly involved in projects related to critical infrastructure protection set the step for further applications.

We had an excellent balance between applications and basic science. As well as of different aspects of generation, detection and applications of THz radiation (Fig. 1). There is no doubt whatsoever that event was fully successful and I hope to keep the "TERA-MIR" series alive with further meetings.

The attendees ranged from early career to experienced researchers from both academia, the industry and one military research/academic institution. The early career researchers had an exceptional opportunity to meet and discuss with leaders in the field in a relaxed environment. We combined basic science and development colleagues at the leading edge of GHz, THz and Mid Infrared field with professionals directly working on explosives and CBRN detection allowing a cross fertilization of ideas and concepts. Furthermore we had colleagues working with protection of critical infrastructures and data fusion for an efficient exchange of ideas.

This book delivers more details about some of the topics presented in the Workshop. There are overlaps in the chapters in terms of the area that they cover, but we can roughly classify them by the following themes:

Fig. 1 The breadth of research topics and directions within Terahertz (THz), Mid Infrared (MIR) and Near Infrared (NIR) Technologies for Protection of Critical Infrastructures against Explosives and CBRN, illustrated by a word cloud compiled from the book of abstract of the Nato ARW held in Chateau Liblice, Central Bohemian Region of the Czech Republic, 2018

State of the Art in sensors for the protection of critical infrastructures:

> Sensor Data Fusion and Autonomous Unmanned Vehicles for the Protection of Critical Infrastructures, by Konstantinos Ioannidis, Georgios Orfanidis, Marios Krestenitis, Stefanos Vrochidis and Ioannis Kompatsiaris.

QCLs, ICLs and their applications to sensing:

> High Power, Widely Tunable, and Beam Steerable Mid-infrared Quantum Cascade Lasers by Manijeh Razeghi and Wenjia Zhou.
>
> Broadband terahertz gas spectroscopy through multimode self-mixing in a quantum cascade laser, by Y. J. Han, J. Partington, R. Chhantyal-Pun, M. Henry, O. Auriacombe, T. Rawlings, L. H. Li, J. Keeley, M. Oldfield, N. Brewster, R. Dong, P. Dean, A. G. Davies, B. N. Ellison, E. H. Linfield and A. Valavanis.
>
> Crucial aspects of the device processing of quantum cascade lasers, by Szerling A., Kosiel K., Prokaryn P., Szymański M., Wasilewski Z., Płuska M., Sakowicz M.

Broadband gas QEPAS detection exploiting a monolithic DFB-QCL array, by Marilena Giglio, Andrea Zifarelli, Pietro Patimisco, Angelo Sampaolo, Giansergio Menduni, Arianna Elefante, Romain Blanchard, Christian Pfluegl, Mark F. Witinski, Daryoosh Vakhshoori, Frank K. Tittel, and Vincenzo Spagnolo.

Global optimization methods for the design of MIR-THz QCLs applied to explosives detection, by Jelena Radovanović, Nikola Vuković, and Vitomir Milanović.

Superlattices and other technologies for GHz-THz sensing*:*

Non-Destructive testing THz systems: fast postal scanner case study, by M. Sypek and J. Starobrat.

Recent advances in superlattice frequency multipliers, by Yuliia Shevchenko, Apostolos Apostolakis, Mauro F. Pereira.

Solid-State Millimeter-Wave through Terahertz Transceivers, by Eric W. Bryerton.

Beyond QCLs, ICLs and Superlattices: competing technologies *for detection of explosives and CBRN*

Transmission and reflection characteristics of textiles in the Terahertz range, by Palka N., Pawlinska E., Szustakowski M., Walczakowski M., Czerwinska E., Ciurapinski W., Jodlowski L., Kowalski M., Zagrajek P., and Marek Zyczkowski.

Transition between localized and delocalized terahertz conductivity in modulated nanostructures studied by Monte-Carlo calculations, by Hynek Němecl and Petr Kužell.

Development of Stand-Off Imaging Systems using Low Cost Plasma Detectors that Work in the GHz to THz range, by Demiral Akbar, Hakan Altan, João Pedro Pavia, Marco A. Ribeiro, A. Behzat Sahin, Cemre Kusoglu Sarıkayal.

Semiconductor components for THz-TDS systems activated by compact fibre lasers, by A. Krotkus, V. Pačebutas, R. Norkus, I. Nevinskas, and A. Arlauskas.

Soft chemical ionization mass spectrometry analyses of hazardous gases and decomposition products of explosives in air, by Kseniya Dryahina and Patrik Spanel.

On the prospect of application of point-contact sensors to solving the global security problems: an analytical review, by G. Kamarchuk, A. Pospelov, A. Savytskyi, V. Gudimenko, V. Vakula, A. Herus, D. Harbuz, L. Kamarchuk and M. F. Pereira.

Development of Gas Sensor Systems in the Infrared Region, by Juliana Carvalho, Sully Quintero and Marbey M. Mosso.

Effective Raman radiation in Decontamination of Translucent Liquids and Gases, by Marina Turcan, Nicolaie Enaki and Tatiana Paslari.

THz Spectroscopy of Advanced Materials, by Can Korall, Gianpaolo Papari and Antonello Andreone.

In summary, this meeting helped the colleagues who attended to get a global view of the state of the art on the applications of THz for CBRN and Explosives' Detection and Diagnostics and provided an environment to discuss joint research and proposal applications; cooperation projects have been submitted based on discussions that took place during this meeting.

Prague, Czech Republic   Mauro Fernandes Pereira
Abu Dhabi, UAE

Prague, Czech Republic   Apostolos Apostolakis
August 2020

Acknowledgements

Contents

Part I
State of the Art in Sensors for the Protection of Critical Infrastructures

Chapter 1
Sensor Data Fusion and Autonomous Unmanned Vehicles for the Protection of Critical Infrastructures

Konstantinos Ioannidis, Georgios Orfanidis, Marios Krestenitis, Stefanos Vrochidis, and Ioannis Kompatsiaris

Abstract Current technology in imaging sensors offers a wide variety of information that can be extracted from an observed scene. Acquired images from different sensor modalities exhibit diverse characteristics such as type of degradation; salient features etc. and can be particularly beneficial in surveillance systems. Such representative sensory systems include infrared and thermal imaging cameras, which can operate beyond the visual spectrum providing functionality under any environmental conditions. Multi-sensor information is jointly combined to provide an enhanced representation, particularly utile in automated surveillance systems such as monitoring robotics. In this chapter, a surveillance framework based on a fusion model is presented in order to enhance the capabilities of unmanned vehicles for monitoring critical infrastructures. The fusion scheme multiplexes the acquired representations from different modalities by applying an image decomposition algorithm and combining the resulted sub-signals via metric optimization. Subsequently, the fused representations are fed into an identification module in order to recognize the detected instances and improve eventually the surveillance of the required area. The proposed framework adopts recent advancements in object detection for optimal identification by deploying a deep learning model properly trained with fused data. Initial results indicate that the overall scheme can accurately identify the objects of interest by processing the enhanced representations of the fusion scheme. Considering that the overall processing time and the resource requirements are kept in low levels, the framework can be integrated in an automated surveillance system comprised by unmanned vehicles.

K. Ioannidis (✉) · G. Orfanidis · M. Krestenitis · S. Vrochidis · I. Kompatsiaris
Information Technologies Institute-Centre for Research and Technology Hellas,
Thessaloniki, Greece
e-mail: kioannid@iti.gr; g.orfanidis@iti.gr; mikrestenitis@iti.gr; stefanos@iti.gr; ikom@iti.gr

1.1   Introduction

Advanced surveillance applications commonly employ multimodal imaging sensors to enhance the exploitation performance and expand the functionalities of vision systems under any environmental conditions, target variations and viewpoint obscurations. Different sensors are exploited to ensure a wider spectral coverage and reliable imaging even in adverse acquisition conditions. The main drawback of the additional robustness is a considerable increment of the image data that are required to be processed simultaneously committing valuable computational resources. Multi-sensor image fusion deals with this data overload by combining images of the same scene acquired using different sensors in a single, composite fused image [1]. The latter provides comprehensive information about the scene such that no multiple post-processing modules are required.

One typical example is a night vision application of context enhancement where Mid-wavelength (MWIR) or Long-wavelength (LWIR) surveillance cameras enhance objects for detection in specific environments. The emitted energy of an object is received from the infrared sensor and is converted into a temperature value based on the sensor's calibration equation and object's emissivity. However, these sensors are not sensitive to the low temperature background while sensors capturing visual spectrum can provide a relatively clear perspective of the environment. On the contrary, visual representations display increased sensitivity in illumination variations. Eventually, multi-sensor image fusion approaches aim at multiplexing all the information across the electromagnetic spectrum for applications such as monitoring critical infrastructures.

Considering the recent advancements and their increased utilization in multiple applications, unmanned vehicles can be enhanced with additional functionalities and operational capabilities if the overall system could process such fused representations. The effectiveness of visual related tasks in robotics could be significantly increased leading to a system with improved operability. For surveillance applications, relevant systems should operate under diverse operational conditions in order to optimize the protection of the desired area, especially when the latter involves critical infrastructures. In this chapter, we propose a complete framework (Fig. 1.1) that combines two individual modules in order to accomplish optimal surveillance of
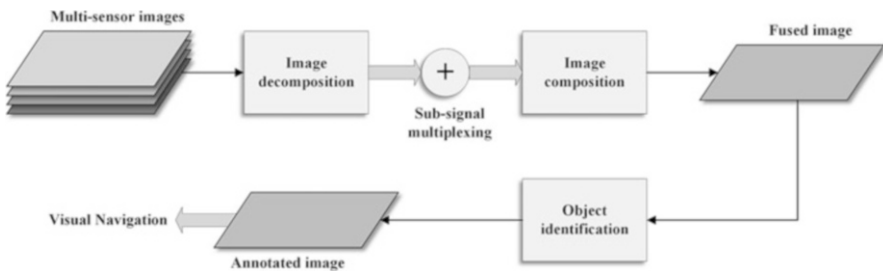
Fig. 1.1 Enhanced identification framework

critical infrastructures by utilizing unmanned vehicles and their sensors. Towards this objective, a multi-sensor image fusion algorithm is initially inserted to multiplex the acquired information and retain the most significant features from images under different spectra. The combined representations are processed further from an object identification module in order to categorize the detected instances and increase the situational awareness of the operational personnel. The identification module relies on a state-of-the-art deep learning architecture, which exhibits sufficient accuracy for such applications. Our initial evaluation tests indicate that the framework is able to provide additional functionalities to the relevant systems. Moreover, the produced images of the multi-sensor fusion scheme are privily beneficial in visual navigation and object identification improving the corresponding accuracy.

The rest of the chapter is organized as follows. In Sect. 1.2, we present in details the multi-sensor image fusion scheme that was deployed for our framework while in Sect. 1.3, the main pillars of the object identification are provided. The identification results of the complete architecture are presented and commented in Sect. 1.4. The chapter is completed with Sect. 1.5 where conclusions are outlined.

1.2 Multi-sensor Image Fusion

Fusion of infrared and visible images has found a large utilization in both civilian and non-civilian applications. For the latter category, monitoring critical infrastructures and terrain surveillance comprise the most prominent applications due to the importance of the systems' objectives. This is attributed to significant variations between the infrared and visible light sensors. Visible images can provide more clear information regarding the background of the captured scene while, the details of the under-detection objects could not be perceived sufficiently as the visual sensor is strictly affected by lighting conditions [2]. As infrared images are responsive to thermal variations, the corresponding information can be collected without illumination constraints. Since the visible and infrared representations have complementary information relating the observation scene, image fusion could provide an enhanced scene representation towards a completely automated surveillance system.

Based on the adopted transform strategy, existing approaches can be categorized into four main classes [3]: (i) multi-scale decomposition methods, (ii) sparse representations, (iii) methods that performs fusion directly to image pixels either in spatial or transform domains and (iv) combinations of the aforementioned techniques. Another key factor that significantly affects the fusion results comprises the fusion strategy based on which eventually the pixel values are combined to produce the required representation. Multiple variations and numerous combinations have been proposed to provide enhanced scene representations properly exploited by surveillance systems.

The first approach relies on decomposing the input images based on a type of a multi-scale transform in which features are represented in a joint space-frequency domain. Subsequently, the resulted representations are combined based on a fusion

rule in which the activity level of coefficients and the correlations among adjacent pixels are considered. Finally, the inverse transformation is applied to the fused representation in order to derive the required enhanced representations. The most widely used decomposition methods involve the application of the Laplacian pyramids [4], the Discrete Wavelet Transform [5] and stationary wavelet decomposition [6]. Wavelet based transforms suffers from some fundamental shortcomings such as shift variance and aliasing leading to pure decomposition results and so, fused representations. Variations of these methods have been proposed to overcome these disadvantages including dual-tree complex wavelet [7], contourlet [8] and shearlet [9]. On the contrary, sparse representation based models display increased fusion accuracy nonetheless; their implementation requires increased computational costs and resources limiting their application in real-time surveillance systems. The sparse representation can describe the images by a sparse linear combination of atoms selected from an over-complete dictionary and representing the weighted coefficients. Initially used in [10] for fusing images, sparse representation and its variations were widely used as fusion models such as [11, 12].

In addition, numerous image fusion methods have been proposed and do not rely on either multi-scale representation or sparse representations. A fraction of these methods computes directly the weighted average of the input pixels or combines their values in other transform domains. For the first case, the required weights are determine based on the activity level of different pixels [13]. Support vector machines [14] and artificial neural networks [15] were also deployed to select the pixels with the highest activity in which the wavelet coefficients were used as features. Besides the above approaches, algorithms that initially convert the input images into other domains where fusion is applied have also been successfully evaluated. Such domains are the principal component analysis [16] and the Intensity-Hue-Saturation transform [17].

1.2.1 Image Decomposition

In general, the aforementioned approaches require a significant amount of computational resources imposing constraints for their application in demanding systems where real-time processing is a prerequisite. Despite their accuracy in combining the multi-sensor information, their application in robotic systems where resources are limited is considered impossible in many cases. Towards surpassing such constrains and delivering an appropriate solution for surveillance robots, we describe a multisensor image fusion algorithm which comprises the initial processing phase of the proposed identification framework. The method comprises a modified version of the two-dimensional version of the Empirical Mode Decomposition algorithm [18], called Fast and Adaptive Bidimensional Empirical Mode Decomposition (FABEMD) [19]. The input images are decomposed into several sub-signals which are combined based on a weighted summation scheme. The corresponding coefficients are calculated so that the entropy of each sub-signal pair is maximized.
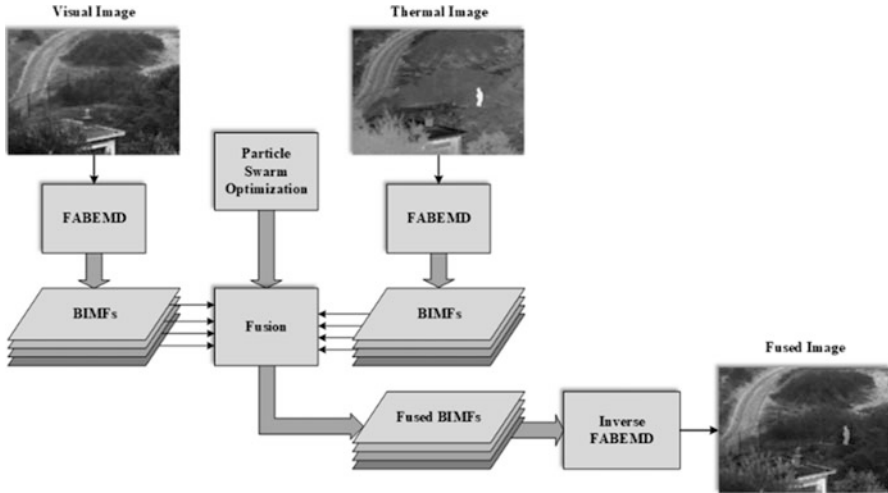
Fig. 1.2 Flowchart of the image fusion module

After multiplexing each sub-component, the fused image is produced by summing all the sub-signals. Figure 1.2 depicts a flowchart of the framework's submodule for fusing images acquired from visual and thermal sensors.

The FABEMD comprises a shifting process that decomposes the original signal into multiple sub-components with specific features, called Bidimensional Intrinsic Mode Functions (BIMFs) and a residue signal. As the process is progressed, lower frequency components are included in the subsequent BIMFs meaning that the higher frequency components of the initial signal are contained in the firstly extracted BIMFs. According to [18], the sub-components must display the following features in order to be denoted as BIMFs: **(i)** the number of local extrema (maxima and minima) and the number of zero crossing must be equal or differ by at most one, **(ii)** there should be only one oscillation mode, **(iii)** the mean value of the upper and the lower envelopes should zero or close to zero at any point and **(iv)** the BIMFs must be orthogonal among each other and as a set.

The decomposition starts with the assumption that the input image corresponds to one BIMF (for Fig. 1.3., $i = 1$). The size w and the number of the required BIMFs to extracted are predefined. Thus, the entire process will be terminated when the fixed number of BIMFs is attained. Initially, both local minima and local maxima are calculated by searching the minimum and maximum pixel value, respectively, within a window of size $w \times w$. The two extrema maps include pixel values equal to the local extrema and zeroes for all other pixels. These arrays are processed further in order to construct the upper (P_j) and the lower (Q_j) envelope of the processed signal. Both instances, P_j and Q_j, are computed with the application of appropriate order statistics and smoothing filters. For both cases, the size of the filters is determined based on the maxima and the minima maps. For each non-zero element, the Euclidean distance to the nearest non-zero element is calculated producing the
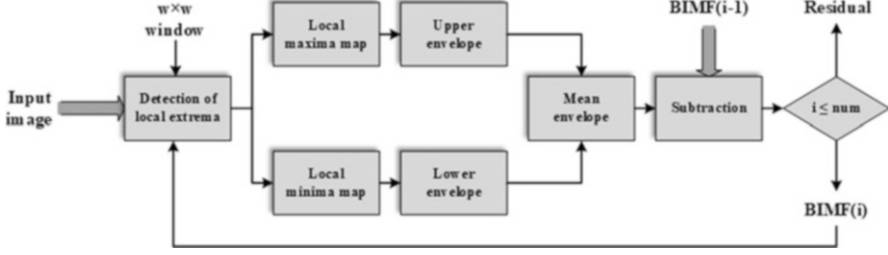
Fig. 1.3 FABEMD process

so-called adjacent maxima ($d_{adj\text{-}max}$) and minima ($d_{adj\text{-}min}$) distance array, respectively. The filter size is defined based on the four below options:

$$
\begin{aligned}
w_{en} = d_1 &= \min\left\{\min\left\{d_{adj\text{-}max}\right\}, \min\left\{d_{adj\text{-}min}\right\}\right\} \\
w_{en} = d_2 &= \max\left\{\min\left\{d_{adj\text{-}max}\right\}, \min\left\{d_{adj\text{-}min}\right\}\right\} \\
w_{en} = d_3 &= \min\left\{\max\left\{d_{adj\text{-}max}\right\}, \max\left\{d_{adj\text{-}min}\right\}\right\} \\
w_{en} = d_1 &= \max\left\{\max\left\{d_{adj\text{-}max}\right\}, \max\left\{d_{adj\text{-}min}\right\}\right\}
\end{aligned}
\tag{1.1}
$$

With the determination of the window size for envelope formation, order statistics filters MAX and MIN are applied to the corresponding BIMF F_{Tj} to obtain the upper and lower envelops, as follows:

$$
\begin{aligned}
U_{Ej}(x, y) &= \mathrm{MAX}\{F_{Tj}(s, t)\} \\
L_{Ej}(x, y) &= \mathrm{MIN}\{F_{Tj}(s, t)\}
\end{aligned}
\tag{1.2}
$$

Essentially, the application of the order statistics filters to the distance maps replaces the zero values with the nearest non-zero element within the distance determined by Eq. (1.1). The process produces abrupt transitions between adjacent pixel values failing to smoothly osculate the original signal. Thus, both maps are smoothed with the application of a smoothing filter of size w_{en}. The resulted smoothed envelopes will be processed further calculating the corresponding mean envelope which is subtracted from the BIMF(i−1) to form BIMF(i). If the BIMF index is smaller or equal to the predefined total number of the BIMFs, the subtraction result is subjected to the same shifting process. Otherwise, it is considered as the residual signal and the process is terminated. The process is considered as entirely reversible since the summation of all the extracted sub-components results to the source image. This feature is eventually utilized to produce the required fused representation of the source images. Figure 1.4 presents the extracted BIMFs for an example source image captured under the infrared spectrum.
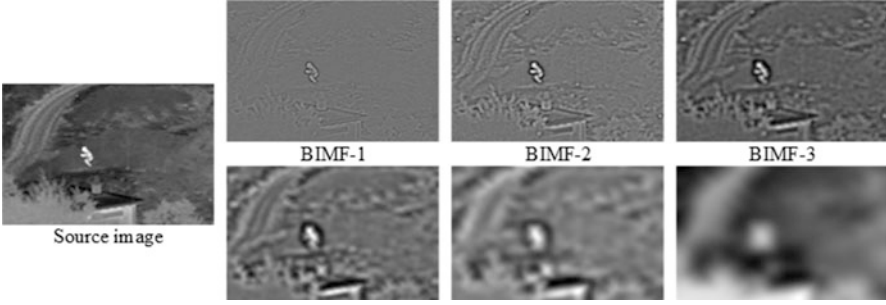
Fig. 1.4 Example of BIMFs

1.2.2 Fusion Scheme

The visible and the infrared representations are decomposed into sub-signals with the application of FABEMD producing equal number of BIMFs for both instances. The decomposed sub-signals with the same indexes are sequentially fused based on the following fusion rule:

$$F(i) = a * BIMF_{vis}[i] + b * BIMF_{the}[i] \tag{1.3}$$

where $BIMF_{vis}$ and $BIMF_{the}$ corresponds to the i BIMF of the visual and the thermal images, respectively. Variables a and b represents the weighting coefficients for the multiplexing to be defined. The main objective is to compute the values of a and b to maximize the efficiency of the rule. The problem is considered as an optimization and thus, a metric function should be defined. The presented fusion scheme aims at maximizing the entropy metric since it represents the amount of information produced by a stochastic source of data and is given by:

$$H(F) = \sum_{-i=1}^{n} P(F_i) \log [P(F_i)] \tag{1.4}$$

where F denotes the discrete random variable (fused BIMFs) and $P(X)$ the probability mass function. To identify the values of a and b which maximize the entropy, a potential solution will be to identify all combinations meaning a brute force solution. However, this requires extensive usage of resources which are limited in surveillance systems like robots. The proposed fusion scheme adopts a computational method which improves the search of the candidate solution (maximized entropy). The method, called Particle Swarm Optimization (PSO) [20], comprises a metaheuristic as it makes no assumption about the problem being optimized and can search large spaces of candidate solutions. In this work, the particles are related to the weights with the fitness function of entropy and so, candidate solutions are doublets of the form [a, b]. Figure 1.5 includes the fused BIMFs of the Fig. 1.4 example. The final
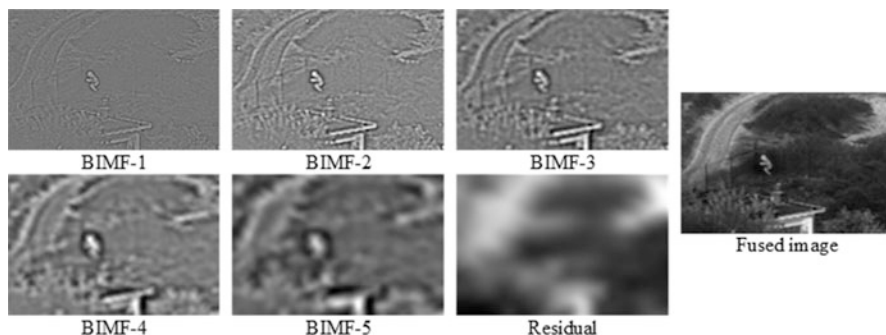
Fig. 1.5 Fused BIMFs and their final fused image
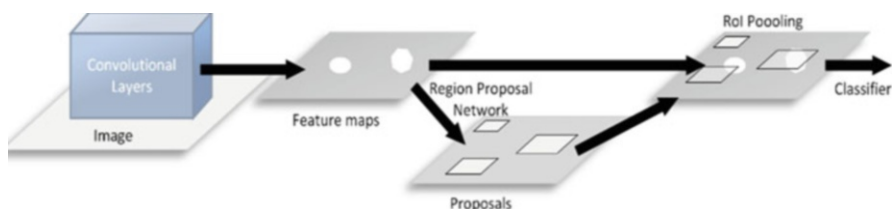
Fig. 1.6 Higher level representation of Faster R-CNN

fused image is resulted by simply adding all the resulted fused BIMFs as inverting the FAEMD process.

1.3 Object Identification for Surveillance Objectives

Overall, intelligent surveillance systems involve two sequential processes of visual data, object detection and the subsequent recognition of the detected instances. Traditional object detection methods initially extract some features (such as Histogram of oriented gradients-HOG etc.) from the captured scene and subsequently classify them based on the training data. Due to the low-level capacity of the features, such models fail to identify accurately the detected instances making their use limited in surveillance operations. The extracted features depend on image primitives such as edges, line intersections etc. which are sensitive in illumination variations etc. Such limitations constrain the identification results and decrease the accuracy of the following classification process. Misclassified instances and false positives are the most common problematic results of these models which eventually affect the results of the monitoring system (Fig. 1.6).

Recent advances in the research field overcome such type of drawbacks due to the model's capabilities to extract high-level internal features. Deep learning architectures and more specific, Convolutional Neural Networks (CNNs) can perform

sufficiently in terms of accurate identification. These characteristics render the models as suitable candidates for object identification in surveillance systems. Nonetheless, the basic CNNs require the classification of a large number of image regions significantly decreasing the processing rate and increasing the processing cost. Therefore, alterations and enhanced architectures were proposed aiming at minimizing the required scanned image regions. Region-CNN (RCNN) [21], Fast R-CNN [22] and Faster R-CNN [23] are CNN alternatives which perform significantly sufficient and in near real-time operations.

Considering the distinctiveness of such surveillance systems, our framework adopts a Faster R-CNN model in order to identify the required instances from visual data. The resulted processing time as well as the identification accuracy of the model render the approach as one of the most proper selection for such system objectives. The model was tweaked and properly trained with public available datasets as well as with manually annotated images (visual and fused) to cover a wider range of objects. In general, the deployed identification model consists of two discrete modules. The first module constitutes a deep fully convolutional network that extracts potential regions of interests while the second unit is the Fast R-CNN detector. The entire system comprises one unified, single network that produces overlayered visualizations marking the processed images with bounding boxes and one scalar value which corresponds to the identification confidence level. The Region Proposal Network (RPN) is comprised by a fully convolutional network where two selections were investigated; the first with five shareable (ZF model) and the second with 13 convolutional layers (VGG-16). Aiming at a decreased processing time framework, both networks (RPN and Fast R-CNN) share a common set of convolutional layers by default in order to mitigate the high computational cost of such architectures. Indicative identification results of the model's application in images of visual spectrum are provided in Fig. 1.7.

Fig. 1.7 Identification results processing images from visual spectrum. Left image is acquired from the OSU Thermal Pedestrian Database [24] while the rest are publicly available images from the web

1.4 Experimental Results

In general, the identification model results increased confidence levels of the detected instances when the training dataset is comprised by a vast number of images. Towards this objective, the Faster R-CNN model was trained with various datasets most of which are publicly available and include representations captured under the visible spectrum. In addition, the entire training set was enriched with images both thermal and fused resulted by the presented fusion scheme. The selection of training the model with images from different spectra is manifold. Considering that the Faster R-CNN comprises a convolutional neural network, the first layers of the network can export low and mid-level image features which are better represented in mid-infrared images. On the other hand, higher-level features are extracted more efficiently in visible spectrum and fused images thus, their classification in training and testing processes is more accurate.

For the conducted experiments, approximately 20 K images were utilized for training purposes while 130 images comprised the testing dataset. In addition, the model was trained to identify three separate instances from the fused representations which are the most common in surveillance objectives: humans, weapons and cars. Thus, three separate classes were identified. Two different sets of experiments were conducted. Initially, the model was tested with visible spectrum images while in the second case, it was evaluated with visual images in low-light conditions and with their corresponding fused representations. The overall performance was measured in terms of average precision and confidence level. Results are provided and commented below.

Figure 1.8 presents some indicative results with testing visual images. The average precision for the class "human" was equal to 0.735 while for the "weapons" class was equal to 0.383. "Car" instances were identified with an accuracy of 0.719. For representation purposes, the resulted identification confidence scores are provided in Table 1.1. per image of Fig. 1.8. All image represented in Figs. 1.7 and 1.8. are publicly available with license either Creative Commons Zero (CC0) [25] or Simplified Pixabay License [26]. In general, the model managed to identify
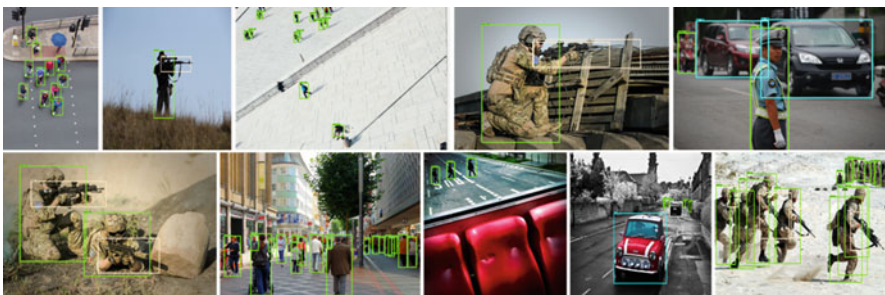
Fig. 1.8 Identification results using visible spectrum images (From top left corner to bottom right corner: Image 1–10). All images used in this Figure are publicly available images from the web

Table 1.1 Resulted confidence levels of visual example images

Objects	Image 1	Image 2	Image 3	Image 4	Image 5	Image 6	Image 7	Image 8	Image 9	Image 10
Human	0.7552	0.9365	0.9785	0.8856	0.9583	0.8019	0.7679	0.9906	0.5335	0.9777
Weapon	–	–	–	–	–	–	0.8776	0.8225	0.8030	0.7888
Car	–	0.9687	0.9025	–	0.7522	0.9660	–	–	–	–

"humans" and "car" instances accurately achieving state-of-the-art identification scores. On the contrary, low identification scores for the class "weapons" are due to the lack of proper training dataset. The detection system achieved a frame rate equal to 5 fps, one of the highest in similar schemes rendering it appropriate for near-real time application such as the surveillance of critical infrastructure.

Nonetheless, the exclusive use of images captured under the visible spectrum inserts many limitations in low-lighting conditions leading to inaccurate identification results. This was verified from the second set of the conducted experiments where both fused and their corresponding visual images were fed to the identification model. A small set of images that resulted from processing fused images and their identification bounding boxes are depicted in Fig. 1.9. The confidence levels are given in Table 1.2 as well as the identification results using only as inputs the visual corresponding images. Major differences in the detection capabilities between the two models are obvious despite the fact that both images represent the exact same scene. The fused mode can accurately identify human figures where the visual mode fails due to the scenery itself (fog, high occlusion etc.). Similar results are valid for the "car" class also. Finally, weapon detection results prove the superiority of the fused model over the visual since no proper identification was achieved.
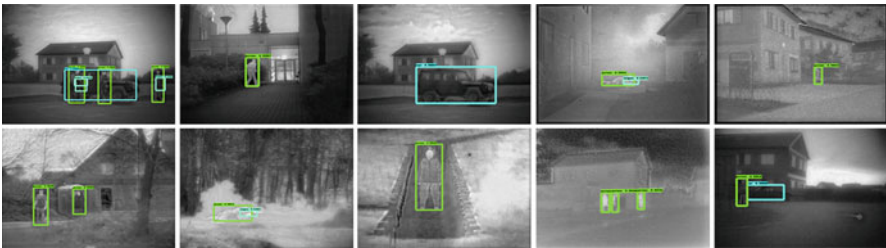
Fig. 1.9 Identification results using fused images. (From top left corner to bottom right corner: Image 1–10). Images are acquired from the TNO Image Fusion Dataset [27]

Table 1.2 Resulted confidence levels of fused example images (UD: undetectable, FD: faulty detection)

	Visual detection			Fused detection		
	Human	Weapon	Car	Human	Weapon	Car
Image 1	UD	–	0.8932	0.9982	0.5257	0.9948
Image 2	UD	–	–	0.9990	–	–
Image 3	–	–	0.9714	–	–	0.9986
Image 4	UD	UD	–	0.9992	0.6287	–
Image 5	UD	–	–	0.9982	–	–
Image 6	UD	–	0.6716 (FD)	0.9960	–	–
Image 7	UD	UD	–	0.9967	0.5195	–
Image 8	UD	–	–	0.9984	–	–
Image 9	UD	–	–	0.9950	–	–
Image 10	UD	–	UD	0.9982	–	0.9986

In general, the identification model fails to detect the required objects of interests in cases where the visual sensors fail to capture the visible light of the scene. Low levels of visible light, fog, dusty environments are the most common, non-ideal conditions of image acquisition leading to insufficient confidence levels of detection. Thus, both navigational and surveillance objectives of the unmanned vehicles are restricted affecting the ultimate goal of protecting critical infrastructures. Enhancing the inputs of the identification model with mid-infrared visualizations can transcend such constraints integrating additional capabilities in the surveillance system, as it is resulted by the conducted experiments.

1.5   Conclusions

In this chapter, a novel framework comprised by two discrete modules was presented. The initial fusion module operates as a complementary pre-processing stage to overcome limitations inserted by the exclusive usage of images under the visible spectrum. The application of the FABEMD algorithm produces multiple sub-signals of the visible and the mid-infrared representations each of which includes specific features. Every visual sub-signal is multiplexed with its corresponding mid-infrared by a weighted summation scheme. Optimum values of weights are calculated using the PSO algorithm to decrease the computational cost of an extensive search approach. The final fused representations are fed into the identification module where a Faster R-CNN was deployed. The model was properly trained in order to be able to identify the most common objects for surveillance tasks, e.g. humans, cars and weapons. Based on the conducted experiments, the identification model performs significantly more efficient due to the inclusion of the mid-infrared information into the visual representations. The desired instances are identified more accurate with increased confidence scores leading to a more precise surveillance system. In addition, the computational cost is kept at low levels rendering the framework proper for real and/or near real-time systems such as unmanned vehicles. Current work can be extended by multiplexing additional information from sources that can capture wavelengths other than visible and/or thermal. Therefore, the identification model will be further retrained with additional image datasets in order to refine it and increase the corresponding confidence levels of detection.

References

1. Stathaki T (2008) Image fusion: algorithms and applications. Academic Press, London
2. Meng F, Guo B, Song M, Zhang X (2016) Image fusion with saliency map and interest points. Neurocomputing 177:1–8
3. Li S, Kang X, Fang L, Hu J, Yin H (2017) Pixel-level image fusion: a survey of the state of the art. Inf Fusion 33:100–112
4. Mertens T, Kautz J, Van Reeth F (2007).Exposure fusion. In: 15th Pacific conference on computer graphics and applications, pp 382–390
5. Ben Hamza A, He Y, Krim H, Willsky A (2005) A multiscale approach to pixel-level image fusion. Integr Comput-Aided Eng 12(2):135–146
6. Li S, Kwok JT, Wang Y (2002) Using the discrete wavelet frame transform to merge Landsat TM and SPOT panchromatic images. Inf Fusion 3(1):17–23
7. Lewis JJ, O' Callaghan RJ, Nikolov SG, Bull DR, Canagarajah N (2007) Pixel- and region-based image fusion with complex wavelets. Inf Fusion 8(2):119–130
8. Li T, Wang Y (2011) Biological image fusion using a NSCT based variable-weight method. Inf Fusion 12(2):85–92
9. Wang L, Li B, Tian L-F (2014) Multi-modal medical image fusion using the inter-scale and intra-scale dependencies between image shift-invariant shearlet coefficients. Inf Fusion 19:20–28
10. Yang B, Li S (2010) Multifocus image fusion and restoration with sparse representation. IEEE Trans Instrum Meas 59(4):884–892
11. Li S, Yin H, Fang L (2012) Group-sparse representation with dictionary learning for medical image denoising and fusion. IEEE Trans Biomed Eng 59(12):3450–3459
12. Nejati M, Samavi S, Shirani S (2015) Multi-focus image fusion using dictionary-based sparse representation. Inf Fusion 25:72–84
13. Gangapure VN, Banerjee S, Chowdhury AS (2015) Steerable local frequency based multispectral multifocus image fusion. Inf Fusion 23:99–115
14. Li S, Kwok JT, Tsang IW, Wang Y (2004) Fusing images with different focuses using support vector machines. IEEE Trans Neural Netw 15(6):1555–1561
15. Li S, Kwok JT, Wang Y (2002) Multifocus image fusion using artificial neural networks. Pattern Recogn Lett 23(8):985–997
16. Shahdoosti HR, Ghassemian H (2016) Combining the spectral PCA and spatial PCA fusion methods by an optimal filter. Inf Fusion 27:150–160
17. Tu T-M, Huang PS, Hung C-L, Chang C-P (2004) A fast intensity-hue-saturation fusion technique with spectral adjustment for IKONOS imagery. IEEE Trans Geosci Remote Sens Lett 1(4):309–312
18. Huang NE, Shen Z, Long S, Wu MC, Shih H, Zheng Q, Yen N-C, Tung CC, Liu HH (1998) The empirical mode decomposition and the Hilbert spectrum for nonlinear and non-stationary time series analysis. Proc R Soc London A Math Phys Eng Sci 454(1971):903–995
19. Bhuiyan S, Adhami R, Khan J (2008) Fast and adaptive bidimensional empirical mode decomposition using order-statistics filter based envelope estimation. EURASIP J Adv Signal Process:1–18
20. Kennedy J, Eberhart R (1995) Particle swarm optimization. Int Conf Neural Netw 4:1942–1948
21. Girshick R, Donahue J, Darell T, Malin J (2014) Rich feature hierarchies for accurate object detection and semantic segmentation. In: Proceedings of the on IEEE conference on computer vision and pattern recogn, pp 580–587
22. Girshick R (2015) Fast R-CNN. In Proceedings of the IEEE international conference on computer vision, pp 1440–1448
23. Ren S, He K, Girshick R, Sun J (2015) Faster R-CNN: towards real-time object detection with region proposal networks. IEEE Trans Pattern Anal Mach Intell 39(6):1137–1149

24. Davis JW, Keck MA (2005) A two-stage template approach to person detection in thermal imagery. In: 2005 Seventh IEEE Workshops on Applications of Computer Vision (WACV/MOTION'05)-Volume 1, January, vol. 1, pp 364–369. IEEE
25. Creativecommons.org (2020) Creative commons – CC0 1.0 Universal. [Online] Available at: https://creativecommons.org/publicdomain/zero/1.0/deed.en. Accessed 31 Aug 2020
26. pixabay.com (2020) Simplified pixabay license. [Online] Available at: https://pixabay.com/service/license/. Accessed 31 Aug 2020
27. Toet A, IJspeert JK, Waxman AM, Aguilar M (1997) Fusion of visible and thermal imagery improves situational awareness. Displays 18(2):85–95

Part II
Beyond QCLs, ICLs and Superlattices: Competing Technologies for Detection of Explosives and CBRN

Chapter 2
High Power, Widely Tunable, and Beam Steerable Mid-infrared Quantum Cascade Lasers

Manijeh Razeghi and Wenjia Zhou

Abstract After more than 20 years of development, quantum cascade lasers (QCLs) have become the leading laser source emitting in the mid-infrared spectrum region between 3 and 12μm, where CBRN and explosives have strong absorption signatures. The Center for Quantum Devices at Northwestern University currently holds the record for both the highest room temperature continuous wave output power of 5.1 W and the most efficient QCL of 53% wall plug efficiency operating at cryogenic temperature. This book chapter presents our latest development results on mid-infrared QCLs with wavelength tuning and high power beam steering capabilities, which significantly enhances QCL's suitability for remote spectroscopy and sensing applications.

2.1 Introduction

Trace amount of CBRN and explosives could be remotely sensed by mid-infrared (MIR) absorption spectroscopy because of their characteristic vibration lines reside in the region. Historically, the development of MIR spectroscopy sensing was slow due to the lack of room temperature, compact, wavelength tunable and high power MIR laser sources. Before the demonstration of quantum cascade lasers (QCLs) [1], only optical parametric oscillators (OPO), lead salt lasers and CO_2 lasers could emit in the MIR. However, OPOs are bulky, lead salt lasers require cryogenic cooling, and CO_2 laser could emit at only a few specific wavelengths. On the other side, QCLs are intrinsically compact since they are based on semiconductor materials. Also, because it is a unipolar device, QCLs is free of non-radiative Auger recombination, which limits room temperature performance of traditional MIR laser diodes.

M. Razeghi (✉) · W. Zhou
Center for Quantum Devices, Department of Electrical Engineering and Computer Science, Northwestern University, Evanston, IL, USA
e-mail: razeghi@eecs.northwestern.edu

21

Furthermore, emission wavelength of QCLs could be tuned in the entire MIR with bandgap engineering which is to change the thickness of multiple quantum wells [2].

The Center for Quantum Devices at Northwestern University has demonstrated high power room temperature continuous wave (CW) InP based QCLs between the 3 and 12μm wavelength range [3, 4]. With steady optimization of the quantum structure design, improvement of material quality and processing techniques, a high room temperature wall plug efficiency (WPE) of 27% was achieved under pulsed mode operation around 4.8μm [5]. Under the proper thermal management, including the use of buried ridge waveguide and epi-layer down bonding, the same laser emits 5.1 W under CW operation at room temperature. It is worth noting that a WPE of 53% was achieved at 80 K by using a single injector design, which means the laser emits more light than heat [6]. The successful development of single-element QCLs with unprecedented performance motivates us to integrate multiple QCL components on a single chip to realize more functionalities. These includes the integration of multiple sampled grating distributed feedback (SGDFB) tunable QCLs for broadband wavelength tuning [7–9] and monolithic beam steering realized by constructing an on-chip QCL phased array [10, 11].

2.2 Monolithic Tunable QCL Array Based on a Heterogeneous Broadband Wafer

Due to the intersubband nature of QCLs, it has a delta-shape gain profile, which makes it possible to construct heterogeneous QCLs with a broadband spectral emission [12–14]. The heterogeneous QCL active region consists of multiple stacks of discrete quantum cascade stages emitting at different wavelengths, grown together during a single epitaxial growth run. The overall net gain of the heterogeneous QCL is obtained by summation of gain spectrum from each quantum cascade stage weighted by appropriate modal confinement factors at each wavelength. We have designed a five sub-core QCL with peak gain energies spaced ~20 meV apart to form a heterogeneous QCL core that targets 6–10μm wavelength range. The designed laser cores are based on the strain balanced $Al_{0.63}In_{0.37}As/Ga_{0.35}In_{0.65}As/Ga_{0.47}In_{0.53}As$ material system as shown in Fig. 2.1a. As shown in Fig. 2.1b, the gain curve of the heterogeneous QCL is predicted to be broad and flat, which allows selection of the laser emitting wavelength over a wide range with an appropriate feedback mechanism. In order to characterize the gain bandwidth and flatness of the designed active region, the grown wafer is characterized with a distributed feedback (DFB) laser array [15]. Electroluminescence (EL) of the heterogeneous QCL wafer is shown in Fig. 2.1c. The EL spectrum has a full width at half maximum (FWHM) of 1050 cm^{-1} with a center near 1420 cm^{-1}. As shown in Fig. 2.1d, single mode DFB emission between 5.8 and 9.9μm is obtained from a twenty-one 3 mm long DFB laser array. The current threshold is relatively flat between 5.8 and 9.0μm. The
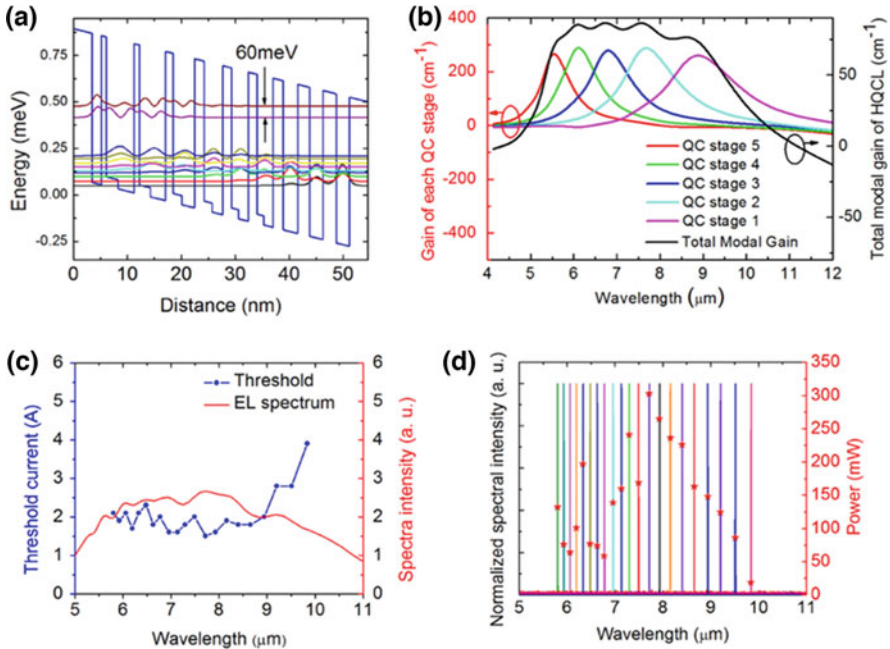
Fig. 2.1 (**a**) Conduction band diagram and relevant wavefunctions for one emitting stage of a QCL based on $Al_{0.63}In_{0.37}As/Ga_{0.35}In_{0.65}As/Ga_{0.47}In_{0.53}As$ material system. (**b**) Simulated gain curve of a five-core heterogeneous QCL. (**c**) Overlay plots of EL curve and single mode DFB laser array threshold as a function of wavelength for the five-core QCL design. (**d**) Overlay plot of compiled emission spectra and single mode peak power as a function of wavelength

maximum power output is about 300 mW per facet at a wavelength of 7.7µm, and most DFB lasers have power output above 100 mW.

Based on the broadband heterogeneous QCL wafer, a wavelength selection mechanism can be implemented for achieving single wavelength emission across the gain bandwidth. This can be accomplished using a SGDFB laser array [16]. The idea is to take many (N) discrete tunable SGDFB lasers with incrementally different wavelengths and integrate them onto one chip. Each laser can be operated independently, and the final monolithic tuning range is N times the tuning range of a single element. As no mechanical elements are present, there is no external alignment necessary, and the tuning (electrically-controlled) is extremely fast. This is especially useful for step changes in wavelength, which simply switches between lasers in the array and can be performed almost as quickly as tuning of an individual element.

Figure 2.2a shows the schematic of the monolithic tunable QCL source. Each SGDFB laser is comprised of a series of short gratings periodically sampled on the two sections with two different sampling periods. The eight lasers are routed to a single output using a three-stage tree array Y-junction and S-bend waveguides. A
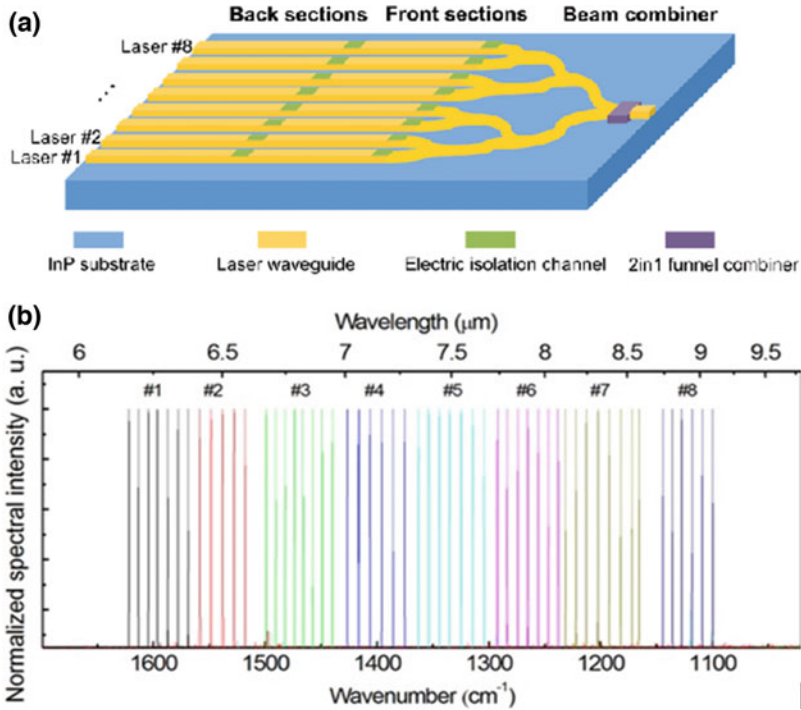
Fig. 2.2 (**a**) Schematic of the wavelength tunable QCL source with monolithically integrated sampled grating distributed feedback (SGDFB) laser array and beam combiner. (**b**) Compiled tuning spectra of the eight SGDFB laser array emitting from a single aperture. The tuning ranges from 1100 to 1622 cm^{-1}. There are eight sets of peaks, represented in different colors, corresponding to laser #1 through #8, respectively

critical consideration for the beam combiner design is the preservation of the fundamental transverse mode. Higher order mode operation has been reported for Y-junction QCLs [17]. As a solution, we replaced the last Y-junction with a two-in-one funnel combiner [18]. The funnel combiner is designed to partially filter out high order modes that may be present at the input waveguide. Mode filtering improves as the relative angle between the input and output waveguide decreases, though there is some tradeoff in power transmission. To use the beam combiner as a single pass amplifier, the front facet is AR-coated with 1300 nm Y_2O_3. During operation, one laser at a time in the SGDFB laser array was selectively biased, and the spectrum of the beam coming out of the single aperture beam combiner was measured. Synchronized pulse currents with 100 ns pulse width and 5% duty cycle (500 kHz repetition rate) were first applied, with separate drivers, to both sections of the selected SGDFB laser to reach threshold (~21 V). The voltage was kept the same on both sections and was further increased until single mode emission could be maintained (~24 V, $I = 1.35I_{th}$). Because the beam combiner section has the same gain material as the laser sections, a third synchronized pulsed current was applied to the beam combiner

section for power amplification. Wavelength tuning is realized by applying additional independent CW currents to the two SGDFB laser sections. The injected CW currents locally change the section temperature, which leads to a change of the effective refractive index. Figure 2.2b shows the combined tuning of 520 cm^{-1} between 6.2 and 9.1 μm of the beam coming out of the single aperture beam combiner.

In order to automatically scan across all available wavelengths for chemical spectroscopy, a self-contained tunable laser system was designed and built as shown in Fig. 2.3a. This system works off a single 48 V DC power supply and contains all the electronics necessary to drive the individual lasers within the array and coordinate the driving of the laser array to produce a desired wavelength. The laser beam comes out as a single collimated output from the front of the system. The system was calibrated using custom automatic calibration software, which records the laser output spectrum with a Fourier transform infrared spectrometer (FTIR) as a function of tuning current combinations. To support high speed scanning, each discrete scan-state is downloaded to a dedicated random access memory chip on the control board. The electronic hardware supports a scan rate of up to 32 kHz. Figure 2.3b shows the setup for an absorption spectroscopy measurement, which
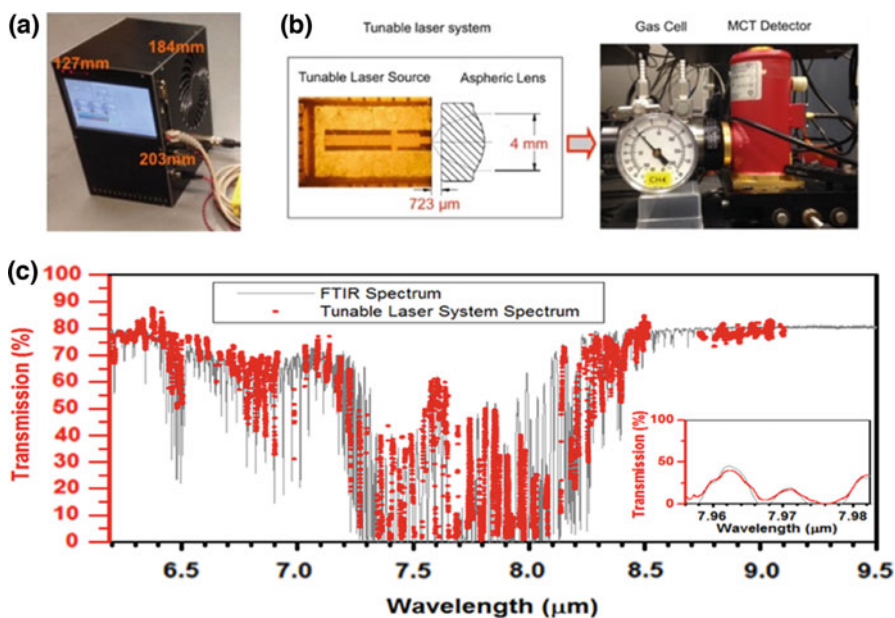
Fig. 2.3 (**a**) Picture of the tunable laser system. (**b**) Optical microscope picture of the tunable laser array with a schematic view of the aspheric lens used to collimate the output beam (left). The laser chip is 2 mm wide and 8.5 mm long, and the output beam diameter is ~4 mm. Also shown are the 15 cm long gas cell filled with methane and the liquid nitrogen cooled mercury cadmium telluride detector used for measurement (right). (**c**) Comparison of the spectrum measured with the tunable laser system (red dots) to the expected spectrum measured with the FTIR. The inset shows a zoomed in region showing the excellent agreement

consists of the tunable laser system, the gas cell, and a cryogenic mercury cadmium telluride detector. In order to measure the broadband absorption spectroscopy of methane in the gas cell, the tunable laser system was scanned from 6.2μm to 9.1μm with a step size of 0.1 nm at a scan rate of 512 Hz, which is limited by the maximum data-sampling rate of our lock-in amplifier. Figure 2.3c shows a comparison of the reference spectrum measured by FTIR (grey) to that measured with the tunable laser system (red points). In general, the tunable laser system is able to accurately measure the spectrum of methane. In particular, the inset of Fig. 2.3c shows excellent agreement with some of the fine spectral features.

2.3 High Performance Broadband Monolithic Tunable QCLs

After the first successful demonstration of broadband monolithic tunable QCLs, efforts were put for increasing the output power of the device [8]. The first optimization is to increase the gain of the broadband wafer. In comparison to the wafer used in the initial demonstration, the overlap between upper laser level and underlying energy levels was largely improved by decreasing the width of the first well of the active region. This is accompanied by a decrease in upper laser level lifetime from 1.55 ps to 1.35 ps and therefore an increase in maximum operating current at the resonant electric field, for similar doping density. Compared to the first demonstration, simulated gain is increased by 20% on average. Experimentally, single mode DFB emission between 5.8 and 9.9μm under pulsed mode operation is obtained from a 3 mm long cavity laser array. The maximum peak power output is about 500 mW per facet at a wavelength of 7.0μm, and most DFB lasers have power output above 200 mW, which is twice as much as the initial wafer.

The beam combiner design is optimized to decrease power transmission loss of the input from the SGDFB laser array. The power transmission of the fundamental mode for each input channel is simulated separately as a function of input wavelength between 6 and 10μm. It is found that due to interference effect, overall power transfer to the output facet shows resonant features, which can either increase or decrease transmission as function of the input waveguide position or wavelength. There are spectral regions, similar in width to the targeted spectral region of each tunable laser (65 cm^{-1}), that the beam combiner has increased transmission. Based on the simulation, we have coupled the tunable lasers to the beam combiner channels which maximize transmission over the specific laser tuning range instead of simply coupling the lasers to combiner channels in an ascending order to increase the power transmission in the specific wavelength range.

The extent of power amplification by the active beam combiner section is limited by its self-lasing. To increase the power amplification, a broadband AR-coating on the front facet of the beam combiner is necessary to inhibit the self-lasing. Therefore, we designed a broadband AR-coating for 6–10μm using a double layer structure of

ZnSe/MgF$_2$ deposited by ion beam deposition. The reflectivity of the facet coating was simulated with a transfer matrix method. The optimum thickness is found to be 800 nm ZnSe and 1400 nm MgF$_2$, but a high-quality AR-coating with less than 2% reflectivity can be achieved with a wide range of the layer thicknesses. Experimentally, the reflectivity between 6 and 10 µm is measured to be below 2% and the minimum reflectivity is as low as 0.1%.

Figure 2.4 shows the combined tuning of 529 cm^{-1} between 6.1 and 9.2 µm for the light coming out of the single aperture of the beam combiner. High SMSR of 25-30 dB are achieved for most conditions, limited by the noise floor of the measurement system. The true linewidth of single mode emission was not measured accurately, and is limited by the resolution of our spectrometer (0.125 cm^{-1}). The wavelength repeatability is measured to be better than 0.1 cm^{-1} when repeatedly turning on and off a selected laser. The high stability is attributed to a well-regulated TEC temperature and precisely controlled driving currents. The average power as a function of wavelength is measured by scanning the laser from 6.1 to 9.2 µm. The SGDFB laser duty cycle is 3.75%, which is used to calculate the peak power per pulse. As also shown in Fig. 2.4, the mean peak power is 25 mW with a range from 8 to 65 mW. The output power is one order of magnitude higher than the previous demonstration.
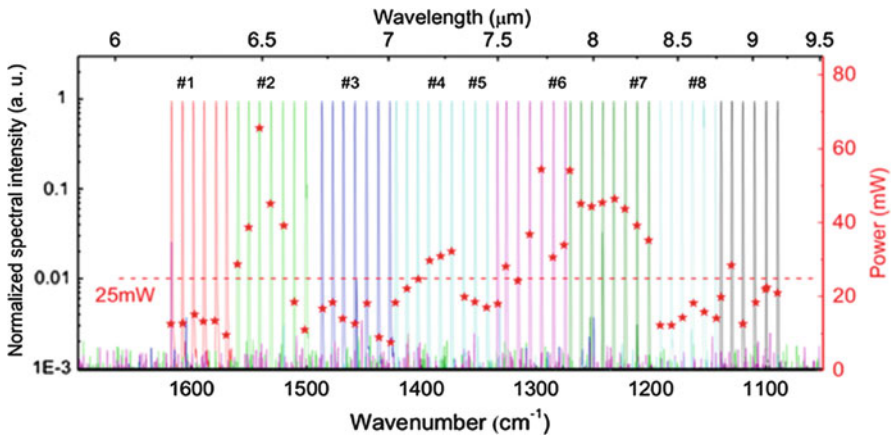
Fig. 2.4 Overlay plot of the compiled tuning spectra of the eight SGDFB lasers emitting from a single aperture and the measured output power. The tuning ranges from 1089 to 1617 cm^{-1}. There are eight sets of peaks, represented in different colors, corresponding to laser #1 through #8, respectively

2.4 High Power Phase-Locked QCL Arrays

Power scaling of QCLs in pulsed mode has been demonstrated using broad area lasers (200μm ridge width) with more than 200 W peak power [19]. In addition, diffraction limited beam has been achieved with an angled cavity design, which led to a record brightness of 156 MW/cm^{-1} sr^{-1} [20]. However, considering the high input power density of QCLs, for specific applications where high average output power is preferred, a narrow laser ridge width is necessary for efficient heat dissipation. Therefore, phase-locking of narrow ridge laser arrays is being widely developed to coherently scale the average output power with good beam quality. Furthermore, besides providing a high output power, phase locked laser arrays could be used for monolithic beam steering by actively controlling the phase relation of the laser elements within the array.

Multimode interferometers (MMIs) have long been used for efficient beam splitting and combining in telecommunications applications [21]. When designed properly, for a narrow bandwidth, MMIs can provide almost lossless 3 dB power splitting and beam combining for the in-phase mode and suppress completely the out-of-phase mode. We have developed a QCL-based MMI tree array which is capable of producing phase-locked, high power emission in the MIR. Figure 2.5a shows the schematic structure of the MMI with input and output waveguide widths of 5μm, which is designed for λ = 4.8μm laser emission. The two output waveguides have a center to center distance of 10μm. According to the theory of MMI, the optimal length for 3 dB power splitting is $L_{MMI} = n_e W_e^2 / 2\lambda$, where n_e is the effective index of the laser waveguide and W_e is effective width of the MMI. We have chosen a physical MMI width of 20μm which is acceptable for high duty cycle or even
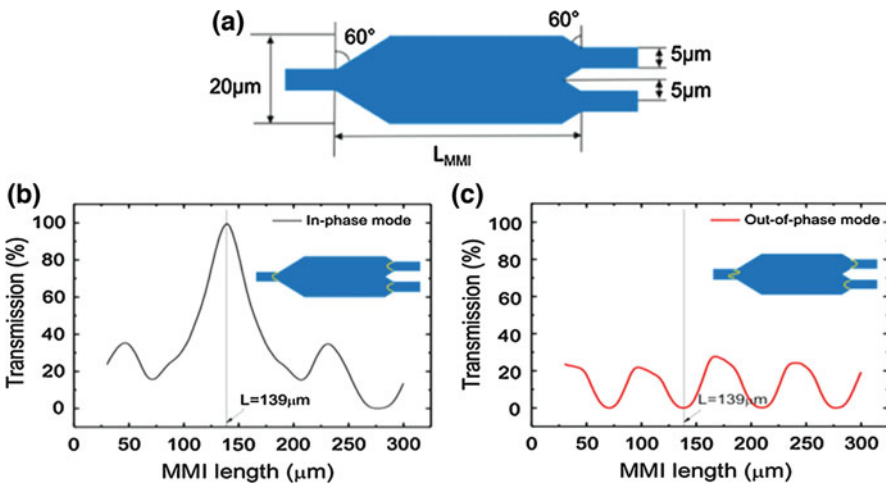
Fig. 2.5 (a) Schematic structure of the multimode interferometer (MMI) with dimensions and tapering shown. Simulated transmission characteristics of the MMI for (b) in-phase and (c) out-of-phase supermode as a function of MMI length

CW operation of a QCL. The effective MMI width, which takes into account the transverse mode penetration into the surrounding SiO_2 layer, is therefore $W_e = W + \lambda/\pi/(n_{core}^2 - n_{SiO2}^2)^{1/2} = 20.5\mu m$ for a standard, TM-polarized QCL ridge waveguide. Based on W_e, the calculated optimum MMI length is 139µm for $n_e = 3.18$ and $\lambda = 4.8\mu m$. The transmission characteristics of the MMI as a function of its length are simulated by the beam propagation method. For the in-phase (out-of-phase) supermode, a fundamental mode (first order mode) input is launched into the single waveguide side. The power of the fundamental mode at the two output waveguides is monitored separately and added together to calculate the power transmission in both cases. As shown in Fig. 2.5b, c, the simulation result shows that power transmission for the in-phase supermode has a maximum transmission reaching almost 100% for the MMI length of 139µm, while the out-of-phase mode transmission is nearly 0. For suppressing reflection of the out-of-phase supermode, the input and output sides of the MMI waveguide are tapered by 60°.

Figure 2.6 shows the schematic structure of a Fabry-Perot (FP) laser and MMI-based tree arrays with two, four and eight elements. The array pitch size is chosen as 100µm for the initial demonstration, but it can be chosen arbitrarily. For this experiment, the tree array MMI section length is 2.6 mm and the straight cavity section length is 2.4 mm. The bending radius of the curved waveguides is 1000µm. The device area ratio with respect to a single 5 mm long FP laser is 1.64, 3.05, 6.06 for the two, four and eight-element laser arrays, respectively. The active region of the wafer is based on a high-efficiency design targeting a emission wavelength of ~4.8µm. The laser core has 40 stages and is of 1.6µm thick. The waveguide is etched by a 'Cl2/Ar/H_2' plasma to preserve the precise shape of curved waveguides and MMIs.
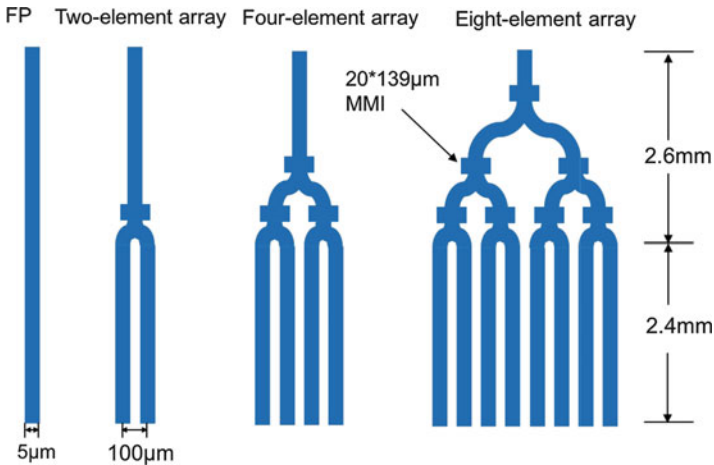
Fig. 2.6 Schematic geometry of a 5 mm long FP QCL and MMI-based tree-arrays with two, four and eight-elements (not to scale)
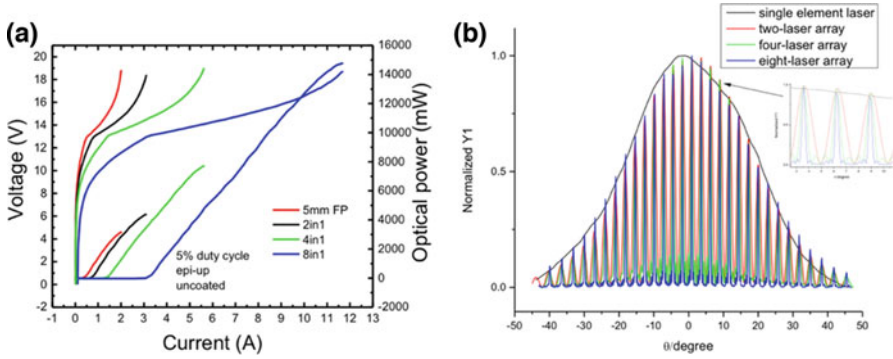
Fig. 2.7 Power-current-voltage (**a**) and far field (**b**) measurement result of the FP laser and beam combiner laser arrays

As shown in Fig. 2.7a, excellent power scaling has been achieved for the MMI combined laser arrays. The fact that all lasers have a close threshold current density (1.8 kA/cm^2) and slope efficiency (1.88 W/A) indicates a low coupling loss the MMIs. The maximum output power is 3.2 W, 4.5 W, 7.4 W and 15 W for the FP, two-element, four-element and eight-element laser array respectively. The power scaling factor is 1.4, 2.3 and 4.7 for the two-element four-element and eight-element laser array respectively, while the area ratio is 1.6, 3.0 and 6.1.

Far fields of the FP laser and laser arrays were measured to demonstrate phase-locking of the arrays, as shown in Fig. 2.7b. The envelopes of measured far field all have a full width at half maximum (FWHM) of 42.5°, which matches the 5µm ridge width. For the arrays, there are additional peaks with a space of about 2.6°, which matches the 100µm laser separation. With increasing number of elements in the array, the linewidth of additional peaks gets smaller. Since the far field distributions of the laser arrays exhibit only one set of peaks with a central maximum, we conclude that the laser arrays operate via the in-phase supermode.

2.5 Single-Mode, High-Power, Phase-Locked QCL Arrays

Since it is advantageous to have a single-mode laser source for non-mechanical beam steering and spectroscopy applications, we utilized on-chip integration of a DFB seed laser, a low-loss tree-array MMI power splitter, and an optical amplifier array to demonstrate single-mode, 16-channel, λ = 4.8µm phase-locked amplifier arrays, as shown in Fig. 2.8a [11]. The device is monolithic and has a compact size of 5 mm × 1 mm. The DFB seed section is 0.5 mm long and first order DFB grating with a duty cycle of nearly 50% and grating period of 755 nm is patterned onto the grating layer. The simulated refractive index for the etched and un-etched part of the grating is 3.17 and 3.194 respectively, and the coupling strength is therefore $\kappa = \frac{1}{\Lambda} \cdot \frac{\Delta n}{n_{eff}} = 100$ cm^{-1}, where Λ is the grating period, Δn and n_{eff} are the refractive
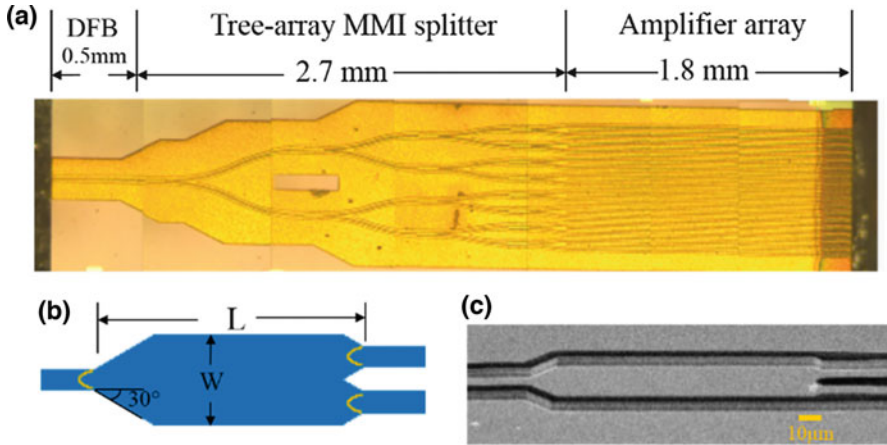
Fig. 2.8 Single mode 16-channel optical phased array. (**a**) Composite microscope image of the phase-locked quantum cascade amplifier (QCA) array integrated with a DFB seed section, and a tree array MMI based power splitter. (**b**) Schematic structure of a 1 × 2 MMI splitter (not to scale). (**c**) Scanning electron microscope image of a fabricated MMI splitter

index step and the effective refractive index. The product of the DFB section length and coupling strength κL is 5, which is a moderate number for achieving a good output power and mode discrimination. The output of the DFB seed is evenly split into a 16-channel amplifier array, which has a ridge width of 6μm and a separation of 50μm. The amplifier array has a 4° facet termination for suppressing light reflection, when AR-coated. Respectively, Fig. 2.8b, c) shows the schematic structure and scanning microscope image of a 1 × 2 MMI for power splitting, which has an identical design and fabrication process as the one described in the previous section.

Figure 2.9a shows the power-current-voltage characteristics of a 16-channel phase-locked quantum cascade amplifier (QCA) array under pulsed mode operation. With epi-layer up bonding, 1% duty cycle operation, and a pulse width of 200 ns, a peak power of 30 W was obtained from the multi-aperture facet side. The lasing current threshold is 15A, and the slope efficiency is 2.72 W/A. In comparison to a 5 mm long, 6μm wide FP laser, which is fabricated by the same process and emits up to 4.7 W (two facets), the output power enhancement factor is 6.4, while the area ratio of the OPA to the FP laser is 9.4. Figure 2.9b shows the emission spectrum of the OPA measured at different current conditions. Near the lasing threshold ($I = 1.25 I_{th}$), the FWHM of the spectrum is only 4 nm. Near the rollover input current of $I = 26.4A$, the FWHM of the spectrum is only 7 nm.

The device architecture is also suitable for high duty cycle operation thanks to the narrow ridge width of the amplifier array and their 50μm separation. One laser was epi-layer down bonded to a diamond submount prior to being bonded to a copper submount for testing at high duty cycles. Figure 2.10a shows the maximum average output power achieved as a function of the duty cycle. At 7.5% duty cycle, an average output power of 1.2 W is achieved. The inset of Fig. 2.10a shows the
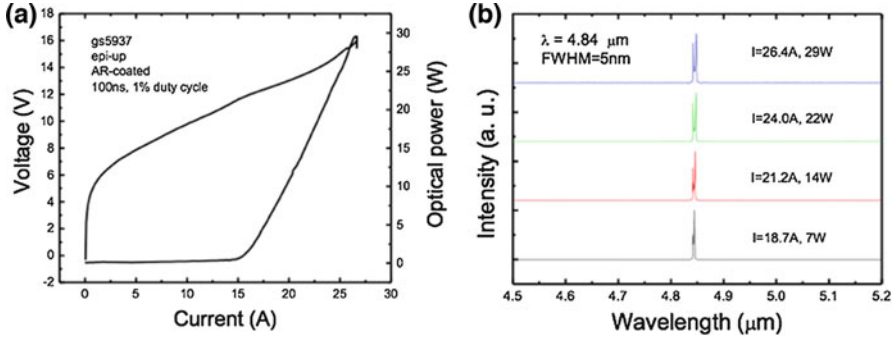
Fig. 2.9 (**a**) Power-current-voltage (PIV) curves of a 16-channel 4.8μm single mode phase-locked QCA array under pulsed mode operation (1% duty cycle). (**b**) Spectrum measurement result of the QCA array under different current conditions plotted in logarithmic scale. Spectra are offset vertically for clarity
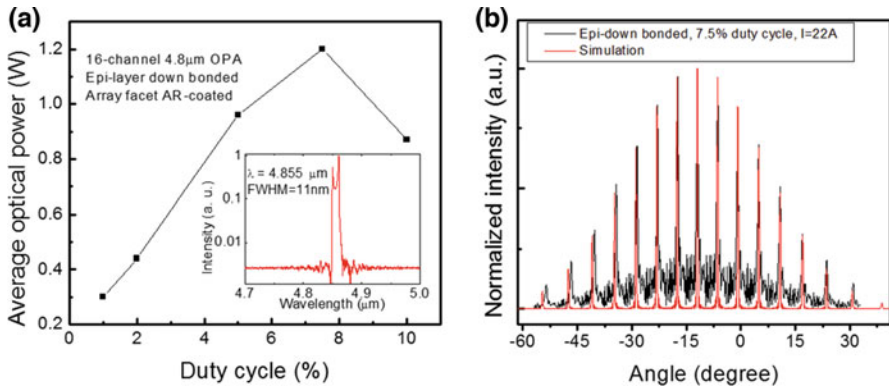
Fig. 2.10 (**a**), Average power of an epi-layer down bonded 16-channel OPA as a function of pulsed operation duty cycle. The inset shows the emission spectrum of the device operating at the roll-over current under 7.5% duty cycle. (**b**) Far field distributions of the 16-channel, single mode phase-locked array operating at the rollover current under 7.5% duty cycle

emission spectrum of the device operating at the roll-over current under 7.5% duty cycle. The peak width is only 11 nm, and the SMSR is over 25 dB. Figure 2.10b shows the measured far field distribution of the device operating at the roll-over current under 7.5% duty cycle. It can be clearly seen that the far field distribution has a Gaussian shape envelope and has modulation peaks which indicate phase-locking behavior of the array output. The far field radiation pattern is compared to the 16-slit Fraunhofer diffraction theory, and an excellent match is achieved between the measurement result and simulation.

2.6 Summary

In this chapter, we have first described a monolithic tunable QCL between 6.2 and 9.1μm by integrating a SGDFB laser array with an on-chip beam combiner. With our tunable laser system, random wavelength access and fast tuning were demonstrated with good stability. Then we have demonstrated a high performance tunable QCL in a similar tuning range with up to 65 mW output power by increasing the gain of the heterogeneous broadband wafer, optimizing the waveguide design and using a broadband AR-coating. We have also demonstrated MMI-based, phase-locked QCL arrays with up to 15 W output power. In-phase supermode operation has been demonstrated over the entire operating range, thanks to the strong selectivity the MMI exhibits between in-phase and out-of-phase supermodes. Lastly, we described single mode, 4.8μm, 16-channel, optical phased arrays with up to 30 W peak output power by including a DFB seed laser. The developed high performance monolithic tunable and high-power beam steerable QCLs will enable new strategies and opportunities for MIR spectroscopy and chemical sensing.

References

1. Faist J, Capasso F, Sivco DL, Sirtori C, Hutchinson AL, Cho AY (1994) Quantum cascade laser. Science 264(5158):553–556. https://doi.org/10.1126/science.264.5158.553
2. Bandyopadhyay N, Bai Y, Slivken S, Razeghi M (2014) High power operation of lambda similar to 5.2-11 mu m strain balanced quantum cascade lasers based on the same material composition. Appl Phys Lett 105(7):071106
3. Razeghi M, Lu QY, Bandyopadhyay N, Zhou W, Heydari D, Bai Y, Slivken S (2015) Quantum cascade lasers: from tool to product. Opt Express 23(7):8462–8475
4. Razeghi M, Zhou WJ, Slivken S, Lu QY, Wu DH, McClintock R (2017) Recent progress of quantum cascade laser research from 3 to 12 mu m at the Center for quantum devices [invited]. Appl Opt 56(31):H30–H44. https://doi.org/10.1364/Ao.56.000h30
5. Bai Y, Bandyopadhyay N, Tsao S, Slivken S, Razeghi M (2011) Room temperature quantum cascade lasers with 27% wall plug efficiency. Appl Phys Lett 98(18):181102
6. Bai YB, Slivken S, Kuboya S, Darvish SR, Razeghi M (2010) Quantum cascade lasers that emit more light than heat. Nat Photonics 4(2):99–102
7. Zhou WJ, Bandyopadhyay N, Wu DH, McClintock R, Razeghi M (2016) Monolithically, widely tunable quantum cascade lasers based on a heterogeneous active region design. Sci Rep 6:25213
8. Zhou WJ, Wu DH, McClintock R, Slivken S, Razeghi M (2017) High performance monolithic, broadly tunable mid-infrared quantum cascade lasers. Optica 4(10):1228–1231. https://doi.org/10.1364/Optica.4.001228
9. Razeghi M, Zhou W, McClintock R, Wu D, Slivken S (2017) Progress in monolithic, broadband, widely tunable midinfrared quantum cascade lasers. Opt Eng 57(1):011018
10. Zhou W, Slivken S, Razeghi M (2018) Phase-locked, high power, mid-infrared quantum cascade laser arrays. Appl Phys Lett 112(18):181106. https://doi.org/10.1063/1.5028281
11. Zhou WJ, Wu DH, Lu QY, Slivken S, Razeghi M (2018) Single-mode, high-power, mid-infrared, quantum cascade laser phased arrays. Sci Rep 8:14866. https://doi.org/10.1038/s41598-018-33024-7

12. Gmachl C, Sivco DL, Baillargeon JN, Hutchinson AL, Capasso F, Cho AY (2001) Quantum cascade lasers with a heterogeneous cascade: two-wavelength operation. Appl Phys Lett 79(5):572–574
13. Bandyopadhyay N, Chen M, Sengupta S, Slivken S, Razeghi M (2015) Ultra-broadband quantum cascade laser, tunable over 760 cm(−1), with balanced gain. Opt Express 23(16):21159–21164
14. Lu QY, Razeghi M, Slivken S, Bandyopadhyay N, Bai Y, Zhou WJ, Chen M, Heydari D, Haddadi A, McClintock R, Amanti M, Sirtori C (2015) High power frequency comb based on mid-infrared quantum cascade laser at lambda similar to 9μm. Appl Phys Lett 106(5):051105
15. Lu QY, Bai Y, Bandyopadhyay N, Slivken S, Razeghi M (2010) Room-temperature continuous wave operation of distributed feedback quantum cascade lasers with watt-level power output. Appl Phys Lett 97(23):231119
16. Slivken S, Bandyopadhyay N, Tsao S, Nida S, Bai Y, Lu QY, Razeghi M (2012) Sampled grating, distributed feedback quantum cascade lasers with broad tunability and continuous operation at room temperature. Appl Phys Lett 100(26):261112
17. Hoffmann LK, Hurni CA, Schartner S, Austerer M, Mujagic E, Nobile M, Benz A, Schrenk W, Andrews AM, Klang P, Strasser G (2007) Coherence in Y-coupled quantum cascade lasers. Appl Phys Lett 91(16):161106
18. Ishii H, Kasaya K, Oohashi H, Shibata Y, Yasaka H, Okamoto K (2007) Widely wavelength-tunable DFB laser array integrated with funnel combiner. IEEE J Sel Top Quant 13(5):1089–1094
19. Bai Y, Slivken S, Darvish SR, Haddadi A, Gokden B, Razeghi M (2009) High power broad area quantum cascade lasers. Appl Phys Lett 95(22). https://doi.org/10.1063/1.3270043
20. Heydari D, Bai Y, Bandyopadhyay N, Slivken S, Razeghi M (2015) High brightness angled cavity quantum cascade lasers. Appl Phys Lett 106(9):091105
21. Pennings E, van Roijen R, Van Stralen M, De Waard P, Koumans R, Verbeck B (1994) Reflection properties of multimode interference devices. IEEE Photonic Technol Lett 6(6):715–718

Chapter 3
Broadband Terahertz Gas Spectroscopy Through Multimode Self-Mixing in a Quantum Cascade Laser

Y. J. Han, J. Partington, R. Chhantyal-Pun, M. Henry, O. Auriacombe, T. Rawlings, L. H. Li, J. Keeley, M. Oldfield, N. Brewster, R. Dong, P. Dean, A. G. Davies, B. N. Ellison, E. H. Linfield, and A. Valavanis

Abstract We present a self-mixing terahertz-frequency gas spectroscopy technique using a multimode quantum cascade laser. A precision-micro-machined external waveguide module and a double-metal quantum cascade laser device are used to increase the optical feedback and the laser's frequency tuning range. Methanol spectra are measured using two laser modes at 3.362 THz and 3.428 THz simultaneously, with more than 8 absorption peaks resolved over a 17-GHz bandwidth, which provides minimum detectable absorption coefficients of $2.7 \times 10^{-4} \, \text{cm}^{-1}$ and $4.9 \times 10^{-4} \, \text{cm}^{-1}$, respectively. In contrast to all previous self-mixing spectroscopy, our multimode technique expands the sensing bandwidth significantly. This broadband spectroscopy technique can potentially be used for the identification and analysis of chemical, biological radiological and nuclear (CBRN) agents and explosives.

3.1 Introduction

Chemical, biological radiological and nuclear (CBRN) agents and explosives have unique spectral signatures in the terahertz (THz) frequency range, which can be used for their identification and analysis [1–3]. Quantum cascade lasers (QCLs) are

Y. J. Han (✉) · J. Partington · R. Chhantyal-Pun · L. H. Li · J. Keeley · R. Dong · P. Dean A. G. Davies · E. H. Linfield · A. Valavanis
School of Electronic and Electrical Engineering, University of Leeds, Leeds, UK
e-mail: y.han@leeds.ac.uk; rc13564@bristol.ac.uk; L.H.Li@leeds.ac.uk; P.Dean@leeds.ac.uk; G.Davies@leeds.ac.uk; E.H.Linfield@leeds.ac.uk; A.Valavanis@leeds.ac.uk

M. Henry · O. Auriacombe · T. Rawlings · M. Oldfield · N. Brewster · B. N. Ellison
Rutherford Appleton Laboratory, STFC, Oxford, Didcot, UK
e-mail: manju.henry@stfc.ac.uk; olivier.auriacombe@stfc.ac.uk; thomas.rawlings@stfc.ac.uk; matthew.oldfield@stfc.ac.uk; nick.brewster@stfc.ac.uk; brian.ellison@stfc.ac.uk

important sources within the 2–5 THz range [4–6], with merits including their compact size, coherence, narrow linewidth, tunable emission frequency, and high output power [7–10]. Heterodyne radiometry and direct-transmission gas spectroscopy have been demonstrated using THz QCLs [11–14], with their resolution and detectivity improved by phase locking, frequency modulation, and photoacoustic techniques [15–18]. These spectroscopy schemes have, until recently, required a separate detector or mixer as well as frequency calibration instrumentation, which increase the complexity and cost of the system. In order to overcome these challenges, a THz gas spectroscopy technique based on self-mixing (SM) in a QCL has been demonstrated [19]. SM interference occurs between the internal and backscattered optical fields in a laser cavity. This induces changes to the terminal voltage, which are sensitive to the amplitude and phase of the reflected radiation, thus enabling the laser device to act both as a radiation source and as a coherent detector [20, 21]. This technique removes the need for additional detectors and enables fast detection and self-calibration [22, 23]. However, the spectral bandwidth of these SM spectroscopy systems has so far been limited by the <2 GHz tuning range of the single-mode QCLs used in previous works.

Here, we present the fabrication of THz frequency quantum cascade lasers (QCLs) emitting at 3.5 THz and a new and robust waveguide integration scheme. Based on the waveguide integrated QCL device, we also present a new technique, which exploits the ability of SM systems to monitor the full emission spectrum of their own laser source, and demonstrate the measurement of methanol spectral features simultaneously from two modes of a multi-mode THz QCL over a 17 GHz range.

3.2 Device Process

The active-region of the QCL used in this work is based on a $GaAs/Al_{0.15}Ga_{0.85}As$ phonon-enhanced bound-to-continuum design, which was grown using molecular beam epitaxy. The layer sequence of an active module in nanometers is **3.7**/10.5/**0.5**/ 12.2/**1**/12.5/**1.9**/11/**2.8**/8.8/**2.8**/7.9/**2.8**/6.6/**2.8**/15.8/**2.8**/13.8, where the $Al_{0.15}Ga_{0.85}As$ barriers are shown in bold and the doping density in the underlined GaAs well is 3.4×10^{16} cm^{-3}. The QCL device was processed into a double-metal (DM) ridge-waveguide structure. Ti/Au of thickness 10/500 nm was deposited on top of the QCL wafer, and also on a second n + -GaAs acceptor wafer. The two wafers were then thermal compression bonded at the metallic interfaces. The substrate of the QCL wafer was lapped to 10 μm, and removed by selective wet-chemical etching. Following wet-etching of the laser ridges, Ti/Au (10/150 nm) was deposited on the top. The substrate was thinned and metallised to improve thermal performance, and the ridges were then cleaved and indium-soldered onto a copper submount.

For the light intensity–current–voltage (L–I–V) characterization, the devices were mounted on the cold finger of a helium-cooled cryostat and operated in continuous

Fig. 3.1 *L–I–V* curves at different temperatures. The device ($980 \times 60\ \mu m^2$) was operated in CW mode
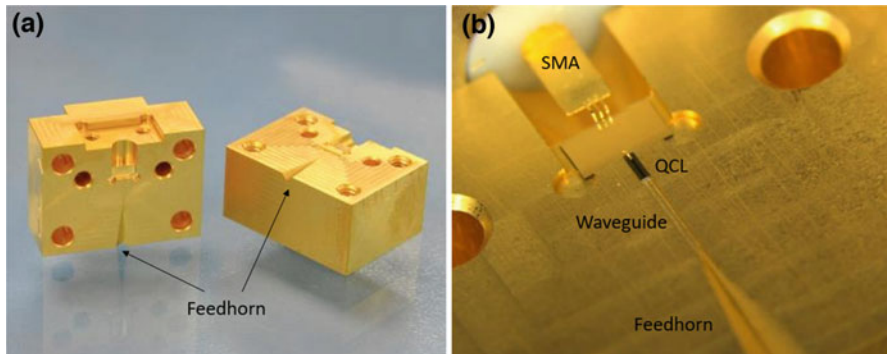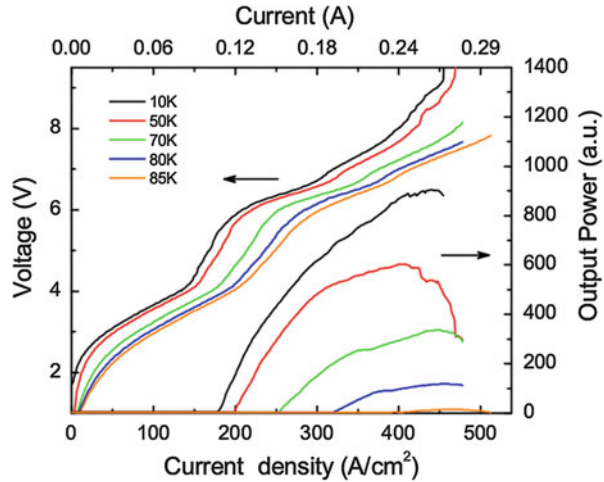
Fig. 3.2 (**a**) Micromachined waveguide block assembly, (**b**) THz QCL mounted within a 150-μm-wide waveguide channel

wave (CW) mode. The laser emission was detected using a cooled Ge:Ga bolometer. Figure 3.1 shows the *L–I–V* characteristics obtained at different temperatures. The maximum operating temperature is 85 K, at the temperature of 10 K, the dynamic range is from 179 A/cm^2 to 454 A/cm^2.

Compared with a semi-insulating surface-plasmon waveguide, DM waveguides yield lower threshold gain, leading to better continuous-wave (CW) performance and wider frequency tunability. However, the wider beam divergence and smaller aperture make optical alignment and feedback more difficult. In order to increase the reinjection efficiency of the optical feedback, a waveguide block with a diagonal feedhorn was micro-machined to couple radiation between the front facet and free space. A separate QCL device with the dimensions of 60 μm × 980 μm was processed as described above. The substrate was reduced to 100 μm using mechanical lapping, and diced into a standalone 100-μm-wide chip. Figure 3.2a shows the

micro-machined waveguide block assembly, including two half-blocks with a diagonal feedhorn, rectangular waveguide, mounting-point for an electrical SMA connector and the QCL-mounting recess. As shown in Fig. 3.2b, the QCL chip was solder-mounted within a precision micro-machined waveguide channel and ribbon-bonded to an integrated SMA connector. The other symmetrical half-block was attached above the QCL to form a rectangular waveguide ($160 \times 80 \ \mu m^2$) enclosure around the device. The feedhorn and waveguide integrated device was shown to offer significantly improved performance over a non-integrated DM QCL [24].

3.3   Experimental Setup

The optical configuration of the spectroscopy system is similar to that in Ref. [23], and is illustrated in Fig. 3.3. The emitted radiation from the QCL was directed through a 96.5-cm-long gas cell and was reflected back using a mechanically-adjustable optical delay-line into the QCL along the same optical path. The SM-perturbations to the QCL voltage were measured as a function of the optical delay time, and a Fast Fourier Transform (FFT) was used to infer the full-band emission spectrum of the QCL. The QCL operated in CW mode using an Arroyo 4320 current source and at a 10-K heatsink temperature within a Janis ST-100 He cooled cryostat. The gas cell has two polymethylpentene (TPX) windows mounted at 45° on each end, which is used to decrease etalon effects within the cell. A dry mechanical pump was used to evacuate the gas cell resulting in a base pressure of 0.03 Torr. A high-purity methanol sample was degassed and evaporated into the gas cell to the desired pressure measured by a capacitance manometer (MKS α-Baratron AA01).

The optical delay time was controlled using Newport ILS-200 motor translation stage, with a speed of 100 mm/s, and with measurements being triggered at 1-μm increments over a maximum distance of 200 mm. The perturbation of the QCL terminal voltage was recorded as a function of the displacement via a Stanford SR 560 preamplifier and a National Instruments USB-6216 data-acquisition board. With

Fig. 3.3 Schematic illustration of the configuration of the gas spectroscopy system
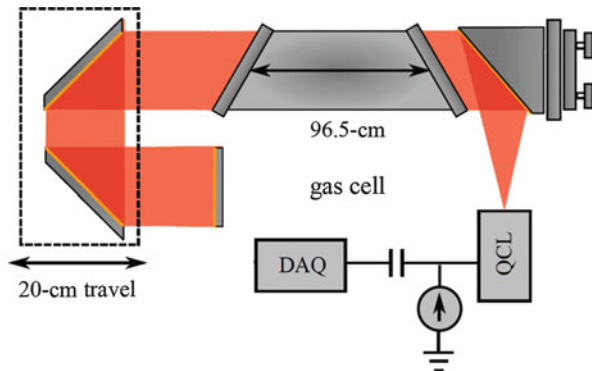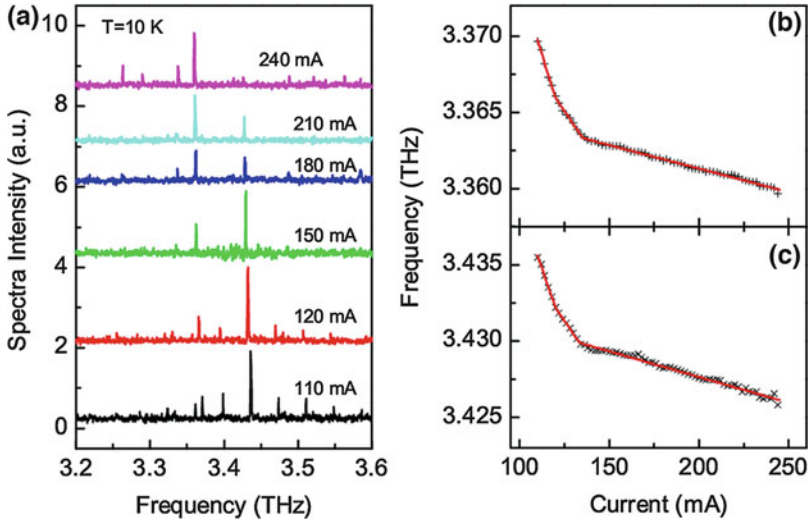
Fig. 3.4 (**a**) Emission spectra of a THz QCL as a function of dc drive current, measured through self-mixing interferometry at 10 K and with the gas cell under vacuum. (**b**) and (**c**) The frequency of the two highest-intensity laser modes as a function of drive current. The red lines are three-segment linear fits to the experiment data (scatters)

this setup, a spectrum can be obtained in 10 s. The maximum 800-mm round-trip delay (using beam-folding optics as in Fig. 3.3) corresponds to an FFT sampling resolution of around 380 MHz, and the 1-μm step size corresponds to an FFT spectral bandwidth of 37 THz.

Emission spectra of the QCL were measured at a temperature of 10 K, with dc driving currents sweeping at a range from 110 to 245 mA, and with the gas cell under vacuum. As shown in Fig. 3.4a, multi-mode emission was obtained with two main emission lines around 3.362 THz (mode A) and 3.428 THz (mode B) being observed simultaneously across the full dynamic range. Several lower-intensity side modes were also observed around the main emission lines over limited current ranges. Effective refractive indices of 4.046 and 4.036 were calculated for the side-modes around the 3.362 and 3.428 THz lines respectively, indicating that they originate from lateral confinement. To estimate the frequency evolution of the two main modes, the emission frequencies are plotted in Fig. 3.4b, c as a function of current. The peak frequencies were obtained by using a Gaussian fit to the measured spectra. As the current was increased, both laser modes were shown to have a red shift with the frequency tuning ranges around 10 GHz in each case: from 3.3696–3.3594 THz and 3.4354–3.4253 THz, respectively. Both tuning curves can be divided into three piecewise-linear segments. This gives tuning rates of −380 MHz/mA, −173 MHz/mA and − 31 MHz/mA for mode A, and − 340 MHz/mA, −171 MHz/mA and − 34 MHz/mA for mode B, respectively. The nonlinear frequency tuning characteristics can be attributed to a bias-induced gain shift and a thermal change in the refractive index.

During the measurement, data were recorded with the translation stage moving in forward or reverse directions to reduce data-acquisition time, and 10 scans were averaged for every current step to decrease noise and remove SM hysteresis effects. A current-sweep step of 1.0 mA was used in Fig. 3.4b, c. As such, a data-acquisition rate of 0.05 samples/s was obtained, giving a total scan time of 2720 s to sweep the whole current range. The finest current step achievable using the DC source is 0.1 mA, corresponding to frequency tuning steps of 38 MHz, 17 MHz and 3 MHz for the three segments respectively. The frequencies in Fig. 3.3 exhibit small perturbations when the current is higher than 135 mA, due to SM frequency-pulling effects [23]. The maximum frequency perturbation is less than 200 MHz, only half of the frequency resolution of the system. Thus, this frequency perturbation has weak influence on the measurement and is neglected during the data processing.

3.4 Self-Mixing Gas Spectroscopy

We assume that different laser modes operate independently in the Fabry-Pérot resonator of the QCL. Thus, the SM induced voltage modulation amplitude can be given by the sum of the contributions from all the individual laser modes [19, 23], using

$$U_{SM} \propto \sum_i T_i \cos \{\varnothing_{0i} - C_i \sin [\varnothing_i - \arctan(\alpha_i)]\}, \qquad (3.1)$$

where i is the index of each laser mode, T_i is single-pass Beer–Lambert power transmission factor, $\varnothing_{0i}$ is the round-trip phase delay without optical feedback, C_i is the feedback strength, $\varnothing_i$ is the phase delay with optical feedback and α_i is the linewidth-enhancement factor. The phase delay can be expressed in terms of the laser mode frequency ν_{0i} and the external cavity round-trip time τ_i as

$$\varnothing_{0i} = 2\pi \nu_{0i} \tau_i. \qquad (3.2)$$

In the case of weak feedback ($C \ll 1$), which can be justified by the long optical path-length in the system, the SM voltage modulation can be simplified to a closed analytical form,

$$U_{SM} \propto \sum_i T_i \cos (2\pi \nu_{0i} \tau_i). \qquad (3.3)$$

Since the voltage modulation U_{SM} is dependent on the power transmission factors of all the laser modes, T_i, the integrated *in situ* frequency monitoring scheme is necessary for the identification of gas absorption features. In the frequency domain, Eq. (3.2) becomes

$$\mathcal{U}_{SM}(\nu) \propto \sum_i T_i \delta_{\nu, \nu_{0i}}. \tag{3.4}$$

As such, the laser mode intensity obtained from the SM interferogram is proportional to the corresponding power transmission factor. The transmission spectra of gases, therefore, can be measured by sweeping the mode frequencies of the QCL, with and without the gas present within the cell, and the gas absorption coefficient, α, can be calculated using the familiar Beer–Lambert law:

$$\alpha = -\ln(A/A_0)/L_{cell}, \tag{3.5}$$

where A and A_0 are the respective amplitudes of the transmission spectra with and without gas in the cell, and L_{cell} is the length of the gas cell. Note that the transmission spectra can be obtained simultaneously for all the laser modes by using this approach, which is much more efficient than SM spectroscopy based on single-mode lasers.

To demonstrate the validity of this approach, the emission frequency and intensity of the two laser modes were measured over the full dynamic current range with and without methanol vapor in the cell. Figure 3.5 shows the normalized transmission spectra of methanol at a pressure of 5.0 Torr. The use of a multi-mode QCL yielded a total measurement bandwidth of 17 GHz, much wider than the 2 GHz obtained using a single mode QCL [19, 23]. As such, eight absorption peaks and one absorption band were resolved. For comparison, the spectra were simulated based on data in the JPL molecular spectroscopy catalog, using a Voigt profile to account for self-broadening and Doppler broadening [23]. A small frequency offset between the
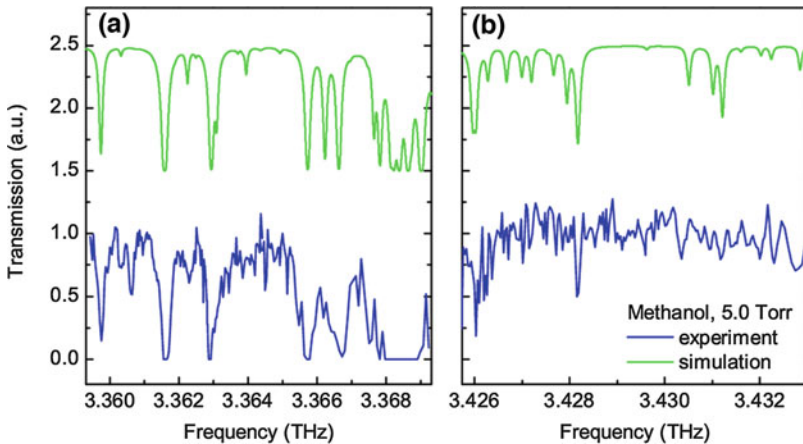
Fig. 3.5 Transmission spectra of methanol at the pressure of 5.0 Torr, measured with (**a**) the laser mode A and (**b**) the laser mode B simultaneously. The green lines are the calculated spectra based on data from the JPL molecular spectroscopy catalog, and the blue lines are the measured results

Table 3.1 Key transitions of methanol, shown in Fig. 3.4, and their related rotational quantum levels. The data are from the JPL molecular spectroscopy catalog, where f is the frequency, J is the total angular momentum, K is the projection along the symmetry a-axis, vt is the torsional symmetry, INT is the base 10 logarithm of the integrated intensity

f (THz)	Upper state (J, K, v_t)	Lower state (J, K, v_t)	INT (nm^2·MHz)
3.35973	22, 6, 1	22, 5, 1	−2.5622
3.36158	10, 9, 1	9, 8, 1	−2.0336
3.36293	15, a3, 0	14, a2, 0	−2.2010
3.36572	17, 14, 0	16, 13, 0	−2.2026
3.36622	21, 6, 1	21, 5, 1	−2.4921
3.36662	9, −5, 1	8, −4, 1	−2.2348
3.42603	22, −4, 2	23, +3, 1	−2.8940
3.42817	29, −7, 1; 29, 7, 1	29, 6, 1; 29, −6, 1	−2.9727 −2.9727

measured and simulated spectra was observed, which could be attributed to a calibration offset in the motion controller. With a correction of −0.6 GHz (0.02%), the measured spectra agree well with the catalogued data. The absorption peaks of methanol and the respective rotational transitions are listed in Table 3.1, in which the peaks at 3.3597 THz, 3.3616 THz, 3.3629 THz, and 3.4282 THz are relatively well resolved. With lower pressure and a smaller current scanning step, more peaks could potentially be resolved within the broad absorption band around 3.3685 THz.

The minimum detectable absorption is an important performance metric for the spectrometer. It is dependent on the power of the laser source and the noise level of the system [14]. In our case, a multi-mode laser is used, and the different intensity of the laser modes will result in different minimum detectable absorption in each measurement band. This difference would also exist for one laser mode whose intensity varies across a wide frequency range. To assess the sensitivity of our SM approach, the minimum detectable absorption coefficient was calculated for the two main laser modes, using the standard deviation of the baseline transmission. The minimum detectable absorption coefficient is 2.7×10^{-4} cm^{-1} and 4.9×10^{-4} cm^{-1} for methanol at 3.3616 THz and 3.4282 THz respectively. The higher sensitivity at 3.3616 THz is due to the higher intensity of the corresponding laser mode. Compared with the minimum detectable coefficient of 1.0×10^{-4} cm^{-1} obtained with a surface plasmon QCL [23], the lower sensitivity of our measurement is mainly attributed to the lower optical feedback power of the double-metal device. Additionally, we note that there are small oscillations in the baseline of the transmission spectra, which also contribute to the higher minimum detectable absorption coefficient. This may be due to thermally-induced optical misalignment and frequency shift, and higher sensitivity can be expected by applying better thermal management.

3.5 Conclusions

In summary, broadband THz gas spectroscopy has been demonstrated using self-mixing interferometry in a multimode double-metal THz QCL for the first time. The transmission spectra of methanol were simultaneously obtained within two distinct frequency ranges from 3.359 THz to 3.369 THz and from 3.426 THz to 3.433 THz. This approach has increased the total measurement bandwidth obtainable using a QCL-based SM scheme by a factor of ~7 and underpins future work to develop the first broadband "detector-free" multi-gas QCL spectroscopy systems.

References

1. Siegel PH (2002) Terahertz technology. IEEE Trans Microw Theory 50:910
2. Tonouchi M (2007) Cutting-edge terahertz technology. Nat Photonics 1:97
3. Baxter JB, Guglietta GW (2011) Terahertz spectroscopy. Anal Chem 83:4342
4. Köhler R, Tredicucci A, Beltram F, Beere HE, Linfield EH, Davies AG, Ritchie DA, Iotti RC, Rossi F (2002) Terahertz semiconductor-heterostructure laser. Nature 417:156
5. Walther C, Fischer M, Scalari G, Terazzi R, Hoyler N, Faist J (2007) Quantum cascade lasers operating from 1.2 to 1.6 THz. Appl Phys Lett 91:131122
6. Wienold M, Röben B, Lü X, Rozas G, Schrottke L, Biermann K, Grahn HT (2015) Frequency dependence of the maximum operating temperature for quantum-cascade lasers up to 5.4 THz. Appl Phys Lett 107:202101
7. Barkan A, Tittel FK, Mittleman DM, Dengler R, Siegel PH, Scalari G, Ajili L, Faist J, Beere HE, Linfield EH, Davies AG, Ritchie DA (2004) Linewidth and tuning characteristics of terahertz quantum cascade lasers. Opt Lett 29:575
8. Qin Q, Reno JL, Hu Q (2011) MEMS-based tunable terahertz wire-laser over 330 GHz. Opt Lett 36:692
9. Vitiello MS, Tredicucci A (2011) Tunable emission in THz quantum cascade lasers. IEEE Trans Terahertz Sci Technol 1:76
10. Li LH, Chen L, Freeman JR, Salih M, Dean P, Davies AG, Linfield EH (2017) Multi-watt high-power THz frequency quantum cascade lasers. Electron Lett 53:799
11. Gao JR, Hovenier JN, Yang ZQ, Baselmans JJA, Baryshev A, Hajenius M, Klapwijk TM, Adam AJL, Klaassen TO, Williams B, Kumar SS, Hu Q, Reno JL (2005) Terahertz heterodyne receiver based on a quantum cascade laser and a superconducting bolometer. Appl Phys Lett 86:244104
12. Richter H, Semenov AD, Pavlov SG, Mahler L, Tredicucci A, Beere HE, Ritchie DA, Il'in KS, Siegel M, Hübers H-W (2008) Terahertz heterodyne receiver with quantum cascade laser and hot electron bolometer mixer in a pulse tube cooler. Appl Phys Lett 93:141108

13. Hübers H-W, Pavlov SG, Richter H, Semenov AD, Mahler L, Tredicucci A, Beere HE, Ritchie DA (2006) High-resolution gas phase spectroscopy with a distributed feedback terahertz quantum cascade laser. Appl Phys Lett 89:061115

14. Hübers H-W, Richter H, Pavlov SG, Richter H (2013) High resolution terahertz spectroscopy with quantum cascade lasers. J Infrared Millim Terahertz Waves 34:325

15. Ren Y, Hayton DJ, Hovenier JN, Cui M, Gao JR, Klapwijk TM, Shi SC, Kao T-Y, Hu Q, Reno JL (2012) Frequency and amplitude stabilized terahertz quantum cascade laser as local oscillator. Appl Phys Lett 101:101111

16. Eichholz R, Richter H, Wienold M, Schrottke L, Hey R, Grahn HT, Hübers H-W (2013) Frequency modulation spectroscopy with a THz quantum-cascade laser. Opt Express 21:32199

17. Hangauer A, Westberg, Zhang JE, Wysocki G (2016) Wavelength modulated multiheterodyne spectroscopy using Fabry-Pérot quantum cascade lasers. Opt Express 24:25298

18. Patimisco P, Borri S, Sampaolo A, Beere HE, Ritchie DA, Vitiello MS, Scamarcio G, Spagnolo V (2004) A quartz enhanced photo-acoustic gas sensor based on a custom tuning fork and a terahertz quantum cascade laser. Analyst 139:2079

19. Hagelschuer T, Wienold M, Richter H, Schrottke L, Biermann K, Grahn HT, Hübers H-W (2016) Terahertz gas spectroscopy through self-mixing in a quantum-cascade laser. Appl Phys Lett 109:191101

20. Lang R, Kobayashi K (1980) External optical feedback effects on semiconductor injection laser properties. IEEE J Quantum Electron 16:347

21. Taimre T, Nikolić M, Bertling K, Lim YL, Bosch T, Rakić AD (2015) Laser feedback interferometry: a tutorial on the self-mixing effect for coherent sensing. Adv Opt Photon 7:570

22. Hagelschuer T, Wienold M, Richter H, Schrottke L, Grahn HT, Hübers H-W (2017) Real-time gas sensing based on optical feedback in a terahertz quantum-cascade laser. Opt Express 25:30203

23. Chhantyal-Pun R, Valavanis A, Keeley J, Rubino P, Kundu I, Han YJ, Dean P, Li LH, Davies AG, Linfield EH (2018) Gas spectroscopy with integrated frequency monitoring through self-mixing in a terahertz quantum-cascade laser. Opt Lett 43:2225

24. Han YJ, Li LH, Valavanis A, Brewster N, Zhu JX, Dong R, Dean P, Bushnell L, Oldfield M, Davies AG, Ellison BN, Linfield EH (2017) Development of terahertz frequency quantum cascade lasers for the applications as local oscillators. In: THz for CBRN and explosives detection and diagnosis, p 123

Chapter 4
Crucial Aspects of the Device Processing of Quantum Cascade Lasers

A. Szerling, K. Kosiel, P. Prokaryn, M. Szymański, Z. Wasilewski, M. Płuska, and M. Sakowicz

Abstract The paper presents the studies on technology of ∼100 µm-emitting (∼3 THz) $Al_{0.15}Ga_{0.85}As$/GaAs QCLs, the optimized scheme of fabrication of such lasers was elaborated. It was a result of the extensive work on decreasing waveguide losses while ensuring the proper performance of the electrical contacts and effective heat removal. The fabrication comprises Au-based claddings and Au-Au-mounting process. The yielded lasers operate up to the maximum temperature $T_{max} = 140$ K, with threshold current density $J_{th} \sim 1$ kA/cm^2 at 77 K.

4.1 Introduction

CBRN and explosives typically have strong absorption signatures in the GHz, THz and Mid Infrared ranges of the spectrum (GIGA-TERA-MIR). Recent advances on theory and simulations of materials, sources, and detectors for this range [1–6] stimulate the search for new methods and solutions.

Quantum Cascade Lasers (QCLs) are unipolar sources of coherent radiation theoretically foreseen since early 70s and realized for the first time in 1994 [7-1], with operation based on tunneling transport of carriers and intersubband optical transitions [7, 8]. They can be fabricated on the basis of many different types of epitaxial semiconductor structures, though most often based on III-V materials. QCLs' operating wavelengths span both mid-infrared (MIR) and terahertz (THz) regions, with the exception of the Reststrahlen band, which for III-V materials lies approximately in the 20–60 µm range. Among the III-V-related QCLs the InP- and GaAs-based ones proved to be particularly effective sources of radiation in MIR [9–11] – especially up to 12 µm, but also for longer wavelengths – in FIR and THz

A. Szerling (✉) · K. Kosiel · P. Prokaryn · M. Szymański · Z. Wasilewski · M. Płuska
M. Sakowicz
Łukasiewicz Research Network – Institute of Microelectronics and Photonics, Warsaw, Poland
e-mail: anna.szerling@imif.lukasiewicz.gov.pl

region [9, 12–16]. The lasers find application in the gas sensing systems (e.g., for detecting NH_3, CO_2, NO, CH_4) [17–19], medical diagnostics [20] and environment monitoring [21].

The main advantages of QCLs above other coherent IR sources are: (i) – a possibility to design a structure to a specific wavelength from a broad spectrum using only one material system, e. g., AlGaAs/GaAs; (ii) – a possibility to change the emission wavelength through temperature change; (iii) – monolithic and with compact sizes; (iv) – high optical energy densities obtained from a small chip.

Despite mentioned above advantages, the main difficulty is a technology of such devices. The overall technology of these devices comprises two main components: epitaxy of the semiconductor structures and fabrication of the devices from the epitaxial structures (device fabrication, device processing). The complex design and operating principle require the highest accuracy of the technology of quantum cascade lasers, uniformity and repeatability of both epitaxy and device processing [22]. The QCL's active region structure is periodic, multimodule, and comprises multi-quantum well injectors and emitters. The overall laser structure typically consists of several 100 nm-thick layers. High requirements for epitaxy are related to ultrathin layers of the periodic active region, where the wave functions are to be properly engineered [23–25]. The thickness and composition accuracy of the structure layers should, in general, be better than a few percent. Another crucial issue is the optimisation of doping, in particular the injector doping, which is necessary to assure a large enough dynamic range of laser operation [17, 24, 26, 27].

High requirements for the device fabrication/device processing are indispensable for yielding operating devices and further increasing of their functionality – like for increasing their optical output power, increasing their maximum operating temperature, decreasing their threshold current or for desired influence on their modal structure. The efforts leading to such improvements must focus on control of key physical issues, like for example: reduction of waveguide optical losses, heat management by reduction of heat generation or effective heat extraction/removal, or suppression of undesired optical modes within the modal structure.

The device processing is a very demanding and complicated part of the overall technology of QCLs, which comprises many various sophisticated techniques like: photolithography, wet chemical etching, chemical and/or plasma cleaning, plasma etching, dielectric or metal deposition using appropriate method (for example sputtering, PECVD, galvanic bath and many others), substrate polishing, die bonding, wire bonding, wafer bonding. All these techniques require appropriate approach adapted to their specific capabilities. The skilful matching of all these techniques within the elaborated technology is the key to fabricating working lasers.

The QCL's bias can generate unintentionally strong self–heating effect. The feeding current may be decreased by reduction of the pumped area that needs an appropriate device processing. There are several technological solutions for restriction of the lateral current spreading, the most common construction of QCLs is a ridge structure device (mesa device). The mesa must be deep enough to separate the whole active region of the device. The next important requirement in this case, in order to reduce the optical losses, are high-quality smooth waveguide sidewalls [28–

30]. There are several known processes, like carrier losses, current spreading, waveguide internal and scattering losses, mirror losses and heat dissipation that can negatively affect the semiconductor laser performance in terms of its threshold current density (J_{th}), slope efficiency (η_S) or characteristic temperature (T_0). The solutions to the mentioned above effects are to be found generally in the fields of device construction or technology. For instance, it is very important to focus on issues associated with scattering losses caused by unintentional roughness of ridge-waveguide sidewalls. The smooth morphology of ridge sidewalls is necessary for lasing, as the rough walls of ridges are the reason of scattering losses, and hence they cause strong deterioration of laser's performance. Scattering losses depend quadratically on mesa-sidewall roughness (Eq. 20.1 in [29]), and because of that the increasing roughness is a reason of fast increase of the threshold current density (Eq. 20.2 in [29]) and fast decrease of the slope efficiency of the laser (Eq. 20.3 in [30]).

The use of ridge waveguide – geometry requires the application of electrical isolation of the region around the ridge. For example, this isolation can be made by deposition of the appropriate dielectric layers [29]. However, the insulating layers used for that reason can introduce additional optical losses [22]. The reason is vibration frequencies of molecular bonds in these dielectric layers fit into the MIR and FIR region inducing thereby strong unintentional absorption of the laser radiation [22]. For example, a SiO_2 insulation layer can absorb the IR radiation [31]. There is a number of publications that associate the shape of absorption spectrum of a given SiO_2 layer with the conditions in which the SiO_2 layer was deposited [32–34]. Obviously also a metal layer could be the source of absorption losses (even for FIR radiation). For lasers emitting the FIR wavelength ($\lambda > 13$ μm) calculations show that there is a threefold increase of the absorption losses when a continuous metal layer is present on a top of the ridge [35].

That is why the two major problems of processing of QCLs with ridge – waveguide should be considered, i.e., absorption induced by dielectric layers and scattering from the roughness of the ridge sidewalls, as both can contribute to the waveguide losses increase [22].

There are different types of QCL-device designs presented in the literature, with corresponding different technological approaches [22, 36]. Page et al. presented the double trench construction (formation of the double trench defines the ridge of the laser) which ensured a good overlapping of the lateral mode with the gain region and enabled stable epi-down mounting necessary for efficient cooling of the device [37]. Sirtori et al. [22] have presented the double trench structures, in which relatively shallow ion implantation was done to the depth of only slightly above the active region (~3.3 μm). It was used for electrical isolation instead of dielectric layers. The presented solution was the construction in which the extended proton-implanted regions were applied in the area defined by the two trenches. In the latter, the channel for current injection was narrower than the ridge width [22, 38]. The paper [67] describes in-depth elaboration of a particular variant of fabrication technology of the $Al_{0.45}Ga_{0.55}As/GaAs$ quantum-cascade laser operating in the MIR range ($\lambda \sim 10$ μm). The difference between this method and the described

earlier standard fabrication technology is that it does not comprise mesa fabrication at all. Instead of mesa fabrication, the ion implantation is used as a means of electrical isolation of a laser. At the same time the optical confinement is also provided. The advantage of such approach is a significant reduction of number of technological stages.

Biasing of QCLs typically places requirements on the application of relatively high voltages of several volts as well as relatively high current densities of several kA/cm^2 (especially for GaAs-based lasers). That is the reason for a special demand for low resistance ohmic contacts in order to maximally reduce the device series resistance and undesired heating effect. High quality ohmic contacts allow to achieve low threshold voltage and minimizes the amount of generated heat in the laser structure. These contacts must be thermally stable, a metal diffusion depth into the semiconductor layers must be minimized. The lateral uniformity of metal–semiconductor interfaces is also a must. The most common contact based on AuGe/Ni/Au sandwich layers are extensively used for fabrication ohmic contacts in n-type GaAs and AlGaAs/GaAs heterostructures [39–44].

In order to enhance functionality of the lasers, the single-mode quantum-cascade lasers (QCLs) should be fabricated. They could be an effective source of electromagnetic radiation in several applications, especially in very selective gas sensing systems as well as free-space communication systems [45–47]. There are a few ways in which such lasers can be fabricated [46–49]. The most common are distributed feedback (DFB) lasers [46–48]. In the DFB laser, the active region of the device is periodically structured as a diffraction grating. The one-dimensional interference grating results in a Bragg scattering and provides optical feedback for the laser. DFB laser acts like a narrow range filter, selecting a given frequency line from gain characteristics, for which the Bragg reflection criterion is met. In order to obtain the feedback the grating period (Λ) must be a multiplication of a half wavelength of radiation generated in the medium [49]. A technology of fabrication of DFB QCLs involves three different well-known fabrication methods (schemes) [46, 50, 51]. For the best effect, the fabrication method should be adjusted to a concrete type of an epitaxial structure.

As it was emphasized above, the proper processing technology of QCLs to achieve a high quality device, i. e., with a low threshold current, high operating temperature, high output power and high efficiency, is very challenging even for MIR QCLs. When one approaches the Reststrahlen band from the side of shorter wavelengths (FIR region) or from the side of longer wavelengths (THz-frequency radiation region) the QCL technology becomes even more and more demanding. Generally, for 12–20 μm wavelengths only limited performance has been demonstrated for high power QCL operation at room temperature [12, 52, 53], despite the existing strategic application areas [12, 52, 53]. In particular, in the 12–16 μm wavelength region, large organic hydrocarbon molecules like the BTX aromatic compounds [45], that are very important in petroleum refining and petrochemical industries [16], can be detected. Longer-wavelength sources would also be valuable for radio-astronomy as local oscillators in heterodyne detectors [16].

THz radiation has a very broad spectrum of already existing and potential applications, ranging from measurements and diagnostics applied in fields such as molecular spectroscopy and three-dimensional imaging for biology, medicine, military and public safety purposes to telecommunications in a free-space data transmission. The THz QCL technology is actually still at its initial stage. The overall problem of all THz QCLs is their considerably low active region pumping efficiency as it is very hard to obtain a population inversion between energy levels spaced ~4–40 meV apart. Another key issue is free carrier absorption with its high intensity for this frequency range, responsible for high waveguide losses. The free carrier absorption and high waveguide losses result in low operating temperatures of THz QCLs that hinder their development and wide application.

Further improvement to the maximum THz QCL operating temperature through the optimization of both the active region and the claddings is likely. There are two most popular waveguide types for THz QCLs: the semi-insulating surface plasmon waveguide, which suffers from relatively high free-carrier losses occurring in the highly doped semiconductor layer, and the metal-metal waveguide [54, 55]. The latter is equipped with two metallic claddings, one on each side of the active region. As the THz skin depth effect only reaches a few tens of nanometers into metal, the metal-metal outlay allows the fabrication of relatively low-loss waveguides with confinement factor approaching unity. Even in metal-metal waveguide THz QCLs, though, 30–70% of the waveguide loss can be associated with the claddings, with a specific value depending on the emission wavelength, active region design and its doping [55]. Optical losses linked with the metal claddings depend on the type of the used metal [55], with just a few types of metal claddings tried out and applied to date with regard to THz quantum cascade lasers. Only a few of papers have been published in relation to the properties of metallic layers that can be used to prepare THz waveguide claddings for QCLs [56]. Research based data regarding the morphology of metallic layers forming waveguide claddings and the corresponding metal/semiconductor interfacial morphology is not wide available. Another point of relevance here is that metallic structures fabricated in order to obtain claddings for low-loss THz waveguides must also serve a function of stable low-resistivity electric contacts. Historically, titanium-gold metallization was used for metallic cladding fabrication. The metal-metal THz QCLs waveguides were produced using low temperature In-Au metallic bonding [57, 58]. It was presented that Ti/Au used as a top cladding was responsible for relatively large threshold voltages [58]. Williams et al. [66, 67] have proposed Ta/Cu for both bottom claddings and the receptor covers. Belkin et al. [55] compared two types of metal claddings for THz QCLs, with the comparison of titanium-gold to copper as the main objective. The results indicated smaller losses on devices with copper claddings of metal-metal waveguides as compared to the ones with titanium-gold claddings [55]. Below, we present our elaboration of the processing of THz QCLs.

4.2 Crucial Aspects of THz QCLs Processing

For fabrication of THz lasers operating at $\lambda \sim 100$ μm ($\nu \sim 3$ THz) it was used the $Al_{0.15}Ga_{0.85}As$/GaAs QCL structures grown by Molecular Beam Epitaxy [59–61]. The scheme is presented in Fig. 4.1.

Their operation was based on 3-quantum-well (3QW) modules with the illustrative layer thickness sequence **4.3**, 8.9, **2.46**, 8.15, **4.1**, 16 given in nm, where the GaAs QWs are separated by $Al_{0.15}Ga_{0.85}As$ barriers bolded in the text. Only 5 nm-thick regions placed in the middle of the 16 nm-thick phonon wells were homogenously n-type doped with silicon, with planar carrier concentration of $3 \times 10^{10} cm^{-2}$. The laser's active region is built by stacking the 228 modules. The heterostructure was grown by molecular beam epitaxy technique.

It was developed of standard fabrication technology of the $Al_{0.15}Ga_{0.85}As$/GaAs quantum-cascade laser operating in the THz frequency range of radiation ($\nu \sim 3$ THz, that corresponds to $\lambda \sim 100$ μm) [59]. The result of the described technological research was attainment of a technological platform of device fabrication that generally provides working lasers, ready for possible further improvements/enhancements. The fact is the technological platform was elaborated for a certain range of similar epitaxial constructions, all approximately based on $Al_{0.15}Ga_{0.85}As$/GaAs-layered active regions designed for emission with $\nu \sim 3$ THz, but with some potential differences of performance (like maximum operating temperature, threshold current density, etc.) inherent to epitaxial details.

The described standard device fabrication technology comprises consecutive technological steps and includes:

Thickness	Material	Doping	Reps.
1000 Å	GaAs: Si n+	$5 \times 10^{18} cm^{-3}$	
41 Å	$Al_{0.15}Ga_{0.85}As$	nd	
160 Å	GaAs: Si	$3 \times 10^{10} cm^{-2}$ (w 50 Å in the middle QW)	
43 Å	$Al_{0.15}Ga_{0.85}As$	nd	x228
89 Å	GaAs	nd	
24,6 Å	$Al_{0.15}Ga_{0.85}As$	nd	
81,5 Å	GaAs	nd	
41 Å	$Al_{0.15}Ga_{0.85}As$	nd	
160 Å	GaAs: Si	$3 \times 10^{10} cm^{-2}$ (w 50 Å in the middle QW)	
43 Å	$Al_{0.15}Ga_{0.85}As$	nd	
1000 Å	GaAs: Si n+	$5 \times 10^{18} cm^{-3}$	

Fig. 4.1 The illustrative schematic sequence of layers in the THz QCL structure

- the fabrication of the bottom metal claddings (Ti/Au) and receptor substrates by means of magnetron sputtering,
- wafer bonding (Au-In),
- QCL substrate mechanical thinning down to about 50–70 μm and its complete removal by selective wet etching, selective wet etching of the etch-stop epitaxial layer,
- fabrication of ridge structures comprising of photolithography and mesa wet etching,
- and finally fabrication of top metal claddings (Ti/Au) that comprises photolithography and magnetron sputtering metallization followed by means of a lift-off process [59].

As revealed above, the standard technology comprised in particular the Au-based claddings, and Au-In-based mounting process (in terms of the process of connecting the laser chip with the receptor wafer).

The crucial technological issue of this elaboration was that the fabricated metallic structures, which are deposited on both sides of the laser active region (i.e., on both sides of the multilayer semiconducting stack), must play the role of thermally stable and low-resistivity electric contacts but at the same time must also serve as metallic claddings of low-loss THz-laser waveguides. These two functions - electrical and optical were elaborated and optimized together with great cohesion.

The technology was initialized by the theoretical studies that generated valuable predictions concerning the waveguide losses in THz QCLs and hence delivered the guidelines for fabrication of THz QCLs.

Apart of the successfully operating Au-cladding-based QCL the paper deals with initial experiments on technology of Cu-based claddings for $Al_{0.15}Ga_{0.85}As/GaAs$ THz QCL, that – as the theoretical research revealed – should deliver comparably promising results.

As a first step, that could offer valuable input towards the desired technology, we performed theoretical investigation of selected metal-metal waveguides designed for THz QCL [54, 59]. From our theoretical predictions it can be concluded that the penetration depth of THz radiation in the metallic layers (Au, Ag, Cu) should be below 100 nm [59]. Thus, it seems not to be necessary to deposit thicker than 300 nm gold as waveguides layers. The correlation between mode confinement and waveguide losses was observed [59]. The more a field leaks into the claddings, the higher α_{wg} is recorded. The application of Ti spacer is necessary from a technological point of view as it helps to increase the adhesion of an Au layer to GaAs as well as suppresses gold diffusion into the laser active region, thus preventing device degradation [62, 63]. It was performed theoretical predictions on the influence of the Ti barrier layer thickness on the waveguide losses. On top of that, a theoretical check shows that up to about 30 nm Ti deposited as a separation layer between Au, Ag or Cu and the semiconductor core does not significantly impact the waveguide losses in THz QCLs [59, 61].

The details of the standard device fabrication technology are described in the paper [59], where among others there is information about: removing substrate and

etch-stop layer, the fabrication of mesa (particular attention was paid to obtainment low roughness of mesa sidewalls). In the paper [59] we focused on the technological developments achieved with regard to $Al_{0.15}Ga_{0.85}As$/GaAs THz QCL fabrication, with particular emphasis placed on the issue of appropriate parameters for metallic cladding fabrication as well as wafer bonding. The latter has a huge impact on the laser performance and is closely associated with the type of cladding metallization.

We started the technological research regarding THz-QCL fabrication with Au-based metal-metal waveguides. Importantly, the fabrication of Au-based metallic claddings is much less demanding than, for instance, the Cu-based cladding technology, for which there is a problem of possible oxidation. Ti/Au system was studied because of necessity to include a titanium separation layer between the gold cladding and the semiconductor core in order to improve the adhesion and at the same time block diffusion of gold into the active layer. The reported diffusion process could be detrimental to the laser as an ultimate cause of a short circuit. The next important research subject beyond cladding fabrication was the correct wafer bonding technology, i.e. the mounting of the QCL on GaAs n + receptor wafers. Our wide study covered the influence of technological parameters such as the thicknesses of metallic layers, process temperatures and durations on the properties of the resulting test structures [59]. For characterization of the fabricated claddings a wide range of techniques was used (electrical characterization, TEM, SEM, AFM and THz-transmission measurements). The numerous test structures have been tested experimentally, the details of these studies are described in the paper [59]. We found that the critical maximum temperature that can be used during processing of THz QCLs with Ti/Au claddings is 400 °C.

On the basis of the research presented in the paper [59], Ti/Au-cladding fabrication parameters were determined to produce the reliable metal-metal waveguide and at the same time low-resistivity stable metal-semiconductor contact of non-ohmic character. 5 nm-thick Ti spacers and 300 nm-thick Au layers were applied and annealed at 400 °C for the fabrication of metal-metal AlGaAs/GaAs QCL waveguide.

The second crucial step during THz QCL fabrication is bonding the laser wafer to a separate wafer called the receptor. The QCL wafer-receptor connection must be long-term stable in terms of both mechanical robustness and the low-resistance electrical contact stability. The wafer bonding must be performed when the laser structure side, that is to be bonded to the receptor, has already been covered with metallic cladding, with the gold layer on top of it in a case of our Ti/Au claddings. The receptor ready for the bonding process is also covered with metallic solder. Indium is the most popular solder material used on top of GaAs:Si receptors with fabricated ohmic contacts (technology of this ohmic contact is described in [64]) and additional Au layers. The gold layer is added to form Au-In alloy necessary for appropriate bonding. A series of experiments concerning AuIn wafer bonding was performed. The details are described in [59]. The final results of these tests are presented in Fig. 4.2.

Finally, the selected technological parameters presented in the paper [59] were used to fabricate THz QCL.

Fig. 4.2 SEM image of soldered receptor wafer and GaAs wafer, where the stack of connected layers was GaAs n + (test wafer)/Ti/Au/In/Au/Ni/AuGe/GaAs n + (receptor) – see the main text for details in the paper [59]
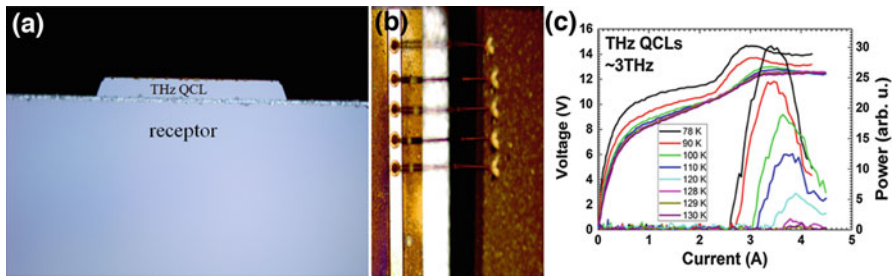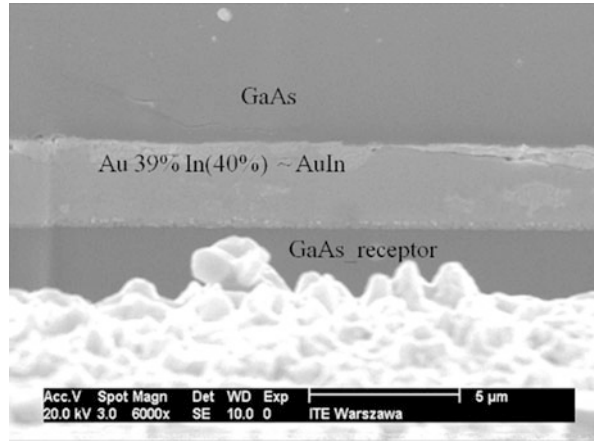
Fig. 4.3 AlGaAs/GaAs THz QCL ridge soldered with receptor wafer (**a**), wire-bonded QCL ridge (**b**), THz QCL basic characteristics for a set of operating temperatures (**c**) [59]

The fabricated devices were soldered ridge side up on a copper mount and then wire bonded (Fig. 4.3a, b). The maximum operating temperature was 130 K (Fig. 4.3c). The threshold current densities were around 1 kA/cm^2 at 77 K and 1.5 kA/cm^2 at 130 K.

Our studies on the technological aspects showed that the critical maximum temperature during processing of THz QCLs is 400 °C.

The calculation of waveguide losses for THz QCLs with Cu claddings, showing copper to be an even more promising material for metal-metal waveguides than gold, encouraged me to perform the experiments concerning Cu-based cladding [58]. Again, the application of a 5 nm-thick Ti spacer, just like the one for Ti/Au claddings, should not increase the losses significantly. As regards the Cu-based claddings investigated, numerous test structures have been tested experimentally, the details of these studies are described in the paper [59]. On the basis of the presented research it can be inferred that Cu-based cladding fabrication may turn out to be a very demanding task if the products are to be thermally stable and operate as ohmic contacts at the same time.
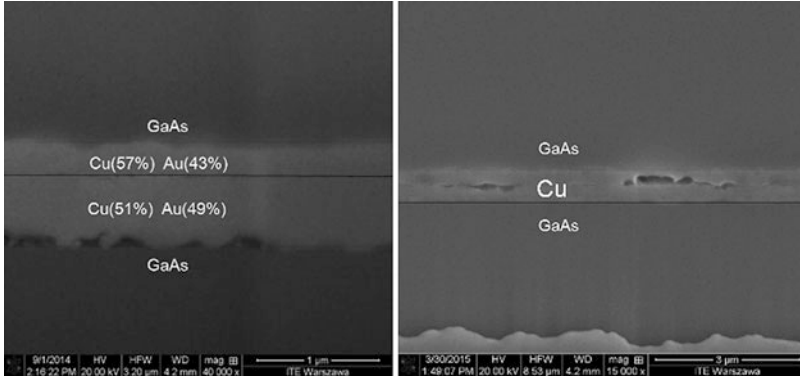
Fig. 4.4 SEM photos of interface regions of test structures (not laser structures): GaAs/5 nmTi/ 300 nmCu/300 nmAu/5 nmTi/GaAs to the left and GaAs/5 nmTi/600 nmCu/5 nmTi/GaAs to the right. Elemental compositions were measured by energy-dispersive x-ray spectroscopy [60]

It was described theoretical estimations of impact of different types of metallic claddings on $Al_{0.15}Ga_{0.85}As$/GaAs THz QCL performance (mainly in terms of the influence on the laser waveguide losses), critically discusses the relevance and practical value of such estimations and generates guidelines for technological strategy in a broad sense [60]. In work [60] we discussed the possibility of improvement of metal-metal waveguides designed for THz QCL because of the decreasing of waveguide losses. The essence of our work was the error analysis. We noticed that the input data, namely the refractive indices of metals, are known with very poor accuracy in the THz range. In support of that, we compared numerous measurements and calculations reported in the literature. In addition, we pointed out that optical properties of materials depend on temperature, which varies throughout the working device [60]. At last, we present our scanning electron microscopy images showing that semiconductor-metal and metal-metal interfaces are not perfect. In adjacent areas mixing of materials occurs and hence the spatial refractive index distribution is perturbed. Our error analysis shows that today's accuracy of refractive index data ($\pm 37\%$ is the best reported in the literature) makes the problem of optimization of considered waveguides ambiguous. According to our calculations, the precision level of about $\pm 10\%$ is required.

Scanning electron microscope (SEM) measurements illustrating our experimental investigations of material mixing near semiconductor-metal and metal-metal interfaces are included in the paper [60] and in Fig. 4.4.

The thin 5-nm titanium layers that are additional components of metallic structures presented in Fig. 4.4 play the role of diffusion barriers for the copper, preventing the copper diffusion into the GaAs phase.

As it was mentioned above, mounting of the THz QCL structure on the receptor substrate is another technological process that can easily lead to interdiffusion issues and hence may cause undesirable changes in the designed cladding structure. A model commonly used for calculations of THz QCL-waveguide performance, e.g.,

waveguide losses, is the planar-waveguide model. The model assumes that all the constituent layers within the waveguide have clearly defined uniform thickness and refractive indices. This implies that the model-based interfaces are sharp [60]. In real multilayer waveguide structures interdiffusion processes usually take place. Generally, they are associated with simultaneous transport of different atomic species through metal-metal or even metal-semiconductor interfaces [59, 60]. The intensity of the particular interdiffusion process strongly depends on conditions used for critical technological processes (such as cladding fabrication and bonding of the THz QCL's active region with receptor substrate) [59]. In the paper [59], it was shown that annealing temperature of the laser structure equipped with claddings is a critical parameter for the laser operation. This is due to too high temperature activating detrimental process of formation of gold grains that grow into the semiconductor structure. However, it should be emphasized, that even in the range of technologically accepted annealing temperature, slight interdiffusion effects in the area of cladding are still observed [60]. The interdiffusion is observed specifically in the range of a few tens of nanometers at the metal-semiconductor interface. They unavoidably influence the refractive index pattern in this region. Taking into account that the penetration depth of electromagnetic radiation into metals is in the similar range, the interdiffusion process must influence the waveguide performance (namely the losses) [60] and it should be taken into account during theoretical calculations.

The next paper [61] describes in-depth elaboration of $Al_{0.15}Ga_{0.85}As$/GaAs THz QCL laser generally based on standard fabrication (described in [59]), however, including meaningful modification of mounting technology. This very important alteration involved pure Au-Au-mounting process (in terms of the process of connecting the laser chip with the receptor wafer), instead Au-In-based mounting process – i.e., the indium solder was not used any more. The result of the described technological research was attainment/evaluation of optimized conditions of Au-Au-mounting process, in particular in terms of the process temperature profile, with focus on maximized tightness of the fabricated connection and its thermal stability. Later on, this technological alteration – though just formally dealing with mounting procedure – was found to have positive influence on purity and performance of the gold cladding [65, 67]. Namely, it allowed to eliminate a problem of Au-In intermixing in the cladding area, and hence it helped to suppress the laser waveguide absorption losses. In further work that resulted in increasing the laser's maximum operating temperature [65, 66].

The lasers were fabricated as gold-gold waveguide devices and were gold-gold mounted on GaAs receptor wafers according to the scheme presented in Fig. 4.5. This bonding was applied without indium, it was pure gold only.

Ti/Au-cladding fabrication parameters were determined to produce reliable metal-metal waveguide and at the same time low-resistivity stable metal-semiconductor contact. Then the connection of THz QCL with receptor substrate was performed. The Au- Au bonding process was performed in the temperature range 350–380 °C [61]. The example of Au-Au bonded test structures is presented in Fig. 4.6a. After wafer bonding, the further steps of processing were performed. The
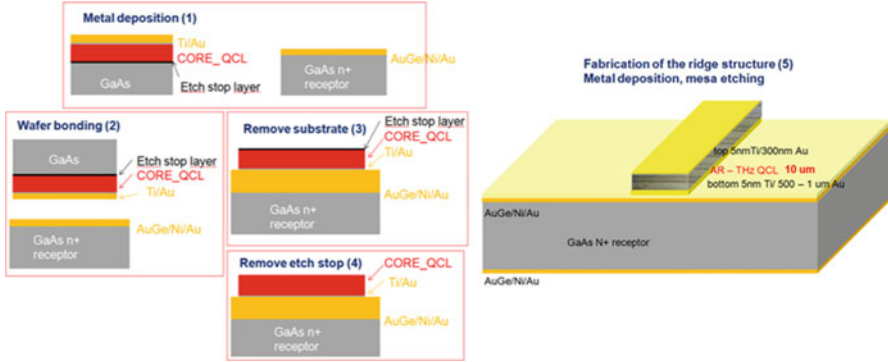
Fig. 4.5 The scheme of the processing of THz QCLs with metal – metal waveguides and the scheme of resulting laser chip [61]
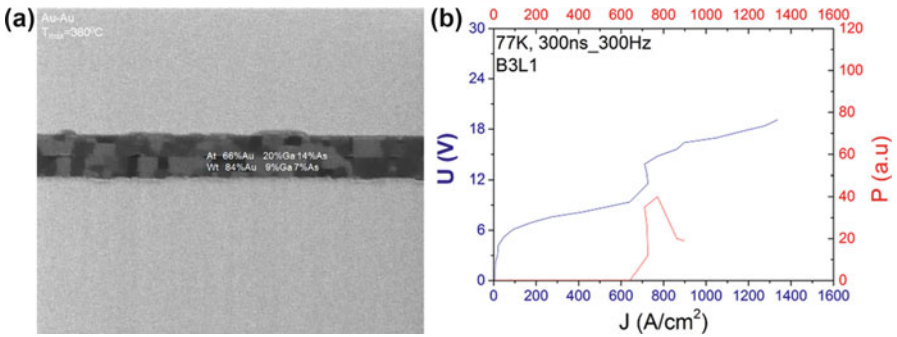
Fig. 4.6 SEM images of bonded GaAs/5nmTi/300nmAu and Au 300 nm /Ti 5 nm /GaAs test structures (**a**) and The $Al_{0.15}Ga_{0.85}As$/GaAs THz QCL basic characteristics (**b**) [61]

details of the further steps are described in [61]. The structures were wet etched into ridges with widths in the range 50–160 microns and lengths 1.8 mm.

The fabricated devices were soldered ridge side up on a copper mount and wire bonded. Afterwards, they were mounted on a cold stage in a vacuum cryostat and fed by 100–300 ns current pulses supplied with 300–1000 Hz repetition frequencies. The threshold current densities were around 650 A/cm^2 at 77 K (Fig. 4.6b).

Summarizing the studies on technology of ∼100 μm-emitting (∼3 THz) $Al_{0.15}Ga_{0.85}As$/GaAs QCLs [59–61], the optimized scheme of fabrication of such lasers was elaborated. It was a result of the extensive work on decreasing waveguide losses while ensuring the proper performance of the electrical contacts and effective heat removal. The fabrication comprises Au-based claddings and Au-Au-mounting process. The yielded lasers operate up to the maximum temperature $T_{max} = 140$ K, with threshold current density $J_{th} \sim 1$ kA/cm^2 at 77 K (Fig. 4.7).

Fig. 4.7 The $Al_{0.15}Ga_{0.85}As$/GaAs THz QCL basic characteristics at 140 K
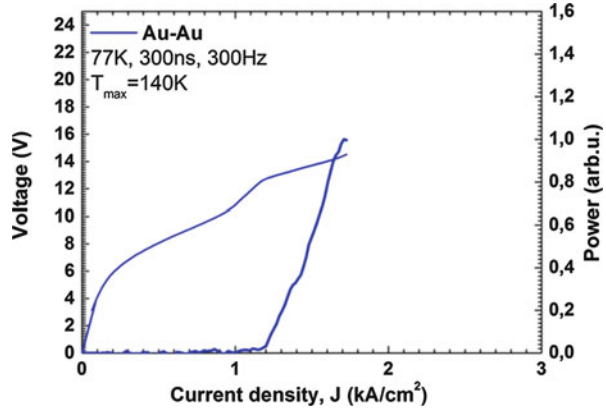
The ongoing technological research, which elements were mentioned in the papers [59–61] covers application of other than gold, though at least equally promising low-lossy-waveguide cladding metal (copper).

4.3 Conclusion

Summarizing the studies on technology of ~100 µm-emitting (~3 THz) $Al_{0.15}Ga_{0.85}As$/GaAs QCLs [59–61], the optimized scheme of fabrication of such lasers was elaborated. It was a result of the extensive work on decreasing waveguide losses while ensuring the proper performance of the electrical contacts and effective heat removal. The fabrication comprises Au-based claddings and Au-Au-mounting process. The yielded lasers operate up to the maximum temperature $T_{max} = 140$ K, with threshold current density $J_{th} \sim 1$ kA/cm^2 at 77 K.

References

1. Pereira MF, Zubelli PJ, Winge DJE, Wacker A, Rondrigues SA, Anfertvev V, Vaks V (2017) Theory and measurements of harmonic generation in semiconductor superlattices with applications in the 100 GHz to 1 THz range. Phys Rev B 96:045306
2. Pereira MF (2016) The linewidth enhancement factor of intersubband lasers: from a two-level limit to gain without inversion conditions. Appl Phys Lett 109:222102
3. Pereira MF (2017) Analytical expressions for numerical characterization of semiconductors per comparison with luminescence. Materials 11:2
4. Oriaku CI, Pereira MF (2017) Analytical solutions for semiconductor luminescence including coulomb correlations with applications to dilute bismides. J Opt Soc Am B 34:321

5. Apostolakis A, Pereira MF (2019) Controlling the harmonic conversion efficiency in semiconductor superlattices by interface roughness design. AIP Adv 9:015022

6. Pereira MF, Anfertev V, Shevchenko Y, Vaks V (2020) Giant controllable gigahertz to terahertz nonlinearities in superlattices. Sci Rep 10:15950

7. Faist J, Capasso F, Sivco DL, Sirtori C, Hutchinson AL, Cho AY (1994) Temperature dependence of the performance characteristics and high T 0 operation. Science 264:553

8. Page H, Becker C, Robertson A, Glastre G, Ortiz V, Sirtori C (2001) 300 K operation of a GaAs-based quantum-cascade laser at $\lambda \approx 9$ µm. Appl Phys Lett 78:3529

9. Razeghi M (2015) Quantum cascade lasers: from tool to product. Opt Express 23(7):8462–8475

10. Bai Y, Slivken S, Darvish SR, Razeghi M (2008) Room temperature continuous wave operation of quantum cascade lasers with 12.5% wall plug efficiency. Appl Phys Lett 021103:1–3

11. Razeghi M, Bandyopadhyay N, Bai Y, Lu Q, Slivken S (2013) Recent advances in mid infrared (3-5µm) Quantum Cascade Lasers. Opt Mater Express 3:1872–1884

12. Szerling A, Slivken S, Razeghi M (2017) High peak power 16 µm InP-related quantum cascade laser. Opto-Electron Rev 25:205–208

13. Lu QY, Bandyopadhyay N, Slivken S, Bai Y, Razeghi M (2011) Room temperature single-mode terahertz sources based on intracavity difference-frequency generation in quantum cascade lasers. Appl Phys Lett 99(13):131106

14. Lu QY, Bandyopadhyay N, Slivken S, Bai Y, Razeghi M (2012) Widely tuned room temperature terahertz quantum cascade laser sources based on difference-frequency generation. Appl Phys Lett 101(25):251121

15. Lu Q, Razeghi M (2016) Photo-Dermatology 3(3):42

16. Rochat M, Hofstetter D, Beck M, Faist J (2001) Long-wavelength ($\lambda \approx 16$ µm), room-temperature, single-frequency quantum-cascade lasers based on a bound-to-continuum transition. Appl Phys Lett 79(26):4271–4273

17. Kosiel K et al (2011) Nato science for peace and security series B: physics and biophysics. Springer, Cham, pp 91–100

18. Kosterev A, Wysocki G, Bakhirkin Y, So S, Lewicki R, Fraser M, Tittel F, Curl RF (2008) Application of quantum cascade lasers to trace gas analysis. Appl Phys B Lasers Opt 90:165

19. Kosiel K, et al (2011) 36th International conference on infrared, Millimeter and Terahertz Waves (IRMMW-THz)

20. Moeskops BWM, Naus H, Cristescu SM, Harren FJM (2006) Appl Phys B Lasers Opt 82:649

21. Tihov MI, Van Den Bergh H, Simeonov V, Taslakov M (2003) Chemical sensors based on DFB quantum cascade laser for environmental monitoring. Master's thesis, Ecole Polytechnique

22. Sirtori C, Page H, Becker C, Ortiz V (2002) GaAs-AlGaAs quantum cascade lasers: physics, technology, and prospects. IEEE J Quantum Electron 38:547

23. Sirtori C (2002) GaAs quantum cascade lasers: fundamentals and performance. EDP Sci

24. Kosiel K et al (2009) Molecular-beam epitaxy growth and characterization of mid-infrared quantum cascade laser structures. Microelectron J 40:565

25. Kosiel K et al (2009) 77 K operation of AlGaAs/GaAs quantum cascade laser at 9 um. Photonics Lett Poland 1:16

26. Höfling S, Kallweit R, Seufert J, Koeth J, Reithmaier JP, Forchel A (2005) Reduction of the threshold current density of GaAs/AlGaAs quantum cascade lasers by optimized injector doping and growth conditions. J Cryst Growth 278:775

27. Höfling S et al (2006) Dependence of saturation effects on electron confinement and injector doping in GaAs/$Al_{0.45}Ga_{0.55}$As quantum-cascade lasers. Appl Phys Lett 88:251109

28. Toor F, Sivco DL, Liu HE, Gmachl CF (2008) Effect of waveguide sidewall roughness on the threshold current density and slope efficiency of quantum cascade lasers. Appl Phys Lett 93:031104-1–031104-3

29. Szerling A, Karbownik P, Kosiel K, Kubacka-Traczyk J, Pruszyńska-Karbownik E, Płuska M, Bugajski M (2009) Mid-infrared GaAs/AlGaAs quantum cascade lasers technology. Acta Phys Pol A 116:S45–S48

30. Szerling A, Kosiel K, Karbownik P, Wójcik-Jedlińska A, Płuska M (2014) Terahertz and mid infrared radiation. Detection of explosives and CBRN (using terahertz). In: NATO science for peace and security series B: physics and biophysics. Springer, Dordrecht, pp 143–151

31. Huang X, Chiu Y, Charles WO, Gmachl C (2012) Ridge-width dependence of the threshold of long wavelength ($\lambda \approx 14$ μm) quantum cascade lasers with sloped and vertical sidewalls. Opt Express 20(3):2539–2547

32. Viana CE, da Silva ANR, Morimoto NI, Bonnaud O (2001) Analysis of SiO_2 thin films deposited by PECVD using an Oxygen-TEOS-Argon mixture. Braz J Phys 31(2):299–303

33. Deschmukh SC, Aydil ES (1996) Investigation of low temperature SiO2 plasma enhanced chemical vapor deposition. J Vac Sci Technol B 14:738

34. Ray SK, Maiti CK, Lahiri SK, Chafrabarti NB (1992) Properties of silicon dioxide films deposited at low temperatures by microwave plasma enhanced decomposition of tetraethylorthosilicate. J Vac Sci Technol B 10:1139

35. Slivken S, Private communication

36. Page H, Dhillon S, Calligaro M, Ortiz V, Sirtori C (2003) Optimised device processing for continuous-wave operation in GaAs-based quantum cascade lasers. Electron Lett 39:1053

37. Page H, Robertson A, Sirtori C, Becker C, Glastre G, Nagle J (2001) Demonstration of (/spl lambda//spl ap/11.5-μm) GaAs-based quantum cascade laser operating on a Peltier cooled element. IEEE Photon Technol Lett 13:556

38. Page H, Dhillon S, Calligaro M, Becker C, Ortiz V, Sirtori C (2004) Improved CW operation of GaAs-based QC lasers: T/sub max/= 150 K. IEEE J Quantum Electron 40:665

39. Lin H-C et al (2003) Optimization of AuGe-Ni-Au ohmic contacts for GaAs mosfets. IEEE Trans Electron Devices 50(4):880–885

40. Murakami M (2002) Development of refractory ohmic contact materials for gallium arsenide compound semiconductors. Sci Technol Adv Mater 3:1–27

41. Heiblum M, Nathan MI, Chang CA (1982) Characteristics of AuGeNi ohmic contacts to GaAs. Solid State Electron 25(3):185–195

42. Aina O, Katz W, Baliga BJ, Rose K (1982) Low-temperature sintered AuGe/GaAs ohmic contact. J Appl Phys 53(1):777–780

43. Shin Y-C, Murakami M, Wilkie EL, Callegari AC (1987) Effects of interfacial microstructure on uniformity and thermal stability of AuNiGe ohmic contact to n-type GaAs. J Appl Phys 62:582–590

44. Vidimari F (1979) Improved ohmic properties of Au-Ge Contacts to thin n-GaAs layers alloyed with an SiO_2 overlayer. Electron Lett 15:674–675

45. Faist J (2002) et. Al. Bound-to-continuum and two-phonon resonance, quantum-cascade lasers for high duty cycle, high-temperature operation. IEEE J Quantum Electron 38(6):533–546

46. Gmachl C et al (2002) Single-mode, tunable distributed-feedback and multiple-wavelength quantum cascade lasers. IEEE J Quantum Electron 38(6):569–581

47. Hofstetter D, Faist J, Beck M, Müller A, Oesterle U (1999) Demonstration of high-performance 10.16 μm quantum cascade distributed feedback lasers fabricated without epitaxial regrowth. Appl Phys Lett 75(5):665–667

48. Fuchs P, Friedl J, Höfling S, Koeth J, Forchel A, Worschech L, Kamp M (2012) Single mode quantum cascade lasers with shallow-etched distributed Bragg reflector. Opt Express 20 (4):3890–3897

49. Gmachl C et al (2000) Mid-infrared tunable quantum cascade lasers for gas-sensing applications. IEEE Circuits Devices Mag 16:10–18

50. Colombelli R et al (2001) Far-infrared surface-plasmon quantum-cascade lasers at 21.5 μm and 24 μm wavelengths. Appl Phys Lett 78(18):2620–2622

51. Szerling A, Kruszka R, Kosiel K, Wzorek M, Gołaszewska K, Trajnerowicz A, Karbownik P, Kuc M, Czyszanowski T, Walczakowski M, Pałka N (2017) $Al_{0.45}Ga_{0.55}As$/GaAs-based single-mode distributed-feedback quantum-cascade lasers with surface gratings. J Nanophotonics 11(2):026004-1–026004-13

52. Baranov AN, Bahriz M, Teissier R (2016) Room temperature continuous wave operation of InAs-based quantum cascade lasers at 15 µm. Opt Express 24(16):18799–18806
53. Vitiello MS, Scalari G, Williams B, De Natale P (2015) Quantum cascade lasers: 20 years of challenges. Opt Express 23(4):5167–5182
54. Szymański M, Szerling A, Kosiel K (2014) Theoretical investigation of metal–metal waveguides for terahertz quantum-cascade lasers. Opt Quant Electron. https://doi.org/10.1007/s11082-014-0007-z
55. Belkin M (2008) et.al. Terahertz quantum cascade lasers with copper metal-metal waveguides operating up to 178 K. Opt Express 16:3242–3248
56. Fathololoumi S et al (2011) On metal contacts of terahertz quantum cascade lasers with a metal–metal waveguide. Semicond Sci Technol 26:1–5
57. Williams BS, Kumar S, Callebaut H, Hu Q, Reno JL (2003) Terahertz quantum-cascade laser at using metal waveguide for mode confinement. Appl Phys Lett 83(11):2124–2126
58. Walther C, Scalari G, Faist J, Beere H, Ritchie D (2006) Terahertz quantum-cascade laser at λ≈100 µm using metal waveguide for mode confinement. Appl Phys Lett 89 (23):231121–231121
59. Szerling A, Kosiel K, Szymański M, Wasilewski Z, Gołaszewska K, Łaszcz A, Płuska M, Trajnerowicz A, Sakowicz M, Walczakowski M, Pałka N, Jakieła R, Piotrowska A (2015) Processing of AlGaAs/GaAs quantum-cascade structures for terahertz laser. J Nanophotonics 9(1): 093079-1-17
60. Szymański M, Szerling A, Kosiel K, Płuska M (2016) A study of different metals employed in metal–metal waveguides for terahertz quantum cascade lasers. J Phys D Appl Phys 49: 275102 (7pp)
61. Szerling A, Kosiel K, Prokaryn P, Szymański M, Trajnerowicz A, Sakowicz M, Karbownik P, Płuska M, Walczakowski M, Pałka N (2017) THz for CBRN and explosives detection and diagnosis, NATO science for peace and security series B: physics and biophysics. Springer. https://doi.org/10.1007/978-94-024-1093-8_17
62. Piotrowska A, Kontakty omowe na bazie złota do związków półprzewodnikowych III-V, rozprawa habilitacyjna
63. Piotrowska A, et al (1993) In MRS Proceedings, vol. 300. Cambridge University Press, p 219
64. Barańska A, Szerling A, Karbownik P, Hejduk K, Bugajski M, Łaszcz A, Gołaszewska-Malec K, Filipowski W (2013) Ohmic contacts for room-temperature AlGaAs/GaAs quantum cascade lasers (QCL). Opt Appl XLIII(1):5–15
65. Szerling A, et al A study of wafer bonding technology for terahertz quantum cascade lasers. Article in preparation
66. Szerling A et al (2017) Technologia wytwarzania terahercowych laserów kaskadowych. Przegląd Elektrotechniczny 8:50–53
67. Szerling A, Kosiel K, Kozubal M, Myśliwiec M, Jakieła R, Kuc M, Czyszanowski T, Kruszka R, Pągowska K, Karbownik P, Barcz A, Kamińska E, Piotrowska A (2016) Semicond Sci Technol. 31(7): 075010 (11pp.)

Chapter 5
Broadband Gas QEPAS Detection Exploiting a Monolithic DFB-QCL Array

Marilena Giglio, Andrea Zifarelli, Pietro Patimisco, Angelo Sampaolo, Giansergio Menduni, Arianna Elefante, Romain Blanchard, Christian Pfluegl, Mark F. Witinski, Daryoosh Vakhshoori, Frank K. Tittel, and Vincenzo Spagnolo

Abstract Mid-infrared spectral "fingerprints" of many hazardous and harmful gaseous substances are characterized by broad absorption bands, resulting from the merging of several absorption lines corresponding to ro-vibrational transitions. Broadband absorption spectroscopy is fundamental to detect and discriminate these substances. Here we report on a quartz-enhanced photoacoustic spectroscopy sensor for broadband absorbers detection, employing a monolithic array of 32, individually addressable, distributed-feedback quantum cascade lasers as the excitation source. This light source combines a fast tuning speed with a large tuning range, from 1190 cm^{-1} to 1340 cm^{-1} together with a high stability. The QEPAS sensor was tested for nitrous oxide (N_2O) and methane (CH_4) detection, exhibiting absorption features in the laser source emission spectral range. The two broad P- and R-absorption branches of N_2O have been accurately reconstructed, as well as several absorption features of CH_4, for gas concentrations ranging from 200 to 1000 part-per-million in nitrogen.

Keywords Quartz-enhanced photoacoustic spectroscopy · Gas sensing · Broadband absorbers · Monolithic distributed-feedback quantum cascade laser array · Nitrous oxide · Methane

M. Giglio (✉) · A. Zifarelli · P. Patimisco · A. Sampaolo · G. Menduni · A. Elefante · V. Spagnolo
PolySense Lab – Dipartimento Interateneo di Fisica, University and Politecnico of Bari, CNR – IFN, Bari, Italy
e-mail: marilena.giglio@uniba.it

R. Blanchard · C. Pfluegl · M. F. Witinski · D. Vakhshoori
Pendar Technologies, Cambridge, MA, USA

F. K. Tittel
Department of Electrical and Computer Engineering, Rice University, Houston, TX, USA

5.1 Introduction

Mid-infrared (Mid-IR) and Terahertz (THz) absorption spectra of Chemical Biological Radiological Nuclear (CBRNs) substances and explosive gases are characterized by intense broad bands, in many cases wider than 50 cm^{-1} [1]. An example of broadband absorbers (in gas phase) in the Mid-IR spectral range is shown in Fig. 5.1, where the absorption bands of the main CBRNs are reported, as simulated by using the HITRAN database [2].

At atmospheric pressure, gases like nitrous oxide, carbonyl sulphide, sulphur dioxide, ozone, carbon dioxide, exhibit high spectral density absorption lines in the Mid-IR spectral range, which merge into bands as wide as 100 cm^{-1}, representing a fingerprint for each molecule. Therefore, broadband absorption spectroscopy is fundamental to recognize the presence of such molecules in atmosphere. Moreover, when a gas sample containing many broadband absorber components is analyzed, it is crucial to investigate a spectral region as wide as possible in order to include absorption features belonging to each component, and better discriminate the individual contribution due to each gas species.

For broadband spectroscopy, laser sources tunable in a wide spectral range are required, such as external cavity QCLs (EC-QCLs) or ICLs (EC-ICLs). As a drawback, these devices are quite bulky, may need external liquid cooling systems and suffer from mechanical instability related to the rotating diffraction grating. As a consequence, the spectroscopic technique adopted must rely on a wavelength insensitive detector. In addition, optics components with high performance within a narrow spectral band, such as filters and high reflectivity mirrors, are not
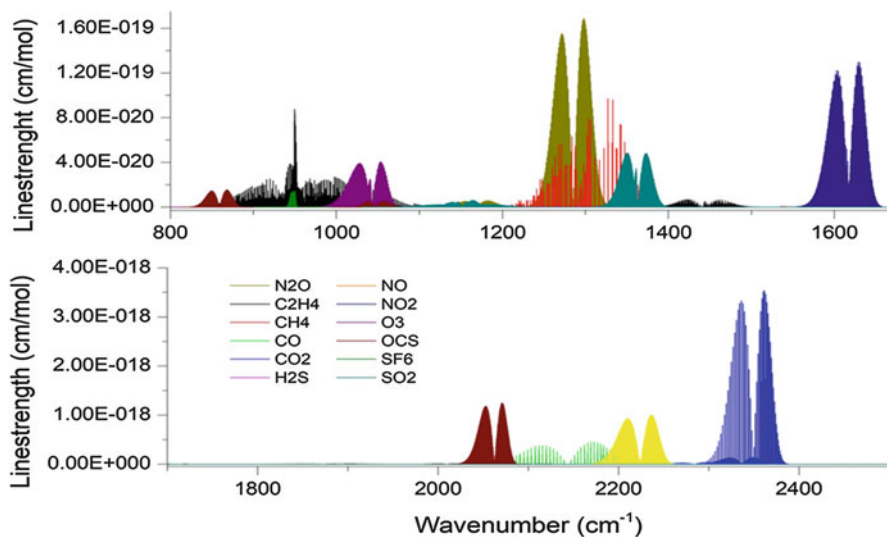
Fig. 5.1 Absorption lines of the main CBRNs and harmful gases in the Mid-IR spectral range simulated by using the HITRAN database

recommended. In this context, Quartz-Enhanced PhotoAcoustic Spectroscopy (QEPAS) can be an excellent candidate for broadband absorption spectroscopy [3–5]. QEPAS consists in exciting the target gas with a laser source whose emission wavelength matches an absorption line or band of the gas. The exciting radiation is modulated in order to generate sound waves, which are detected by a quartz tuning fork (QTF). The radiation is focused between the prongs of the QTF. When the light modulation matches the frequency of a natural flexural vibration of the QTF, electric charges appear on the QTF surface due to the piezoelectric effect. The current signal is proportional to the optical power exciting the gas molecules, the gas absorption coefficient, the QTF quality factor and acousto-electric transduction efficiency [6]. Therefore, QEPAS does not need of an optical detector, whose responsivity is wavelength-dependent. Indeed, QEPAS detection of broadband absorbing molecules has been demonstrated using a widely tunable EC-QCL [7]. In this work, we employed a monolithic distributed-feedback quantum cascade laser array as the light source for a QEPAS sensor, which combines fast tuning speed over a wide spectral range with high stability [8–10]. In addition, the source operates in pulsed mode, suitable for low-power consumption optical sensors technology. This QEPAS sensor has been tested for nitrous oxide (N_2O) and methane (CH_4) detection in the 1190 cm^{-1}–1340 cm^{-1} spectral range, at atmospheric pressure.

5.2 Experimental Setup

The experimental setup used in this work is shown in Fig. 5.2. The employed laser source is an array of 32 individually addressable pulsed DFB-QCLs, powered by a FPGA-based driver capable to control both the injection current and the thermoelectric cooling (TEC). The beams of the different QCLs are spatially overlapped by means of beam combining optics placed inside the laser housing [11]. Emitted beams are spatially filtered using a pinhole and then focused between the prongs of a QTF by an antireflection-coated ZnSe lens with focal length $f = 50$ mm. The QTF is acoustically coupled with a pair of micro-resonator tubes, forming the QEPAS spectrophone, to amplify the sound waves generated by the absorbing gas. The spectrophone is placed inside an acoustic detection module (ADM), consisting in a stainless-steel vacuum-tight cell equipped with two antireflection-coated ZnSe windows and two connectors for gas inlet and outlet. Transmitted power through the ADM is monitored by a power meter.

The laser driver and temperature controller unit are controlled by a LabVIEW-based software and the pulses repetition frequency is triggered by a waveform generator (Wavetek Model 29) to match the QTF resonance frequency f_0. The electric current produced by the QTF is collected and converted into a voltage signal by a transimpedance pre-amplifier (feedback resistance $R_{fb} = 10$ MΩ). This signal is demodulated by a lock-in amplifier (EG&G Instrument 7265) at the reference signal f_0, with an integration time of 100 ms. The analog output signal of the lock-in amplifier is sent to an USB data acquisition device (National Instrument myDAQ) to
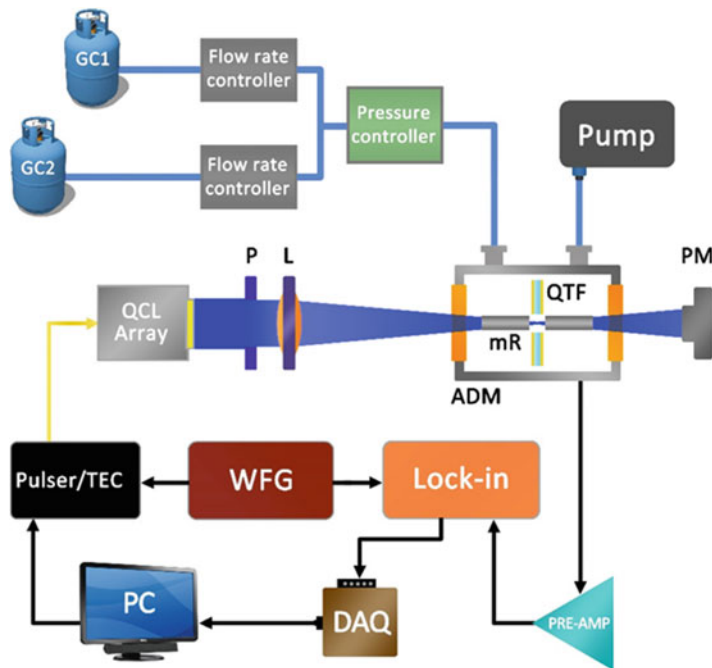
Fig. 5.2 Schematic of the experimental setup. Black lines indicate electrical connections, while blue lines mimic the gas tubes. The golden line indicates the array of cables used to drive the laser source. *GC* Gas Cylinder, *QCL Array* Quantum Cascade Laser array, *P* Pinhole, *L* Lens, *ADM* Acoustic Detection Module, *mR* Micro Resonator tubes, *QTF* Quartz Tuning Fork, *PM* Power Meter, *TEC* Temperature Controller unit, *WFG* Waveform Generator, *PRE-AMP* Pre-amplifier, *DAQ* Data Acquisition board, *PC* Personal Computer

be converted into a digital signal and recorded on the PC using a LabVIEW-based software. The target gas is pumped into the gas line by means of a rotative pump (Adixen Pascal 2021D). Gas flow inside ADM is controlled using flow rate controllers (Brooks Instruments) and a pressure controller (MKS type 649). Flow rate and pressure operation conditions were set at 30 sccm and 760 Torr, respectively.

5.3 Laser Source Characterization and Sensor Configuration

The QCLs comprising the monolithic array are operated in pulsed mode, with a maximum duty cycle of 1%. The devices can be turned on and off in arbitrary sequences. All measurements were performed setting the drive voltage providing the highest optical power output, a pulsewidth of 300 ns and a repetition frequency of 33 kHz (duty cycle of $\approx 1\%$). The spectral emission of the DFB-QCL array was
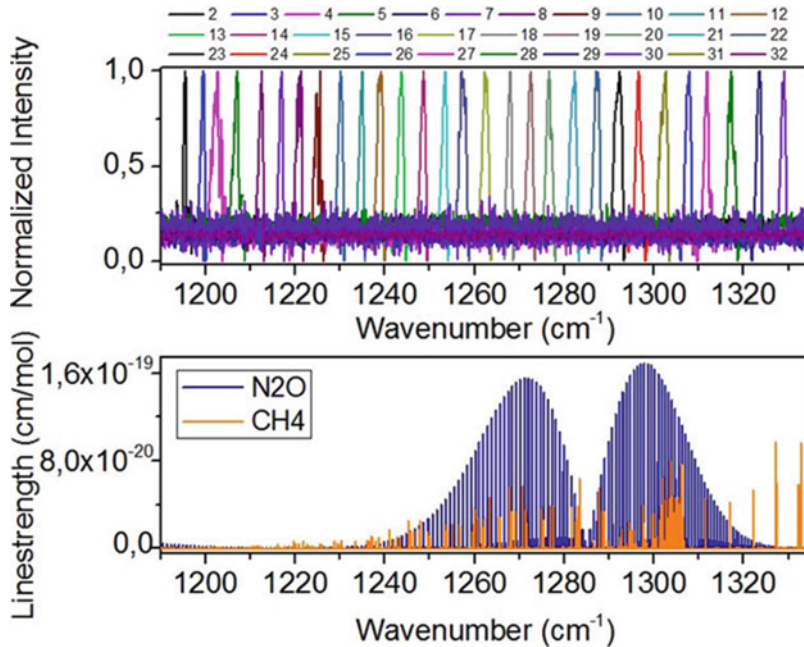
Fig. 5.3 (Upper panel) Normalized spectra of the QCL array acquired by an FTIR. (Lower panel) N_2O and CH_4 absorption lines falling in the QCL array emission spectral range

analysed using a Fourier-transform interferometer (FTIR - Thermo Nicolet 470), with a spectral resolution of 0.125 cm^{-1}. Laser beams exhibit single mode emissions with spectral linewidth of about 1.5 cm^{-1}. As shown in the upper panel of Fig. 5.3, the spectral emission of the array ranges from 1190 cm^{-1} to 1340 cm^{-1}, with a gap between adjacent laser emissions <5 cm^{-1}. In this spectral range, absorption lines of N_2O and CH_4 occur, as shown in the lower panel of Fig. 5.3.

The center emission of each QCL can be tuned by varying the operating temperature. A tuning coefficient of about -0.09 cm^{-1}/°C was measured for each device.

The analysis of the beam profiles was performed by using a pyroelectric-camera (Spiricon Pyrocam III) with pixel size of 100 μm $\times 100$ μm, placed in the focal plane of the lens. Figure 5.4a, b show the center position (black squares) and the beam diameter (black solid bars) of each device of the array in x- and y-direction, respectively.

Within the camera resolution, no shift was observed along the x-direction, while a 200 μm shift was observed along the y-direction. This allows the estimation of an overall focusing area measuring ~ 600 μm in the x-direction and ~ 800 μm in the y-direction in order to take into account all shifts related to different devices. Based on these measurements, a 1 mm-prong spacing custom QTF was used in this work,
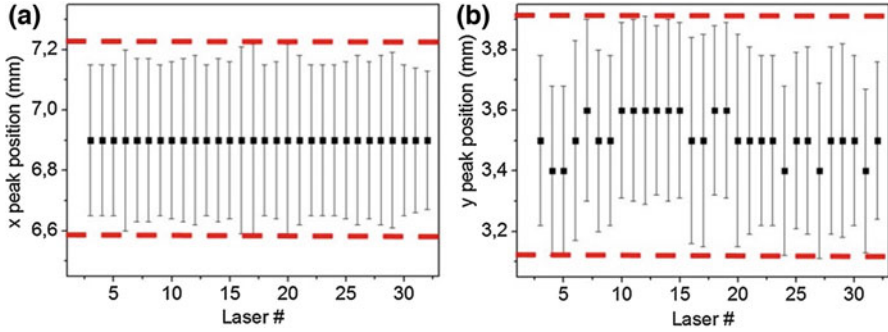
Fig. 5.4 Center position (black squares) and diameter (black solid bars) of the beam profile for each QCL comprising the array. The beam profiles were acquired in the lens focal plane, in x- (**a**) and y- (**b**) direction. Red dashed lines indicate the size of the beam focusing overall region in both directions
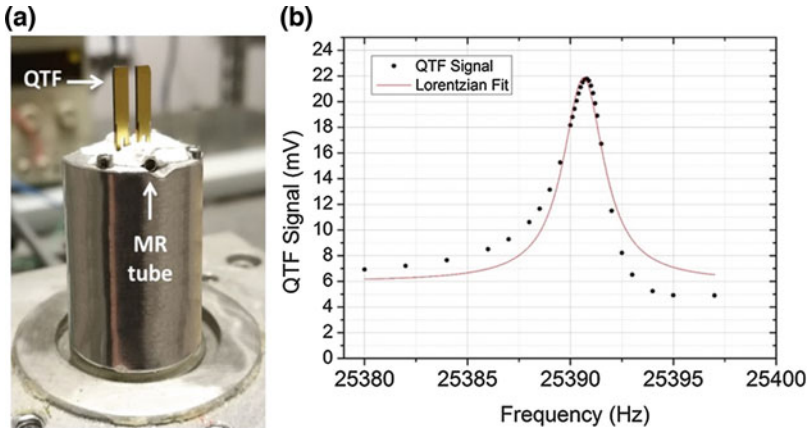
Fig. 5.5 Spectrophone picture (**a**) and electrical characterization at atmospheric pressure (**b**)

having a prong length of 19 mm, a prong width of 1.4 mm and a crystal thickness of 0.8 mm. The QTF was operated at the first overtone flexural mode [12]. Two micro resonator tubes, with internal diameter of 1.52 mm and length of 5.33 mm, were used to amplify the intensity of the photoacoustic waves [12]. A picture of the spectrophone is shown in Fig. 5.4a.

The spectrophone was electrically characterized to determine its resonance frequency and quality factor Q. The obtained resonance curve is shown in Fig. 5.5b as well as the Lorentzian fit. First overtone resonance frequency calculated by the fit is $f_0 = 25390.6$ Hz while quality factor is $Q = 10,550$.

5.4 Broadband Absorbers Detection and Sensor Performance

As shown in Fig. 5.3, nitrous oxide and methane show broadband absorption features in the emission spectral range of the employed source. A gas cylinder with a certified concentration of 10,000 part-per-million (ppm) of N_2O in N_2 and a gas cylinder with a certified concentration 1000 ppm of CH_4 in N_2 were used in this work. A cylinder of pure nitrogen was used for further dilutions. Photoacoustic signal generated by the absorbing target gas inside the ADM was collected using two different acquisition modes. The first mode (fixed-temperature mode) consisted in a fast-switching acquisition performed by setting the temperature of the QCLs at 25°C and switching the devices in sequence. Total acquisition time is about 8 min. Spectral resolution is given by the wavenumber distance between two adjacent devices (about 5 cm^{-1}). The second mode (temperature-tuning mode) was performed by tuning the operating temperature of each QCL and switching the devices in sequence. Temperature tuning is performed from 15°C to 50°C, with steps of 3°C, corresponding to a spectral resolution of 0.27 cm^{-1}, resulting in a total measurement time of about 120 minutes.

5.4.1 Nitrous Oxide Detection and Spectrum Reconstruction

The QEPAS signal for a $N_2O:N_2$ concentration of 1000 ppm, scaled to the QCLs normalized optical power curve of the array, is shown in Fig. 5.6a. Measurements performed in fixed-temperature mode (orange squares) and temperature-tuning mode (blue solid line and dots) are both showed and compared with the HITRAN
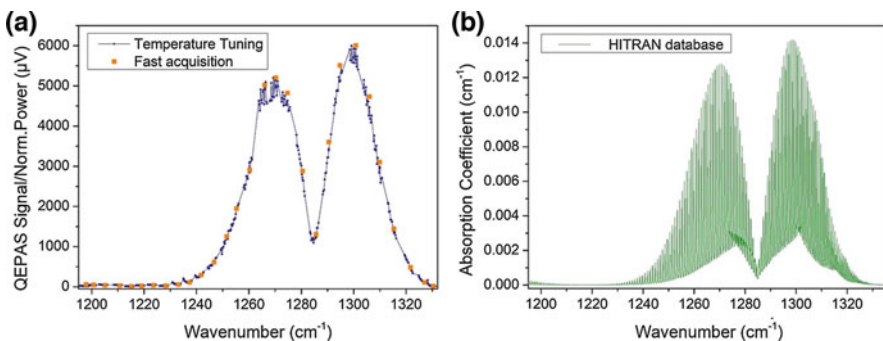
Fig. 5.6 (**a**) QEPAS signals scaled to the normalized optical power as a function of the QCLs wavenumber, for a $N_2O:N_2$ concentration of 1000 ppm, in fast-switching (orange squares) and temperature tuning (blue solid line and dots) acquisition mode. (**b**) Absorption spectrum of 1000 ppm of N_2O in N_2, simulated using HITRAN database at atmospheric pressure

database-simulation of the N_2O absorption spectrum related to the same concentration [2], reported in Fig. 5.6b.

Measurements acquired in the fast switching acquisition mode overlap the ones obtained in the temperature tuning mode, reducing the acquisition time but worsening the overall spectral resolution of the band reconstruction. Compared with HITRAN simulation, the collected QEPAS measurements trace the envelope of the nitrous oxide absorption spectrum with an excellent matching, both for the fast acquisition and for the temperature tuning acquisition mode. Experimental data well reconstruct the N_2O P- and R- branches, centered at 1270 cm^{-1} and 1298 cm^{-1}. Spectral features of N_2O are well recognizable by using both modes [13]. The certified concentration of nitrous oxide was subsequently diluted in pure nitrogen to test the sensor linearity. QEPAS spectra of 800 ppm, 600 ppm, 400 ppm and 200 ppm $N_2O:N_2$ were acquired. The QEPAS signal of the acquired spectra linearly scales with the N_2O concentration while the shape was preserved. In particular, the maximum QEPAS signal, which occurs in correspondence of the device emitting at 1274.5 cm^{-1}, was calculated to vary with a slope of 5 μV/ppm.

5.4.2 Methane Detection and Spectrum Reconstruction

Methane measurements were performed using the same procedure followed for nitrous oxide. Figure 5.7a shows the QEPAS signal scaled to the normalized optical power of each device of the array, for a certified $CH_4:N_2$ concentration of 1000 ppm. Measurements obtained with fixed-temperature (orange squares) and temperature-tuning (blue solid line and dots) acquisition modes are reported. As a comparison, the absorption spectrum of the same concentration of $CH_4:N_2$ simulated by using the HITRAN database at atmospheric pressure is reported in Fig. 5.7b.
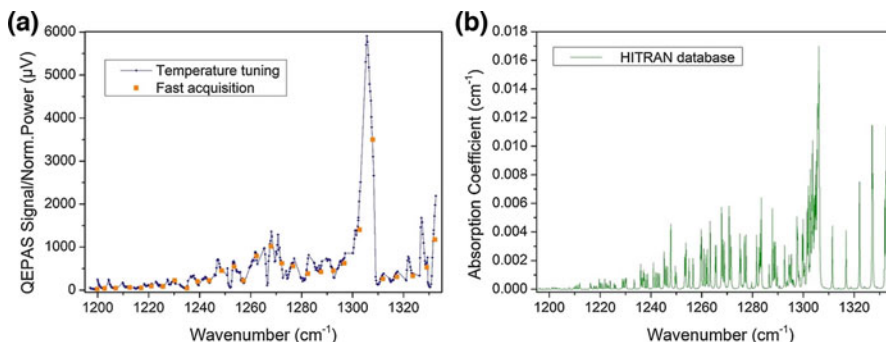
Fig. 5.7 (a) QEPAS signals scaled to the normalized optical power as a function of the QCLs wavenumber, for a $CH_4:N_2$ concentration of 1000 ppm, in fast-switching (orange squares) and temperature tuning (blue solid line and dots) acquisition mode. (b) Absorption spectrum of 1000 ppm of CH_4 in N_2, simulated using HITRAN database at atmospheric pressure

Measurements acquired in the fast switching acquisition mode overlap the ones obtained in the temperature tuning mode and the absorption peak at 1306.13 cm^{-1}, corresponding to the Q-branch of the methane ro-vibrational transitions, is well traced by both acquisition modes. However, lower intensity peaks are less distinguishable. A linear response of the QEPAS sensor for methane detection was demonstrated by diluting the certified concentration of methane in pure nitrogen. The maximum QEPAS signal of the methane spectrum, which occurs in correspondence of the device emitting at 1306 cm^{-1}, was calculated to vary with the methane concentration with a slope of 2 μV/ppm [14].

5.5 Conclusion

In this work, broadband detection of nitrous oxide and methane was demonstrated by using QEPAS-based sensor employing a monolithic array composed of 32 individually addressable distributed feedback-quantum cascade lasers as the light source. Within the laser source emission spectral range, from 1190 cm^{-1} to 1340 cm^{-1}, the two broad P- and R- absorption branches of nitrous oxide were reconstructed, as well as the Q-branch of methane. Two acquisition modes were tested, a fast-switching of individual devices in sequence, fixing the operation temperature at 25°C for each device, and higher resolution mode, tuning the operating temperature of each device together with the device switching in series. Sensor linearity for gases concentration in the 1000 ppm–200 ppm range was also demonstrated, both for methane and nitrous oxide.

References

1. Herzberg G (2016) Molecular spectra and molecular structure, vol 1. Read Books, New York
2. http://hitran.org/
3. Sampaolo A, Csutak S, Patimisco P, Giglio M, Menduni G, Passaro V, Tittel FK, Deffenbaugh M, Spagnolo V (2019) Methane, ethane and propane detection using a compact quartz enhanced photoacoustic sensors and a single interband cascade laser. Sens Act B Chem 282:952–960
4. Giglio M, Elefante A, Patimisco P, Sampaolo A, Sgobba F, Rossmadl H, Mackowiak V, Wu H, Tittel FK, Dong L, Spagnolo V (2019) Quartz-enhanced photoacoustic sensor for ethylene detection implementing optimized custom tuning fork-based spectrophone. Opt Express 27(4):4271–4280

5. Sampaolo A, Patimisco P, Giglio M, Chieco L, Scamarcio G, Tittel FK, Spagnolo V (2016) Highly sensitive gas leak detector based on a quartz-enhanced photoacoustic SF6 sensor. Opt Express 24:15872–15881
6. Patimisco P, Sampaolo A, Dong L, Tittel FK, Spagnolo V (2018) Recent advances in quartz enhanced photoacoustic sensing. Appl Phys Rev 5:011106
7. Lewicki R, Wysocki G, Kosterev AA, Tittel FK (2007) QEPAS based detection of broadband absorbing molecules using a widely tunable, cw quantum cascade laser at 8.4 μm. Opt Express 15(12):7357–7366
8. Lee BG, Belkin MA, Pflugl C, Diehl L, Zhang HA, Audet RM, MacArthur J, Bour DP, Corzine SW, Hofler GE, Capasso F (2009) DFB quantum cascade laser arrays. IEEE J Quantum Electron 45:554–565
9. Witinski MF, Blanchard R, Pfluegl C, Diehl L, Li B, Krishnamurthy K, Pein BC, Azimi M, Chen P, Ulu G et al (2018) Portable standoff spectrometer for hazard identification using integrated quantum cascade laser arrays from 6.5 to 11 μm. Opt Express 26:12159
10. Lee BG, Belkin MA, Audet R, MacArthur J, Diehl L, Pflügl C, Capasso F, Oakley DC, Chapman D, Napoleone A et al (2007) Widely tunable single-mode quantum cascade laser source for mid-infrared spectroscopy. Appl Phys Lett 91:231101
11. Lee BG, Kansky J, Goyal AK, Pflügl C, Diehl L, Belkin MA, Sanchez A, Capasso F (2009) Beam combining of quantum cascade laser arrays. Opt Express 17:16216
12. Patimisco P, Sampaolo A, Zheng H, Dong L, Tittel FK, Spagnolo V (2016) Quartz enhanced photoacoustic spectrophones exploiting custom tuning forks: a review. Adv Phys X 2:169–187
13. Giglio M, Patimisco P, Sampaolo A, Zifarelli A, Blanchard R, Pfluegl C, Witinski MF, Vakhshoori D, Tittel FK, Spagnolo V (2018) Nitrous oxide quartz-enhanced photoacoustic detection employing a broadband distributed-feedback quantum cascade laser array. Appl Phys Lett 113:171101
14. Giglio M, Zifarelli A, Sampaolo A, Menduni G, Elefante A, Blanchard R, Pfluegl C, Witinski MF, Vakhshoori D, Wu H, Passaro VMN, Patimisco P, Tittel FK, Dong L, Spagnolo V (2020) Broadband detection of methane and nitrous oxide using a distributed-feedback quantum cascade laser array and quartz-enhanced photoacoustic sensing. Photoacoustics 17:100159

Chapter 6
Global Optimization Methods for the Design of MIR-THz QCLs Applied to Explosives Detection

Jelena Radovanović, Nikola Vuković, and Vitomir Milanović

Abstract In this Chapter we explore the possibilities of using advanced optimization methods to obtain structural parameters of gain-maximized quantum cascade lasers emitting at specified wavelengths, suitable for detection of targeted chemicals. This involves the application of specialized techniques for the so-called "quantum engineering", including sophisticated methods of quantum mechanics, such as supersymmetry and inverse spectral theory, that have been successfully transferred into applied research areas. Particular attention is devoted to modern methods for global optimization: simulated annealing algorithm, multi-objective evolutionary algorithms, procedures based on applying the optimal control theory, which eliminate the unnecessary constraints from the optimization process.

6.1 Introduction

Quantum cascade laser (QCL) is a unipolar device based on intersubband transitions [1], with its active region incorporating a large number of periodically repeated epilayers. Each period (stage) comprises a gain and injection/relaxation regions (both regions are essentially superlattices [2]). While the gain region serves to create a population inversion between the two levels of the lasing transition, the purpose of the injection/relaxation region is to depopulate the lower lasing level and to provide injection of electrons in the upper lasing level of the next stage [3, 4].

Because of their high output power, narrow linewidth, tunability, compactness and portability, continuously operating QCLs in the MIR (3.5–20 μm) are extremely suitable for stand-off detection of chemical, biological, radiological and nuclear (CBNR) threats due to their favourable wavelength range [5–9]. Namely, many hazardous chemical species have strong characteristic absorption lines (signatures)

J. Radovanović (✉) · N. Vuković · V. Milanović
School of Electrical Engineering, University of Belgrade, Belgrade, Serbia
e-mail: radovanovic@etf.bg.ac.rs; nvukovic@etf.bg.ac.rs; milanovic@etf.bg.ac.rs

in the infrared. In order to fully exploit this potential, further improvements are needed in terms of detection sensitivity and selectivity, which stimulates exploration of novel material platforms for laser sources, comprehensive modelling and simulations of light-material interactions so as to better match explosives' signatures. Recent theoretical studies and advances in simulations of materials, sources and detectors for GIGA-TERA-MIR spectral range [3, 5, 10–12] confirm the importance of detailed theoretical modelling, the need for deeper understanding of underlying physics of these devices and stimulate the exploration for novel methods and solutions.

A careful design of the quantized states in the QCL heterostructure is essential for the development and optimization of experimental QCLs since the lasing frequency is determined by the energy difference between the upper and lower laser level and a careful energy alignment of the levels is necessary for an efficient injection into the upper (laser) level and depopulation of the lower level. Likewise, careful engineering of the wave functions is necessary because it governs the strength of both the optical and nonradiative transitions. The eigenenergies and wave functions are determined by solving the stationary Schrödinger equation or, if space charge effects are taken into account, the Schrödinger-Poisson equation system [3]. It is therefore rewarding to search for the new procedures for global (unconstrained) optimisation of MIR-THz QCLs' design with the goal to improve their performance in explosives detection.

In this contribution particular attention is devoted to modern methods for global optimization: simulated annealing algorithm, multi-objective evolutionary algorithms, procedures based on applying the optimal control theory, which eliminate the unnecessary constraints from the optimization process. This Chapter is organized in the following manner: Section 6.2 reviews global optimization methods used to optimize gain of MIR-THz QCL, in particular *Simulated Annealing Algorithm*, *Genetic Algorithm* and *Variational Calculus*; Section 6.3 offers an insight into *Supersymmetric Transform* and *Coordinate Transform*, convenient ways for constrained optimization of QW profile (and thus QCL active region); and Section 6.4 briefly wraps up the Chapter.

6.2 Global Optimization Methods Used on QCLs

Development of powerful optimization routines, to be embedded in the calculation of QCL device performance parameters, is essential for optimized and intelligent search and evaluation of candidate devices through the design space [13–28], especially when considering specific design requirements for a particular application. In general, global and direct optimization techniques that are being applied to the design of QCLs include iterative or direct optimization [13, 14, 21], simulated annealing algorithms [22, 23], single-objective genetic algorithms [15–17, 24–28], particle swarm optimization [18], and multi-objective genetic algorithms [19, 20]. Since QCL structures are complex multi-layer systems, optimization

routine needs to handle a large number of variables with complex interactions. Each of these methods has some benefits and disadvantages and one needs to make a compromise between accuracy and computational efficiency. For example, direct and iterative optimization methods lack the ability to efficiently search the parameter space. Similarly, simulated annealing methods, while capable of global search, are inefficient for a large number of variables and do not take advantage of parallel computing. On the other hand, evolutionary algorithms such as genetic algorithms and particle swarm optimization are well suited for parallel computation and are better candidates when one needs to cover a large parameter space of a QCL design. For a successful optimization algorithm the choice of the target or fitness function (s) is crucial. This function takes into account the features that are being evaluated and classifies the appropriateness of a design. Most of the studies present in literature use a form of gain as a fitness function [13, 14, 21–23, 25], or a measure related to gain such as wall-plug efficiency [26], population inversion [17, 19, 27], oscillator strength [17, 27], and period length [27]. It is also possible to use a target function specific to the design, for example a non-linear susceptibility for second-harmonic generation [15, 28] and third harmonic power [18].

Optimization algorithms are usually limited to the active region of a QCL design. However, since there is a delicate interplay between the injector and the active region it is necessary to either set strict limits on the position of the upper and lower state energy levels to suit a given injector design or additional optimization is needed to find a suitable injector [13, 15, 17, 21, 22, 25, 27, 28]. Various methods for calculating the relevant physics have been used including rate equation modelling [14, 22, 23, 25, 27, 28], density matrix transport model [21, 26], Monte Carlo methods based on Boltzmann transport [17], Pauli master equation [18], and Schrödinger–Poisson solver [13, 20, 24].

6.2.1 Simulated Annealing Algorithm

The simulated annealing (SA) algorithm [29] is a single-individual stochastic global optimization method which uses the Metropolis function [30] for the acceptance probability. In metallurgy thermal annealing refers to heating and gradually cooling of a material in order to give atoms the time to attain the lowest energy states thus achieving perfect crystallization. The simulation of annealing is used to find an approximation of a global minimum (maximum) of a target function with a large number of variables subject to various constraints, by a sequence of steps modelled in analogy to the physical process of annealing [31, 32].

Suppose that we use $E(i)$ to denote the energy of a specific configuration i of the atoms in some material. The probability that the system of atoms is in configuration i is given as:

$$P(i) = \frac{e^{-\frac{E(i)}{kT}}}{\sum_j e^{-\frac{E(j)}{kT}}} \tag{6.1}$$

where k is Boltzmann's constant, T is the temperature of the system at equilibrium, and the sum in the denominator is taken over all possible configurations j [31]. Now suppose that we have a system that is in configuration q, and we randomly select a configuration r that is a candidate for the system configuration at the next time step. If $E(r){<}E(q)$, then we accept r as the configuration at the next time step with probability equal to 1. However, if $E(r) > E(q)$, then we move to r at the next time step with a probability that is proportional to the relative energy of q and r:

$$P(r|q) = e^{\frac{E(q)-E(r)}{kT}} \tag{6.2}$$

The annealing algorithm in each step randomly generates new configurations and calculates a fitness function value (which is analogous to the energy of a crystalline structure). Any downhill step is automatically accepted while an uphill step may be accepted according to the Metropolis criteria described above. The algorithm starts initially with annealing control parameter set to a high value (i.e. we start with "high temperature" so that the candidate solution is likely to change to some other configuration), and as the annealing proceeds, the value of annealing control parameter declines. In this way, the system is expected to wander initially towards a broad region of the active parameter space containing good solutions and then the search towards minimum is narrowed down [22, 23]. The literature often distinguishes SA from evolutionary algorithms (EAs) because SA does not involve a population of candidate solutions. As an example of application to QCL desing, in [22] the objective is to optimize the optical gain of a MIR-QCL at selected wavelength, hence the fitness function is taken in the following form [22, 25]:

$$F = -\frac{g}{\left[\left(\frac{\varepsilon - E_2}{\hbar\omega} - 1\right)^2 + \Theta^2\right]\left[\left(\frac{E_2 - E_1}{\hbar\omega} - 1\right)^2 + \Theta^2\right]} \tag{6.3}$$

where the denominator favours achieving specified emission wavelength (i.e. photon energy $\hbar\omega$) and the LO-phonon resonance. In addition, Θ is a nonzero constant, which ensures that function F is strongly driven towards resonance during the optimization process but without divergence at the exact resonance conditions, and g is the optical gain of the structure in normal operating conditions [22].

Alternatively, since modal gain is proportional to the following figure of merit $\Xi = (1 - \tau_{21}/\tau_{32})\tau_3\mu_{31}^2\mu_{23}^2$ (obtained from the rate equations model), where $\mu_{ij} = \langle i|\mu|j \rangle$ is the dipole matrix element, and the transition lifetime τ_{ij} is the reciprocal of the sum of acoustic and polar optical phonon scattering rates, which

Fig. 6.1 The active region of QCL, optimized using SA for emission at $\lambda = 10$ μm
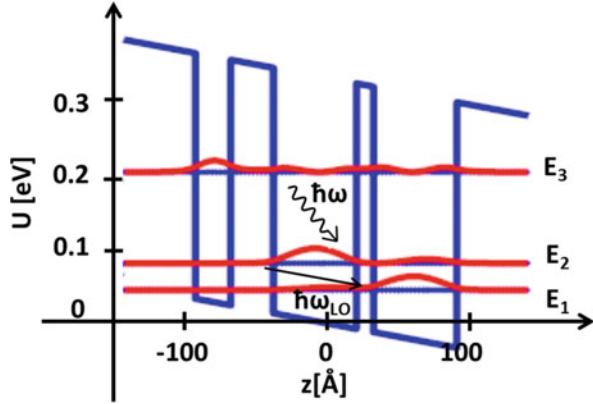
also depend on state wave functions and energies, and $1/\tau_3 = 1/\tau_{31} + 1/\tau_{32}$ [4], we can do the maximization of Ξ, by changing the QW profile.[1]

Gain-optimized MIR QCL active region configuration with corresponding wave functions squared, obtained using SA with fitness function given by Eq. (6.3) is given in Fig. 6.1. The structural parameters for the QCL active region for $\lambda = 10$ μm are 25, 30, 59, 12 and 59 Å (starting from the first well on the left) and the applied electric field in the z direction is K = 35,81 kV/cm [22]. The obtained Al mole fraction is $x = 0.4$, so the structure may be realized by GaAs/Al$_{0.4}$Ga$_{0.6}$As. The optimization routine can be modified and also applied for the THz spectral range.

6.2.2 Genetic Algorithm

Evolutionary computation is a rapidly growing area of artificial intelligence and it provides a set of optimization algorithms that use the basic processes of Darwin's theory of evolution: selection, breeding, mutation, inheritance, for finding a solution to the optimization problems. The final result is sought by selecting the "fittest" solution which is allowed to survive. The algorithm starts with a collection of candidate solutions called population, which is used to form a new collection of offspring, with the best possible features (expressed by the value of the predefined objectives, i.e. the fitness (target) function). The use of EAs is well suited for any choice or even variation of the QCL material system [21].

Genetic algorithm (GA) is one of the best-known evolutionary algorithms, developed by Holland [33]. Several varieties of this algorithm can be found in the literature [31, 32]. As already pointed out, GA begins with an entire set of solutions

---

[1]Nevertheless, state energies are essentially fixed, constrained by the pump or lasing frequency, and the energy difference between the lower laser level and the ground level is approximately LO phonon energy- feature that provides fast relaxation of the lower laser level.

called "population", which is used as a basis for generating another set of "off-springs" with best possible characteristics defined by the fitness function. This process is repeated until some termination criterion is satisfied. The performance of the algorithm is mainly influenced by the settings associated with the recombination (or crossover) and the mutation probability. The crossover represents a set of rules for creating new offsprings ("children") from parents' data. Mutations introduce random changes in the offspring resulting from the crossover and their purpose is to prevent the solutions from falling into a local optimum. In [25] mutation function is of Gaussian-type whose standard deviation decreases as the algorithm progresses. Predefined percentage of offsprings is generated by adding a random number taken from the Gaussian distribution to individual parent vectors, thus changing the parents' "genes". The crossover function which specifies how the algorithm combines two parents to form a crossover offspring, was taken as scattered. It creates a random binary vector and selects the genes where the vector element is equal to 1 from the first parent, and the genes where the vector element is a 0 from the second parent, and combines the genes to form the "child". Since in [25] the objective is again to optimize the optical gain at a selected wavelength, the fitness function is taken in the form of Eq. (6.3), the same fitness function that we used for SA. The role of the GA is to simultaneously vary all six free parameters which influence the fitness function (barriers heights and layers' thickness), while searching for the optimal solution, and this procedure has resulted in the structure presented in Fig. 6.2.

The structure is gain-optimized for emission at $\lambda \approx 7.3$ μm, which corresponds to a characteristic line in the spectrum of sulphur dioxide SO_2 [34]. The structural parameters for this optimized QCL active region design read: 11, 32, 39, 23 and 38 Å (starting from the first well on the left) and $U_b = 0.3175$ eV (the barrier height), which corresponds to aluminium mole fraction of $x = 0.38$, so the structure may be realized using GaAs/$Al_{0.38}Ga_{0.62}As$ [25]. The applied electric field in the z-direction is $K = 48$ kV/cm, and the relevant energy differences between the subbands are $\Delta E_{32} = 170$ meV and $\Delta E_{21} = 36$ meV.

Fig. 6.2 The conduction band diagram of the active region of QCL, optimized for emission at $\lambda \approx 7.3$ μm which corresponds to a characteristic line in the spectrum of SO_2. The relevant energies and the wavefunctions squared are also displayed
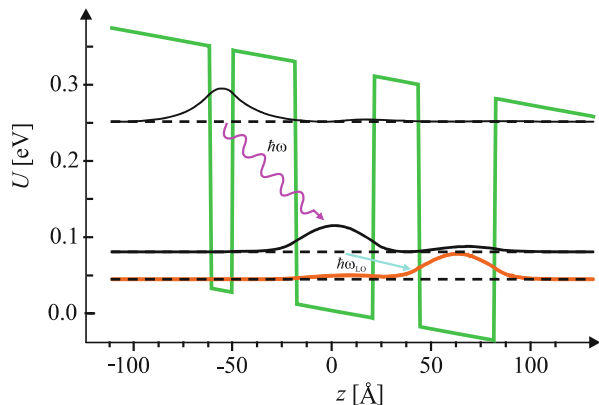
6.2.3   Variational Calculus

In this subsection, we present another procedure for the QW profile optimization, which may perform a global optimization (with no unnecessary constraints). It relies on the variational calculus (part of the optimal control theory) and starts with some initial QW profile which is then variationally refined towards the globally optimal smooth function. Instead of changing some finite set of structural parameters (such as layers widths and composition in step-graded QWs), here the profile is completely freely varied, i.e. this method is used for finding extrema of functions with infinite number of variables. In such a case, maxima and minima are reached on functions which are determined by solving a corresponding system of differential equations. In [35] the procedure is applied to find the best QW profile for the largest value of optical rectification coefficient. Nevertheless, changing the objective of QW profile optimization with respect to the second- or third-order nonlinearities, electro-optical coefficient [36], intersubband laser gain (as we did in previous sections) and similar ones is quite straightforward, so we will retain this example to illustrate the procedure.

The polarization response of the structure to incident radiation with photon energy $\hbar\omega$ is essentially determined by intraband transitions between quantized states E_i. Taking the incident electromagnetic field in the form $E(t) = \frac{1}{2}\widetilde{E}e^{j\omega t} + c.c$ the QW polarization, up to and including the second-order terms may be written as $P(t) = \left(\varepsilon_0\chi^{(1)}\widetilde{E}e^{j\omega t} + \varepsilon_0\chi^{(2)}_{2\omega}\widetilde{E}^2 e^{2j\omega t}\right) + c.c + \varepsilon_0\chi^{(2)}_0\widetilde{E}^2$ where ε_0 is the vacuum dielectric permittivity, $\chi^{(1)}$ is the linear susceptibility, $\chi^{(2)}_{2\omega}$ is the second-order susceptibility at twice the incident frequency and $\chi^{(2)}_0$ is second-order susceptibility at zero frequency (also known as the optical rectification coefficient, describing the dc field generation by an optical beam). It is explained in detail in [35] that under usual operating conditions the rectification coefficient will be largest at exact resonance (i.e. $\hbar\omega_{21} = E_2 - E_1 = \hbar\omega$), and it is proportional to the product of the square of the effective transition matrix element $\mu_{12,\ eff}$ and the difference of permanent dipole moments of the two states δ_{12}, i.e. $\chi^{(2)}_{0,\max}\widetilde{\Pi}^{(0)}_{eff} = \mu^2_{12,eff}\delta_{12}$.

In the variational approach the optimization problem can be reduced to varying one continuous function (the potential U(z)) instead of tens of free structural parameters. First, it is necessary to define a target functional encompassing the physical goal that needs to be accomplished. In case of optimizing the OR coefficient, we define the target functional in the following way:

$$J = \frac{\mu^2_{12,eff}\delta_{12}}{\Delta\omega^2_{21} + \Gamma^2}, \qquad (6.4)$$

where Γ is equal to the linewidth [35, 37]. The potential *U(z)* may take arbitrary shape in the segment $[-z_L, z_R]$ in which it is optimized, and is constant outside it. Envelope wavefunctions and its derivatives are taken to be zero at the endpoints of

the optimization segment. The maximization of the functional J is a constrained type optimization, because the functions Ψ_i satisfy the effective-mass Schrödinger equation:

$$-\frac{\hbar^2}{2}\frac{d}{dz}\left(\frac{1}{m^*(z)}\frac{d\Psi_i}{dz}\right) + U(z)\Psi_i = E_i\Psi_i \qquad (6.5)$$

where $i = 1, 2, 3$ is the wavefunction/energy index and $m^*(z) = m(z)m_0$ is the position-dependent electron effective mass, m_0 is the free electron mass.

While the constrained optimization is performed in the usual way by introducing Lagrange multipliers $\lambda_i(z)$ [38], for unconstrained optimization the new functional is given in the following form [35]:

$$J^* = J - \sum_{i=1}^{3}\int_{-z_L}^{z_R}\lambda_i(z)\left[\frac{\Psi_i''}{m} - \frac{m'}{m^2}\Psi_i' + q[E_i - U(z)]\Psi_i\right]dz \qquad (6.6)$$

The conditions for the extremum of Eq. (6.6) are obtained by equating its variation δJ^* to zero:

$$\delta J^* = \delta\int_{-z_L}^{z_R}\Phi(z)dz = 0 \qquad (6.7)$$

The unknown functions y_i (in this case $\Psi_i(z)$ and $U(z)$) maximizing Eq. (6.6) are to be obtained by solving the system of Euler–Lagrange equations:

$$\frac{\partial\Phi}{\partial y_i} - \frac{d}{dz}\left(\frac{\partial\Phi}{\partial y_i'}\right) + \frac{d^2}{dz^2}\left(\frac{\partial\Phi}{\partial y_i''}\right) = 0 \qquad (6.8)$$

which in our case becomes:

$$\begin{aligned}
&\lambda_1'' - \frac{m'}{m}\lambda_1' + \lambda_1 b_1 m = mz(K_1\Psi_2 + K_3\Psi_3) = F_1(z)\\
&\lambda_2'' - \frac{m'}{m}\lambda_2' + \lambda_2 b_2 m = mz(K_1\Psi_1 + K_2\Psi_3) = F_2(z)\\
&\lambda_3'' - \frac{m'}{m}\lambda_3' + \lambda_3 b_3 m = mz(K_2\Psi_2 + K_3\Psi_1) = F_3(z)\\
&G = q[\lambda_1\Psi_1 + \lambda_2\Psi_2 + \lambda_3\Psi_3] - \frac{1}{mU}\left[\lambda_1'\Psi_1' + \lambda_2'\Psi_2' + \lambda_3'\Psi_3'\right] = 0
\end{aligned} \qquad (6.9)$$

The details on solving such a set of equations, together with the approach of selecting the initial potential profile in combination with the SA method are

presented in [35]. Applications to various nonlinear optical effects, along with numerical examples are provided in Refs. [36, 39].

6.3   Isospectral Transformations of the Hamiltonian

In this Section we will present a procedure from quantum mechanics which enables one to start from any given one-dimensional potential $U_1(z)$ with n bound states and then construct m-parameter family of strictly isospectral potentials $U_{SS}(z; \lambda_1, \lambda_2, \ldots, \lambda_m)$ i.e., potentials with eigenvalues, reflection and transmission coefficients identical to those for $U_1(z)$.

6.3.1   Supersymmetric Transform

A convenient way of carrying out constrained optimization of QW profile is by the use of the supersymmetric quantum mechanics (SUSYQM). A comprehensive review of SUSYQM theory may be found in [40–43]. This method begins with a selection of a one-dimensional potential $U_1(z)$, with suitably positioned eigenenergies E_n and the corresponding wave functions ψ_{1_n}, and then generates a family of potentials $U_{SS}(z; \ldots, \lambda_j, \ldots)$ with different shapes, nevertheless fully isospectral to the original $U_1(z)$. The shape of U_{SS}, and therefore of the wave functions is controlled by scalar parameters λ_j.

In the simplest case of single-parameter transform ($m=1$) shown in Fig. 6.3, and constant effective mass Hamiltonian, the SUSYQM *partner potential* $U_{SS}(z, \lambda)$, isospectral to the original $U_1(z)$, is given by $U_{SS}(z, \lambda) = U_1(z) - (\hbar^2/m) \times (d^2/dz^2) \ln [\lambda + I(z)]$, and the corresponding normalized wave functions ψ_{SS_n} read [40, 44]:
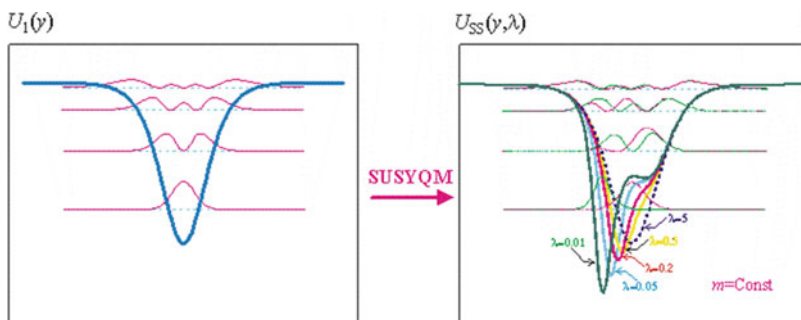
Fig. 6.3 Illustration of supersymmetric transform: (**a**) the original and (**b**) supersymmetric potential $U_{SS}(y, \lambda) = U_1(y) - (\hbar^2/m) \times (d^2/dy^2) \ln [\lambda + I(z)]$ for 5 values of scalar parameter λ

$$\psi_{SS_l} = \frac{\sqrt{\lambda(\lambda+1)}}{\lambda + I(z)} \varphi(z),$$

$$\psi_{SSi} = \psi_{1_i} - \frac{\varphi(z)}{\lambda + I(z)} \int\limits_{-\infty}^{z} \varphi(z') \, \psi_{1_i}(z')dz', \qquad (i \neq l) \tag{6.10}$$

where ψ_{1_i} is the ith state wave function (of discrete non-degenerate or 1-degenerate continuous spectra) for the potential $U_1(z)$, $I(z) = \int_{-\infty}^{z}\varphi^2(z')dz'$, and $\varphi(z) = \psi_{1_l}$ is the wave function of arbitrarily chosen l^{th} state of the original, via which the transform is performed. The real parameter λ is allowed to take any value outside the segment $[-1, 0]$ (if $I(z)$ is represented in the way designated above).

This procedure may be iterated as $U_1(z) \to U_{SS}(z, \lambda_1) \to U_{SS}(z, \lambda_1, \lambda_2) \to \dots$ to deliver multiparameter families of potentials [44, 45].

Note that if we start from Schrödinger Eq. (6.5) with position-dependent effective mass, this would result in the following value of supersymmetric potential [46]:

$$U_{SS}(z, \lambda) = U_1(z) - \frac{\hbar^2}{\sqrt{m(z)}} \frac{d}{dz} \left[\frac{1}{\sqrt{m(z)}} \frac{d}{dz} \{ \ln [\lambda + I(z)] \} \right] \tag{6.11}$$

In addition, if the effective mass is also energy-dependent, we change $m(z) \to m(z, E^{(i)})$ in Schrödinger equation, as in the graded ternary alloy $A_xB_{(1-x)}C$ QWs, and include the Kane model of nonparabolicity:

$$m\left(z, E^{(i)}\right) = \left(\frac{m_{AC} - m_{BC}}{\Delta U} U_{SS}(z) + m_{BC} \right)$$
$$\times \left[1 + \frac{E^{(i)} - U_{SS}(z)}{E_g(z)} \right] \tag{6.12}$$

For potential (6.11) and effective mass (6.12) we then solve Schrödinger equation (6.5). Enforcing the effective mass to follow the optimized potential $U_{SS}(z)$ and inclusion of the nonparabolicity results in the loss of state energy differences (state energies are essentially fixed, see footnote 4). This can be amended (i.e. we restore the desired energy differences) by simple coordinate scaling: we define the final potential $U_{SS}^*(z') = U_{SS}(z)$ with $z' = \alpha z + \beta|z|$, and the effective mass following it, where the symmetric and asymmetric scaling coefficients α and β are determined by numerical experimenting, for details please see [46] and [47].

Despite the fact that it is possible to derive sypersymmetric transform expressions applicable to the case of position-dependent effective mass, these expressions are not applicable for semiconductor heterostructures. Namely, this is because the effective-mass profile remains uncorrelated to the potential, which is not suitable for description in modulated structures: in these systems the potential (the conduction-band edge) and the effective-mass variation are related because they are both determined by the alloy composition [44]. In some cases (e.g. graded $Al_xGa_{1-x}N$ alloys) the

situation is even more complex: while the effective mass depends on the local value of alloy composition x, the potential depends on x in a nonlocal manner.[2]

To sum up, SUSYQM transform produces Hamiltonians with constant effective mass and variable potential which cannot be utilized in compositionally modulated semiconductor structures with position dependent effective mass. To overcome this obstacle the *coordinate transform* (CT) method should be included in the SUSYQM transform procedure, meaning that the real space with variable-mass Hamiltonian becomes mapped into a space with constant mass, and then SUSYQM transform is applied in the mapped space. CT method ensures that $U(z) \sim m(z)$.

6.3.2   Coordinate Transform

In the envelope function effective-mass Schrödinger equation (6.5) we introduce an invertible coordinate transform $z = g(y)$, to map $m(z)$, $U(z)$, $\Psi(z) \rightarrow m(g(y))$, $U(g(y))$, $\Psi(g(y)) = u(y)\sqrt{m(g(y))}\frac{dg(y)}{dy}$ [44, 45]. Equation (6.5) then becomes:

$$\frac{d^2u}{dy^2} + \left[A(y) - \frac{2m(g(y))g'^2}{\hbar^2}[\theta m(g(y)) - E]\right]u = 0$$

$$A(y) = -\frac{1}{4}\left(\frac{1}{m(g(y))g'}\frac{d(m(g(y))g')}{dy}\right)^2 + \frac{1}{2}\frac{d}{dy}\left(\frac{1}{m(g(y))g'}\frac{d(m(g(y))g')}{dy}\right)$$

$$(6.13)$$

Then, if the coordinate transform function g satisfies:

$$m(g(y))g'^2 = m^* > 0$$

$$A(y) - \frac{2m(g(y))g'^2}{\hbar^2}\theta m(g(y)) = -\frac{2m(g(y))g'^2}{\hbar^2}U_0(y) \qquad (6.14)$$

where m^* is independent on z, and $U_0(y)$ is any suitable function, specified in advance, Eq. (6.13) takes the standard Schrödinger form:

$$\frac{d^2u}{dy^2} - \frac{2m^*}{\hbar^2}[U_0(y) - E]u = 0. \qquad (6.15)$$

---

[2]This is because of a strong internal polarization present in these alloys, which depends on the composition variation across the structure, only the field-free conduction-band-edge part of the total potential is locally dependent on x.
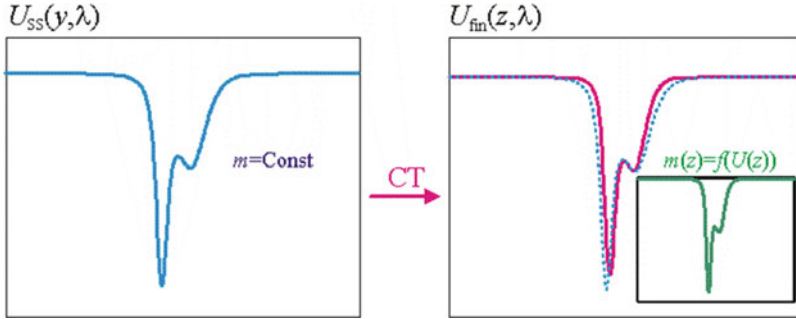
Fig. 6.4 The results of the coordinate transform performed on the supersymmetric potential, valid for conventional materials such as AlGaAs.

The spectra of Eqs. (6.5) and (6.15) are identical and it is advantageous to choose $U_0(y)$, with the constant mass $m*$, so that its eigenenergies and eigenfunctions are explicitly known. The wave functions $\Psi(z)$ in real space will become uniquely and straightforwardly determined once the function $g(y)$ (equivalently $m(z)$) is known [44]. The CT method is illustrated in Fig. 6.4.

We have seen so far that a very convenient way of achieving the required state energies in a QW with a continuous profile (so that $\Xi = (1 - \tau_{21}/\tau_{32})\tau_3\mu_{31}^2\mu_{23}^2$ or some other figure of merit is optimized) is by using SUSYQM and CT methods. From a practical realization perspective the best way towards approximate realization of the optimal smooth potential is via *digitally graded* (DG) structures, which comprise just two different alloy compositions. DG has already been used for approximate realization of triangular QWs and for QW infrared detectors and it has been shown that this technique may provide a very good reproduction of the transition energies or the density of states, as compared to the corresponding values in the optimized potential [48]. It is therefore possible to realize a gain-optimized QCL active region by DG, as it is shown in Fig. 6.5, [49]. Clearly, the same digitalization procedure can be applied to the QWs obtained by variational calculus method.

At this point, it is noteworthy to mention that there are other devices based on superstructure, such as superlattice multipliers (SSLMS) under current investigation for generating radiation in a range of the GHz-THz spectrum for which structures such as the QCLs considered in this paper cannot easily operate [50–56]. Our global optimization methods have strong potential for application to SSLMs as well, but also to different material systems [57] and more complex models of nonparabolicity [58, 59].

6.4 Conclusions

Optimisation problems arise in every field of scientific and technological interest. This Chapter reviews various advanced optimization methods used to acquire structural parameters of gain-maximized quantum cascade lasers emitting at

Fig. 6.5 Quantum cascade laser with digitally graded active region optimized for emission at 9.3 μm. Inset shows a nonrectangular potential profile (magenta) obtained using SUSYQM which is then digitally graded. Reprinted from [49], with the permission of AIP Publishing
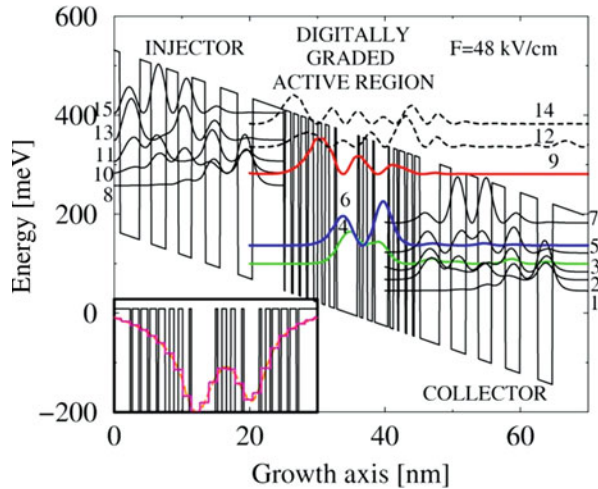
specified wavelengths at which CBRN and explosives possess strong absorption signatures. Global optimisation problems are generally very difficult, and some are essentially impossible to solve. Therefore, clear understanding of problem structure, constraints, data characteristics and limits of the applied algorithms is essential.

References

1. Faist J, Capasso F, Sivco DL, Sirtori C, Hutchinson AL, Cho AY (1994) Quantum cascade laser. Science 264:553–556
2. Pereira MF, Anfertev VA, Zubelli JP, Vaks VL (2017) Terahertz generation by gigahertz multiplication in superlattices. J Nanophotonics 11:046022
3. Jirauschek C, Kubis T (2014) Modeling techniques for quantum cascade lasers. Appl Phys Rev 1:011307
4. Faist J (2013) Quantum cascade lasers. Oxford University Press, Oxford
5. Vitiello MS, Scalari G, Williams B, De Natale P (2015) Quantum cascade lasers: 20 years of challenges. Opt Express 23:5167
6. Fuchs F, Hugger S, Kinzer M, Aidam R, Bronner W, Lösch R et al (2010) Imaging standoff detection of explosives using widely tunable midinfrared quantum cascade lasers. Opt Eng 49:111127
7. Ostendorf R, Butschek L, Hugger S, Fuchs F, Yang Q, Jarvis J et al (2016) Recent advances and applications of external cavity-QCLs towards hyperspectral imaging for standoff detection and real-time spectroscopic sensing of chemicals. Photonics 3:28
8. Sharma RC, Gupta S, Deepuk K, Sanchit G, Chandra H (2014) Standoff quantum cascade laser photoacoustic spectroscopy based explosive detection system. J Lasers Opt Photonics 1:2

9. Li JS, Yu B, Fischer H, Chen W, Yalin AP (2015) Contributed review: quantum cascade laser based photoacoustic detection of explosives. Rev Sci Instrum 86:031501

10. Pereira MF, Zubelli JP, Winge D, Wacker A, Rodrigues AS, Anfertev V, Vaks V (2017) Theory and measurements of harmonic generation in semiconductor superlattices with applications in the 100 GHz to 1 THz range. Phys Rev B 96:045306

11. Pereira M (2017) Analytical expressions for numerical characterization of semiconductors per comparison with luminescence. Materials 11:2

12. Oriaku CI, Pereira MF (2017) Analytical solutions for semiconductor luminescence including Coulomb correlations with applications to dilute bismides. J Opt Soc Am B 34:321

13. Ko YH, Yu JS (2010) Design optimization of quantum cascade laser structures at $\lambda \sim$ 11-12 μm. Phys Status Solidi A 207:2190–2197

14. Valavanis A, Dinh TV, Lever LJM, Ikonić Z, Kelsall RW (2011) Material configurations for n-type silicon-based terahertz quantum cascade lasers. Phys Rev B 83:195321

15. Gajic A, Radovanovic J, Milanovic V, Indjin D, Ikonic Z (2014) Optimizing optical non-linearities in GaInAs/AlInAs quantum cascade lasers. Nucl Technol Radiat Prot 29:10–16

16. Radovanović J, Milanović V, Ikonić Z, Indjin D (2007) Application of the genetic algorithm to the optimized design of semimagnetic semiconductor-based spin-filters. J Phys D Appl Phys 40:5066–5070

17. Matyas A, Chashmahcharagh R, Kovacs I, Lugli P, Vijayraghavan K, Belkin MA, Jirauschek C (2012) Improved terahertz quantum cascade laser with variable height barriers. J Appl Phys 111(10):103106

18. Mojibpour A, Pourfath M, Kosina H (2014) Optimization study of third harmonic generation in quantum cascade lasers. Opt Express 22:20607

19. Kleeman M.P., Lamont G.B., Cooney A., Nelson T.R. (2007) A Multi-tiered Memetic Multiobjective Evolutionary Algorithm for the Design of Quantum Cascade Lasers. In: Obayashi S., Deb K., Poloni C., Hiroyasu T., Murata T. (eds) Evolutionary Multi-Criterion Optimization. EMO 2007. Lecture Notes in Computer Science, vol 4403. Springer, Berlin, Heidelberg. https://doi.org/10.1007/978-3-540-70928-2_17

20. Mueller D, Triplett G (2016) Development of a multi-objective evolutionary algorithm for strain-enhanced quantum cascade lasers. Photonics 3:44

21. Dinh TV, Valavanis A, Lever LJM, Ikonić Z, Kelsall RW (2012) Extended density-matrix model applied to silicon-based terahertz quantum cascade lasers. Phys Rev B 85:235427

22. Smiljanić J, Žeželj M, Milanović V, Radovanović J, Stanković I (2014) MATLAB-based program for optimization of quantum cascade laser active region parameters and calculation of output characteristics in magnetic field. Comput Phys Commun 185:998–1006

23. Mirčetić A, Indjin D, Ikonić Z, Harrison P, Milanović V, Kelsall RW (2005) Towards automated design of quantum cascade lasers. J Appl Phys 97:084506

24. Waldmueller I, Wanke MC, Lerttamrab M, Allen DG, Chow WW (2010) Inverse-quantum-engineering: a new methodology for designing quantum cascade lasers. IEEE J Quant Electron 46:1414–1420

25. Daničić A, Radovanović J, Milanović V, Indjin D, Ikonić Z (2010) Optimization and magnetic-field tunability of quantum cascade laser for applications in trace gas detection and monitoring. J Phys D Appl Phys 43:045101

26. Bismuto A, Terazzi R, Hinkov B, Beck M, Faist J (2012) Fully automated quantum cascade laser design by genetic optimization. Appl Phys Lett 101:021103

27. Dupont E, Fathololoumi S, Wasilewski ZR, Aers G, Laframboise SR, Lindskog M et al (2012) A phonon scattering assisted injection and extraction based terahertz quantum cascade laser. J Appl Phys 111:073111

28. Gajić A, Radovanović J, Milanović V, Indjin D, Ikonić Z (2014) Genetic algorithm applied to the optimization of quantum cascade lasers with second harmonic generation. J Appl Phys 115:053712

29. Kirkpatrick S, Gelatt CD, Vecchi MP (1983) Optimization by simulated annealing. Science 220:671–680

30. Metropolis N, Rosenbluth AW, Rosenbluth MN, Teller AH, Teller E (1953) Equation of state calculations by fast computing machines. J Chem Phys 21:1087–1092
31. Simon D (2013) Evolutionary optimization algorithms. Wiley, Chichester
32. Bozorg-Haddad O, Solgi M, Loáiciga HA (2017) Meta-heuristic and evolutionary algorithms for engineering optimization. Wiley
33. J.H. Holland (1975) Adaptation in Natural and Artificial Systems, University of Michigan Press, Ann Arbor, Michigan; re-issued by MIT Press (1992)
34. www.hitran.com. (n.d.)
35. Radovanović J, Milanović V, Ikonić Z, Indjin D (2002) Global optimization of semiconductor quantum well profile for maximal optical rectification by variational calculus. Semicond Sci Technol 17:716–720
36. Radovanović J, Milanović V, Ikonić Z, Indjin D (2001) Quantum well shape optimization by variational calculus: maximizing the Stark effect and quantum interference derived electro-optic susceptibility. Opt Commun 194:181–190
37. Pereira MF (2016) The linewidth enhancement factor of intersubband lasers: from a two-level limit to gain without inversion conditions. Appl Phys Lett 109:222102
38. Gross P, Ramakrishna V, Vilallonga E, Rabitz H, Littman M, Lyon SA, Shayegan M (1994) Optimally designed potentials for control of electron-wave scattering in semiconductor nanodevices. Phys Rev B 49:11100–11110
39. Radovanović J, Milanović V, Faschinger W, Ikonić Z, Indjin D (2001) Two methods of quantum well profile optimization for maximal nonlinear optical susceptibilities. Phys Rev B 63:115327
40. Cooper F, Khare A, Sukhatme U (1995) Supersymmetry and quantum mechanics. Phys Rep 251:267–385
41. Cooper F, Khare A, Sukhatme U (2001) Supersymmetry in quantum mechanics. World Scientific, Singapore
42. Abraham PB, Moses HE (1980) Changes in potentials due to changes in the point spectrum: Anharmonic oscillators with exact solutions. Phys Rev A 22:1333–1340
43. Sukumar CV (1985) Supersymmetric quantum mechanics of one-dimensional systems. J Phys A Math Gen 18:2917–2936
44. Radovanović J, Milanović V, Ikonić Z, Indjin D (2004) Quantum well shape optimization of continuously graded AlxGa(1-x)N structures by combined supersymmetric and coordinate transform methods. Phys Rev B 69:115311
45. Radovanović J, Milanović V, Ikonić Z, Indjin D (1999) Quantum-well shape optimization for intersubband-related electro-optic modulation properties. Phys Rev B 59:5637–5642
46. Tomić S, Milanović V, Ikonić Z (1997) Optimization of intersubband resonant second-order susceptibility in asymmetric graded AlxGa(1-x)As quantum wells using supersymmetric quantum mechanics. Phys Rev B 56:1033–1036
47. Milanovic V, Ikonic Z (1996) On the optimization of resonant intersubband nonlinear optical susceptibilities in semiconductor quantum wells. IEEE J Quantum Electron 32:1316–1323
48. Tomić S, Indjin D, Ikonić Z, Milanović V (2002) Digitally graded active region for optically pumped intersubband lasers and nonlinear wavelength convertors. J Appl Phys 91:9423–9425
49. Indjin D, Tomić S, Ikonić Z, Harrison P, Kelsall RW, Milanović V, Kočinac S (2002) Gain-maximized GaAs/AlGaAs quantum-cascade laser with digitally graded active region. Appl Phys Lett 81:2163–2165
50. Apostolakis A, Pereira MF (2019) Controlling the harmonic conversion efficiency in semiconductor superlattices by inter-face roughness design. AIP Adv 9:015022
51. Apostolakis A, Pereira MF (2019) Numerical studies of superlattice multipliers performance. Quantum Sens Nano Electron Photon XVI:109262
52. Apostolakis A, Pereira MF (2019) Potential and limits of superlattice multipliers coupled to different input power sources. J Nanophotonics 13:036017

53. Pereira MF, Shulika O (2011) Terahertz and mid infrared radiation: generation, detection and applications, NATO science for peace and security series-b: physics and biophysics. Dordrecht: Springer
54. Pereira MF, Shulika O (2014) Terahertz and mid infrared radiation: detection of explosives and CBRN (using te-rahertz), NATO science for peace and security series-b: physics and biophysics. Dordrecht: Springer
55. Apostolakis A, Pereira MF (2020) Superlattice nonlinearities for Gigahertz-Terahertz generation in harmonic multi-pliers. Nanophotonics 9:3941–3952
56. Pereira MF, Anfertev V, Shevchenko Y, Vaks V (2020) Giant controllable gigahertz to terahertz nonlinearities in superlattices. Sci Rep 10:15950
57. Dubajić M, Daničić A, Vuković N, Milanović V, Radovanović J (2018) Optimization of cubic GaN/AlGaN quantum cascade structures for negative refraction in the THz spectral range. Opt Quantum Electron 50:373
58. Vuković N, Milanović V, Radovanović J (2014) Influence of nonparabolicity on electronic structure of quantum cascade laser. Phys Lett A 378:2222–2225
59. Vukovic N, Radovanovic J, Milanovic V (2014) Enhanced modeling of band nonparabolicity with application to a mid-IR quantum cascade laser structure. Phys Scr T162:014014

Part III
Superlattices and Other Technologies for GHz-THz Sensing

Chapter 7
Non-destructive Testing THz Systems: Fast Postal Scanner Case Study

M. Sypek and J. Starobrat

Abstract The paper presents a THz based non-destructive testing (NDT) method in comparison to the others NDT techniques used commercially. The wavelength of an electromagnetic radiation of the THz region in air varies from a fraction of millimetre to single millimetres. This provides – for example – similar spatial resolution as ultrasound based methods. In the paper the NDT system operating on the 0.3 THz frequency is described. System was devoted to the postal applications, especially for envelopes inspection. Such a device can be integrated with a sorting device of a pneumatic drive, which ensures the working speed of tens of envelopes per second.

7.1 Introduction

In the recent years, the range of non-destructive testing methods of material screening was extended with the progression of Terahertz radiation technology. It is an especially valuable addition due to a very good transmission of the Terahertz spectrum through the nonpolar and non-metallic materials, which most often do not transmit the visual spectrum of light. It is worth noting that many common materials belong to this group of substances, such as paper, synthetics, clothing, wood, porcelain, paperboard etc.

The wavelength of an electromagnetic radiation of the THz region in air varies from a fraction of millimetre to single millimetres. In this report we describe an exemplary case study of a postal scanner of envelopes contents, which works with a

M. Sypek (✉)
Faculty of Physics, Warsaw University of Technology, Warsaw, Poland

Orteh Sp. zo.o., Warsaw, Poland
e-mail: maciej.sypek@orteh.pl

J. Starobrat
Faculty of Physics, Warsaw University of Technology, Warsaw, Poland
e-mail: joanna.starobrat@fizyka.pw.edu.pl

0.3 THz source. The main task of such a device is to determine whether an envelope contains anything other than paper. The speed of processing required from a THz parcel scanner at a post office usually reaches dozens of A4 envelopes per second. In case the atypical contents of the envelope are detected, the envelope should be directed to advanced inspection.

7.2 Non-destructive Material Testing

In the recent years, the range of non-destructive testing methods of material screening was extended with the progression of Terahertz radiation technology. It is an especially valuable addition due to a very good transmission of the Terahertz spectrum through the nonpolar and non-metallic materials, which most often do not transmit the visual spectrum of light. It is worth noting that many common materials belong to this group of substances, such as paper, synthetics, clothing, wood, porcelain, paperboard etc.

The means of material inspection that do not affect the examined devices and objects are considered to be valuable source of information about screened materials' properties, without altering their structure and surface properties.

As defined by Gholizadeh [1], the following solutions can be considered in regards to machines and devices:

– visual examination (external inspection);
– endoscopic examination;
– penetrative examination;
– magnetic particle inspection;
– ultrasound examination;
– Eddy-currents testing;
– industrial radiography.

The authors would like to extend the list with the additional methods that they have researched. Chronologically, first of these methods is optical holography [2] in the visible light spectrum. In the simplest case the method is based on recording two separate holograms on the same holographic plate. One of them is recorded without, and the other with the applied small external tension, leading to slight deformations of the object. The reconstruction of the combined hologram shows a distribution of interference fringes, which can be translated to a three-dimensional map of deformations by the means of computer analysis. The precision of this measurements is comparable to a fraction of the wavelength used to record and reconstruct the hologram, being as low as 10^{-7} m. The detailed analysis can verify the accordance to design assumptions and the lack or the presence of internal faults of the examined objects. For implementing this solution in the industrial applications, digital holography methods can be used [3]. This way, the hologram is recorded not on a holographic plate, which requires the dark room and chemical processing, but on a CMOS or CCD sensor. Reconstructing and combining the holograms is realized by

computer software. However, a serious disadvantage of the method is the necessity of creating a system to apply the tension in time intervals. It increases the complexity of the whole set-up while simultaneously decreasing the speed of the measurements. Digital holography limits also the maximal dimensions of the examined object, which in practice do not exceed a few dozens of centimeters for each dimension.

The active thermography [4] is another method that is worth noticing among the non-destructive testing methods. In its basic form, the being analyzed object is periodically heated with a MHz frequency using i.e. infrared radiators, ultrasounds or Eddy-currents. Simultaneously, the thermal response of the surface of the object is detected. The lock-in phase analysis of a recorded thermographic video leads to imaging of hidden faults and non-uniformities in the examined object. Such a recording usually lasts a few of minutes with a few dozen frames per second. The depth of penetration of the method is strongly dependent on the thermal properties of the inspected material. The duration of the measurement and its low spatial resolution limit the industrial applications of the active thermography, as well.

In the recent years, the Terahertz radiation based systems have joined the list of non-invasive screening methods.

7.3   Terahertz Radiation

Until recently, there has been a range of the electromagnetic radiation which was absent in the published research. In the range of the electromagnetic radiation spectrum is placed in between the microwaves and infrared radiation (Fig. 7.1).

Named after the frequencies of waves in this range, the electromagnetic waves in this spectrum are called Terahertz radiation, or simply THz radiation. It is worth noting that due to the neighboring microwave and infrared ranges, Terahertz technologies can make use of a combination of both electronical and optical techniques.

Terahertz radiation was first observed over a century ago [5, 6]. In spite of that fact, till this day it remains the least researched and understood range of the electromagnetic spectrum, because of the lack of cheap and compact THz sources. The industrial level sources and detectors of the neighboring radiation ranges were

Fig. 7.1 Terahertz region of the electromagnetic radiation
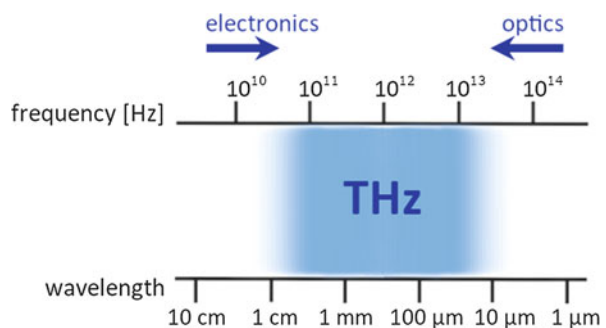
not enough to reach such frequencies. For that reason, the Terahertz range of the electromagnetic radiation is also called a "THz gap". In the last 20 years, the "gap" has been bridged, thanks to the rapid technology advancements.

The limits of the ranges in electromagnetic spectrum are not often sharply defined, and the Terahertz radiation has not yet been clearly defined. The common presumption is that this kind of radiation is contained in the range from 0.1 up to 30 THz. However, the range between 10 and 30 THz is already covered by the far infrared, and partially the mid-wave infrared radiation. In this report the authors will assume the Terahertz range of 0.1–10 THz, which, in the air, corresponds to wavelengths from 30 μm to 3 mm.

The unique nature of the Terahertz radiation each year attracts more and more attention, despite the still-remaining challenges in its generation and detection. Among the notable properties of the THz spectrum, the following can be listed:

– High absorption in the atmosphere in comparison to the neighboring ranges of electromagnetic radiation. On the other hand, the "atmospheric windows" are observed, that is the ranges of frequencies that are absorbed relatively little. The high absorption of the Terahertz radiation is caused by the presence of many molecules in the atmosphere that have spectral absorption lines in the THz range. This is due to the rotation and vibration of the moving molecules. The water vapor present in the atmosphere is a dominant source of the absorption [7].
– High reflectivity of the Terahertz radiation at metallic surfaces, due to high electric conductivity of metals [7].
– High transmission of Terahertz radiation through nonpolar and nonmetallic materials that are usually known for low transmissivity of visible light spectrum. Among such materials some commonly used dielectrics ones can be names, such as paper, synthetics, clothing, wood, porcelain, cardboard and many others [7].
– Polar substances illuminated with Terahertz radiation have strong absorbing and dispersive properties, due to a specific molecule structure that enables rotations and vibrations of particles. In general, each material has its own unique oscillation properties and the absorption distribution can be used as a "finger print" of the material [7].
– Photons of the Terahertz frequencies have low energy, that is around 4 meV for the frequency of 1 THz. It's about a one millionth of the energy of the photon from the X radiation spectrum [8].
– Thanks to the low energy of the photons in the Terahertz range of the spectrum, this radiation does not cause the ionization of tissues, unlike the X-rays. Additionally, since it is highly absorbed by water, the Terahertz wave do not penetrate the human body as deep as the microwaves. For that reason, the health risks, if present at all, would be limited to the external layers of skin. As such, the Terahertz waves are safe for both the scanner operator and for the tested tissues.
– Imaging process in the THz range is mostly based on wave reflection rather than dispersion, which would be typical for the visible light spectrum.
– Spatial resolution of the resulting images is dependent on the length of the THz wave in the medium and varies in practice from tens of micrometers to single millimeters.

– The THz radiation is easier to focus and collimate than longer centimeter waves.

With that knowledge, some exemplary industrial, THz-based solutions of the non-invasive scanning can be discussed.

– Remote detection of dangerous items (such as metallic or composite fire arms, cold steel weapon, explosives or their ingredients) hidden under clothing.
– Remote detection of the improvised explosive devices (IED) in dry environment or under dry layers of asphalt or concrete.
– Non-invasive remote detection of concealed microphones installed in the volume of the walls.
– Non-invasive remote methods of substance analysis of potentially dangerous materials based on imaging and spectral analysis.
– Non-invasive methods of study of artworks and sculptures based on imaging and spectral analysis of both transmission and reflection.
– In vivo analysis of human skin tissue in order to detect cancer cells for medical diagnostics. Additionally, real-time analysis of defected tissue that needs to be removed during the surgery. The two solutions often use approaches based on both imaging and spectra analysis.
– Set-ups for control of the assembly lines, inspecting the contains of cardboard and plastic packages. For example, those can be used for liquid dispensers to opaque – in visible – bottles, for checking the number of chocolates in a box, the amount of contains of coffee capsules etc. They can also serve for supervision of mass production of pharmaceuticals before sealing off the package, detecting whether the plastic packages contain the right number of pills, whether they are correctly placed, and the pills are not damages.

Such applications do not require high dynamics, in some cases accepting binary information (single bit, 1 – is/0 – is not) but demand high speed of the measurements (up to tens of packages per second).

However, it should be noted that higher-dynamics non-invasive diagnostics systems in the THz spectrum already exist, i.e. banknotes counting systems, which detect the watermarks and require 16-bit or even 32-bit dynamics.

– Postal package scanners, which detect whether the envelope contains anything other than paper. The required speed of such a scanner is typically as high as a few dozens of A4 envelopes per second. In a case when the envelope contains anything else that is not paper, the envelope is redirected to a more detailed scanner that uses i.e. X-rays and mass spectroscopy. The more precise scanning takes, however, up to seconds or even minutes for a single package.

In the next part of this paper, the authors will focus in detail on the fast-scanning postal system. In general, the system is composed of the following list of components:

– THz source;
– 'optical-like' illumination system working in the THz range;

- 'optical-like' system working in the THz range to focus the wave on the detectors;
- 2D or 3D arrays of THz detectors;
- electronic systems for detection and data processing, based on field-programmable gate arrays (FPGA);
- high-level programming to classify the packages for further additional inspection.

7.4 Postal Fast-Scanning System in the THz Range

It is assumed that the scanning system is integrated with a sorting device of a pneumatic drive, which ensures the working speed of tens of envelopes per second. It is assumed as well that the envelope in a scanning area moves with a constant speed of few meters per second. The maximal thickness of a single envelope is between 10 and 15 mm. The width of the scanning area is 250 mm. The only mechanically moving part of the system is the envelope itself. The basic idea of the scanning process is presented in Fig. 7.2. The moving element – an A4 envelope – is marked in green.

A VDI source was implemented as a THz source of the envelope illuminating wave [9], working with a 0.3 THz frequency and the power of 18 mW. It corresponds to a 1 mm wavelength in air. The following figure (Fig. 7.3) presents an optical system that projects 3 horizontal lines whose lengths are equal to 250 mm each and their half-width is around 2 mm. The lines (marked in red in Fig. 7.2.) are divided by spaces of 5 mm.

Fig. 7.2 The basic idea of the scanning process
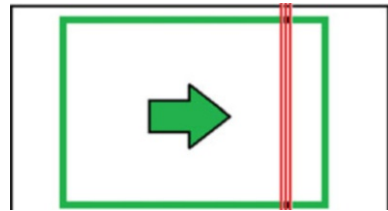
Fig. 7.3 Illumination system. Reproduced from Orteh
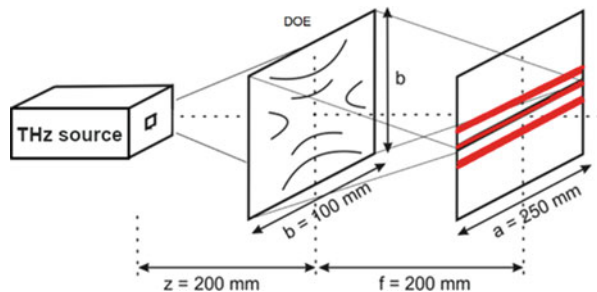
The main element of the illumination system is a diffractive optical element (DOE) with a square working area of a 100 m width and height, which has three functions in one. Firstly, the element collimates the divergent THz wave coming from the source. Secondly, forms a projection of a line whose width equals 250 mm in the surface of the scanned envelope. Lastly, the diffractive structure multiplies the projected line to obtain three separate stripes. From the diffractive optics point of view, the element combines: off-axis spherical converging lens, off-axis hyperbolic lens and specially optimized phase diffraction grating. The off-axis designs were chosen due to high values of the deflection angles. The DOE element was manufactured of from polyamide (PA12) with the use of the 3D-printing technology (SLS – selective laser sintering). The index of refraction of the PA12 material for the 0.3 THz frequency is equal to 1.59 (Fig. 7.4).

The Terahertz radiation, after passing the examined envelope, reaches the array of detectors. In this case, a single detector panel contains three lines of 12 detectors each. The diameter of each detector is equal to 1.8 mm. The distance between the centers of detectors in the same line equals to 5 mm and the distance between the detector lines is equal to 5 mm as well. Figure 7.5 shows the displacement of each detector line by 5/3 mm from the previous line. Combined with the previously mentioned distance between the three scanning lines also being equal to 5 mm, this solution increases the spatial resolution of the scanner. To cover the whole

Fig. 7.4 Diffractive optical element (DOE) created with the means of 3D-printing. Reproduced from Orteh
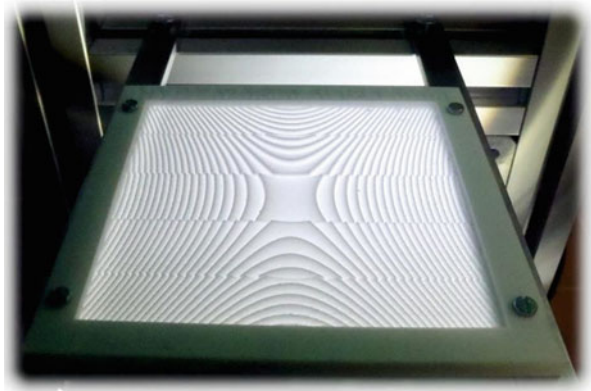
Fig. 7.5 Single detector panel containing 3 × 12 detectors. Reproduced from Orteh

scanning area (240 mm wide), four detector panels are used, each of a width of 60 mm. In a whole, the device combines $4 \times 36 = 144$ detectors which enable, with some margin, the analysis of the contains of the A4 envelope (210×197 mm).

The detectors chosen for the scanner were the HEM FET transistors in ceramic casing (working in ranges of 8–12 and 18–27 GHz: X and K ranges) or dedicated GaN-based detectors produced by Unipress (Institute of High Pressure Physics of the Polish Academy of Sciences). It is necessary to note that in case of the commercial transistors working in the ranges X and K ranges, which were based on GaAs technology, these elements acted not as high frequency amplifiers, but as detectors of surface plasmons [11], which are generated by the radiation of the 0.3 THz frequency. The maximal modulation frequency of the carrier 0.3 THz radiation (300 GHz) reaches up to 1 GHz. The noise-equivalent power (NEP) parameter of each detector is of tens to hundreds of picowatts per square root Hz. It is worth mentioning that the commercial GaAs-based transistors have highly repeatable parameters when acting as amplifiers. However, for non-standard applications, such as detectors in the described system, their parameters are highly variable. For that reason, advanced calibration procedures had to be developed to independently set each of 144 detectors in a desired operation point. Said calibration process ensures that each of the transistors works with repetitive accuracy as a detector of the THz radiation of 0.3 THz frequency.

In order to further increase the quality of the detection, the arrays of lenses are used [12], which are, as well, 3D-printed from PA12 polyamide. The role of the lens arrays (Fig. 7.6) is to improve the focus of the radiation on detectors and to decrease the optical crosstalk between the single detectors. The array of lenses consists of single lenses, each of a square aperture with width equal to 5 mm. The focal length of each lens is equal to 5 mm. As mentioned before, each detector that is covered with a lens has a cross section of 1.8 mm, which means that the value of its area is around 2.5 mm^2. With the area of a single lens equal to 25 mm^2, ideally the sensitivity of the system would be increased 10 times, however due to Fresnel reflection and material absorption the actual increase is somewhat lower.

Fig. 7.6 Arrays of lenses 3D-printed from polyamide. Reproduced from Orteh
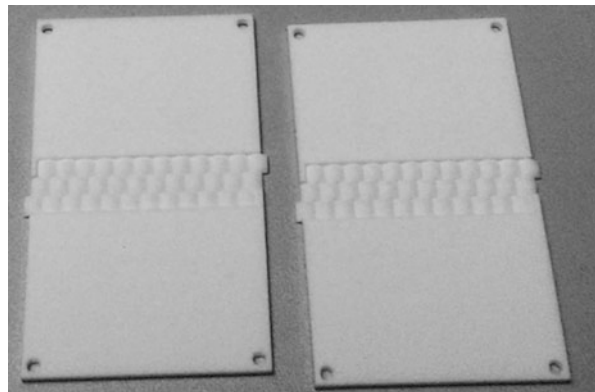
The combined systems of 4 detector panels with mounted lens arrays is presented in Fig. 7.7. This set-up enables scanning of the envelopes up to 240 mm wide.

The method of detecting the signal on each panel is quite advanced. Due to the expected speed of scanning, multiplexing cannot be applied. In the postal fast-scanning system, each detector is addressed simultaneously, which means that each detector has its own dedicated analog-to-digital converter (working in 12–14 bits). Their readout is independent and for each detector and is equal to 100 kHz. The digital signal is then processed with the use of originally designed standards of transmission based on FPGA circuits. The software employs advances averaging and processing algorithms in order to improve the signal to noise (SNR) ratio at the cost of decreasing the effective sampling to 1–10 kHz. However, it corresponds to the maximal scanning speed of 5–50 m/s, which means that the system scans 15–150 A4-sized envelopes per second.

Preliminary processing on the FPGA circuits enables reduction of the transmitted data quantity in order to be able to use USB 2.0 standard. Figure 7.8 presents the flowchart of the electronic part of the device.

The working postal scanner (Fig. 7.9) detected and analysed contains of A4-sized envelopes, such as scissors and Orteh company logo cut out of the aluminium foil. In the resulting images (Fig. 7.10) the interference fringes can be observed. They are caused by the reflection of the THz wave from both upper and lower cover of the envelope, due to the high temporal coherence of the THz radiation source.

Reducing of the temporal coherence was achieved by fast (over 10 kHz) modulation of frequency in the range of 0.28–0.29 THz. Additionally, the scanner was

Fig. 7.7 Combined 4 detector panels with mounted lens arrays. Reproduced from Orteh
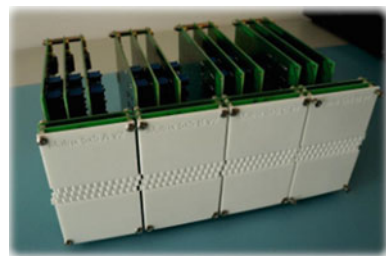
Fig. 7.8 Flowchart of the electronic part of the device
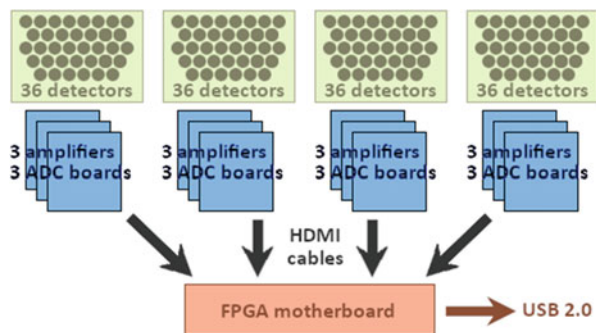
Fig. 7.9 The internal view of the scanner (with removed side cover). Reproduced from Orteh
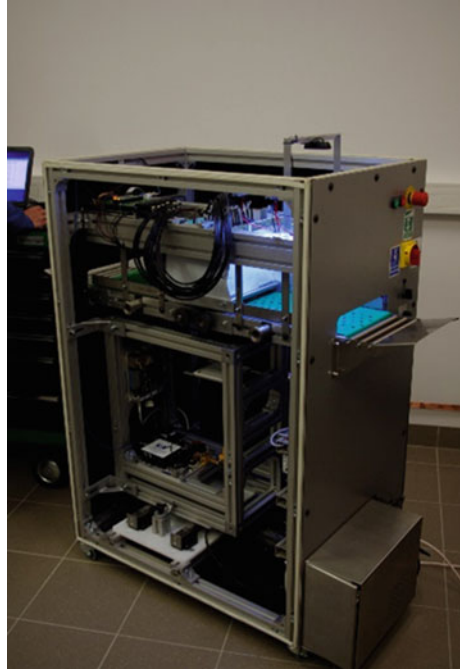
Fig. 7.10 Images obtained by scanning. It contains of A4-sized envelopes. Reproduced from Orteh
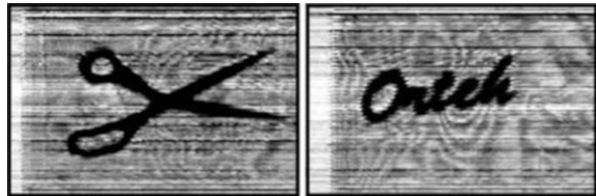
Fig. 7.11 Imaging in 'fusion vision' mode: a combination of visible light and THz imaging of an A4-sized envelope. Reproduced from Orteh
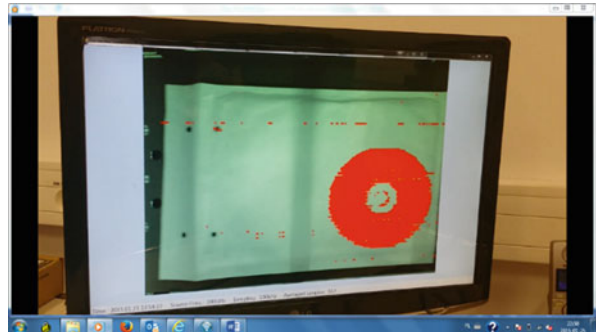
equipped with a camera working in the visible light spectrum, so that the final device can work in a 'fusion vision' mode (Fig. 7.11). In said mode the two images are combined: the visible light imaging showing the upper side of the envelope, and the

transmission imaging in the 0.28–0.29 THz range showing the contains of the envelope.

Before concluding we would like to mention that advanced materials [13–18] and compact sources for the THz region such as quantum cascade lasers and superlattice multipliers [19–25] are also being investigated by other teams and can deliver complementary devices that could potentially be included in our system, to further broaden its range of application.

7.5 Summary and Further Developments

According to some research groups working in the field of the non-invasive testing, the task of analysing of the materials, objects and supervising the production line with speeds of man metres per second are not trivial. Most of the currently applied methods work too slow or, in high speeds, lack the sensitivity of detection. On the other hand, the use of strong radiation sources can be problematic, as in industrial radiography which is based on X and γ rays.

However, the non-ionizing THz radiation of the power in tens of mW enables fast-scanning processes while simultaneously preserving good resolution and expected dynamics.

As the high temporal coherence of the THz sources influences the imaging, the future works might include employing the methods similar to those present in digital holography. It is expected that these methods might lead to the possibility of examining the volume of three-dimensional objects. In the postal applications, it would mean that scanner of a next generation might be capable of fast-scanning of thick packages. It would, however, require much higher resolutions of detector panels.

References

1. Gholizadeh S (2016) A review of non-destructive testing methods of composite materials. Procedia Struct Integrity 1:50–57
2. Schnars U, Hartmann H-J, Jüptner W (1995) Digital recording and numerical reconstruction of holograms for nondestructive testing. In: Proceedings of the SPIE 2545, Interferometry VII: applications, 23 June 1995
3. Schnars U, Jüptner W (1994) Digital recording and reconstruction of holograms in hologram interferometry and shearography. Appl Opt 33(20):4373–4377
4. Breitenstein O, Warta W, Langenkamp M (2010) Lock-in thermography, basics and use for evaluating electronic devices and materials. Springer, Berlin

5. Coutaz JL, Garet F, Wallace VP (2018) Principles of terahertz time-domain spectroscopy. taylorfrancis.com

6. Gallerano G Overview of terahertz radiation sources. In: Proceedings of the 2004 FEL conference, pp 216–221

7. Lee Y (2009) Principles of terahertz science and technology. Springer, New York

8. Milles RE, Zhang X, Eisele H, Krotkus A (2007) Terahertz frequency detection and identification of materials and objects. Springer, Dordrecht

9. http://www.vadiodes.com

10. Suszek J et al (2015) 3-D-printed flat optics for THz linear scanners. IEEE Trans Terahertz Sci Technol 5(2):314–316

11. Knap W et al (2009) Field effect transistors for terahertz detection: physics and first imaging applications. J Infrared MilliTerahz Waves 30:1319–1337

12. Szkudlarek K et al (2016) Terahertz 3D printed diffractive lens matrices for field-effect transistor detector focal plane arrays. Opt Express 24(18):20119

13. Oriaku CI, Pereira MF (2017) Analytical solutions for semiconductor luminescence including Coulomb correla-tions with applications to dilute bismides. J Opt Soc Am B 34:321

14. Pereira MF (2018) Analytical expressions for numerical characterization of semiconductors per comparison with luminescence. Materials 11:2

15. Pereira MF (2016) The linewidth enhancement factor of intersubband lasers: from a two-level limit to gain with-out in-version conditions. Appl Phys Lett 109:222102

16. Winge DO, Franckié M, Verdozzi C, Wacker A (2016) Simple electron-electron scattering in non-equilibrium Green's function simulations. J Phys Conf Ser 696:012013

17. Pereira MF, Shulika O (2014) Terahertz and mid infrared radiation: detection of explosives and CBRN (using te-rahertz), NATO science for peace and security series-B: physics and biophysics. Springer, Dordrecht

18. Pereira MF, Shulika O (2011) Terahertz and mid infrared radiation: generation, detection and applications, NATO Science for peace and security series-B: physics and biophysics. Springer, Dordrecht

19. Pereira MF, Zubelli PJ, Winge D, Wacker A, Rondrigues SA, Anfertvev V, Vaks V (2017) Theory and measurements of harmonic generation in semiconductor superlattices with applications in the 100 GHz to 1 THz range. Phys Rev B 96:045306

20. Pereira MF, Anfertev V, Zubelli JP, Vaks V (2017) Terahertz generation by gigahertz multiplication in su-perlattices. J Nanophoton 11(4):046022

21. Apostolakis A, Pereira MF (2019) Controlling the harmonic conversion efficiency in semiconductor superlattices by in-terface roughness design. AIP Adv 9:015022

22. Apostolakis A, Pereira MF (2019) Numerical studies of superlattice multipliers performance. Quantum Sens Nano Electron Photonics XVI:109262

23. Apostolakis A, Pereira MF (2019) Potential and limits of superlattice multipliers coupled to different input power sources. J Nanophoton 13:036017

24. Apostolakis A, Pereira MF (2020) Superlattice nonlinearities for Gigahertz-Terahertz generation in harmonic multipliers. Nanophotonics 9(12):3941–3952. https://doi.org/10.1515/nanoph-2020-0155

25. Pereira MF, Anfertev V, Shevchenko Y, Vaks V (2020) Giant controllable gigahertz to terahertz nonlinearities in superlattices. Sci Rep 10:15950

Chapter 8
Recent Advances in Superlattice Frequency Multipliers

Yuliaa Schevchenko, Apostolos Apostolakis, and Mauro F. Pereira

Abstract Semiconductor superlattice frequency multipliers have emerged as a nonlinear medium able to generate radiation in a wide frequency range. This property facilitates the potential of sources suitable for sensing and spectroscopy applications. In this study, we further investigate the consequences on harmonic generation in a superlattice multiplier after excitation by an input signal oscillating at different frequencies. Here we provide a rigorous description of our theoretical model including a semiclassical Boltzmann approach to nonlinear miniband transport and non-equilibrium Green's functions calculations treating scattering processes under forward and reverse bias. To fully exploit the features of this radiation source, we focus on the effects of elastic scattering and systematic imperfections in the superlattice structure which lead to asymmetric current flow.

Keywords Frequency multiplication · Gigahertz · Terahertz · Superlattices · CBRN agents · Harmonic generation · Elastic scattering

8.1 Introduction

The physical mechanisms of interactions between THz waves and matter can involve lattice vibrations, molecular rotations, spin waves and internal excitations of bound electron-hole pairs [1–4]. It therefore should come as no surprise that the THz technology and applications which might detect the phase and amplitude of

Y. Schevchenko · A. Apostolakis
Department of Condensed Matter Theory, Institute of Physics CAS, Prague, Czech Republic
e-mail: shevchenko@fzu.cz; apostolakis@fzu.cz

M. F. Pereira (✉)
Department of Condensed Matter Theory, Institute of Physics CAS, Prague, Czech Republic

Department of Physics, Khalifa University of Science and Technology, Abu Dhabi, UAE
e-mail: pereira@fzu.cz; mauro.pereira@ku.ac.ae

generated electromagnetic radiation in the THz range are important components of spectroscopic tools with enhanced temporal and spatial resolution [1, 2]. These properties would be especially desirable for a wide range of chemical, biological, radiological and nuclear defence (CBRN) agents and explosives which exhibit acute sensitivity at GHz, THz and Mid Infrared (TERA-MIR) frequency ranges [5]. This represents further evidence for the growing interest in materials and devices which can detect or generate GHz and TERA-MIR radiation. In particular, semiconductor superlattices (SSLs) [6, 7] are auspicious devices operating at GHz-THz frequencies due to their tuneable electro-optic properties [8–10]. These type of artificial structures are created by periodical layering of two different semiconductor materials with different energy bands which results to the modulation of potential energy only in one direction and the formation of narrow energy minibands. SSL is a strongly nonlinear medium which makes possible to study interesting electrical phenomena such as negative differential conductivity (NDC) and Bloch oscillations which are difficult to be observed in conventional materials [8, 9]. These inherited nonlinear properties are widely regarded as crucial features to develop devices suitable for harmonic generation and amplification of THz radiation. In fact, when Bragg reflected miniband electrons interact with an oscillating electric field, spontaneous frequency multiplication effect takes place. Superlattice frequency multipliers are being developed as a promising approach for the generation of submillimeter to THz waves [9, 12, 13]. A number of recent works have focused on describing THz-GHz nonlinearities covering both "even" and "odd" responses produced from higher-order multipliers based on SSL devices [9, 11, 14, 15]. Among them, we would like to highlight our joint theoretical and experimental study of harmonic generation in a SSL frequency multiplier at room temperature after excitation by a GHz input signal [9]. The theoretical model in this work was formulated by adopting a hybrid approach that combined a nonequilibrium Green's function (NEGF) implementation and using Boltzmann transport equation under relaxation time approximation [9, 11]. This model predicted accurately the unexpected generation of even harmonics for an unbiased SSL. Such kind of response was attributed to imperfections in the structure which led to asymmetric flow and scattering processes under forward and reverse bias. In a follow-up study we investigated the power-conversion efficiency in irradiated SSLs and how the even harmonic output power is affected by controlling the interface quality and thus the interface roughness relaxation processes [14]. Hence, the previous approach was extended by employing the SLs balance equations to incorporate the effect of interface (elastic) scattering and the NEFG input [8, 14, 16, 17]. Further theoretical studies examined the performance of SSL multipliers and their dependence on different input power sources. The latter study confirmed the unique potential of integrating SLED devices with SSL multipliers [18]. A case of particular interest might arise if someone considers an interplay between the asymmetric current flow, applied static voltages and the input oscillating field [19] that might lead to photon-assisted transport [8, 20, 21]. The photon-assisted transport and the absolute negative conductivity (ANC) has been experimentally observed in weakly coupled superlattices in good agreement with theoretical calculations [20, 21].

Before further discussing our specific case of nonlinear behavior, it is worth noting that nonlinear optical effects in semiconductor materials have been strongly investigated in the near infrared and visible spectra, using a combination of semiconductor Bloch equations and NEGF methods for both interband [23–31] and intersubband cases [32–40] with the optical response due to the transitions between well-defined subbands in both quantum wells, superlattices and quantum cascade device. Here in contrast we exploit a different mechanism, in which a current within a single superlattice miniband generates the optical response and nonlinear effects.

The present work further develops the study in Ref. [14] by providing additional information of the output power of the even harmonics generated by a superlattice multiplier resulting from the differences in the interface structure of the superlattice layers. In addition, we revisit the derivation of Balance equations [8, 16, 17] in detail which involves an implicit connection with the NEGF approach. Finally, we study the rectification effects and how they affect the harmonic emission with or without asymmetric current flow. The Chapter is organized as follows. In Sect. 8.2, we discuss the details of the mathematical formalism describing the electron transport and the power output. Section 8.3 reviews our research for the even harmonics generation in quantum superlattices, providing additional data for a straightforward comparison with the power output of the odd harmonics. Section 8.4 provides a short review of photon-induced transport in SSLs and a preliminary study for the related corrections due to rectification effects. Concluding remarks are given in the end.

8.2   Mathematical Formalism

We focus on the nonlinear current response in the case of the tight-binding dispersion relation $\varepsilon_q = \varepsilon(q) = E_a - 2 \mid T_1^\alpha \mid \cos q\, d$ where q is the crystal momentum, d is the lattice period of the SSL and E_a designates the center of the first miniband [8, 9]. The dispersion relation ε_q can be obtained for typical SSL parameters and next-neighbor coupling T_1^α [8].

Considering a superlattice which is excited by an oscillating field $E(t) = E_{dc} + E_{ac} \cos (2\pi\nu t)$ which is parallel to its growth direction, one can get the general current response and its spectral components [8, 9]

$$j(t) = j_{dc} + \sum\nolimits_{l=-\infty}^{\infty} j_l^c \cos (2\pi\nu l t) + j_l^s \sin (2\pi\nu l t),$$

$$j_{dc} = \sum\nolimits_{p=-\infty}^{\infty} J_p^2(\alpha) Y(U),$$
$$j_l^c = \sum\nolimits_{p=-\infty}^{\infty} J_p(\alpha) \big[J_{p+l}(a) + J_{p-l}(a)\big]\, Y(U), \qquad (8.1)$$
$$j_l^s = \sum\nolimits_{p=-\infty}^{\infty} J_p(\alpha) \big[J_{p+l}(a) - J_{p-l}(a)\big]\, K(U).$$

Here J_p represents the Bessel function of the first kind and order p. The parameter $\alpha = eE_{ac}\,d/\hbar\omega$ designates the modulation degree of Bloch frequency oscillations and therefore controls effectively the nonlinear response of the system [12]. This scheme holds for miniband transport within relaxation time approximation and functions Y, K given by

$$Y(U) = j_0 \, \frac{2U/\Gamma}{1+(U/\Gamma)^2}, K(U) = \frac{2j_0}{1+(U/\Gamma)^2}, \tag{8.2}$$

where $U = eE_{dc}d + p\hbar\omega$ is the total energy drop per period under irradiation. The parameter j_0 denotes the peak current whereas $\Gamma = \hbar/\tau$ is the scattering induced broadening. Both of these parameters can be microscopically calculated by implementation of NEGF approach, as in Refs. [9, 11]. It is crucial to note that it is possible to consider the domain-formation effects in superlattices under irradiation [8, 13]. This situation is typically unstable with respect to the formation of inhomogeneous field distributions and starts to appear if $a > a_c = U_c/h\nu$. The latter condition corresponds to the NDC state and the onset of Bloch oscillations. However, in this work we restrict ourselves by studying the current response in the absence of electric field domains. It is well-established that in absence of domains, or of any other asymmetry, the *I-V* characteristic can be described adequately by Eq. (8.2) with considering a purely dc biased SL. One can identify two basic aspects of miniband transport under irradiation by means of harmonic radiation:

(i) For a perfectly symmetric structure only odd harmonics can appear if $E_{dc} = 0$.
(ii) For a superlattice structure with asymmetric interfaces both even and odd harmonic orders can occur, indicating that spectral tuning of high-order harmonics is feasible beyond the parametric amplification mechanisms [40].

These effects were revealed by NEGF approach by including systematically the possibility that interface of GaAs over AlAs is worse than that of AlAs over GaAs [9]. This resulted in a deviation from the standard Esaki-Tsu model which can be represented by the following ansatz

$$j_0 = \begin{cases} j_0^-, & U < 0 \\ j_0^+, & U \geq 0 \end{cases}, \Gamma = \begin{cases} \Gamma^-, & U < 0 \\ \Gamma^+, & U \geq 0. \end{cases} \tag{8.3}$$

The above compact solution implies that the parameters j_0^+, j_0^-, i.e. the maximum and minimum current density, correspond to the critical energies U_c^+ and U_c^-. A direct connection between calculated global dephasing and these extrema is given by $\Gamma^+ = U_c^+$ and $\Gamma^- = U_c^-$.

To determine the power output of a superlattice multiplier in the presence of an ac field, we calculate the average emitted power due to the harmonic which is directly

obtained from the Poynting vector [11, 14]. Hence, the generated power can be expressed as

$$P_l(\omega) = \frac{A\,\mu_0\,c\,L^2}{8\,\mathrm{n_r}} I_l^2(\nu),$$ (8.4)

where A is the area of the mesa of a superlattice element, μ_0 is the permeability of the vacuum and c is speed of light in the vacuum, L is the effective path length through the crystal and n_r is the refractive index of the SL material. The term $I_l(\nu)$ is the root-mean-square value of the lth component of the expansion of the induced current density in Eq. (8.1).

8.2.1 Balance Equations and Effect Of Interface Roughness Scattering

The dynamical evolution of distribution function f(q, $\mathbf{k}$, t), which can be analyzed by adopting the semiclassical theoretical framework, is determined by Boltzmann transport equation (BTE) [8]

$$\frac{\partial \mathrm{f}(q,\ \mathbf{k},t)}{\partial t} + \frac{\mathrm{e}E(t)}{\hbar}\frac{\partial \mathrm{f}(q,\mathbf{k},t)}{\partial \mathrm{q}} = St(\mathrm{f}),$$ (8.5)

where $E(t)$ is the input oscillating field. To overcome the limitations of the relaxation-time model we employ a collision integral which can describe additionally the elastic lattice scattering and leads to the following formal definition [8, 16, 17]

$$St(\mathrm{f}) = -\frac{f(q,\mathbf{k},t) - n_{\mathrm{F}}(\mathrm{E}(q,\mathbf{k}) - \mu)}{\tau_\varepsilon} + \frac{f(-q,\mathbf{k},t) - f(q,\mathbf{k},t)}{2\tau_{int}}.$$ (8.6)

Here, we consider the effects of different scattering processes which affect the electron energy and the miniband electron velocity; they are contained within the phenomenological scattering constants τ_ε and $1/\tau_\nu = 1/\tau_\varepsilon + 1/\tau_{int}$, where τ_{int} is the scattering rate related to the elastic processes, namely the interface scattering with which we are primarily concerned in the current study. The distribution function in thermal equilibrium and in the absence of external fields is described by Fermi-Dirac distribution $n_{\mathrm{F}}(E(q,\boldsymbol{k}) - \mu) = \frac{1}{e^{\frac{|\varepsilon(q)-\mu|}{k_B T_e}}+1}$. Now, the dynamical equations of the

average miniband energy and the current density are determined by the distribution function $f(q, \mathbf{k}, t)$ as

$$w(t) = \frac{2}{(2\pi)^3 n_e} \iint_{-\infty}^{\infty} d\mathbf{k} \int_{-\frac{\pi}{d}}^{\frac{\pi}{d}} dq \varepsilon_q f(q, \mathbf{k}, t), \tag{8.7a}$$

$$J(t) = \frac{2e}{(2\pi)^3} \iint_{-\infty}^{\infty} d\mathbf{k} \int_{-\frac{\pi}{d}}^{\frac{\pi}{d}} dq v(q) f(q, \mathbf{k}, t), \tag{8.7b}$$

where $n_e(t)$ denotes the density of electrons and again is determined by the distribution function

$$n_e(t) = \frac{2}{(2\pi)^3} \iint_{-\infty}^{\infty} d\mathbf{k} \int_{-\frac{\pi}{d}}^{\frac{\pi}{d}} dq f(q, \mathbf{k}, t). \tag{8.8}$$

To obtain the dynamical equations of the above-mentioned physical quantities, we start by multiplying Eq. (8.5) by either ε_q or $v(q)$ and then performing the integral $\frac{2}{(2\pi)^3 n_e} \iint_{-\infty}^{\infty} d\mathbf{k} \int_{-\frac{\pi}{d}}^{\frac{\pi}{d}} dq$ and $\frac{2e}{(2\pi)^3} \iint_{-\infty}^{\infty} d\mathbf{k} \iint_{-\frac{\pi}{d}}^{\frac{\pi}{d}} dq$, respectively, over the same equation. In particular, multiplying by miniband energy gives the following equation

$$\frac{\partial}{\partial t} \frac{2}{(2\pi)^3 n_e} \iint_{-\infty}^{\infty} d\mathbf{k} \int_{-\frac{\pi}{d}}^{\frac{\pi}{d}} dq \, \varepsilon_q f(q, \mathbf{k}, t) + \frac{eE(t)}{h}$$

$$\times \frac{2}{(2\pi)^3 n_e} \iint_{-\infty}^{\infty} d\mathbf{k} \int_{-\frac{\pi}{d}}^{\frac{\pi}{d}} \frac{\partial f(q, \mathbf{k}, t)}{\partial q} \varepsilon_q dq$$

$$= \frac{1}{\tau_\varepsilon} \frac{2}{(2\pi)^3 n_e} \iint_{-\infty}^{\infty} d\mathbf{k} \int_{-\frac{\pi}{d}}^{\frac{\pi}{d}} n_F \, \varepsilon_q dq - \frac{1}{\tau_\varepsilon}$$

$$\times \frac{2}{(2\pi)^3 n_e} \iint_{-\infty}^{\infty} d\mathbf{k} \int_{-\frac{\pi}{d}}^{\frac{\pi}{d}} dq \, \varepsilon_q f(q, \mathbf{k}, t) - \frac{1}{2\tau_{int}}$$

$$\times \frac{2}{(2\pi)^3 n_e} \iint_{-\infty}^{\infty} d\mathbf{k} \int_{-\frac{\pi}{d}}^{\frac{\pi}{d}} dq \, \varepsilon_q [f(-q, \mathbf{k}, t) - f(q, \mathbf{k}, t)] \tag{8.9}$$

The third term on the right hand side of the Eq. (8.9) would be identically zero since the product $\varepsilon_q[f(-q, \mathbf{k}, t) - f(q, \mathbf{k}, t)]$ is an odd function. Using the Eqs. (8.7a), (8.7b), and (8.9) and the integration by parts for the second term on the left hand side of Eq. (8.9), we finally obtain

$$\dot{w}(t) - \frac{E(t)J(t)}{n_e} = \frac{w_{eq}(\mu, T) - w(t)}{\tau_\varepsilon} \tag{8.10}$$

with the miniband energy in thermal equilibrium in the absence of an external electric field given by

$$w_{eq}(\mu, T) = E_a - \frac{2}{(2\pi)^3 n_0} \iint_{-\infty}^{\infty} d\mathbf{k} \int_{-\frac{\pi}{d}}^{\frac{\pi}{d}} dq \, 2 \, T \cos(qd) n_F. \tag{8.11}$$

In this case the electron density is obtained from Eq. (8.8), which can be represented with

$$n_e = n_0 = \frac{2}{(2\pi)^3} \iint_{-\infty}^{\infty} d\mathbf{k} \int_{-\frac{\pi}{d}}^{\frac{\pi}{d}} dq f(q, \mathbf{k}, t).$$

Similarly, multiplying Eq. (8.5) by $v(q)$ we obtain

$$\begin{aligned}
\frac{\partial}{\partial t} \frac{2e}{(2\pi)^3} &\iint_{-\infty}^{\infty} d\mathbf{k} \int_{-\frac{\pi}{d}}^{\frac{\pi}{d}} dq v(q) f(q, \mathbf{k}, t) + \frac{eE(t)}{\hbar} \\
&\times \frac{2e}{(2\pi)^3} \iint_{-\infty}^{\infty} d\mathbf{k} \int_{-\frac{\pi}{d}}^{\frac{\pi}{d}} \frac{\partial f(q, \mathbf{k}, t)}{\partial q} v(q) dq \\
&= \frac{1}{\tau_\varepsilon} \frac{2e}{(2\pi)^3} \iint_{-\infty}^{\infty} d\mathbf{k} \int_{-\frac{\pi}{d}}^{\frac{\pi}{d}} n_F v(q) dq - \frac{1}{\tau_\varepsilon} \\
&\times \frac{2e}{(2\pi)^3} \iint_{-\infty}^{\infty} d\mathbf{k} \int_{-\frac{\pi}{d}}^{\frac{\pi}{d}} dq v(q) f(q, \mathbf{k}, t) - \frac{1}{2\tau_{int}} \\
&\times \frac{2e}{(2\pi)^3} \iint_{-\infty}^{\infty} d\mathbf{k} \int_{-\frac{\pi}{d}}^{\frac{\pi}{d}} dq \, v(q) [f(-q, \mathbf{k}, t) - f(q, \mathbf{k}, t)] \tag{8.12}
\end{aligned}$$

Here again

$$\dot{J}(t) + \frac{d^2 eE(t)}{\hbar^2} [w(t) - E_a] = -\frac{J(t)}{\tau_v} \tag{8.13}$$

The balance Eqs. (8.10) and (8.13) describe the dynamics of a quantum particle in a miniband of a semiconductor superlattice [16, 17]. The Bragg reflections are consistently included in the description of these dynamical equations by assuming the condition $f(-\pi/d, \mathbf{k}, t) = f(\pi/d, \mathbf{k}, t)$ for the distribution function. Hereafter, we construct the stationary solution of the dynamical Eqs. (8.10) and (8.13) by assuming that a static field E_{dc} is applied and therefore we obtain
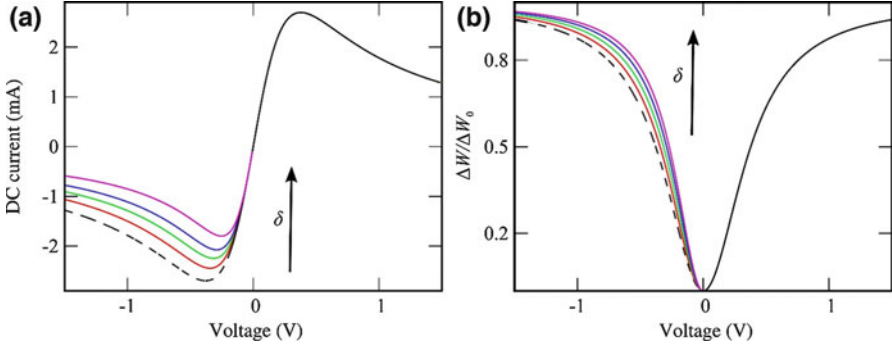
Fig. 8.1 (**a**) Current-voltages curves calculated with a variation of the asymmetry parameter which increases by $\delta = 1$, 1.1, 1.2, 1.3, 1.4 (**b**) The average miniband energy W as a function of the applied voltage. The curves above the dashed line (symmetric superlattice) calculated for different asymmetry parameter same as I-V curves in (**a**)

$$J(U) = \beta\, j_0 \; \frac{2\,\frac{U\,\tau_{eff}}{\hbar}}{1 + \left(\frac{U\,\tau_{eff}}{\hbar}\right)^2} \tag{8.14}$$

with the effective scattering time $\tau_{eff} = \sqrt{\tau_\varepsilon \tau_v}$ and $\beta = \sqrt{\tau_v/\tau_\varepsilon}$ and the magnitude of the peak current $j_0 = (edn_0/2\hbar)(E_a - w_{eq})$. The connection between voltage and energy is $U = eV = eE_{dc}d$. In a similar way we obtain the relationship that describes how far from the middle of the miniband is the average energy of electrons

$$\frac{\Delta W(U)}{\Delta W_0} = \frac{1}{1 + \left(\frac{\hbar}{U\,\tau_{eff}}\right)^2}. \tag{8.15}$$

Here $\Delta W = (w - w_{eq})$ and $\Delta W_0 = (E_\alpha - w_{eq})$.

The voltage-current characteristic corresponding to the analytical formula of Esaki-Tsu curve is illustrated in Fig. 8.1a. The magnitude of the peak current is decreased by the factor β in comparison with Eq. (8.1). By increasing the voltage beyond the point where the current obtains its maximum value, the electrons are allowed to proceed along the dispersion curve $\varepsilon_q(q)$, and finally to reach the edge of Brillouin zone. This results in the suppression of electron transport which is manifested in the reduction of current density with the increase of U. On the contrary, the average minband energy increases with increasing U. In particular, in the limit $U \gg U_{cr}$ the fraction $\Delta W/\Delta W_0$ approaches unity and therefore W is located in the vicinity of the center of the miniband ($W \to E_a$). An important practical question arises: how the balance equations approach is naturally linked with the hybrid approach we discussed earlier in the previous section. The approach based on the SSL balance equations is already known to offer equivalent solutions with the Boltzmann equation in the absence of magnetic field [8]. Thus, we now turn to the

consideration of the effects which are related to the asymmetric scattering processes under forward and reverse bias. The presence of the ansatz should naturally lead to a new approximation of the collision integral into the following form

$$St^{as}(f) = -\frac{f(q, \mathbf{k}, t) - n_F(E(q, \mathbf{k}) - \mu)}{\tau_\varepsilon} + \frac{f(-q, \mathbf{k}, t) - f(q, \mathbf{k}, t)}{2\tau_{int}^{as}} \qquad (8.16)$$

with

$$\tau_{int}^{a_s} = \frac{\tau_{int}}{a_s\,\theta(\mp sgn\,(v)) + 1} \qquad (8.17)$$

Such kind of elastic scattering allows to connect in a straightforward manner the effective scattering time τ_{eff} with the parameter Γ predicted by the NEGF calculations and resulted in the ansatz Eq. (8.3) [14]. The parameter a_s is related to the parameters used to describe the characteristics of each interface and the interface roughness self-energy. The negative (positive) sign in theta function [see Eq. (8.17)] is directly determined by the polarity of the electric field which allows a larger peak current $j_0^+\,(\,j_0^-)$.

Then, the existence of an asymmetric interface roughness design dictates necessary corrections directly in balance Eqs. (8.10) and (8.13) which are incorporated as follows

$$j_0 = \begin{cases} \beta^+\,j_0, & U < 0 \\ \beta^-\,j_0, & U \geq 0 \end{cases},$$

where the factor $\beta^+(\beta^-)$ simply reduces (increases) the maximum (minimum) current j_0. Therefore, the resulting ansatz permits the use of a parameter $\delta = \beta^-/\beta^+ = \left(\tau_{eff}^-/\tau_{eff}^+\right)$ which controls the asymmetry in the current flow and can be obtained from

$$\frac{j_0^+}{\Gamma^+} = \frac{j_0^-}{\Gamma^-}. \qquad (8.18)$$

Here $\delta = j_0^+/j_0^-$ and for a perfectly symmetric superlattice ($\delta = 1$) the corresponding relaxation time is $\tau = 31$ fs. This way the differences in the SSL interfaces can lead to deviation from a completely antisymmetric current-voltage characteristic. The parameters extracted from NEGF calculations (see Refs. [9, 11]) and used in Eqs. (8.1) and (8.2) are: Γ^+, Γ^- =21, 20 meV and j_0^+, j_0^- =2.14, 1.94 $\times 10^9$ A/m^2.

The peak current j_0^- decrease significantly with increasing δ and therefore results in a strong enhancement of the asymmetry observed in current-voltage curves. This kind of situation is illustrated in Fig. 8.1a. Thus, applying static voltage may lead to

increase of average miniband energy depending on the field direction as shown in Fig. 8.1b. These effects which appear due to processes of intraminiband electron scattering can most likely be utilized in generation and amplification of radiation of high-frequency radiation in SSLs [8]. In this work, to estimate the generated power efficiency we will use the following parameters for a GaAs/AlGaAs SSL: period d=6.23 nm, electron density $n_0 = 1.5 \times 10^{18}$ cm^{-3} and refractive index $n_r = \sqrt{13}$ (GaAs).

8.3 Even-Harmonic Generation due to Designed Structural Variations of SSLs.

In this section, we analyze the superlattice response to a monochromatic field and consider the effects in terahertz radiation by varying the parameter δ within reasonable limits. We previously modelled the microscopic frequency multiplication mechanism by determining the conversion efficiency for both even and odd order nonlinearities [14]. However, these calculations did not address a direct comparison between the power output of even harmonics and odd harmonics. To answer this question, we study the response to an ac electric field oscillating at different frequencies and for different asymmetry coefficients δ. Figure 8.1 demonstrates the output powers of the even-order harmonics (second and fourth harmonics) as a function of parameter α in response to an input field which oscillates at 150 GHz. These frequency-doubling and frequency-quadrupling effects would not appear in a perfectly symmetric SSL. On the other hand, as the asymmetry increases the generated harmonics become comparable with the third harmonics produced by a superlattice subjected to irradiation with input fields at different frequencies [see Fig. 8.1a and b]. But, of course, when electrons are able to be efficiently Bragg-reflected, the power output of the third harmonics surpass clearly the even-harmonic radiation.

Note that the NDC state in SSLs is accompanied by an instability of homogeneous electric field resulting in formation of high-field domains. These electric domains can affect dramatically the spontaneous frequency multiplication. Figure 8.2 demonstrates the power emitted by second harmonics, but now after the excitation of the SL sample by higher frequency input signals. Here we notice that the enhanced asymmetry increases considerably the component of the second harmonic generation for frequencies at 300 GHz and 600 GHz. In this case, the excitation of a perfectly symmetric superlattice with an input signal close to 100 GHz should generate a weaker power output sensitive to a wide range of a parameter values, even beyond a_c. All the results presented in this section were obtained to complement the effects predicted in [9, 11, 14, 15] (Fig. 8.3).
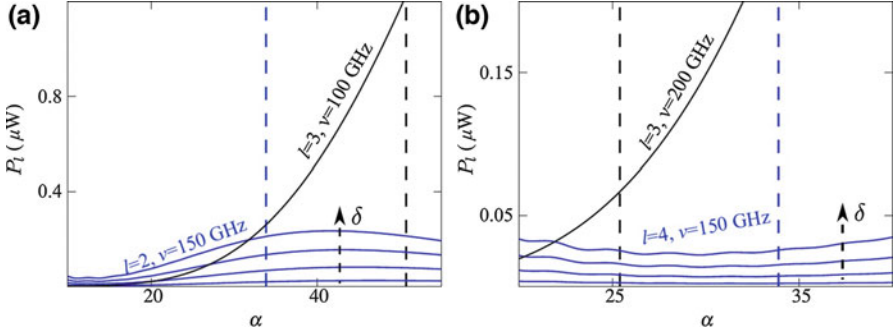
Fig. 8.2 Comparison of the power output generated by frequency multipliers consisted of either symmetric superlattice or asymmetric ones. (**a**) Emitted optical power for third harmonic generated by a field oscillating 100GHz and second harmonic generated by a field oscillating 150 GHz. (**b**) Emitted optical power for third harmonic generated by a field oscillating 200 GHz and fourth harmonic generated by a field oscillating 150 GHz. The blue curves have been calculated using our theory and varying the asymmetry parameter $\delta = \Gamma^+/\Gamma^-$, which increases by δ=1.1, 1.2, 1.3, 1.4. Note that parameter α determines the input power inside the SSL
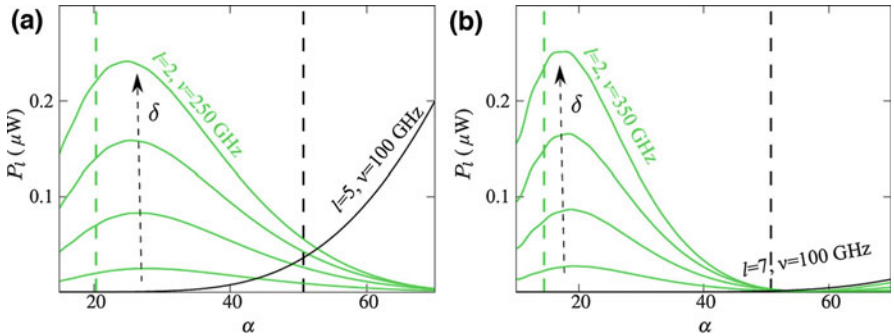
Fig. 8.3 Comparison of the power output generated by frequency multipliers consisted of either symmetric superlattice or asymmetric ones. (**a**) Emitted optical power for fifth harmonic generated by a field oscillating 100 GHz and second harmonic generated by a field oscillating 250 GHz. (**b**) Emitted optical power for seventh harmonic generated by a field oscillating 100 GHz and second harmonic generated by a field oscillating 350 GHz. The blue curves have been calculated using our theory and varying the asymmetry parameter $\delta = \Gamma^+/\Gamma^-$, which increases by δ=1.1, 1.2, 1.3, 1.4. Note that parameter α determines the input power inside the SSL

8.4   Photon-Assisted Transport and Harmonic Emission

Here we discuss the dc-current density in the presence of the ac field, the possibility of formation of photon-assisted peaks and the effects of current rectification on frequency multiplication. The principle underlying SSL multiplication and rectification [8] can be summarized as follows: perpendicular charge transport in biased superlattices is dominated by resonances due to the alignment of energy levels in different wells. These resonances yield various peaks in the current-voltage (I -V)
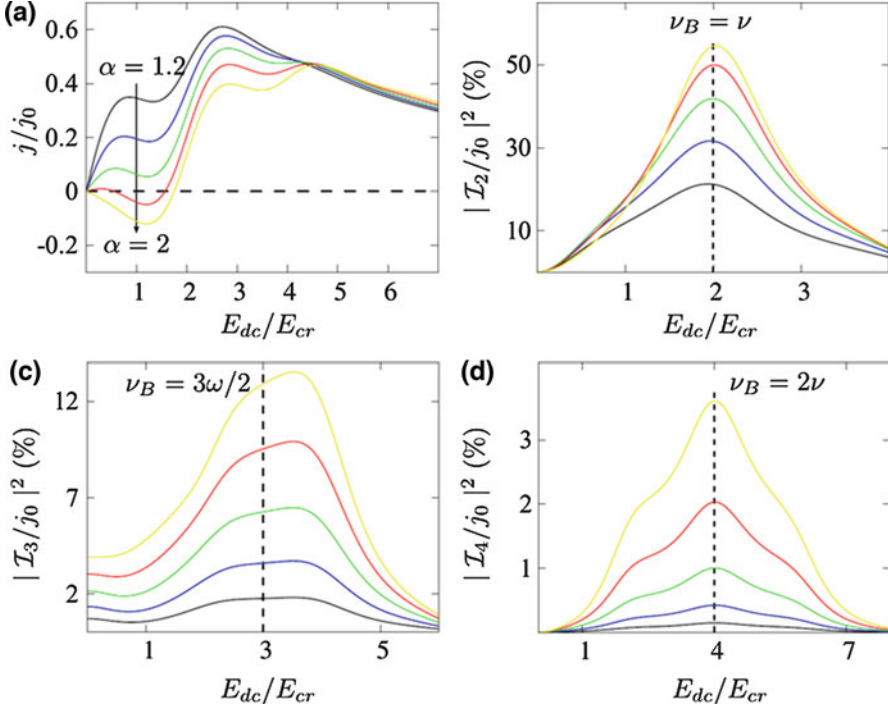
Fig. 8.4 (**a**) I–V characteristic calculated with input radiation at oscillating frequency $\frac{h\nu}{\Gamma} = 2$. The different colors designate different amplitude of the parameter $\alpha = 1.2, 1.4, 1.6, 1.8, 2$. (**b**)–(**d**) The dependence of the harmonic emission $|\mathcal{I}_1(\nu)|^2$ on the static electric field and the different values of parameter $\alpha = eE_{ac}d/(h\nu)$ which causes photon-assisted transport as shown in the panel (**a**). From (**b**)–(**d**) the harmonics are, respectively the 2nd, 3rd and 4th. The vertical dashed lines designate the maximum harmonic output at $\nu_B = l\nu/2$

characteristics connected with negative differential conductivity [8, 20]. If the SSL is subjected to an external oscillating field, photon assisted tunnelling is possible and replica of the resonances are observed at biases which differ from alignment conditions by integer multiples of the photon energy. Such kind of resonances are demonstrated in Fig 8.4a at $eE_{dc}d = ph\nu + \Gamma$ where p is positive integer. The current voltage characteristics produced by the model calculations with 10.6 THz radiation. Note that these resonance peaks have magnitude proportional to $J_p^2(\alpha)$. There is however another effect which arises, namely the ANC, when the direction of the dc current is opposite to its direction in a normal conductor [e.g. yellow curve in Fig. 8.4a]. Furthermore, the physical origin of ANC and the strong suppression of the dc current [red curve in Fig. 8.4a] at small values of static bias can be attributed to dynamical localization, when the electron periodically returns to the initial state both in real and quasi-momentum space [21, 22]. The condition for dynamical localization is $J_0(\alpha) = 0$ [22]. It should be noticed the maximum response of harmonics corresponds to the resonant condition where both harmonic motions come to
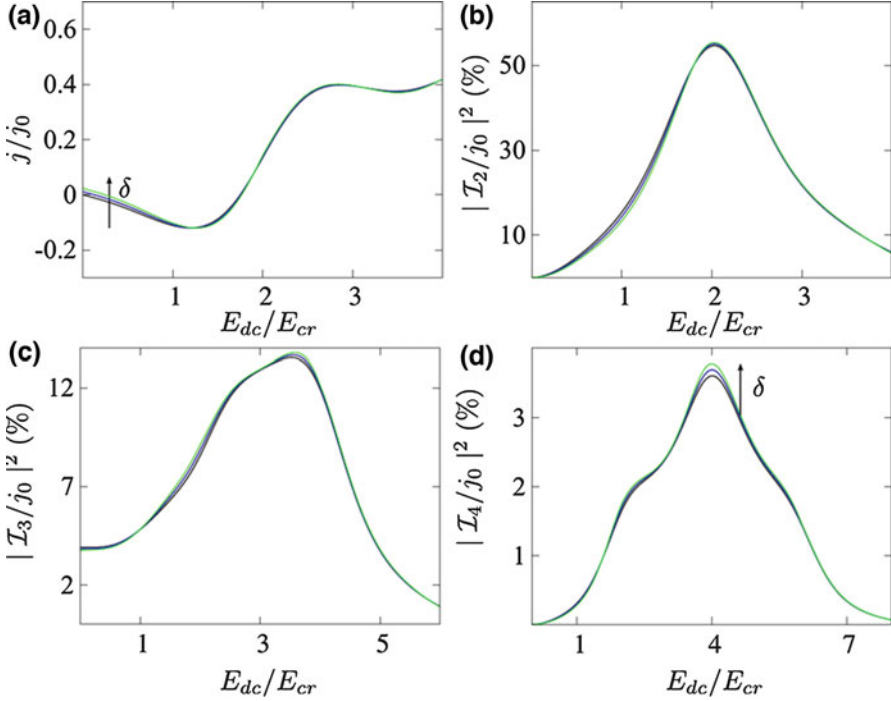
Fig. 8.5 (a) I–V characteristic calculated with input radiation at oscillating frequency ($\frac{h\nu}{\Gamma} = 2$, $\nu = 10.6$ Thz) $\alpha = 2$ and different values of the asymmetry parameter δ. (b)–(d) panels show the dependence of the harmonic emission $|\mathcal{I}_l(\nu)|^2$ on the static electric bias E_{dc}. From (b)–(d) the harmonics are, respectively the 2nd, 3rd and 4th. From bottom to the top asymmetry parameter increases by $\delta = 1.05, 1.1$. The black lines correspond to calculations for an ideal superlattice $\left(\delta = \frac{\Gamma^+}{\Gamma^-} = 1\right)$

resonance, i.e. the one corresponding to the Bloch oscillations due to static voltage $\nu_B = eE_{dc}d/h$ and other one due to frequency modulated Bloch oscillations. Figure 8.4b–d demonstrate the effectiveness of this condition, i.e. $\nu_B = l\nu/2$ where l denotes the order of the harmonic as we have already discussed. However, we underline that dynamic localization, ANC and the synchronization of the ac field with Bloch oscillations is valid in the limit $\frac{h\nu}{\Gamma} > 1$. Now we further examine the effect asymmetric current flow on the rectification and eventually on the harmonic output. Figure 8.5a shows that behavior of the I-V characteristic only slightly changes with the increase of the asymmetry parameter and the emergence of ANC is hardly affected. However, for $E_{dc} \to 0$ the current is clearly rectified and it demonstrates small but non-zero values. As a result, the peak power output for the 4th harmonic notably increases whereas the response of the 2nd and 3rd harmonics remain almost the same [see Fig. 8.4(b)–(d)].

Before stating our concluding remarks, it is noteworthy to consider that SSLMs, given the recent theoretical and experimental advances [42, 43], can be used as

sources for imaging on medical and security applications, but that the resolution is in principle not as sharp due to the larger wavelengths in the GHz-THz range. However, this may be an opportunity to combined designs with superlensing structures, which can dramatically improve both the transmission and the resolution of the imaged signal [44–46].

8.5   Conclusion

In this chapter we revisited the recent progress that has occurred in controllable nonlinear optics for superlattice multipliers in the GHz-THz ranges. Using an extended Boltzmann kinetic approach, we obtained an asymmetry ratio (16) which is consistent with the solution stemmed from NEGF calculations. This study further confirms the potential advantages of generating THz radiation with controlling the superlattice interfaces quality and numerically estimating the nonlinear electromagnetic response. As a further development of this activity, we also presented here preliminary results investigating the rectification effects combined with asymmetrical current flow on the harmonic response for far-infrared wavelength radiation. Currently we are performing different numerical simulations in order to include self-consistently the effect domains in a semiconductor superlattice under the action of GHz field. A different output power can be expected at various frequency ranges by integrating a superlattice multiplier with a SLED oscillator [10]. In order to obtain a more accurate estimation of the conversion efficiency for an irradiated SSL, the effects of different designs of external waveguide delivering the input field power should be considered.

References

1. Tonouchi M (2007) Cutting-edge terahertz technology. Nat Photonics 1:97
2. Kampfrath T, Tanaka K, Nelson Keith A (2013) Resonant and nonresonant control over matter and light by intense terahertz transients. Nat Photonics 7:680–690
3. Jepsen PU, Cooke DG, Koch M (2010) Terahertz spectroscopy and imaging-modern techniques and applications. Laser Photon Rev 5:124–166
4. Pereira MF (2015) TERA-MIR radiation: materials, generation, detection and applications II. Opt Quant Electron 47:815–820
5. Pereira MF, Shulika O (2014) Terahertz and mid infrared radiation: detection of explosives and CBRN (using terahertz). NATO science for peace and security series-B: physics and biophysics. Springer, Dordrecht
6. Pereira MF (1995) Analytical solutions for the optical absorption of superlattices. Phys Rev B 52:1978–1983
7. Apostolakis A, Awodele MK, Alekseev KN, Kusmartsev FV, Balanov AG (2017) Nonlinear dynamics and band transport in a superlattice driven by a plane wave. Phys Rev E 95(6):062203
8. Wacker A (2002) Semiconductor superlattices: a model system for nonlinear transport. Phys Rep 357:1–111

9. Pereira MF, Winge D, Wacker A, Zubelli JP, Rodrigues AS, Anfertev V, Vaks V (2017) Theory and measurements of harmonic generation in semiconductor superlattices with applications in the 100 GHz to 1 THz range. Phys Rev B 96:045306

10. Eisele H, Li L, Linfield EH (2018) High-perfomance GaAs/AlAs superlattice electronic devices in oscillators at frequencies 100-320 GHz. Appl Phys Lett 112:172103

11. Pereira MF, Anfertev V, Zubelli JP, Vaks V (2017) THz generation by GHz multiplication in superlattices. J Nanophotonics 11:046022

12. Winnerl S, Schomburg E, Brandl S, Kus O, Renk KF, Wanke M, Allen S, Ignatov A, Ustinov V, Zhukov A, Kopev P (2000) Mup doubling and tripling of terahertz radiation in a GaAs/AlAs superlattice due to frequency modulation of Bloch oscillations. Appl Phys Lett 77:1762

13. Klappenberger F, Renk KF, Renk P, Rieder B, Koshurinov YI, Pavelev DG (2004) Semiconductor-superlattice frequency multiplier for generation of submillimeter waves. Appl Phys Lett 84:3924

14. Apostolakis A, Pereira MF (2019) Controlling the harmonic conversion efficiency in semiconductor superlattices by interface roughness design. AIP Adv 9:015022

15. Apostolakis A, Pereira MF (2019) Numerical studies of superlattice multipliers performance. Quantum Sens Nano Electron Photonics XVI:109262G

16. Ignatov AA, Dodin EP, Shashkin VI (1991) Transient response theory of semiconductor superlattices: connection with Bloch oscillations. Modern Phys Lett B 05(16):1087–1094

17. Ignatov AA, Shashkin VI (1983) A simplified approach to nonlinear HF response theory of superlattice materials. Phys Lett A 94A(3–4):169–172

18. Apostolakis A, Pereira MF (2019) Potential and limits of superlattice multipliers coupled to different input power sources. J Nanophotonics 3:1–11

19. Pereira MF, Anfertev V, Shevchenko Y, Vaks V (2020) Giant controllable gigahertz to terahertz nonlinearities in superlattices. Sci Rep 10:15950

20. Wacker A, Jauho AP, Zeuner S, Allen SJ (1997) Sequential tunnelling in doped superlattices: fingerprints of impurity bands and photon-assisted tunnelling. Phys Rev B 56:13268

21. Keay BJ, Zeuner S, Allen SJ, Maranowski KD, Gossard AC, Bhattacharya U, Rodwell MJW (1995) Dynamic localization, absolute negative conductance, and stimulated, multiphoton emission in sequential resonant tunneling semiconductor superlattices. Phys Rev Lett 75:4102

22. Holthaus M (1992) Collapse of minibands in far-infrared irradiated superlattices. Phys Rev Lett 69:351

23. Pereira MF, Koch SW, Chow WW (1991) Many-body effects in the gain spectra quantum-wells. Appl Phys Lett 59:2941–2943

24. Oriaku CI, Pereira MF (2017) Analytical solutions for semiconductor luminescence including Coulomb with applications to dilute bismides. J Opt Soc Am B 34:321–328

25. Pereira MF (2018) Analytical expressions for numerical characterization of semiconductors per comparison with luminescence. Materials 11:1–15

26. Grempel H, Diesel A, Ebeling W, Gutowski J, Schüll K, Jobst B, Hommel D, Pereira MF, Henneberger K (1996) High-density effects, stimulated emission, and electrooptical properties of ZnCdSe/ZnSe single quantum wells and laser diodes. Phys Status Solidi B 194:199

27. Pereira MF, Binder R, Koch SW (1991) Theory of nonlinear optical absorption in coupled-band quantum wells with many-body effects. Appl Phys Lett 64:279–281

28. Pereira MF, Henneberger K (1998) Microscopic theory for the optical properties of coulomb-correlated semiconductors. Phys Status Solidi B 206:477–491

29. Chow WW, Pereira MF, Koch SW (1992) Many-body treatment on the modulation response in a strained quantum well semiconductor laser medium. Appl Phys Lett 61:758

30. Jin R, Okada K, Khitrova G, Gibbs HM, Pereira MF, Koch SW, Peyghambarian N (1992) Optical nonlinearities in strained-layer InGaAs/GaAs multiple quantum wells. Appl Phys Lett 61:1745

31. Pereira MF, Henneberger K (1997) Gain mechanisms and lasing in II-VI compounds. Phys Status Solidi B 202:751–762

32. Pereira MF (2018) Analytical expressions for numerical characterization of semiconductors per comparison with luminescence. Materials 11:2
33. Pereira MF, Nelander R, Wacker A, Revin DG, Soulby MR, Wilson LR, Cockburn JW, Krysa AB, Roberts JS, Airey RJ (2007) Characterization of intersubband devices combining a nonequilibrium many body theory with transmission with transmission spectroscopy experiments. Sci Mater Electron 18:689
34. Pereira MF, Tomić S (2011) Intersubband gain without global inversion through dilute nitride band engineering. Appl Phys Lett 98:061101
35. Pereira MF, Faragai IA (2014) Coupling of THz radiation with intervalence band transitions in microcavities. Opt Express 22:3439
36. Pereira MF (2011) Microscopic approach for intersubband-based thermophotovoltaic structures in the terahertz and mid-infrared. JOSA B 28:2014–2017
37. Pereira MF, Schmielau T (2009) Momentum dependent scattering matrix elements in quantum cascade laser transport. Microelectron J 40:869–871
38. Nelander R, Wacker A, Pereira MF, Revin DG, Soulby MR, Wilson LR, Cockburn JW, Krysa AB, Roberts JS, Airey RJ (2007) Fingerprints of spatial charge transfer in quantum cascade lasers. Appl Phys 102:11314
39. Pereira MF (2016) The linewidth enhancement factor of intersubband lasers: from a two-level limit to gain without inversion conditions. Appl Phys Lett 109:222102
40. Schmielau T, Pereira MF (2009) Nonequilibrium many body theory for quantum transport in terahertz quantum cascade lasers. Appl Phys Lett 95:231111
41. Hyart T, Shorokhov AV, Alekseev KN (2007) Theory of parametric amplification in superlattices. Phys Rev Lett 98:220404
42. Apostolakis A, Pereira MF (2020) Superlattice nonlinearities for Gigahertz-Terahertz generation in harmonic multi-pliers. Nanophotonics 9(12):3941–3952. https://doi.org/10.1515/nanoph-2020-0155
43. Pereira MF, Anfertev V, Shevchenko Y, Vaks V (2020) Giant controllable gigahertz to terahertz nonlinearities in superlattices. Sci Rep 10:15950
44. Rose TP, Di Gennaro E, Abbate G, Andreone A (2011) Isotropic properties of the photonic band gap in quasicrystals with low-index contrast. Phys Rev B 84:125111
45. Savo S, Di Gennaro E, Andreone A (2009) Superlensing properties of one-dimensional dielectric photonic crystals. Opt Express 17:19848–19856
46. Di Gennaro E, Morello D, Miletto C, Savo S, Andreone A, Castaldi G, Galdi V, Pierro V (2008) A parametric study of the lensing properties of dodecagonal photonic quasicrystals. Photonics and Nanostruct Fundam Appl 6:60–68

Chapter 9
Solid-State Millimeter-Wave Through Terahertz Transceivers

E. Bryerton

Abstract Schottky diode technology has been used for the generation and detection of millimeter waves for decades. The advantages of this solid-state approach are compact size, frequency tunability, and relatively low cost. Recent drivers from the wideband communications, security imaging, spectroscopy, as well as test and measurement markets have pushed this technology further in recent years. This chapter highlights the most recent advances in Schottky diode based sources and detectors. This includes wideband tunable frequency sources up to 1 THz, such as a multiplier chain that provides -16 dBm typical output power over the full WM-250 750–1100 GHz band. Examples of narrowband high-power sources are also given, such as a 250 mW multiplier chain at 260 GHz, and a highly compact complete transmitter with 10 mW output power from 270–290 GHz for imaging applications. Several examples are also given of diode-based wideband receivers, for terrestrial and orbital applications, including broadband millimeter-wave downconverters operating up to 1.1 THz. Millimeter-wave heterodyne receivers for CubeSat atmospheric radiometry are also described, including a 880 GHz heterodyne receiver for ice cloud measurements and a 183 GHz 4-channel radiometer for tropical storm tracking.

9.1   Introduction

CBRN and explosives typically have strong absorption signatures in the THz and Mid Infrared ranges of the spectrum (TERA-MIR). The combination of advances in millimetre-wave amplifier technology, integration, and simulation tools for millimetre and THz waveguide and circuits has allowed for the miniaturization and development of highly integrated sources, receivers, and transceivers based on

E. Bryerton (✉)
Virginia Diodes, Inc., Charlottesville, VA, USA
e-mail: bryerton@vadiodes.com

all solid-state and conventional machined structures targeted to the TERA-MIR frequency range. These highly compact and low-power receivers have been used in security imaging systems, gas spectroscopy, and space-based radiometers. Market demand for high-precision test and measurement equipment in the millimetre and sub-millimetre bands has also spurred the development of more compact, higher power, and more sensitive transmitters and receivers. In this chapter is given a short overview of millimeter-wave sources and receivers based on Schottky diode multipliers, mixers, and detectors, along with many recent examples of components and systems based on these approaches.

9.2 Diode Frequency Multiplier Based Sources

High-power tunable solid-state sources using diode-based frequency multipliers are critical for radio astronomy, atmospheric studies, spectroscopy, as well as many other important scientific applications. The millimeter-wave source technology described in this chapter utilizes commercial signal sources and power amplifiers at microwave frequencies (below 40 GHz) followed by diode-based frequency multiplier to translate the signal to a higher frequency. This is in contrast to Terahertz approaches based on translating optical techniques downward in frequency. The primary benefits of the RF/microwave based approach described here include broad frequency operation, excellent frequency control and tuning, the possibility for pulsed and modulated signals, small size and weight, reliable operation and lower cost. The primary drawback is output power. In the past 25 years, a few key technology developments driven by large scientific projects with millimeter-wave requirements beyond the state-of-the-art at that time have made diode-based frequency multipliers up to 2–3 THz a viable product useful for numerous applications. First of all, the development of a planar Schottky diode process [1] allowed for integration of multiple diodes with associated transmission line matching circuitry along with rugged and reproducible assembly. This planar Schottky diode technology in combination with the emergence of powerful electromagnetic simulation tools allowed for the successful design of numerous topologies for efficient frequency multiplication and mixing over a broad frequency range. Finally, the need for hundreds of broadband frequency multipliers over several bands up to 1 THz provided by large scientific endeavors such as the Atacama Large Millimeter Array (ALMA) [2] provided the crucial initial market driver for these new technologies.

9.2.1 Varistor Multiplier Sources

There are two general classes of multiplier-based millimeter-wave sources. The first type is for broadband application, where broadband here refers to the full, or nearly

full, range of single-mode propagation in rectangular waveguide. For example, a broadband WR-3.4 source refers to the IEEE-1785.1 standard [3] 220–330 GHz range. These full waveguide band applications include general laboratory test and measurement, device characterization, channel propagation, spectroscopy, local oscillators for broadband heterodyne receivers, etc. The diode multipliers used in these sources rely on the resistance nonlinearity of the diode in forward bias to generate harmonics of the input signal. This nonlinear resistance can be impedance matched over a wide bandwidth at the desired output harmonic. However, being a resistive nonlinearity, it is inherently limited in efficiency to $1/n^2$, where n is the multiplication factor [4]. Practically speaking, a typical full waveguide-band diode frequency doubler will have a conversion efficiency of no more than half this ideal case. For example, commercially available doubler modules have a conversion efficiency of approximately 10% at an output frequency of 140–220 GHz, trending lower for higher frequencies, to approximately 5% at 330–500 GHz. Full waveguide-band diode frequency triplers will have conversion efficiencies ranging from 5% for a 70–110 GHz output frequency to approximately 1% at a 750–1100 GHz output frequency.

Microwave components and frequency sources are typically commercially available up to approximately 40 GHz. Therefore, to produce a frequency source at several hundreds of GHz, as cascade of millimeter-wave frequency doublers and triplers is required. As discussed in the previous paragraph, the conversion efficiency of broadband frequency multipliers is relatively low. The consequence of these fairly low conversion efficiencies for each multiplier stage is that the overall efficiency of the entire multiplier is quite low, i.e. a large amount of microwave power is required to achieve a relatively low amount of millimeter-wave of THz power. There are also power limits introduced by the thermal handling of the Schottky diodes, which need to be of ever reducing area as operating frequency is increased so that junction capacitance does not dominate performance. For these reasons (conversion efficiency and diode power handling), the currently achievable output power from full waveguide band millimeter-wave diode multiplier chains (Fig. 9.1) ranges from approximately +10 dBm (10 mW) over the WR-4.3, 170–260 GHz band to approximately −17 dBm (0.02 mW) over the WM-250, 750–1100 GHz band. Besides lower conversion efficiency and output power, the other tradeoff to a wideband multiplier source is the presence of unwanted harmonics. While each frequency doubler and tripler in the chain will, via symmetries in the circuit design, reject unwanted harmonics to at least 20–30 dB below the desired tone, the presence of unwanted harmonics at the multiplier input can result in mixing products being generated in addition to the desired multiplication. Unfortunately, this mixing can be quite efficient, resulting in a rise in the unwanted harmonic level relative to the input. For example, an unwanted harmonic 30 dB down relative to main tone at the multiplier input can be mixed so that it is only 20 dB down at the output. After a cascade of three or more frequency multipliers, the result in a cascade of a multipliers can be a forest of tones spaced apart by the frequency of the original synthesizer. Careful analysis and filtering throughout the multiplier chain must be done to minimize this problem, but without a tunable filter in the chain, some unwanted harmonics are unavoidable.
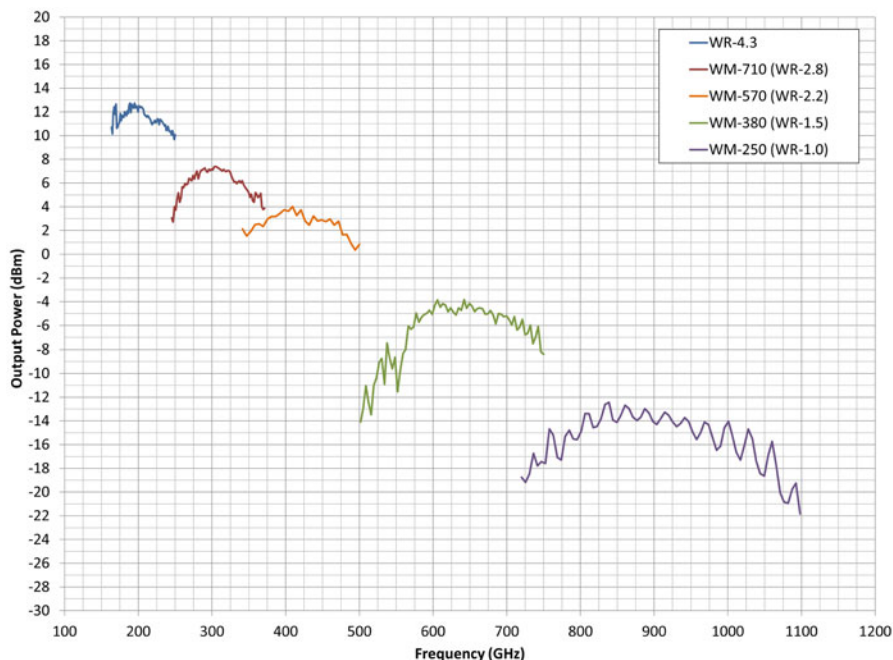
Fig. 9.1 Output power as a function of frequency for a series of full waveguide band sources based on Schottky diode varistor frequency multipliers

9.2.2   Varactor Multiplier Sources

The previous paragraphs discussed the design and performance of frequency multipliers that cover full, or nearly full, single-mode waveguide bands. There are numerous applications where higher output power and conversion efficiency takes precedence over tuning bandwidth. For many applications, a 5–10% fractional bandwidth or less is sufficient. For these applications, the same general Schottky diode fabrication and assembly processes can be used, but instead of using the forward-biased resistive nonlinearity, the capacitance vs voltage nonlinearity of a reverse biased Schottky diode is used to generate signals at integer multiples of the input frequency. By properly terminating the unwanted harmonics and impedance matching the desired harmonic, a varactor frequency multiplier can be extremely efficient (100% efficient in theory, if losses are removed and all possible harmonics are terminated properly [5]). In practice, varactor frequency doublers can be nearly 50% efficient [6] and varactor frequency triplers nearly 20% efficient [7] at lower frequencies where the losses are lower. Because it is a reactance nonlinearity, the matching and terminations can only be fully optimized at a single frequency and the bandwidth is limited. Typical 3dB bandwidths are 15–20% for a varactor frequency doubler and 5–10% for a varactor frequency tripler.
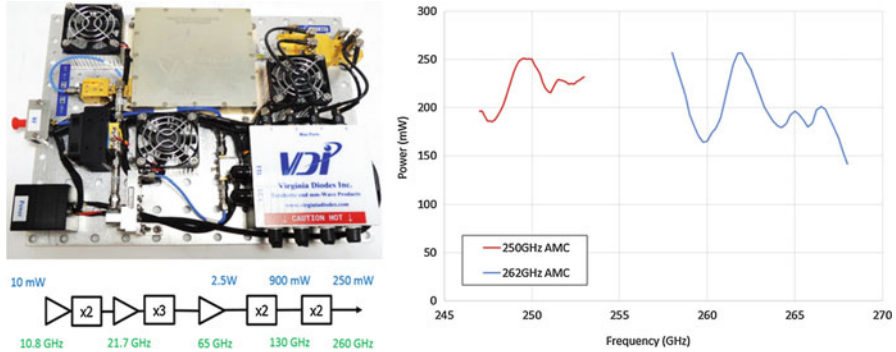
Fig. 9.2 Block diagram and photograph (left) of a 250/260 GHz active multiplier chain, along with measured output power (right) for an active multiplier chain tuned to 250 GHz (red trace) and 260 GHz (blue trace)

To increase the power handling of these varactor frequency multipliers, arrays of diodes can be integrated onto a single substrate. The size of the array is constrained by electromagnetic design constraints, and trends downward with frequency as the wavelength gets smaller. Further increases in power can be achieved by combining multiple diode integrated circuits using waveguide power combining techniques. Until very recently, the maximum power at 260 GHz was a few tens of milliwatts (260 GHz is an important frequency for many electron spin resonance experiments.) Even at this modest power level, these sources found applications in many continuous-wave (CW) experiment, or as the input source for travelling-wave tube (TWT) amplifiers, or even as a "seed" source to help stabilize Gyrotron oscillators. More recently, >500 mW has been achieved at 190 GHz [8] and >250 mW has been achieved at 260 GHz [9] (this system is shown in Fig. 9.2). Other recent results include 35 mW at 330 GHz, 30 mW at 550 GHz, and 2 mW at 1.03 THz [10]. Yet, higher power is desired. Most importantly, if the power level of the solid-state sources can be increased sufficiently, it should be possible in some experiments to replace very costly Gyrotron systems with more compact and frequency agile traveling-wave tube amplifiers (TWTs) (pumped by solid-state sources), and the solid-state sources will replace even the TWTs for a significant class of experiments.

9.2.3   Compact Tunable Multiplier Based Millimeter-Wave Sources

High power tunable compact sources are an important enabling technologies for emerging millimeter-wave applications, such as millimeter-wave short-range radar and imaging systems. Higher resolution is possible and large dynamic ranges can be obtained assuming sufficient transmitter power is available. In addition to output power, size and frequency tuning are also very important considerations for these

systems to gain wider acceptance in the market. Compact size, as well as overall dc power, is extremely important for millimeter-wave sources on CubeSat platforms. Nanosatellite platforms, such as CubeSats, offer significant advantages for remote sensing platforms in terms of cost and time from mission inception to launch. The use of nanosatellites offers significant promise for many Earth science applications, where an entire constellation of small satellites can be placed in orbit at relatively low cost, with increased planetary coverage and time resolution.

Gunn oscillators were the traditional component for this application. They offer the advantage of a high fundamental frequency, compact size, and relatively high overall dc efficiency. The high fundamental frequency of oscillation provides intrinsically low harmonic content without the need for extra filtering. The primary drawback of a Gunn oscillator is the available electronic tuning bandwidth. Gunn oscillators can be mechanically tuned over larger bandwidths, but this is not feasible for a FMCW system. Varactor tuning of Gunn oscillators can provide a tuning bandwidth up to a few GHz at 100 GHz. The output power of a Gunn oscillator at 100 GHz is typically 10–30 mW with a DC input power of a few Watts. To obtain higher transmitter powers at a few hundred GHz or higher, a W-band power amplifier followed by frequency multiplication is then required.

An alternative to a W-band Gunn oscillator is a broadband microwave voltage-controlled oscillator (VCO) followed by a cascade of amplifiers and diode-based frequency multipliers of the types described in the previous section. The final power amplifier will typically be in the 80–100 GHz range, driven by the availability of MMIC amplifiers. Careful filtering is required in the multiplier chain to control the harmonic content, given the large harmonic number of the final output. But this is very manageable with planar filter technology up to fractional tuning bandwidths of 25% or higher. Larger electronic tuning bandwidths are possible with this approach than with a Gunn oscillator. With high levels of MMIC integration, compact size can be achieved with the entire source up to the final frequency contained in a single housing on the order of 20 cm^3.

Figure 9.3 shows a photograph and measured output power of a 270–290 GHz integrated transmitter [11]. This is a complete tunable transmitter, including a
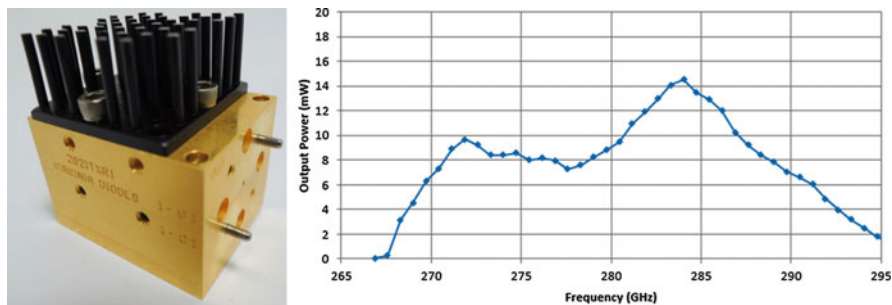
Fig. 9.3 Photograph (left) and measured output power (right) of 270–290 GHz integrated transmitter

microwave VCO. This module was designed for +10 dBm output power centered at 282 GHz with a tuning bandwidth greater than 10 GHz. A high-efficiency varactor frequency tripler is used for the final stage. This varactor tripler is the bandwidth-limiting component in this module. In addition to the VCO, power amplifier, and frequency multiplier components, there are several filters and attenuators for harmonic suppression. The total multiplication factor is x36. The VCO is a commercial surface mount component. After the VCO, everything is planar IC and bondwire technology. The first two frequency doublers are passive MMIC doublers. The first tripler is a WR-10 broadband varistor tripler. This is followed by a 88–98 GHz MMIC power amplifier with 19–21 dBm output power. This drives the varactor frequency tripler, which has approximately 10% conversion efficiency. Amplifying and filtering is employed throughout the chain to minimize harmonic content. The frequency is tuned via a pin connected directly to the VCO tuning port. For the wideband MMIC VCO used here, a 6.5–7.9 V tuning voltage corresponds to a 270–290 GHz output range. There is also a TTL ON/OFF capability for pulsing up to approximately 50 kHz rate. The module requires approximately 650 mA from a +9 V supply, for a total power dissipation of just under 6 W. To limit overall power dissipation, switching DC-DC converters are used to generate the amplifier bias voltages. If a more stable, lower phase noise output is required, then linear regulation would be required, increasing the overall power dissipation. Broader bandwidths are possible at the expense of lower output power by using a varistor, rather than varactor, tripler in the final stage.

9.3 Diode Mixer and Detector Based Receivers

The nonlinear resistance characteristic of a Schottky diode can also be used to implement an efficient broadband frequency mixer. By coupling and impedance matching the diode to the desired detection band in the millimeter-wave spectrum and to a higher power (a few mW typically) millimeter-wave local oscillator, the difference frequency $f_{IF} = f_{RF} - f_{LO}$ is generated (as well as other, typically unwanted, mixing products). This frequency mixer forms the core of a millimeter-wave heterodyne receiver. The local oscillator for this mixer needs to be at a nearby frequency to the desired detected frequency, necessitating the generation of a low-noise millimeter-wave signal with several mW output power. This requirement is often the primary driver for total DC power. In compact, low-power environments, such as a nanosatellite or unmanned aerial vehicle (UAV), there are typically severe limits to available DC power. The diode multiplier-based sources described in the previous section are often used for the local oscillation generation in a heterodyne receiver. Since these multipliers are in the same technology as the mixers, a high level of integration can be achieved, with the entire downconverter housed in the same compact waveguide module. Several stages of local oscillator frequency multiplication can be integrated in the housing, such that the local oscillator supplied by the user can be a microwave signal of a few mW, easily supplied by a

e.g. compact dielectric resonator oscillator (DRO). Several examples of these compact downconverters are described in following paragraphs.

The first set of examples are for broadband applications, where the band of interest is approximately a full single-mode waveguide band (e.g. 220–330 GHz for WR-3.4). Besides general test and measurement, applications that require a compact integrated downconverter include antenna testing, broadband communication channel sounding, broadband survey spectroscopy, and others. The integrated downconverters described here use a frequency multiplied local oscillator input to convert a low frequency IF to a millimeter wave carrier. The mixer is a Schottky diode second-harmonic double sideband (DSB) mixer. The mixer requires approximately +3 dBm LO power at one-half the RF frequency. The module requires a LO input of up to 20 GHz with approximately 0 dBm. The module includes buffer amplifiers, frequency multipliers, filters, and power amplifiers to convert the LO input to the frequency and power required at the mixer LO input. A combination of commercial and custom ICs are integrated into a waveguide module with a waveguide flange interface for the RF detection band. A photograph of a complete integrated downconverter is showed in Fig. 9.4 along with typical performance for one of the common waveguide bands. Compact converters such as these have been developed for all waveguide bands up to WM-250 (750–1100 GHz). The available IF bandwidth of the converter is proportional to the RF band, and it typically limited to about 15% of the highest RF frequency in that waveguide band. For communication applications, flat response as a function of IF is critical to faithfully transform the wideband digitally modulated signal. Although image-rejecting, or singlesideband mixers, can be implemented in this technology, the required circuitry can be complex and often introduces extra losses, reducing sensitivity. Therefore, in the downconverter modules described here, the mixers are double sideband (DSB), meaning signals appear at the IF originating from both $f_{LO}+f_{IF}$ and $f_{LO}-f_{IF}$. (The unwanted band is often labeled the image band.) To filter the image band, a bandpass waveguide filter can be used. In addition to general measurement and wideband communications, broadband millimeter-wave receivers are used in plasma
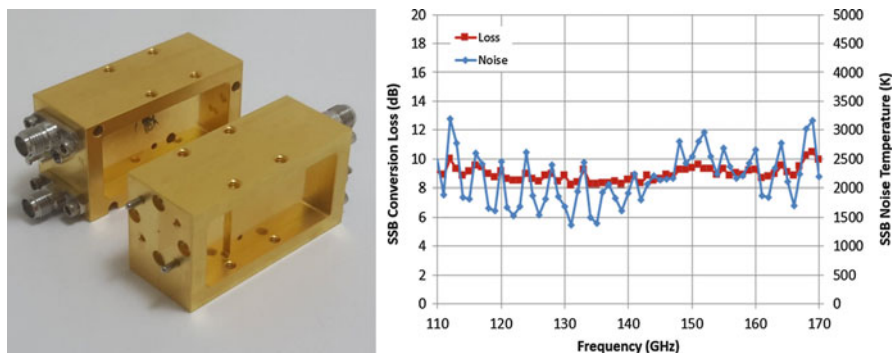
Fig. 9.4 Photograph (left) of integrated millimeter-wave downconverter. Measured conversion loss and noise temperature of a typical WR-6.5 (110–170 GHz) integrated downconverter
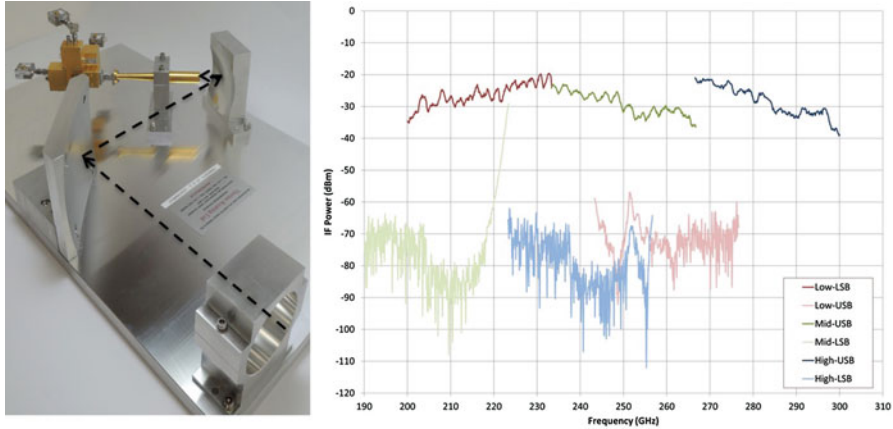
Fig. 9.5 Photograph (left) of a 200–300 GHz receiver for electron cyclotron emission diagnostics. Measured mixer IF outputs (right) versus detection frequency for each of the three downconverter outputs

diagnostics. Figure 9.5 shows a 200–300 GHz receiver for electron cyclotron emission diagnostics [12]. A set of three compact waveguide diode-based receivers are integrated with a waveguide triplexer to provide complete spectral coverage from 200 to 300 GHz.

The second set of examples are for heterodyne detection over narrower bands. This includes many earth and atmospheric remote sensing applications, where observations are only possible in certain millimeter-wave atmospheric bands or where only certain molecule spectral lines are of interest. In these cases, where the local oscillator does not need to operate over a wide frequency band, varactor frequency multipliers can be used in the local oscillator chain to increase the conversion efficiency, reducing the overall DC power requirements, critically important for many of these Cubesat (nanosatellite) platforms. Submillimeter-wave radiometry is a technique that shows considerable promise for remote sensing and characterization of ice cloud properties in the upper troposphere, important for developing more accurate climate models. IceCube, funded by NASA's Earth Science Technology Office (ESTO), was a low earth orbit CubeSat mission successfully launched and deployed from the International Space Station (ISS) in May 2017 [13]. The primary objective of IceCube was to validate the technological readiness of an 870 GHz commercial receiver for use in future spaceflight missions. The secondary objective of this mission was to demonstrate 0.1 K Noise Equivalent Temperature Difference (NETD) and 2 K maximum calibration error performance. It is a possible precursor for an entire network of CubeSats to provide cost-effective and global mapping of ice clouds. The Mixer LO Assembly (MLA) is **a 2nd harmo**nic mixer assembly that down-converts an 871–895 GHz passband to an Intermediate Frequency (IF) output spanning 6–12 GHz. The entire MLA, including DRO, is required to fit within a 9 cm × 9 cm × 3 cm volume. This prohibited the use
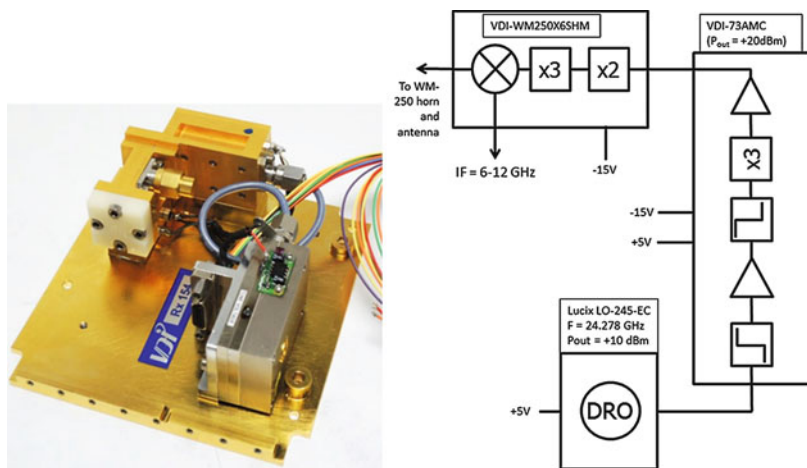
Fig. 9.6 Photograph (left) and block diagram (right) of the 883-GHz IceCube MLA. The MLA is composed of three modules: the 24.278 GHz DRO, active tripler (73AMC), and 883-GHz second-harmonic mixer (WM250X6SHM)

of discrete components for each of the LO amplifiers, multipliers, and mixer. The receiver consists of only three modules (DRO, 72.8 GHz active tripler, and 870 GHz mixer) with the modules specifically designed for a compact configuration. A photograph and block diagram of the MLA is shown in Fig. 9.6. The fundamental LO source is a commercial DRO and runs off a +12 V, 130mA dc supply. The 73 GHz active tripler module contains a commercial MMIC amplifier at the DRO frequency followed by a WR-13 diode frequency tripler followed by a MMIC power amplifier with +20 dBm output power. The varactor multiplier and mixer module contains a varactor frequency doubler, varactor frequency tripler, and second-harmonic mixer with a WM-250 (WR-1.0) interface to the waveguide horn antenna. The varactor multipliers allow for only 100 mW at 74 GHz to optimally pump a 883 GHz second-harmonic Schottky mixer. The 148 GHz varactor doubler and 442 GHz varactor tripler have respective efficiencies of approximately 35% and 8%. The IF amplifiers and baseband processing are on a plate above the mixer and LO plate, not shown here. The total required DC power for the LO, including the 24.278 GHz dielectric resonator oscillator (DRO), is less than 3.75 W. For the best flight model, the measured mixer noise temperature is 4000K DSB with 11.5dB conversion loss**.** More technical details from the design phase can be found in [14].

The final example of a compact receiver for remote sensing applications is not a heterodyne receiver, but a direct detection radiometer. It therefore does not contain a diode frequency mixer, but a Schottky diode millimeter-wave detector. The Schottky diode is used as a millimeter-wave square-law detector, where the output DC voltage is proportional to the incident millimeter-wave power. The nonlinearity of the diode is used to rectify the incident signal. The critical aspects of performance are given by the responsivity (typically in V/W), a measure of how efficiently the detector

transforms the millimeter-wave incident power to a DC output, and noise-equivalent power (NEP), which characterizes the sensitivity of the detector. The NEP is simply the output voltage noise of the detector divided by the responsivity, all divided by the square root of the integration bandwidth (i.e. inverse of integration time), and therefore typically given in W/sqrt(Hz), the square root originating from the square-law behavior of the detector. The physical implementation of a detector is often very similar to that of a frequency mixer—the diode still needs to be coupled to the incident millimeter-wave signal in the same way, but there is no requirement for a local oscillator, and the output is a DC voltage rather than a IF difference frequency. As with a mixer, being a resistive nonlinearity based element, the diode detector can be used over a full waveguide bandwidth. The TROPICS (Time Resolved Observations of Precipitation structure and storm Intensity with a Constellation of Smallsats) mission [15] is a constellation of CubeSats intended to dramatically increase the temporal resolution of several key measurements required to better determine the intensity and evolution of tropical storms. One of the instruments on this platform is a G-band (WR-5.1) radiometer based on a diode direct-detect architecture with three detection channels near the 183 GHz water vapor absorption line to measure water vapor profiles and one detection channel at 206 GHz for cloud ice measurements. Because the CubeSat is already a small platform with limited volume and available power, and because the same CubeSat will also contain instruments for 118 GHz and 90 GHz observations, the G-band radiometer must be contained in a very small form factor and consume a small amount of power. A photograph and performance of the G-band radiometer module is shown in Fig. 9.7. This G-band radiometer includes three stages of RF low-noise amplifiers, a noise diode for calibration, 2 GHz wide waveguide bandpass filters for each of the four channels, and diode detectors for each of the four channels, along with all the necessary regulation and video amplification. The prototype integrated radiometer fits in a single 3.8 cm × 5.7 cm × 1.3 cm split-block waveguide housing. At room temperature, the measured noise temperature ranges from 900 to 1200 K for the four channels, resulting in a total sensitivity of 0.5K rms for each channel when integrated for 10 ms.
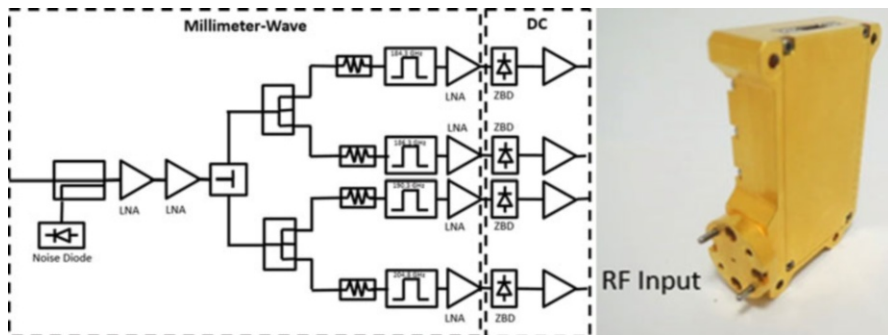
Fig. 9.7 Block diagram (left) and photograph (right) of the TROPICS G-band radiometer

At this point, we would like to mention that advanced materials [16, 17] and compact sources for the GHz-THz region such as quantum cascade lasers and superlattice multipliers [18–28] are also being investigated by other teams and can deliver complementary devices that could potentially be used in combination our systems, to further broaden the range of targets for detection.

References

1. Hesler J, Hall W, Crowe T, Weikle R, Deaver B, Bradley R, Pan S-K (1997) Fixed-tuned submillimeter wavelength waveguide mixers using planar Schottky barrier diodes. IEEE Trans Microwave Theory Technol 45(5):653–658
2. Bryerton E, Saini K, Morgan M, Stogoski M, Boyd D, Thacker D (2004) Development of electronically tuned local oscillators for ALMA. In: 2005 Joint 30th International conference on infrared and millimeter waves and 13th international conference on terahertz electronics
3. 1785.1-2012 – IEEE Standard for Rectangular Metallic Waveguides and their interfaces for frequencies of 110 GHz and Above – Part 1: frequency bands and waveguide dimensions
4. Page CH (1956) Frequency conversion with positive nonlinear resistors. J Res Natl Bur Stand 56:179–182
5. Faber M, Chramiec J, Adamski M (1995) Microwave and millimeter-wave diode frequency multipliers. Artech House, Boston
6. Porterfield D, Crowe T, Bradley R, Erickson N (1999) A high-power fixed-tuned millimeter-wave balanced frequency doubler. IEEE Trans Microwave Theory Technol 47(4):419–425
7. Porterfield D (2007). High-efficiency terahertz frequency triplers. In: 2007 IEEE MTT-S international microwave symposium
8. Crowe T, Hesler J, Retzloff S, Kurtz D (2017) Higher power terahertz sources based on diode multipliers. In: Proceedings of the 42nd international conference Infrared, Millimeter, and THz (IRMMW-THz)
9. Bryerton E, Retzloff S, Hesler J (2019) High-power submillimeter wave solid-state sources. In: 2019 12th Global Symposium Millimeter Wave (GSMM)
10. Siles J, Cooper K, Lee C, Lin R, Chattapadhay G, Mehdi I (2018) A new generation of room-temperature frequency-multiplied sources with up to 10x higher power in the 160 GHz to 1.6 THz range. IEEE Trans THz Sci Technol 8:6
11. Bryerton E, Hesler J (2016) A compact electronically tunable 282 GHz high-power transmitter. In: Proceedings of the 41st international conference Infrared, Millimeter, and THz (IRMMW-THz)
12. Bryerton E, Koller D, Hesler J, Crowe T (2014) A compact and reliable 200-300 GHz receiver for the ITER ECE system. In Proceedings of the 39th international conference Infrared, Millimeter, and THz (IRMMW-THz)
13. Wu D, Peipmeier J, Esper J, Ehsan N, Racette P, Johnson T, Abresch B, Bryerton E (2019) IceCube: spaceflight demonstration of 883-GHz cloud radiometer for future science. In: Proceedings of the SPIE Vol. 1131, CubeSats and smallsats for remote sensing III
14. Bryerton E, Hesler J, Retzloff S, Crowe T (2015) A compact low-power 874 GHz Schottky receiver for the IceCube radiometer. In: Proceedings of the 26th International SymposiumSpace THz Technology
15. Blackwell W, Eshbaugh J, Erickson N, Bryerton E (2019) Development and flight qualification of the millimeter wave receivers for the NASA TROPICS CubeSat constellation mission. In: Proceedings of the 4the International Conference Infrared, Millimeter, and THz (IRMMW-THz)
16. Oriaku CI, Pereira MF (2017) Analytical solutions for semiconductor luminescence including Coulomb correla-tions with applications to dilute bismides. J Opt Soc Am B 34:321

17. Pereira MF (2018) Analytical expressions for numerical characterization of semiconductors per comparison with luminescence. Dent Mater 11:2
18. Pereira MF (2016) The linewidth enhancement factor of intersubband lasers: From a two-level limit to gain with-out in-version conditions. Appl Phys Lett 109:222102
19. Pereira MF, Zubelli PJ, Winge D, Wacker A, Rondrigues SA, Anfertvev V, Vaks V (2017) Theo-ry and measurements of harmonic generation in semiconductor superlattices with applications in the 100 GHz to 1 THz range. Phys Rev B 96:045306
20. Pereira MF, Anfertev V, Zubelli JP, Vaks V (2017) Terahertz generation by gigahertz multiplication in su-perlattices. J Nanophoton 11(4):046022
21. Apostolakis A, Pereira MF (2019) Controlling the harmonic conversion efficiency in semiconductor superlattices by in-terface roughness design. AIP Adv 9:015022
22. Apostolakis A, Pereira MF (2019) Numerical studies of superlattice multipliers performance. Quantum Sens Nano Electron Photonics XVI:109262
23. Apostolakis A, Pereira MF (2019) Potential and limits of superlattice multipliers coupled to different input power sources. J Nanophotonics 13:036017
24. Winge DO, Franckié M, Verdozzi C, Wacker A (2016) Simple electron-electron scattering in non-equilibrium Green's function simulations. J Phys Conf Ser 696:012013
25. Pereira MF, Shulika O (2014) Terahertz and mid infrared radiation: detection of explosives and CBRN (using te-rahertz), NATO Science for peace and security series-B: physics and biophysics. Springer, Dordrecht
26. Pereira MF, Shulika O (2011) Terahertz and mid infrared radiation: generation, detection and applications, NATO science for peace and security series-B: physics and biophysics. Springer, Dordrecht
27. Apostolakis A, Pereira MF (2020) Superlattice nonlinearities for Gigahertz-Terahertz generation in harmonic multipliers. Nanophotonics 9(12):3941–3952. https://doi.org/10.1515/nanoph-2020-0155
28. Pereira MF, Anfertev V, Shevchenko Y, Vaks V (2020) Giant controllable gigahertz to terahertz nonlinearities in superlattices. Sci Rep 10:15950

Chapter 10
Transmission and Reflection Characteristics of Textiles in the Terahertz Range

N. Pałka, E. Pawlinska, M. Szustakowski, M. Walczakowski, E. Czerwinska, W. Ciurapinski, L. Jodlowski, M. Kowalski, P. Zagrajek, and M. Zyczkowski

Abstract The main aim of this chapter is to present spectral characteristics of clothing textiles in the THz range. Such characteristics are important for understanding the interaction of the THz radiation with person wearing clothes as well as for design of modern THz body scanners. The proposed TDS-based setup provided automated textiles scanning both in transmission and reflection configurations. The presented transmission and reflection spectra of three selected materials reveal their different interaction with the incident THz radiation depending on the angle of incident and orientation angle between the threads and the electromagnetic vector.

10.1 Introduction

The last 20 years is characterized by a strong development of techniques using radiation from the border of the far-infrared and microwave radiation in the range of about 0.1–10 THz, which due to its unique characteristics is called terahertz band (THz). Formally speaking, the waves with a frequency of 0.03–0.3 THz create a sub-range of millimetre waves (MMW), while the frequency range of 0.3–10 THz belongs to the far infrared radiation (FIR). The THz radiation permeates through the most of non-metallic and non-polar substances such as paper, cardboard, plastic, clothes, etc., and perfectly reflects from metal, which in relation to the non-ionizing, and therefore safe character, is the basis of operation of body scanners detecting

N. Pałka (✉) · E. Pawlinska · M. Szustakowski · M. Walczakowski · E. Czerwinska
W. Ciurapinski · L. Jodlowski · M. Kowalski · P. Zagrajek · M. Zyczkowski
Institute of Optoelectronics, Military University of Technology, Warsaw, Poland
e-mail: norbert.palka@wat.edu.pl; ewelina.pawlinska@wat.edu.pl;
mieczyslaw.szustakowski@wat.edu.pl; michal.walczakowski@wat.edu.pl;
elzbieta.czerwinska@wat.edu.pl; wieslaw.ciurapinski@wat.edu.pl; leon.jodlowski@wat.edu.pl;
marcin.kowalski@wat.edu.pl; przemyslaw.zagrajek@wat.edu.pl; marek.zyczkowski@wat.edu.pl

suspicious objects (e.g. dangerous objects) under human clothing [1–3] or non-destructive testing of materials, e.g. composites [4, 5]. In this spectral range many substances, including some explosive materials have characteristic absorption features (spectral signatures) resulting from vibrations and interactions between molecules [3], which can be used to identify explosives that are covered or hidden in a package. Quite a big limitation for THz wave propagation over long distances is very high attenuation of the atmosphere (in the order of 100–10.000 dB/km) related to the presence of many absorption lines of water. Terahertz band in the electro-magnetic spectrum remained poorly used in the early 90's due to the lack of both effective radiation sources and detectors. In the 80's the first system for generation and detection of pulsed electromagnetic radiation called Time Domain Spectroscopy (TDS), was demonstrated [6, 7]. Its spectrum was in the range of about 0.1–3 THz and it was the exact fulfilment of the so-called terahertz gap. Techniques of detection and identification of hidden bombs on persons are crucial considering public safety especially in terms of a growing number of recent terrorist attacks and unfortunately non diminishing threat of such acts in future.

The main aim of this chapter is to determine spectral characteristics of clothing textiles in the THz range. Although such materials were already studied [8–11], we present novel orientation dependent measurements. Such characteristics are impor-tant for understand the interaction of the THz radiation with person wearing clothes and for design of modern THz body scanners.

10.2   Time Domain Spectroscopy

TDS is a synchronised emitting-detecting setup (Fig. 10.1a). The optical beam from a femtosecond laser (usually at 800 nm) is split into two arms, one of which is directed to the emitter, while the other is passing through the delay line and reaches the receiver. Pulses of the electromagnetic radiation (electric field) lasting about 0.5 ps are generated in the emitter with repetition rate of 80 MHz. Thanks to the optical system (mirrors and/or lenses) they reach the receiver. In the receiver the THz pulse is synthetized due to the use of the delay line and femtosecond laser.

It should be underlined that in TDS system the electric field is measured and not the intensity of radiation, therefore the pulse has also negative part. This pulse (Fig. 10.1b) has very broad spectrum mostly in the 0.1–4 THz range, which in practice is determined by the fast Fourier transform of the pulse (Fig. 10.1c). Although the average power of generated radiation is rather small, being in the range of hundreds of microwatts, the big advantage of this technique is its high signal-to-noise ratio (S/N) being in the range of 90 dB for the maximum (~0.5 THz), which decreases as the frequency increases. To suppress the influence of water vapour from atmosphere, the THz part of the optical setup is purged with dried air or nitrogen. The THz emitter consists of two metal electrodes located on the semiconductor substrate forming the photoconductive antenna (PCA) – Fig. 10.2a. The supply voltage (~50 V) is applied between electrodes distant about 5–10μm
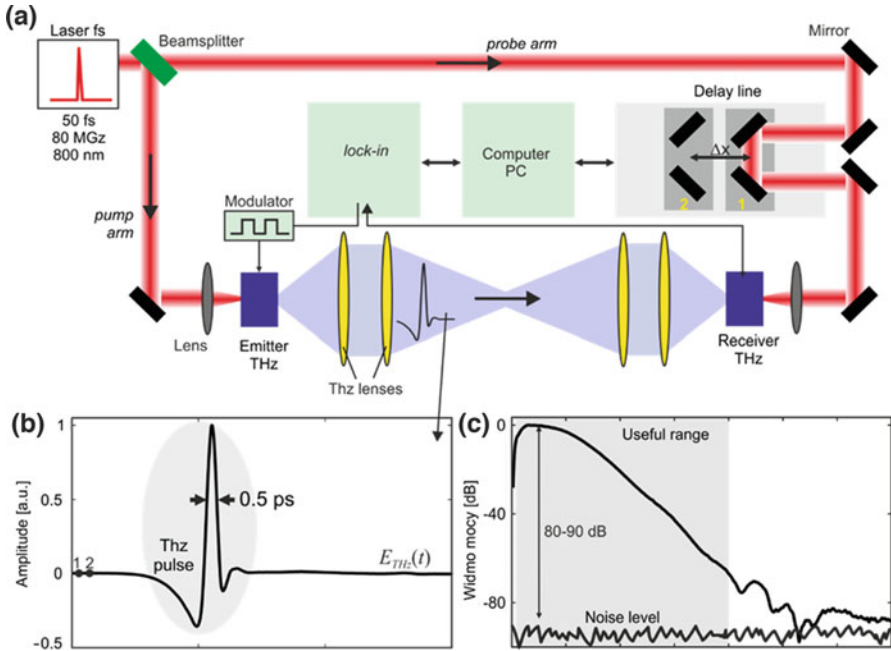
Fig. 10.1 The scheme of TDS system (**a**) typical THz pulse (**b**), and its power spectrum (**c**)
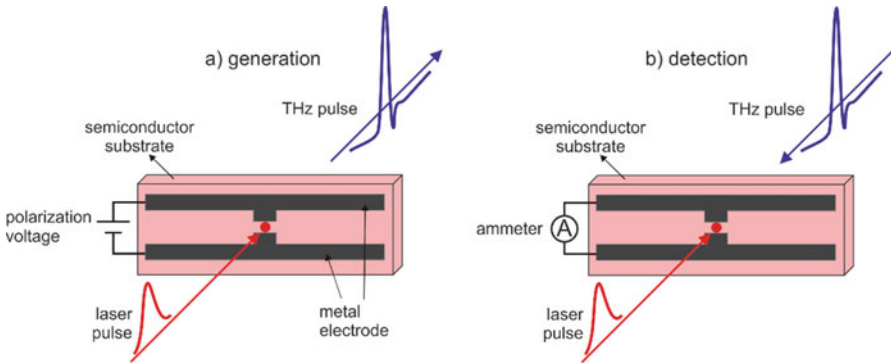
Fig. 10.2 Generation and detection of THz pulse in the photoconductive switch

from each other. Femtosecond optical pulses with the energy higher than the forbidden band of the semiconductor generate electron-hole pairs in the gap between electrodes. The appropriate electric field causes the acceleration of carriers. The current pulse arising from the acceleration and then carrier interception is the source of sub-picosecond (terahertz) pulses of electromagnetic radiation. Such geometry of antenna results in the fact that the THz pulse is a linearly polarized, in approximation Gaussian-like, beam. The width of the beam in the focus depends on the frequency,

the diameter of the exit pupil and the focal length of the optical setup. The higher the frequency is, the smaller is the diameter of the focal spot. THz radiation gathered and directed by mirrors forms the useful flux, which reaches the THz receiver constructed in the same manner as the THz emitter. However, instead of polarization voltage a very sensitive ammeter is connected to electrodes of the photoconductive antenna (Fig. 10.2b). The laser pulse generates charges in the area between antenna's electrodes.

During the lifetime of charges the THz pulse impinges the antenna and its electromagnetic field shifts charges, which results in the flow of current. The induced current is proportional to the amplitude of the field related to the THz pulse. The typical current is on the range of few picoamperes and therefore a low-noise current amplifier must be used. To increase the S/N ratio the phase sensitive amplifier is used (called lock-in) together with the optical modulator.

Classical delay line consists of the retroreflector placed on the moving stage (Fig. 10.1a) whose motion introduces time delay or acceleration of the laser pulse in relation to the THz pulse. Together with changing position of the delay line the relatively broad THz pulse is scanned in the receiver point by point by means of shifted in time laser pulse. As a result a single THz pulse is sampled point by point (mostly 1024 or 2048 points) and the value of each point, thanks to the phase sensitive detection, is averaged from large number of subsequent pulses.

10.3 Measurement Setup

The analysis of different textiles for different orientations and configurations requires a very sophisticated optical setup to provide full information about the sample. Therefore, the measurement arrangement described in this section was developed in order to determine spectral characteristics. The system is based on the TDS setup from MenloSystems [12]. A fiber-coupled Terahertz Spectrometer Tera K15 setup was used to build the THz system measuring textiles. The main advantage of this solution is its large flexibility of the manipulation of its emitter and detector positions. Both devices are connected with the laser using optical fibres which provides different configurations of the optical setup. The exploited spectrometer can work in the frequency range 0.1–3 THz and has the dynamics of 35 dB at maximum (Fig. 10.3).

The experimental measurement setup (Fig. 10.4) was built on the basis of the above described spectrometer. The THz radiation coming from the emitter propagates through the set of two lenses and illuminates the examined textile placed in the holder. Depending on the configuration of the measurement (in reflection or in transmission) the radiation is either reflected from the sample or propagates through it. Next, the radiation (reflected or transmitted) is coming through the set of two lenses and is directed to the detector. The detector has the possibility of automatic azimuthal and elevation angles scanning. It consists of: large rotation platform, linear stepper motor stages and a rotational stepper motor stage. The sample placed in the
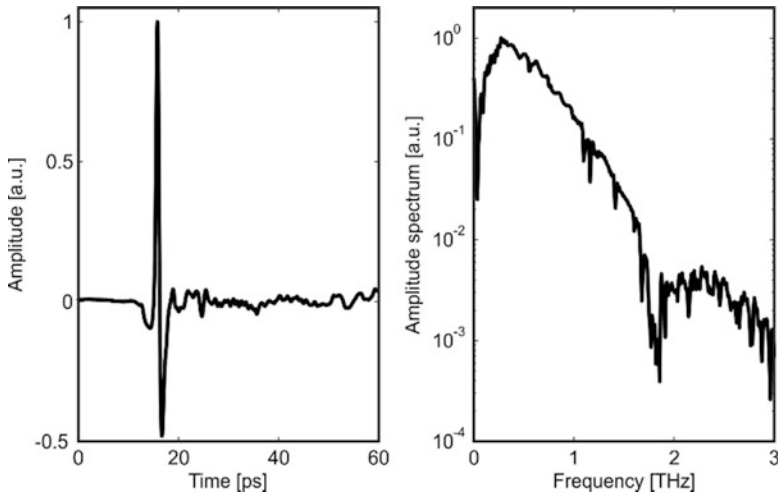
Fig. 10.3 Tera K15 spectrometer: registered pulse (on the left) and its spectrum (on the right)
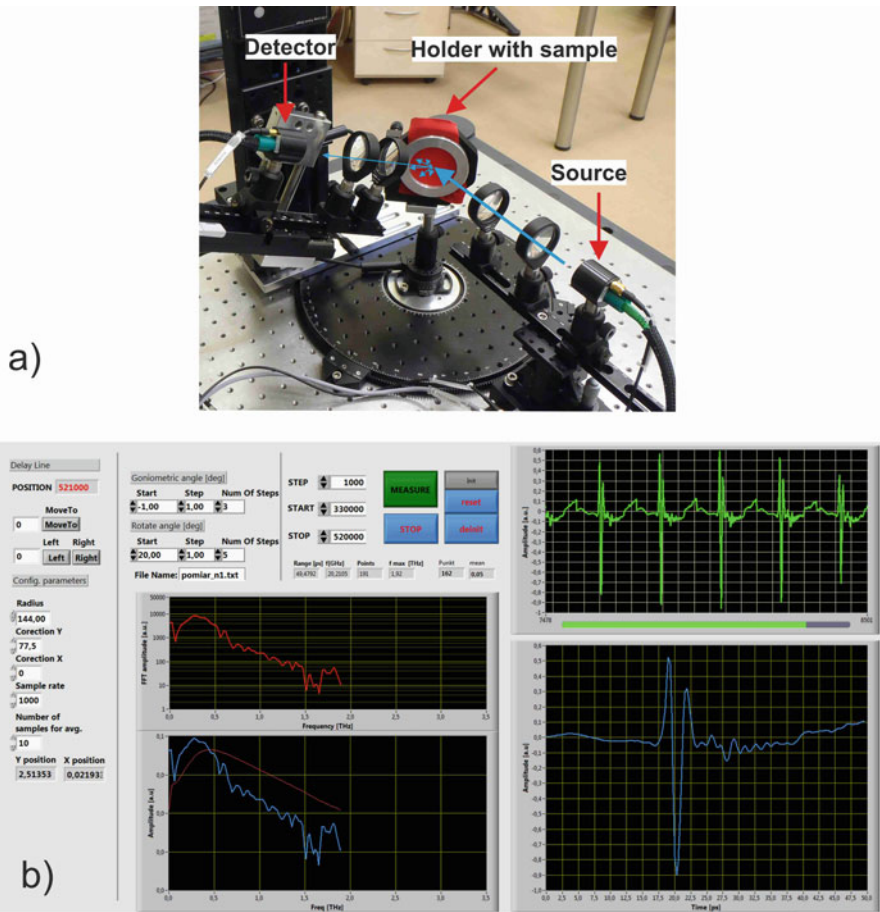
Fig. 10.4 The measurement setup (**a**) and its GUI (**b**)

Fig. 10.5 Sample holder
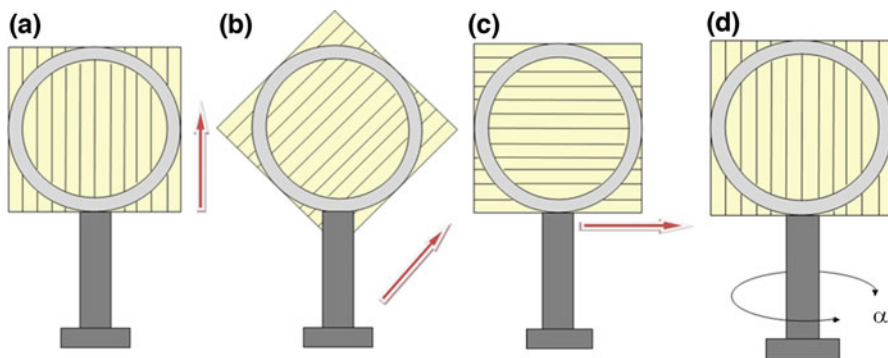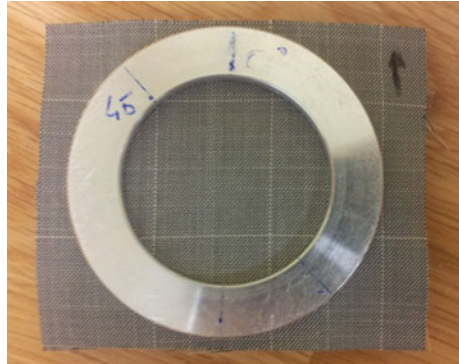
Fig. 10.6 Position of the sample for rotation: $\beta = 0^0$ (**a**), $\beta = 45^0$ (**b**), $\beta = 90^0$ (**c**) and rotation around vertical axis (**d**)

holder is also mounted on the rotational stage which ensures proper measurement requirements. The graphical user interface (GUI) of the used machine program is shown in Fig. 10.4 (on the right). It contains a window enabling the control over the spectrometer and the mechanical setup of the unit. After registration of the THz signal the graph of the pulse and its spectrum is created.

The special sample holder with magnets was designed and manufactured to ensure uniform stretch of the textile in all directions, see Fig. 10.5. Proper textile mounting was crucial for further measurements for different textile fibre orientations and different incidence angles both in reflection and in transmission. Moreover, the reflection measurements required the flat surface of the textile to avoid additional influence of the textile curvature.

During the tests, the sample was placed in the holder in three positions (Fig. 10.6a–c). The first position, i.e. the arrangement of the material at the angle $\beta = 0°$, means that the wrap is vertical. In the second position, the material was turned over $\beta = 45°$, and then in the last position with $\beta = 90°$ in relation to the first setting. In this situation, the wrap is horizontal. Moreover, the sample was also rotated around the vertical axis and pulses were detected for different angles $\alpha = 0°$, 15°, 30°.

10.4   Samples

Three textile samples were chosen for spectral analysis in the THz range. They had different thicknesses (thin, medium and thick material) and different weight in the range of 166–270 g/m^2. List of samples used in measurements is presented in Table 10.1. Due to the fact that single thread has submillimetre size and cloth design contain microscopic structure it was anticipated that additional parameters for sample characterization might be used. Example of one sample with its additional characterization is presented in Fig. 10.7.

10.5   Transmission Configuration – Setup, Methodology and Results

The scheme of the optical setup used for the measurement of the spectral characteristics in transmission configuration is illustrated in Fig. 10.8a. The designed sample holder is placed on the rotational stage and additionally provides the possibility of rotating the sample around the main optical axis (along the direction of the propagating THz beam). During our measurements the sample was rotated around the vertical axis, pulses were detected for different angles $\alpha = 0°$, 15°, 30°, and moreover the sample holder with the textile was rotated around the optical axis which resulted in different orientations of the fibres $\beta = 0°$, 45°, 90°. Altogether, each sample is measured for nine different combinations of angles. The scheme of the signal processing is shown in Fig. 10.8b. At first, the reference pulse was

Table 10.1 List of samples

No.	Composition	Grammage [g/m^2]
1	Polyester 100%,	170
2	Polyester 65%, cotton 35%	270
3	Polyester 65%, viscose 30%, spandex 4%	166

Cloth thickness	0.25 mm
Wrap diameter	0.15 mm
Thread diameter	0.15 mm
Period	0.45 mm
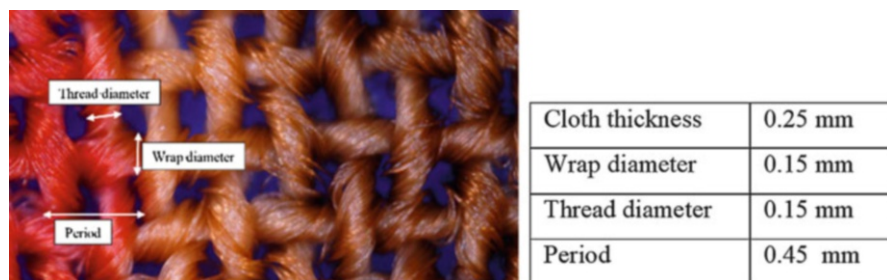
Fig. 10.7   Picture of sample 1. 40× magnification (left) and its parameters (right)
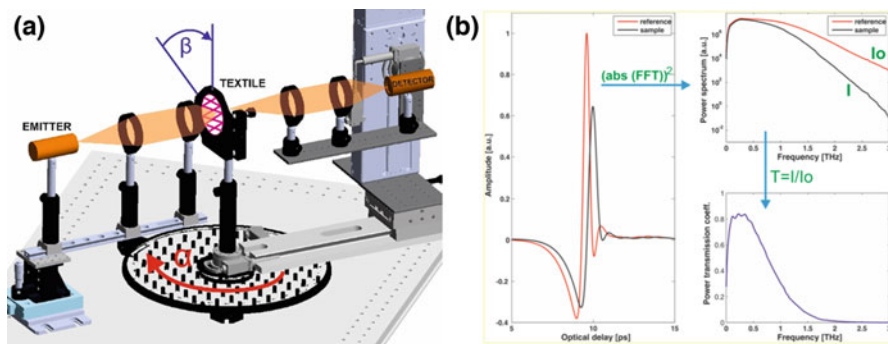
Fig. 10.8 The transmission configuration: the scheme of the optical setup (**a**) and the signal processing scheme (**b**)

registered (the one without the sample) and then the sample was placed in the holder and the transmitted pulse was recorded. When the reference and the sample signals were registered, their power spectrums were calculated (and were equal to the modulus of the Fourier transform of the registered pulse). At the end the power transmission coefficient was calculated ($T = I/I_0$) as a function of frequency. I and I_0 are power spectra of the reference and the sample pulses, respectively.

Figure 10.9 presents transmission results for sample 1 for various combinations of angles. It can be noticed, that the characteristics are quite similar, although usually for $\beta = 0°$ transmission coefficient is higher, what suggests that the textile is polarization sensitive.

10.6 Reflection Configuration – Setup, Methodology and Results

The optical setup used for the spectral characteristic's measurement in the reflection configuration is illustrated in Fig. 10.10a. The possibility to rotate the detector is provided due to the fibre connection between the emitter and the laser and between the detector and the laser. During our measurements the sample was rotated around the vertical axis, pulses were detected for different angles $\alpha = 0°$, 15°, 30°, and moreover the sample holder with the textile was rotated around the optical axis which resulted in different orientations of the fibres $\beta = 0°$, 45°, 90°.

The scheme of signal processing is illustrated in Fig. 10.10b. At first the pulse reflected from the mirror located in the place of the sample is registered (called reference). Then, the signal reflected from the sample is recorded (and named sample). The measured pulse has the beginning and the end different from zero which results in the difficulties in FFT calculation. Therefore, the signal was apodized using Blackmann-Harris third order filter. The power spectrum of the
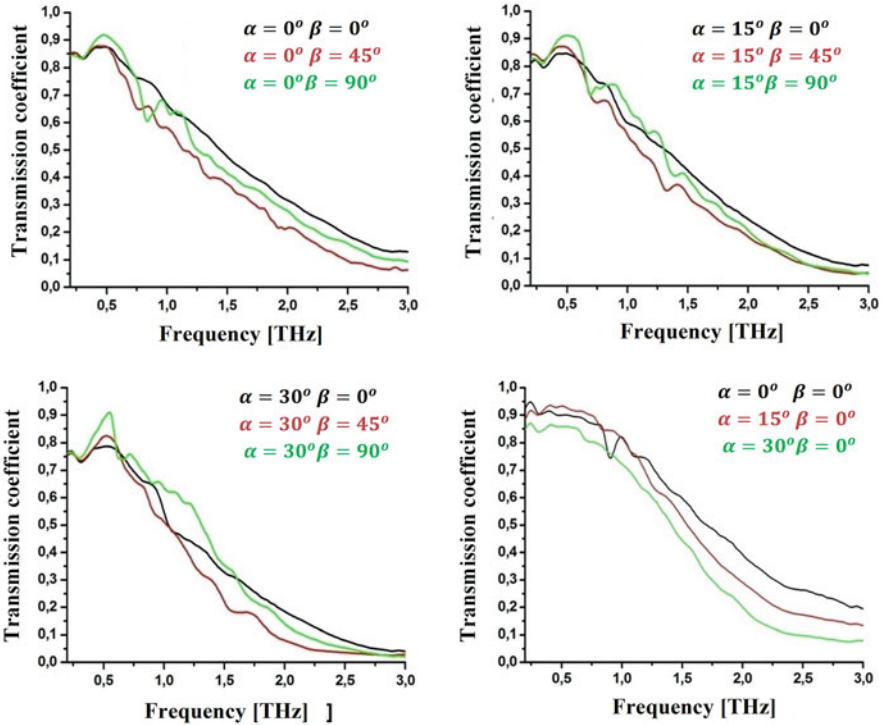
Fig. 10.9 Results of measurements in the transmission configuration for various combinations of angles

reflected pulse contains local minima which obstruct the proper determination of the reflection coefficient. Due to this fact the power spectrum was approximated with a carefully selected envelope and then the power reflection coefficient (R) as a function of frequency (f) can be calculated as the ratio of the power spectrum of the sample and the power spectrum of the reference.

Figure 10.11 shows the reflectance R as the function of frequency for three samples. The same angles were set for all samples in order to compare terahertz reflection under the same measurement conditions. For sample orientations $\beta = 0°$ and $90°$, the measurements indicate that the highest reflectance in the range of 0.1–0.7 THz shows sample 3 made of polyester, viscose, and spandex with the grammage of 166 g/m^2. The material with the lowest reflectance index is sample 2 made of polyester and cotton with the grammage of 270 g/m^2. The reflectance of each sample has similar values in both orientations. However, sample 3 shows significantly higher reflectance than the other two materials. It can results from its composition, because viscose is a shiny material, while lurex is the artificial fibre with a metallic appearance. Materials with such characteristics reflect terahertz signals quite well. For $\beta = 45°$ orientation, the order of the samples regarding the
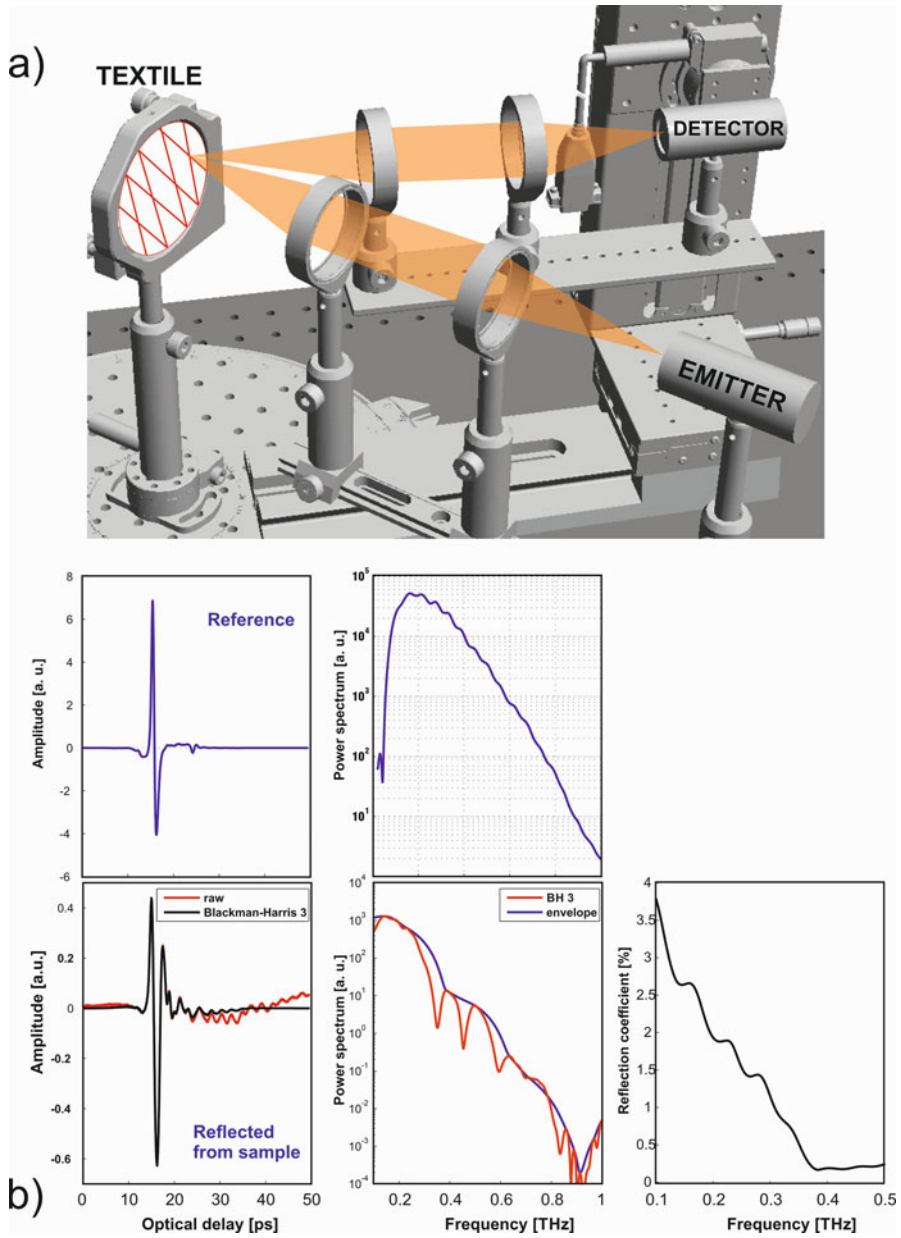
Fig. 10.10 The reflection configuration: the scheme of the optical setup (**a**) and signal processing (**b**)
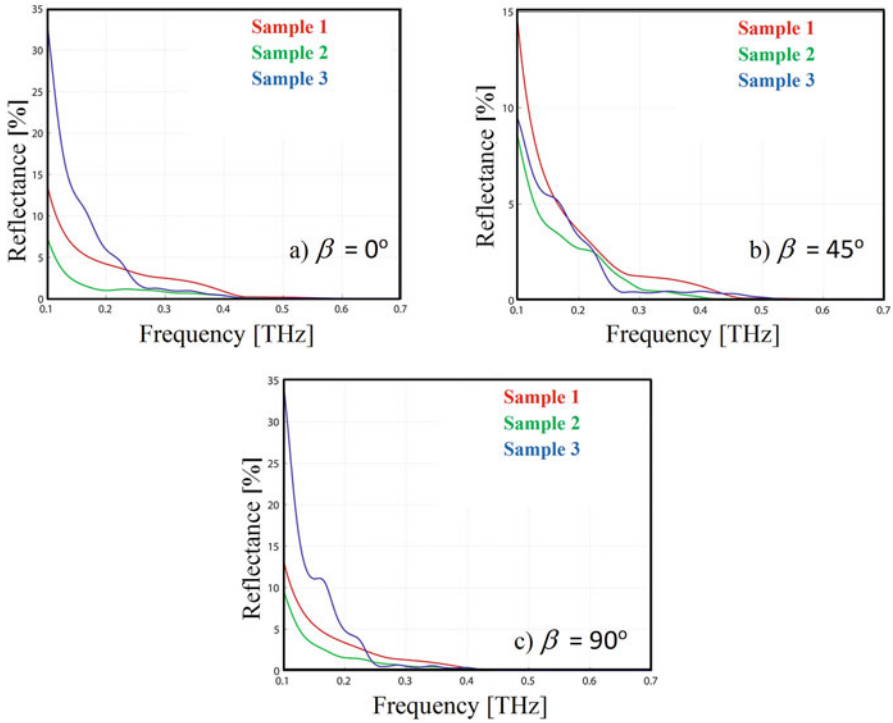
Fig. 10.11 Reflectance of the samples for $\beta = 0°$ (**a**) $\beta = 45°$ (**b**), and $\beta = 90°$ (**c**). The incidence angle equal to 20°

value of the reflectance has changed compared to previous fabric settings (Fig. 10.11b).

Analyzing the measurement results for sample 1, it has been noticed that the angle of incidence is important for the reflectance result. The larger the angle of incident the lower the reflection value, regardless of the orientation of the fabric. In addition, the reflectance values are comparable for all three settings (Fig. 10.12).

Before concluding we would like to mention that advanced materials [13, 14] and compact sources for the THz region such as quantum cascade lasers and superlattice multipliers [15–25] can lead to less expensive and portable systems, with potential for a large societal impact of our technology.
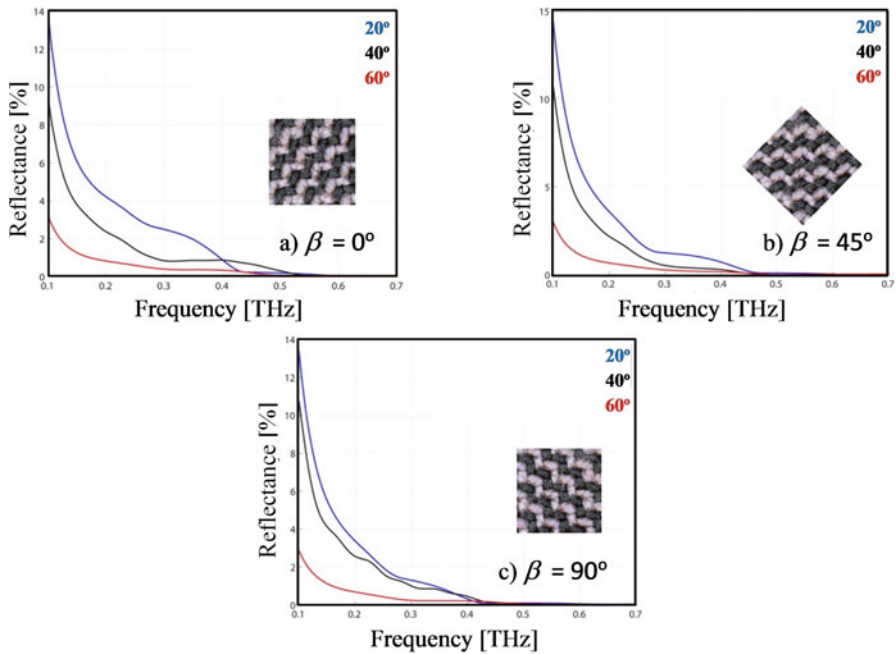
Fig. 10.12 Reflectance of the sample 1 for $\beta = 0°$ (**a**) $\beta = 45°$ (**b**), and $\beta = 90°$ (**c**). The incidence angle equal to 20°, 40°, and 60°

10.7 Summary

To sum up, we designed and built the TDS optical setup dedicated to the measurement of transmission and reflection characteristics of textiles. The dedicated sample holder with magnets was designed and manufactured to ensure uniform stretch of the textile in all directions. Three selected textiles were investigated. We have determined the measurement methodology allowing us to obtain the set of characteristics. For this reason we have proposed the signal processing, which provided calculation of the transmission and the reflection characteristics. In case of the transmission configuration we measured textile spectra for three different incident angles and three different orientations. For the reflection configuration we carried out measurements of the specular reflections. Such characteristics could be interesting for designers of active and passive terahertz body scanners as well as for general understanding of the interaction of the THz radiation with complicated structures like textiles.

References

1. Luukanen A, Appleby R, Kemp M, Salmon N (2012) Millimeter-wave and terahertz imaging in security applications. Springer Ser Opt Sci 171:491

2. Kemp MC (2008) Millimetre wave and terahertz technology for the detection of concealed threats – a review. In: 32nd International conference on infrared and millimeter waves and the 15th international conference on terahertz electronics, IEEE

3. Pałka N, Szustakowski M, Piszczek M, Kowalski M, Czerwinska E, Wróbel J (2014) THz and MMW body scanners – state of the art and own research. Electro-Technical Rev 90:1

4. Amenabar I, Lopez F, Mendikute A (2013) In introductory review to THz non-destructive testing of composite mater. J Infrared Millim Terahertz Waves 34:152

5. Palka N, Panowicz R, Ospald F, Beigang R (2015) 3D non-destructive imaging of punctures in polyethylene composite armor by THz time domain spectroscopy. J Infrared Millim Terahertz Waves 36:770

6. Kemp MC, Taday P, Cole BE, Cluff JA, Fitzgerald AJ, Tribe WR (2003) Security applications of terahertz technology. Proc SPIE 5070:168

7. Auston DH, Cheung KP (1985) Coherent time-domain far-infrared spectroscopy. J Opt Soc Am B 2:606

8. Knipper R, Brahm A, Heinz E, May T, Notni G, Meyer HG, Tünnermann A, Popp J (2015) THz absorption in fabric and its impact on body scanning for security application. IEEE Trans Terahertz Sci Technol 5:999

9. Bjarnason JE, Chan TLJ, Lee AWM, Celis MA, Brown ER (2004) Millimeter-wave, terahertz, and mid-infrared transmission through common clothing. Appl Phys Lett 85:519

10. Kowalski M, Kastek M, Palka N, Polakowski H, Szustakowski M, Piszczek M (2013) Investigations of concealed objects detection in visible, infrared and terahertz ranges. Photonics Lett Pol 5:167

11. Molloy J, Naftaly M (2014) Wool textile identification by terahertz spectroscopy. J Text Inst 105:794

12. https://www.menlosystems.com/

13. Oriaku CI, Pereira MF (2017) Analytical solutions for semiconductor luminescence including Coulomb correla-tions with applications to dilute bismides. J Opt Soc Am B 34:321

14. Pereira MF (2018) Analytical expressions for numerical characterization of semiconductors per comparison with luminescence. Materials 11:2

15. Pereira MF (2016) The linewidth enhancement factor of intersubband lasers: from a two-level limit to gain with-out in-version conditions. Appl Phys Lett 109:222102

16. Pereira MF, Zubelli PJ, Winge D, E J, Wacker A, Rondrigues SA, Anfertvev V, Vaks V (2017) Theory and measurements of harmonic generation in semiconductor superlattices with applications in the 100 GHz to 1 THz range. Phys Rev B 96:045306

17. Pereira MF, Anfertev V, Zubelli JP, Vaks V (2017) Terahertz generation by gigahertz multiplication in su-perlattices. J Nanophoton 11(4):046022

18. Apostolakis A, Pereira MF (2019) Controlling the harmonic conversion efficiency in semiconductor superlattices by interface roughness design. AIP Adv 9:015022

19. Apostolakis A, Pereira MF (2019) Numerical studies of superlattice multipliers performance. Quantum Sensing and Nano Electronics and Photonics XVI:109262

20. Apostolakis A, Pereira MF (2019) Potential and limits of superlattice multipliers coupled to different input power sources. J Nanophotonics 13:036017

21. Winge DO, Franckié M, Verdozzi C, Wacker A (2016) Simple electron-electron scattering in non-equilibrium Green's function simulations. J Phys Conf Ser 696:012013

22. Pereira MF, Shulika O (2014) Terahertz and mid infrared radiation: detection of explosives and CBRN (using te-rahertz). NATO science for peace and security series-B: physics and biophysics. Springer, Dordrecht

23. Pereira MF, Shulika O (2011) Terahertz and mid infrared radiation: generation, detection and applications, NATO science for peace and security series-B: physics and biophysics. Springer, Dordrecht
24. Apostolakis A, Pereira MF (2020) Superlattice nonlinearities for Gigahertz-Terahertz generation in harmonic multipliers. Nano 9(12):3941–3952. https://doi.org/10.1515/nanoph-2020-0155
25. Pereira MF, Anfertev V, Shevchenko Y, Vaks V (2020) Giant controllable gigahertz to terahertz nonlinearities in superlattices. Sci Rep 10:15950

Chapter 11
Transition Between Localized and Delocalized Terahertz Conductivity in Modulated Nanostructures Studied by Monte-Carlo Calculations

Hynek Němec and Petr Kužel

Abstract Monte-Carlo calculations are employed for the investigation of the terahertz response of degenerate electron gas in a potential modulated on nanometer distances. There is a continuous transition from the Drude response to an oscillator-like response as the Fermi energy becomes smaller than the modulation depth.

Terahertz conductivity spectra encode information about the charge transport on nanometre distances. Broadband measurements of the terahertz conductivity using e.g. time-domain terahertz spectroscopy is thus a powerful approach for gaining insight into mechanisms and parameters of the charge transport inside semiconductor nanoparticles as well as for investigating interactions of charges with the nanoparticles boundary and inter-nanoparticle charge transport [1–3]. In order to fully exploit this information, it is important to have simple theoretical models at hand, ready for basic microscopic interpretation of the experimental THz conductivity spectra. Despite the efforts in the past decade, toy models of the terahertz conductivity σ (or mobility μ; $\sigma = e_0 N \mu$, where N is the carrier density) in many simple situations are still lacking. In this chapter, we recall the available simple theoretical models, and we present a new model describing the response of degenerate carrier gas in a potential modulated on the nanoscale.

The response of free charges in most bulk semiconductors follows the Drude mobility spectrum (Fig. 11.1a)

H. Němec (✉) · P. Kužel (✉)
FZU – Institute of Physics of the Czech Academy of Sciences, Prague, Czech Republic
e-mail: nemec@fzu.cz; kuzelp@fzu.cz
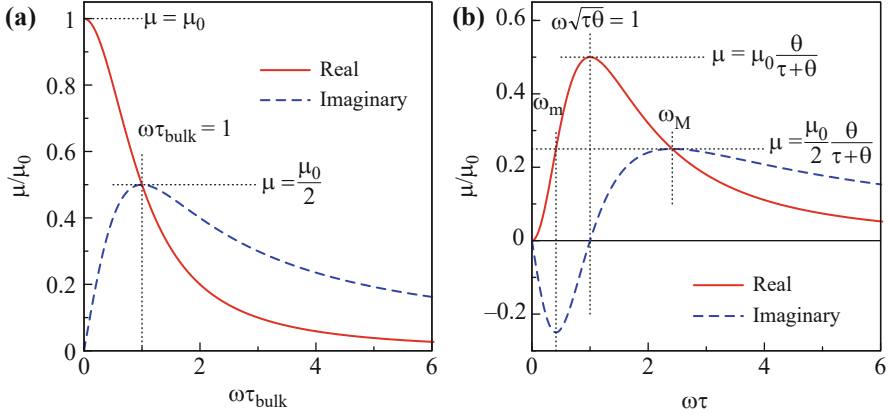
Fig. 11.1 (**a**) Drude conductivity described by Eq. (11.1). (**b**) Example of the mobility spectrum described by the modified Drude-Smith model [12] given by Eq. (11.2). Important points are marked directly in the graphs; extrema in the imaginary part occur at frequencies $\omega_{\mathrm{m}} = \frac{\sqrt{\tau^2 + \theta^2 + 6\tau\theta} - \tau - \theta}{2\tau\theta}$ and $\omega_{\mathrm{M}} = \frac{\sqrt{\tau^2 + \theta^2 + 6\tau\theta} + \tau + \theta}{2\tau\theta}$. For τ considerably different from θ, these expressions simplify to $\omega_{\mathrm{m}} = 3/[2 \max(\tau, \theta)]$ and $\omega_{\mathrm{M}} = 1/\min(\tau, \theta)$

$$\mu(\omega) = \frac{e_0 \tau_{\mathrm{bulk}}}{m_{\mathrm{eff}}} \cdot \frac{1}{1 - i\omega\tau_{\mathrm{bulk}}} \equiv \frac{\mu_0}{1 - i\omega\tau_{\mathrm{bulk}}} \qquad (11.1)$$

This is an inductive-type response characterized by the real part decreasing with frequency as a result of inertial mass m_{eff} of the charges. Due to the absence of any restoring force, the mobility peaks at zero frequency; the peak width is related to the charge scattering time τ_{bulk} (Fig. 11.1a).

The response of charges confined in isolated semiconductor nanoparticles is qualitatively different. A restoring force preventing the escape of charges from the nanoparticle exists at least close to the surface; this force is responsible for the resonant-like character of the conductivity spectrum with non-zero eigenfrequency (an illustration is shown in Fig. 11.1b). The dc conductivity must vanish since no permanent current can flow through an isolated nanoparticle. While these qualitative characteristics are rather obvious, the exact nature of the conductivity spectra of confined charges has been debated for a long time (e.g [4–6].). The analysis of the conductivity spectra is complicated by the fact that the measured (effective) conductivities differ from the local conductivities due to the influence of depolarization fields, which inevitably emerge in any inhomogeneous structure [2, 7–9]. In the rest of this text, we will discuss just the response of charges to the local probing electric field, keeping in mind that an appropriate effective medium approximation is needed [9, 10] to obtain results (effective conductivities) directly comparable with the output of experiments.

One of the first microscopic models of the terahertz conductivity spectra of non-degenerate electron gas was based on a combination of the Kubo formula and

Monte-Carlo calculations [11]. Although these calculations are time consuming due to the requirement of calculating a large number of trajectories representing the thermal motion, their advantage is the possibility to describe arbitrarily shaped nanoparticles.

Later on, an analytical formula describing the response of non-degenerate spherical nanoparticles was developed by Cocker et al. [12]. The functional form for isolated nanoparticles

$$\mu(\omega) = \frac{\mu_0}{1 - i\omega\tau} \left[1 - \frac{1}{1 - i\omega\theta} \right] \equiv \frac{-i\omega\theta\mu_0}{(1 - i\omega\tau)(1 - i\omega\theta)} \tag{11.2}$$

strongly resembles to the phenomenological Drude-Smith model [13]. Unlike in the Drude-Smith model, the characteristic time in the second term (marked as θ) is now different from τ and has its origin in the diffusion; it reads $\theta = t_\circ(t_\circ + 2\tau_{\text{bulk}})/(12\tau_{\text{bulk}})$ where t_o is the time that a charge needs to traverse the nanoparticle with the thermal velocity. In this way, the nanoparticle size explicitly appears in this modified Drude-Smith model. The second characteristic time $\tau = \left(\tau_{\text{bulk}}^{-1} + 2t_\circ^{-1} \right)^{-1}$ predominantly describes the effective scattering, which becomes enhanced with the decreasing nanoparticle size. It is interesting to note that for isolated nanoparticles, the shape of the mobility spectrum (not its amplitude) is invariant with respect to the interchange of the characteristic times τ and θ. This means that further information is needed to correctly assign the characteristic times measured in the experiments.

Finally, quantum calculations based on the Kubo formula were developed recently [14]. The relaxation time approximation commonly employed in the optical spectral range is not valid in the THz region. Due to the broken translation symmetry on the nanoscale, the THz field induces a redistribution of the carrier concentration inside nanoparticles, while the relaxation time approximation in the Kubo formula inherently (erroneously) assumes that a charge scattering event leads to an instantaneous relaxation of this inhomogeneous charge density towards equilibrium. However, the charge density is restored via a finite-time thermalization current, which was evaluated in Ref. [14], thus providing a physically sound model of THz conductivity spectra. It was also confirmed that the modified Drude-Smith formula (11.2) is a semi-classical limit of these quantum-mechanical calculations [15].

Nanostructures like artificial graphene are not composed of isolated nanoparticles; instead, they are characterized by a modulation of the potential on the nanoscale [16]. For shallow modulation depths, these nanostructures permit an efficient dc charge transport, but they also keep certain signatures of the restoring force close to the potential minima [17].

Here we investigate in detail the response of degenerate electron gas in a potential with harmonic modulation $V(x, y, z) = \Delta V \cdot [1 + \sin(2\pi x/L)]$ (Fig. 11.2a). We employ Monte-Carlo calculations [11] generalized for the case of Fermi-Dirac statistics. By calculating the probability density distribution (Fig. 11.2b), we confirm that for Fermi energy much lower than the modulation depth, charges remain in the potential
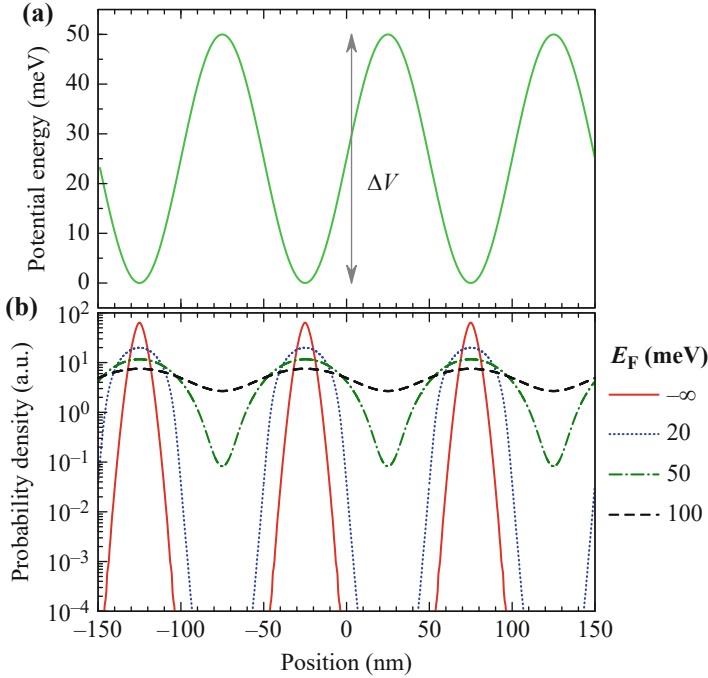
Fig. 11.2 (**a**) Scheme of the spatially modulated potential. (**b**) Distribution of the carrier density for various Fermi energy levels (measured from the bottom of the potential). Parameters of calculations: effective mass $m_{eff} = 0.067m_e$, bulk scattering time $\tau_{bulk} = 2$ ps and temperature $T = 20$ K (1.7 meV)

valleys for most of the time and only occasionally they jump between the valleys; conversely, for elevated Fermi energies, the charges move almost freely.

Using this simple picture, we can understand also the calculated mobility spectra (Fig. 11.3). For non-degenerate electron gas ($E_F \rightarrow -\infty$ and $\Delta V \ll k_B T$), charges move only close to the potential minima, their motion is thus harmonic and the response is equivalent to that of an oscillator with its linewidth determined by the bulk scattering time. As the Fermi energy increases, this resonance broadens and redshifts. This indicates that the displacement of charges increases, and they start to feel the anharmonicity of the potential. For even higher Fermi energy, the motion over the ridge becomes frequent and a Drude peak (resonance at zero frequency) emerges. For the highest Fermi energies, the modulation of the potential loses its importance and only the Drude peak persists with the linewidth determined by the bulk scattering time. The amplitude of the Drude response for $E_F = +\infty$ is the same as that of the oscillator response for $E_F = -\infty$ due to the conservation of the spectral weight.

The dependence of the mobility at a particular frequency on the Fermi energy is more complex (Fig. 11.4). The dc mobility correlates with the static picture

Fig. 11.3 Mobility spectra of charges moving in the modulated potential. The parameters of the calculation are the same as in Fig. 11.2
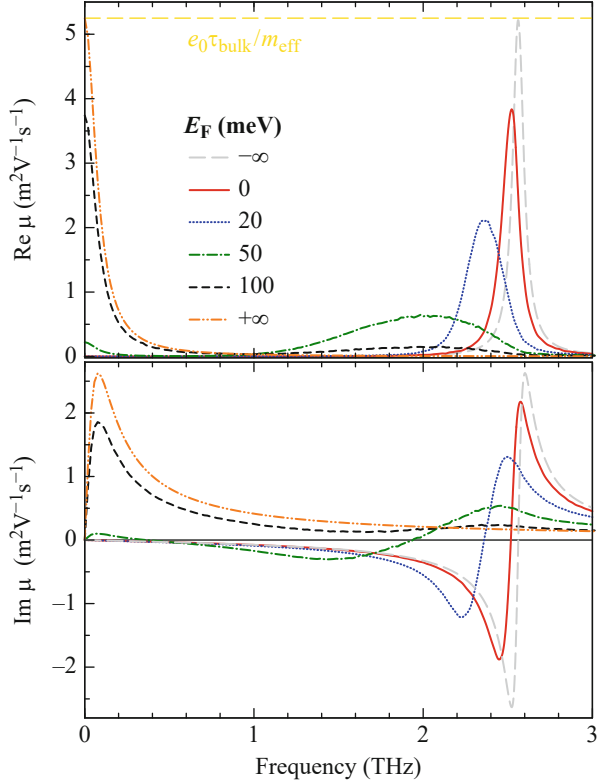
Fig. 11.4 Real part of the mobility of charges moving in the modulated potential as a function of the Fermi energy, calculated with the same parameters as in Fig. 11.2. Blue solid line: illustration of Eq. (11.3)
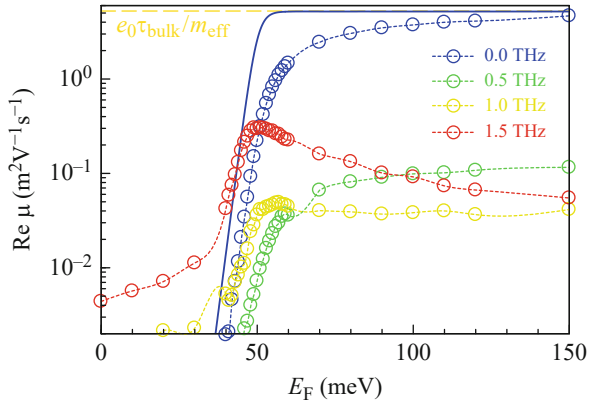
described by the Fermi-Dirac function; the mobility can be qualitatively approximated by the formula

$$\mu(E_{\mathrm{F}}) = \frac{e_0 \tau_{\mathrm{bulk}}}{m_{\mathrm{eff}}} \cdot \frac{1}{1 + \exp\left[-\frac{E - \frac{\Delta V}{2}}{k_{\mathrm{B}} T}\right]} \qquad (11.3)$$

For higher frequencies, the effect of the carrier confinement is less severe and the transition becomes considerably smeared, as illustrated e.g. by the 1.5 THz curve in Fig. 11.4. This is an important message for the interpretation of THz experimental data: higher frequencies are less sensitive to the charge localization; in turn, the dependence on the chemical potential as well as Arrhenius plots of ac mobility versus temperature become distorted compared to the dc mobility.

In summary, we employed Monte-Carlo calculations to investigate the transition between the localized and delocalized response of an electron gas in a model modulation potential. The spectral weight of the conductivity is transferred between the oscillator and Drude peak as the Fermi energy passes over the height of the modulation of the potential. While Fermi-Dirac formula at least qualitatively reproduces the dc conductivity, this transition is smeared for higher frequencies. An evidence of the transition between more and less localized state has been observed for example in CdS nanocrystals [18].

References

1. Ulbricht R, Hendry E, Shan J, Heinz TF, Bonn M (2011) Carrier dynamics in semiconductors studied with time-resolved terahertz spectroscopy. Rev Mod Phys 83:543
2. Lloyd-Hughes J, Jeon T-I (2012) A review of the terahertz conductivity of bulk and nano-materials. Int J Infrared Millimeter Waves 33:871
3. Kužel P, Němec H (2019) Terahertz spectroscopy of nanomaterials: a close look at charge-carrier transport. Adv Opt Mater 7:1900623
4. Beard MC, Turner GM, Schmuttenmaer CA (2002) Size-dependent photoconductivity in CdSe nanoparticles as measured by time-resolved terahertz spectroscopy. Nano Lett 2:983
5. Cooke DG, Meldrum A, Jepsen PU (2012) Ultrabroadband terahertz conductivity of Si nano-crystal films. Appl Phys Lett 101(21):211107–211104
6. Joyce HJ, Boland JL, Davies CL, Baig SA, Johnston MB (2016) A review of the electrical properties of semiconductor nanowires: insights gained from terahertz conductivity spectroscopy. Semicond Sci Technol 31(10):103003–103021
7. Nienhuys H-K, Sundström V (2005) Influence of plasmons on terahertz conductivity measurements. Appl Phys Lett 87:012101
8. Hendry E, Koeberg M, O'Regan B, Bonn M (2006) Local field effects on electron transport in nanostructured TiO_2 revealed by terahertz spectroscopy. Nano Lett 6:755
9. Němec H, Zajac V, Rychetský I, Fattakhova-Rohlfing D, Mandlmeier B, Bein T, Mics Z, Kužel P (2013) Charge transport in TiO_2 films with complex percolation pathways investigated by time-resolved terahertz spectroscopy. IEEE Trans THz Sci Technol 3:302
10. Kužel P, Němec H (2014) Terahertz conductivity in nanoscaled systems: effective medium theory aspects. J Phys D Appl Phys 47:374005
11. Němec H, Kužel P, Sundström V (2009) Far-infrared response of free charge carriers localized in semiconductor nanoparticles. Phys Rev B 79:115309

12. Cocker TL, Baillie D, Buruma M, Titova LV, Sydora RD, Marsiglio F, Hegmann FA (2017) Microscopic origin of the Drude-Smith model. Phys Rev B 96:205439
13. Smith NV (2001) Classical generalization of the Drude formula for the optical conductivity. Phys Rev B 64:155106
14. Ostatnický T, Pushkarev V, Němec H, Kužel P (2018) Quantum theory of terahertz conductivity of semiconductor nanostructures. Phys Rev B 97:085426
15. Ostatnický T (2019) Linear THz conductivity of nanocrystals. Opt Express 27:6083
16. Nádvorník L, Orlita M, Goncharuk NA, Smrčka L, Novák V, Jurka V, Hruška K, Výborný Z, Wasilewski ZR, Potemski M, Výborný K (2012) From laterally modulated two-dimensional electron gas towards artificial graphene. New J Phys 14:053002
17. Mrozek J, Němec H (2012) Calculation of terahertz conductivity spectra in semiconductors with nanoscale modulation. Phys Rev B 86:075308
18. Mics Z, Němec H, Rychetský I, Kužel P, Formánek P, Malý P, Němec P (2011) Charge transport and localization in nanocrystalline CdS films: a time-resolved terahertz spectroscopy study. Phys Rev B 83:155326

Chapter 12
THz Sources and Detectors Fabricated from High Temperature Superconductors

Yasemin Demirhan, Fulya Turkoglu, Hakan Altan, Cumali Sabah, and Lutfi Ozyuzer

Abstract High temperature superconductors have unique properties that can be useful in the THz region, single crystal constituted from superconducting CuO_2-layers could sustain high voltages across the junctions and they are coupled through the intrinsic Josephson Effect this maintains the potential for very intense, coherent radiation which spreads over the THz gap. We investigated various experimental techniques to fabricate THz sources, bolometers and filters for efficient THz emission and detection. Rectangular mesa structures were fabricated on $Bi_2Sr_2CaCu_2O_{8-x}$ (Bi2212) single crystal superconductors using standard e-beam lithography and Ar ion beam etching systems and an emitted power as high as 60 μW at frequencies up to 0.85 THz was detected from micron sized continuous wave terahertz sources. We also fabricated bolometric microchips for THz detection purpose from Bi2212 single crystals. Bi2212 microchips detected the signals and response time were calculated, our results have clearly shown that Bi2212 single crystals are potential candidates for THz detection. The detection properties and sensitivity of bolometer chips can be further improved by integrating an antenna and filter structures. In order to investigate this we have fabricated metamaterial THz filters based on metals and $YBa_2Cu_3O_x$ superconducting thin films with metal-mesh shape and a unique fourcross shape pattern. Both a THz time domain spectrometer and a Fourier transform infrared spectrometer (FTIR) were used to investigate the performance

Y. Demirhan · F. Turkoglu · L. Ozyuzer (✉)
Department of Physics, Izmir Institute of Technology, Izmir, Turkey
e-mail: yasemindemirhan@iyte.edu.tr; fulyaturkoglu@iyte.edu.tr; lutfiozyuzer@iyte.edu.tr

H. Altan
Department of Physics, Middle East Technical University, Ankara, Turkey
e-mail: hakan.altan@metu.edu.tr

C. Sabah
Department of Electrical and Electronics Engineering, Middle East Technical University – Northern Cyprus Campus, Güzelyurt, Turkey
e-mail: sabah@metu.edu.tr

of these filters and the results were compared with simulations done with a commercially available electromagnetic simulation software.

12.1 Introduction

Terahertz (THz) radiation lies between microwaves and the infrared regions of the electromagnetic spectrum. Terahertz (THz) radiation region spreads over frequencies extending from 0.3 to 10 THz and wavelengths in the range 1–0.03 mm. The development of compact THz detection systems operating in the aforementioned frequency range that can remotely sense the presence of explosive materials, poisonous gases, ceramic weapons, and biological warfare agents is a priority for military and defense organizations [1–4]. Moreover, using non-invasive approaches it has been demonstrated that THz waves can be utilized to determine the existence of certain types of skin diseases proving that investigations based on THz waves are becoming a more significant research area than ever before [5]. These studies combined with a diverse range of applications from pharmaceuticals to agricultural investigations are driving the requirements to improve compact and tunable coherent THz devices. Due to the difficulty for materials to interact, generate or detect radiation due to weak electromagnetic response in the region from 0.1 to 10 THz, this frequency range is customarily called the THz gap. In this gap spectrum, remarkable efforts have taken place with the purpose of filling this vacancy [6–9]. Development of an efficient THz source will bring about an advantage to many fields such as imaging, spectroscopy, information technology, and medical diagnosis. Exploration of coherent THz emission from stacks of intrinsic Josephson junctions (IJJs) fabricated by using the high temperature superconductor $Bi_2Sr_2CaCu_2O_8$ (Bi2212) has come to the fore as a fundamental research area in recent years as evidenced by experimental as well as theoretical studies [10–12]. A superconducting a.c. current will pass through the Josephson frequency after the utilization of a dc voltage across a Josephson junction. The strong emission of electromagnetic waves from a mesa of Bi2212 crystal without an applied external magnetic field has been successfully observed [13, 14], where the mesa shaped THz device with sizable power operates as a dc voltage to high frequency converter.

As with sources, bolometric detection in the submillimeter or terahertz range can be efficiently done using superconducting Hot Electron Bolometers (HEBs). In such a device two thick metal pads which are attached by a small superconducting microbridge. A small variation in temperature or absorbed power is detected by maintaining HEBs in the transition state from a superconductor to normal metal at which a great change in resistance is achieved which is a consequence of the creation of "hot electrons" on the bridge. Responsivity, response time and simplicity of operation are some of the most important specifications for a detector and is such that superconducting bolometers have a smaller response time compared with other bolometer detectors. In order to develop HEB from superconducting materials numerous studies have been performed. Amongst them, with the purpose of

fabricating bolometric detectors with smaller response times, Nb and NbN superconducting thin film is generally favoured [15]. While these devices are highly sensitive the drawback lies in their operational cost due to their necessity for low temperature cryogenic cooling. By utilizing high temperature superconductor $YBa_2Cu_3O_{7-x}$ (YBCO) thin film for the fabrication of the bolometer, Hammar et al. obtained response times almost at the range of picoseconds [16]. These technologies can be tailored for specific frequency bands with the use of metamaterial MM) structures.

In its most fundamental configuration, the metamaterial structure can be considered as electrical circuits much smaller in size than the wavelength, thus these structures are substitutes for atoms as the basic unit of interaction with electromagnetic radiation. This research area has witnessed a great progress in the recent past [17, 18] where studies have achieved the development of electromagnetic MMs which show novel specifications namely magnetic response at terahertz and optical frequencies, negative index of refraction, and huge chirality [19, 20]. In the production of conventional THz MMs either dielectrics or normal conducting metals are utilized. Although sub-wavelength structures established on these conventional materials have exhibited low insertion loss at microwave frequencies substantial losses displayed in the terahertz frequency range have been one of the vital limitations, and this stands as a driving force to explore novel structures based on novel materials to minimize losses. In opposition to normal conducting metals, electromagnetic properties embraced by superconductors can be employed for the purpose of fabricating almost ideal and novel metamaterial structures. For the purpose of greatly reducing losses, metallic structures are replaced by superconducting structures [21]. In these materials, values of the surface resistance at microwave frequencies are also small [22]. The nonlinear THz transmission through films composed of the high-T_c superconductor $YBa_2Cu_3O_7$ (YBCO) has already been measured [23]. In our investigations, design and fabrication of superconducting metamaterial filters possessing a unique geometry which operates in the THz frequency band has been achieved [24, 25]. In the patterning of the structures, normal conductive metallic films as well as High T_c superconductor YBCO thin films were utilized. It is demonstrated that both the resonance frequency and transmittance at resonance of the metamaterial structure can be adjusted by altering the geometrical parameters of the structure and superconducting properties which depend on temperature. These properties supply the conditions to produce very effective and compact metamaterial-based filters with a high selectivity. Extremely specific filters of these types can be employed to eliminate unacceptable transmitted signals in pre-defined frequency bands and have potential utilizations in the field of THz diagnostics.

12.2 Terahertz Sources

Numerous shapes of Bi2212 resonators are employed in THz emission investigations of superconducting mesas. Using e-beam lithography and ion beam etching techniques resonators having nearly rectangular shape are patterned onto Bi2212 crystals. Characteristic dimensions of the resonators are approximately 1–2 mm in height (corresponding to roughly 1000 IJJs), with a width of approximately 40–100 μm and certain hundreds of micrometers in length. Our earlier investigations demonstrate that, it is achievable to synchronize more than N = 650 junctions to oscillate in phase, which in turn produces continuous and coherent radiation with power up to 60 μW at emission frequencies in the region 0.36–0.85 THz and this is inversely proportional to the mesa width from 100 to 40 μm. In Fig. 12.1a, b THz emission characteristics and current–voltage (*I–V*) characteristics of the mesa with $55 \times 300 \ \mu m^2$ at $T = 22$ K are presented. In the case where spin polarized current is injected through the *c*-axis of the as-grown mesa, it is observed from the *I–V* data that the magnitude of Josephson critical current is 18 mA. Due to injection of spin polarized current, J_c i.e. the Josephson critical current density has the value of 120 A/cm^2 at 22 K and when compared to as-grown Bi2212 crystals it is 2–3 times smaller and associated with other THz emitting mesas.

In our former studies we have established decrement in J_c depending on the spin injection where we have compared spin degenerate and spin polarized cases. The bolometer determines the heating of the mesa in the pattern of unpolarized black

Fig. 12.1 *I–V* (**a**) and bolometer (**b**) measurements of mesa at 22 K
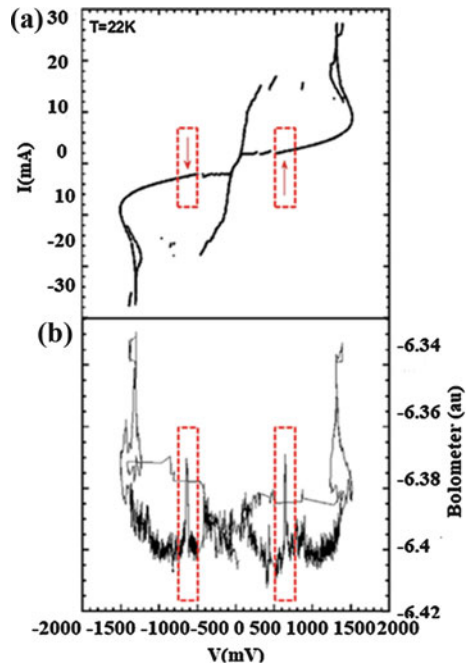
Fig. 12.2 (**a**) R-T measurements of 300–50 µm², 200–50 µm², 100–50 µm² triple mesa structures on the same crystal 100 µm apart from each other. (**b**) I–V Characteristics of 300–50 µm², 200–50 µm², 100–50 µm² triple mesa structures on same crystal at 20 K
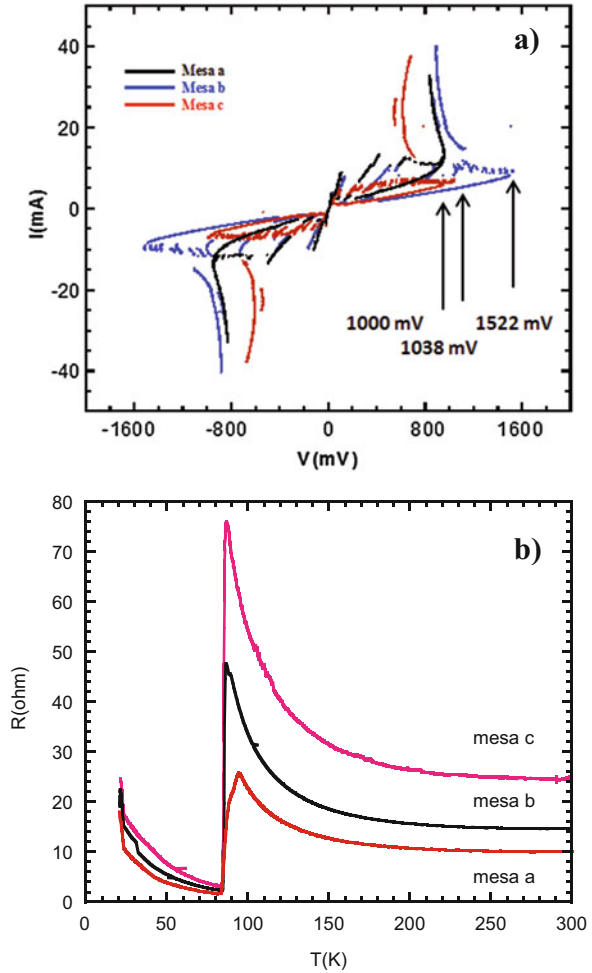
body radiation in the case of backbending observed in the *I–V* curve at high bias voltages. There is a straightforward relation between heating and the power generated in mesa structures. The voltage is proportional to the number of IJJs in the stack where as The current is proportional to the junction area. Therefore, for the purpose of decreasing the amount of heating, it is useful to decrease either of these parameters to an appropriate doping level. R-T and I-V measurement data of triple mesa sample, which is annealed at 450 °C for 4 h are displayed in Fig. 12.2a, b. In our experimental studies we have demonstrated that the superconducting properties as well as the critical supercurrent density of an intrinsic junction stack can be altered by the annealing procedure. The areas of mesa a, mesa b and mesa c structures are recpectively, 300–50 µm², 200–50 µm², 100–50 µm². It has been shown that THz emitting meshes are below a certain doped level with a relatively small critical current, unlike the best folded and over-folded Bi2212. Large area mesas produced

using under-doped crystals give rise to less heating due to the small critical current and afterwards the cavity resonance in the voltage scale backbending is observed. Hence, it is feasible to achieve powerful THz radiation in advance of serious effect of heating on the local mesa temperature. In particular, the mesa having an area of 100–50 μm^2 indicates many quasiparticle branches in Fig. 12.2b. It is observed that the critical currents of the produced mesa a, mesa b and mesa c are 10.03, 8.05 and 5.03 mA, respectively.

12.3   Terahertz Detectors

For the detection of THz waves we have developed a microbolometer chip made from high temperature superconducting $Bi_2Sr_2CaCu_2O_{8+\delta}$ (Bi2212) single crystals. In the fabrication process of the microbolometer chips, Bi2212 single crystals were transferred on substrate as thin films and electron beam lithography, ion beam etching techniques were realized. Resistance versus temperature behavior of the bolometer chips were investigated by the four probe technique in liquid nitrogen cryostat. Bi2212 microchips were characterized using our specially designed cryogenic bolometer system. The microchips detected signals at a significant level from the Stefan-Boltzmann lamp which contains a portion of THz radiation. The detected power and response time were investigated for Bi2212 thin film like microbolometer chips. A logperiodic antenna structure designed and simulated for the microbolemeters (Figs. 12.3 and 12.4).

Fig. 12.3 SEM image of Log Periodic Antenna
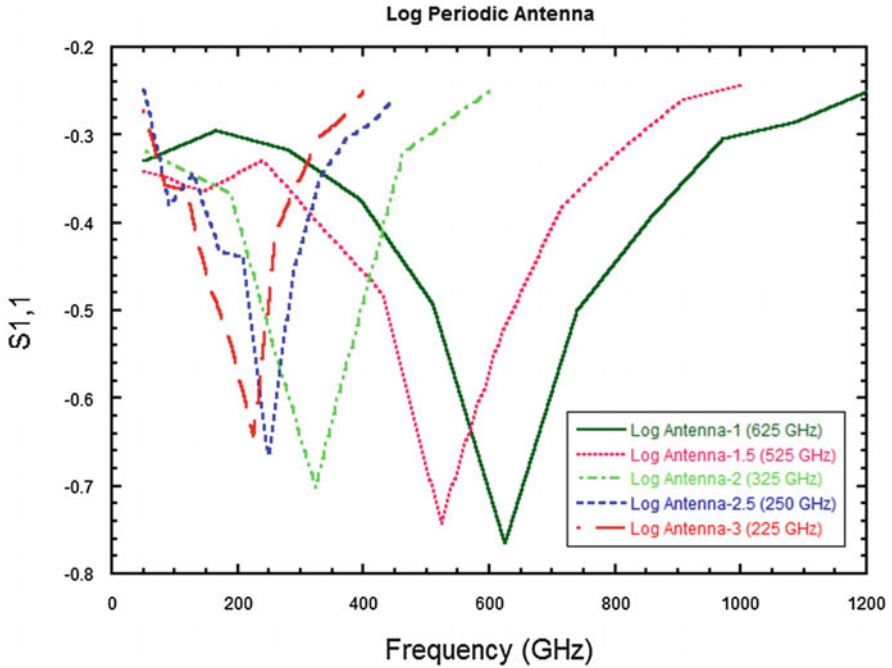
Fig. 12.4 CST simulation result of Log periodic Antenna

To investigate the micro-bridge response to the incoming optical power, we have carried out the bolometric measurements by adjusting the power to 20, 30, 40, 50 W during a 30 s constant time period. When correctly oriented, a linear relationship was observed between the measurements of Stephan Boltzmann lamp intensity and the final response resistance of the microchips during the measurements, as shown in Fig. 12.5. It was shown that the final response resistance of the microchips is increased via increasing power of the signal from the source.

After bolometric measurements are performed with increasing power level, the power value which gives almost zero resistance can be identified. If we curve fit the "change of resistance with different signal power" graph, we observed that the power of 1.95 Watt gives the zero resistance value as shown in Fig. 12.6. It implies that the designed bolometric detector has sensitivity until the 1.95 Watt power level. Above this power level, detector can show only slight resistance change in return signals which is negligible and microchips are no longer appropriate for bolometric detection.
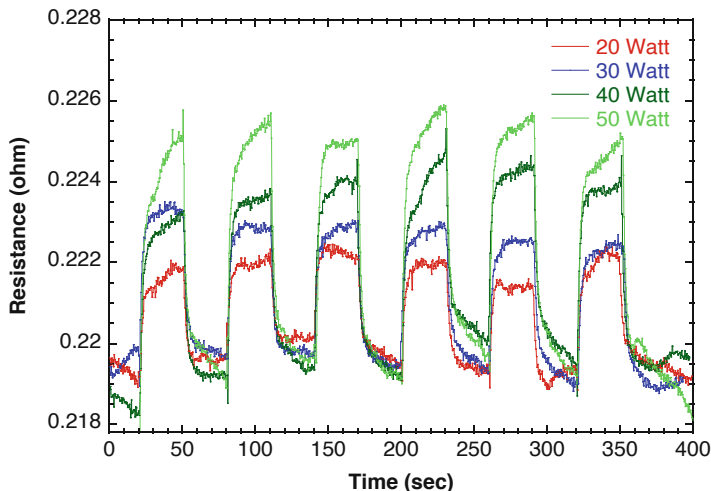
Fig. 12.5 Change of the microbridge resistance with different signal power

Fig. 12.6 Curve fit graph of resistance-power measurement
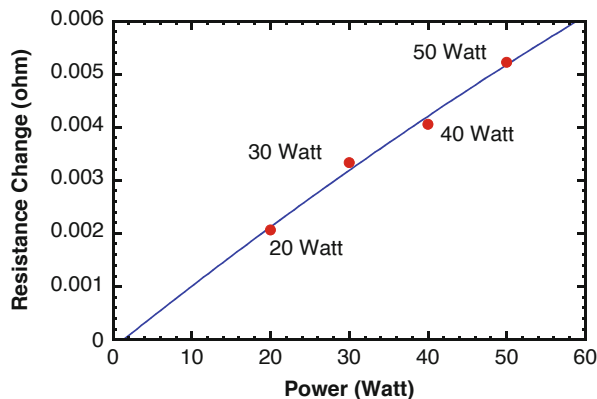
12.4 THz Filters

A unique and new fourcross shaped metamaterial Terahertz (THz) filter fabricated using two thin films namely, gold thin films and YBa2Cu3O7-d high Tc superconducting thin films is also investigated. In order to design and optimize the metamaterial filter structures we utilized a commercially available electromagnetic simulation software, CST Microwave Studio. Fourcross shaped rectangular filter structure that was used here is comprised of periodic metallic rings in which strip lines are placed at the sides of the ring (Fig. 12.7).

Simulations are performed for a 130 nm thick patterned gold layer and 80 nm thick patterned YBCO layer deposited on 900 μm thick fused silica and 500 μm thick sapphire substrates respectively. Utilizing e-beam lithography and ion beam etching
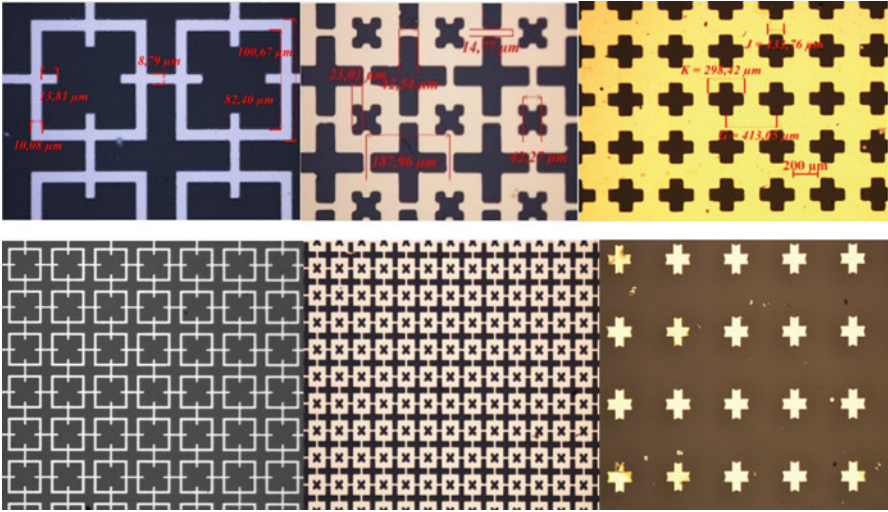
Fig. 12.7   THz filters designed in different geometries

techniques, fourcross metamaterial filters are fabricated. For the simulations, the electrical permittivity values are extracted by THz-TDS measurements of the fused silica and sapphire substrates in the THz region. The design predictions for the center frequencies and bandwidths of the resonances due to the fourcross structures are formalized by the measurements of terahertz time-domain spectroscopy. Lowering the temperature below the critical transition temperature it was possible to investigate the resonance switching of the transmission spectra. When the filters are produced from metals this resonance switching effect was not observed.

Figure 12.8a gives the measured transmission spectra for two different metamaterial filters given together with the numerical results on the same plot ((Au)01 and (Au)02). The experimental measurements of the metamaterials are compatible with that of the simulation results. Resonance frequency of this structure is at 0.92 THz in accordance with the simulation results. It is clearly seen from the figure that sample 1 has a resonance at 0.9 THz, sample 2 has a resonance at 0.92 THz with respect to the THz-TDS measurement. The metamaterial structure comprising from rectangular resonator displays bandstop characteristics. In Fig. 12.8b THz transmission measurement together with the simulation result of YBCO fourcross filter at 20 K, which is much lower than T_c, are presented on the same plotted graph. In comparison to other temperatures, the metamaterial filter reveals a strong resonance ν_1 at 20 K. After an increase in temperature and when reaching towards T_c, a redshift of the resonance frequency ν_1 (7%) is observed. The THz transmission amplitude of the band stop filters varies from 26% at 20 K to 53% at 90 K, displaying about a 51% change in the amplitude for the ν_1 resonance. In a recent work, it is verified that when the metamaterials are produced from thinner
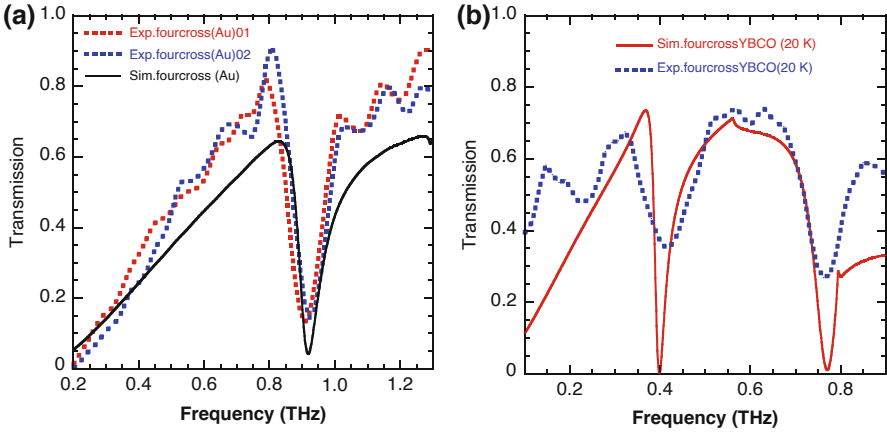
Fig. 12.8 (**a**) THz time-domain measurements of two identical gold fourcross filters (fourcross(Au) 01-dashed red line- and Fourcross(Au)02-dashed blue line), plotted with simulation results (solid black line) on the same graph. (**b**) THz time-domain measurement of YBCO fourcross filter at 20 K, plotted with simulation result on the same graph

YBCO superconducting films their resonance frequency will have a low value which leads to more efficient resonance switching and frequency tuning [24].

Before we proceed to concluding remarks, we would like to mention that there in parallel with the studies presented in this paper, based in high temperature semi-conductors, there are other materials also being investigated for the THz range, notably based on superlattices and quantum-cascade structures [25–37].

12.5 Conclusion

We have achieved powerful THz emission from mesa structures fabricated from intrinsic Josephson junction in Bi-2212 crystals. Furthermore, Bi2212 single crystals were used to fabricate microchip bolometers which showed a change in resistance for applied Powers using a broadband THz source. To investigate THz frequency dependent response, a unique metamaterial based on a fourcross patterned on metallic gold films and thin high temperature superconducting YBCO films was utilized as an active band-stop filter. In YBCO fourcross filters, resonance switching and frequency shifting with respect to temperature are observed. It has been dem-onstrated using simulated results and THz-TDS measurements that when the YBCO fourcross filters are used under the critical temperature, a noteworthy spectral tunability of the resonance can be realized. Aforementioned investigations evidently confirm the feasibility of temperature switched, low loss, THz active high temper-ature superconductor based devices.

References

1. Tonouchi M (2007) Cutting-edge terahertz technology. Nat Photon 1:97–105
2. Ferguson B, Zhang X-C (2006) Materials for terahertz science and technology. Nat Mater 1:26–33
3. Pickwell E, Wallace VP (2006) Biomedical applications of terahertz technology. J Phys D 39: R301–R310
4. Ozyuzer L, Koshelev AE, Kurter C, Gopalsami N, Li Q, Tachiki M, Kadowaki K, Yamamoto T, Minami H, Yamaguchi H et al (2007) Emission of coherent THz radiation from superconductors. Science 318:1291
5. Woodward RM, Cole BE, Wallace VP, Pye RJ, Arnone D, Linfield EH, Pepper M (2002) Terahertz pulse imaging in reflection geometry of human skin cancer and skin tissue. Phys Med Biol 47:3853–3863
6. Kleiner R, Steinmeyer F, Kunkel G, Müller P (1992) Intrinsic Josephson effects in $Bi_2Sr_2CaCu_2O_8$ single crystals. Phys Rev Lett 68:2394
7. Kadowaki K, Yamaguchi H, Kawamata K, Yamamoto T, Minami H, Kakeya I, Welp U, Ozyuzer L, Koshelev A, Kurter C, Gray KE, Kwok WK (2008) Direct observation of terahertz electromagnetic waves emitted from intrinsic Josephson junctions in single crystalline $Bi_2Sr_2CaCu_2O_{8+\delta}$. Physica C Supercond 468:634–639
8. Wang HB, Guénon S, Yuan J, Iishi A, Arisawa S, Hatano T, Yamashita T, Koelle D, Kleiner R (2009) Hot spots and waves in $Bi_2Sr_2CaCu_2O_8$ intrinsic Josephson junction stacks-a study by low temperature scanning laser microscopy. Phys Rev Lett 102:017006
9. Demirhan Y, Saglam H, Turkoglu F, Alaboz H, Ozyuzer L, Miyakawa N, Kadowaki K (2015) Area dependence and influence of crystal inhomogeneity on superconducting properties of Bi2212 mesa structures. Vacuum 120:89–94
10. Guénon S, Grünzweig M, Gross B, Yuan J, Jiang Z, Zhong Y et al (2010) Interaction of hot spots and THz waves in Bi2Sr2CaCu2O8 intrinsic Josephson junction stacks of various geometry. Phys Rev B 82:214506
11. Kadowaki K, Tsujimoto M, Yamaki K, Yamamoto T, Kashiwagi T, Minami H et al (2010) Evidence for a dual-source mechanism of terahertz radiation from rectangular mesas of single crystalline $Bi_2Sr_2CaCu_2O_{8+\delta}$ intrinsic Josephson junctions. J Phys Soc Jpn 79:023703
12. Ozyuzer L, Simsek Y, Koseoglu H, Turkoglu F, Kurter C, Welp U et al (2009) Terahertz wave emission from intrinsic Josephson junctions in high-Tc superconductors. Supercond Sci Technol 22:114009
13. Turkoglu F, Koseoglu H, Demirhan Y, Ozyuzer L, Preu S, Malzer S, Simsek Y, Müller P, Yamamoto T, Kadowaki K (2012) Interferometer measurements of terahertz waves from Bi2Sr2CaCu2O8+d mesas. Supercond Sci Technol 25:125004
14. Turkoglu F, Ozyuzer L, Koseoglu H, Demirhan Y, Preu S, Malzer S et al (2013) Emission of the THz waves from large area mesas of superconducting Bi2Sr2CaCu2O8+d by the injection of spin polarized current. Phys C Supercond 491:7
15. Karasik BS, McGrath WR, Wyss RA (1999) Optimal choice of materials for HEB superconducting mixers. IEEE Transc Appl Supercond 9:4213–4216
16. Hammar A, Cherednichenko S, Bevilacqua S, Drakinskiy V, Stake J (2011) Terahertz direct detection in YBa2Cu3O7 microbolometers. IEEE Trans Terahertz Sci Technol 1(2):390–394
17. Smith DR, Pendry JB, Wiltshire MCK (2004) Metamaterials and negative refractive index. Science 305:788

18. Soukoulis CM, Wegener M (2010) Materials science. Optical metamaterials--more bulky and less lossy. Science 330:1633

19. Singh R, Tian Z, Han J, Rockstuhl C, Gu J, Zhang W (2010) Cryogenic temperatures as a path toward high-Q terahertz metamaterials. Appl Phys Lett 96(7):071114

20. Zhang CH, Wu JB, Jin BB, Ji ZM, Kang L, Xu WW, Chen J, Tonouchi M, Wu PH (2012) Low-loss terahertz metamaterial from superconducting niobium nitride films. Opt Express 20:42–47

21. Chen H-T, Yang H, Singh R, O'Hara JF, Azad AK, Trugman SA, Jia QX, Taylor AJ (2010) Tuning the resonance in high-temperature superconducting terahertz metamaterials. Phys Rev Lett 105:247402

22. Kang L, Jin BB, Liu XY, Jia XQ, Chen J, Ji ZM, Xu WW, Wu PH, Mi SB, Pimenov A, Wu YJ, Wang BG (2011) Suppression of superconductivity in epitaxial NbN ultrathin films. J Appl Phys 109(3):033908

23. Glossner A, Zhang C, Kikuta S, Kawayama I, Murakami H, Muller P, Tonouchi M (2012) Cooper pair breakup in YBa2Cu3O7−under strong terahertz fields arXiv:1205 1684v1

24. Singh R, Chowdhury DR, Xiong J, Yang H, Azad AK, Taylor AJ, Jia QX, Chen HT (2013) Influence of film thickness in THz active metamaterial devices: a comparison between super-conductor and metal split-ring resonators. Appl Phys Lett 103:061117

25. Oriaku CI, Pereira MF (2017) Analytical solutions for semiconductor luminescence including Coulomb correla-tions with applications to dilute bismides. J Opt Soc Am B 34:321

26. Pereira MF (2018) Analytical expressions for numerical characterization of semiconductors per comparison with luminescence. Materials 11:2

27. Pereira MF (2016) The linewidth enhancement factor of intersubband lasers: from a two-level limit to gain with-out in-version conditions. Appl Phys Lett 109:222102

28. Pereira MF, Zubelli PJ, Winge D, E J, Wacker A, Rondrigues SA, Anfertvev V, Vaks V (2017) Theo-ry and measurements of harmonic generation in semiconductor superlattices with appli-cations in the 100 GHz to 1 THz range. Phys Rev B 96:045306

29. Pereira MF, Anfertev V, Zubelli JP, Vaks V (2017) Terahertz generation by gigahertz multi-plication in su-perlattices. J Nanophoton 11(4):046022

30. Apostolakis A, Pereira MF (2019) Controlling the harmonic conversion efficiency in semicon-ductor superlattices by in-terface roughness design. AIP Adv 9:015022

31. Apostolakis A, Pereira MF (2019) Numerical studies of superlattice multipliers performance. Quantum Sens Nano Electron Photon XVI:109262

32. Apostolakis A, Pereira MF (2019) Potential and limits of superlattice multipliers coupled to different input power sources. J Nanophoton 13:036017

33. Winge DO, Franckié M, Verdozzi C, Wacker A (2016) Simple electron-electron scattering in non-equilibrium Green's function simulations. J Phys Conf Ser 696:012013

34. Pereira MF, Shulika O (2014) Terahertz and mid infrared radiation: detection of explosives and CBRN (using te-rahertz). NATO science for peace and security series-B: physics and biophys-ics. Springer, Dordrecht

35. Pereira MF, Shulika O (2011) Terahertz and mid infrared radiation: generation, detection and applications, NATO science for peace and security series-B: physics and biophysics. Springer, Dordrecht

36. Apostolakis A, Pereira MF (2020) Superlattice nonlinearities for gigahertz-terahertz generation in harmonic multipliers. Nanophotonics 9(12):3941–3952. https://doi.org/10.1515/nanoph-2020-0155

37. Pereira MF, Anfertev V, Shevchenko Y, Vaks V (2020) Giant controllable gigahertz to terahertz nonlinearities in superlattices. Sci Rep 10:15950

Chapter 13
Semiconductor Components for THz-TDS Systems Activated by Compact Fibre Lasers

A. Krotkus, V. Pačebutas, R. Norkus, I. Nevinskas, and A. Arlauskas

Abstract This contribution reviews the investigations on semiconductor optoelectronic components of terahertz time-domain-spectroscopy (TDS) systems that were performed over the last years at the laboratories of the Optoelectronics Department of the Centre for Physical Sciences and Technology in Vilnius, Lithuania. The first research topic was THz pulse emission from femtosecond laser excited semiconductor surfaces. By using an original experimental technique based on the laser source providing femtosecond optical pulses with the wavelength that can be changed over a wide range from 2600 to 350 nm, THz excitation spectra of numerous semiconductor crystals were investigated and compared. This research was complemented with experiments performed on the samples with different doping level and different crystallographic orientation, which has allowed to elucidate the microscopic origin of the effect of surface THz emission. In the second part of the article the main achievements in the development of dilute bismide based optoelectronic THz frequency range devices will be presented. Epitaxial layers of these semiconducting compounds grown on GaAs or InP substrates were shown to be suitable for the fabrication of ultrafast photoconductive antennas serving as THz radiation emitters and detectors activated by femtosecond pulses with the wavelengths from 1000 to 2000 nm that are typical for modern fiber laser oscillators.

A. Krotkus (✉) · V. Pačebutas · R. Norkus · I. Nevinskas
Optoelectronics Department, Centre for Physical Sciences and Technology, Vilnius, Lithuania
e-mail: arunas.krotkus@ftmc.lt; vaidas.pacebutas@ftmc.lt; ricardas.norkus@ftmc.lt; ignas.nevinskas@ftmc.lt

A. Arlauskas
Light Conversion, Ltd., Vilnius, Lithuania
e-mail: andrius.arlauskas@lightcon.com

13.1   Introduction

Various materials excited by femtosecond laser pulses radiate electromagnetic transients with characteristic frequencies in terahertz (THz) range. THz radiation was first generated in dielectric crystals by optical rectification [1], and later in semiconductor surfaces due to the ultrafast photocurrents [2]. Recently, the list of materials as potential THz surface emitters has been widely extended and includes laser excited organic crystals [3], ferromagnetic [4] materials and their structures, and hybrid organic-inorganic perovskites [5]. Investigations of such emitters aim at the development of THz time-domain spectroscopy (TDS) systems in which sizeable and expensive Ti:sapphire lasers are replaced by their more compact and cost-effective counterparts – femtosecond fibre or diode lasers emitting at longer wavelengths of 1 µm or 1.55 µm. Fibre laser based TDS systems can largely facilitate their use in applications like the detection of CBRN and explosives that typically have strong absorption signatures in the THz frequency range of the spectrum.

Most often studied are semiconductor surface emitters. They are already becoming a good alternative to photoconductive antennas (PCAs) as THz pulse emitters in TDS systems activated by long-wavelength femtosecond lasers. Surface emitters do not require an external bias and they do not suffer from thermal noise originating from the dark currents in electrically biased PCAs. The performance of different semiconductors as THz emitters is determined by their fundamental characteristics: energy bandgap, electron and hole effective masses, etc. Consequentially, the study of THz pulse emission can provide a unique information on the semiconductor material properties. The first part of this article will summarize recent research of our group devoted to the THz emission spectroscopy of various semiconducting materials and semiconductor nanostructures.

Ultrafast photoconductors made from semiconductors with sub-picosecond carrier lifetimes and having metallic contacts shaped as a high-frequency antenna with a photosensitive gap have lately been found to have many important applications in both the generation and detection of pulsed or continuous-wave (cw) terahertz (THz) radiation signals. Most popular optoelectronic THz radiation systems are based on mode-locked Ti:sapphire lasers emitting femtosecond optical pulses with a central wavelength in the 700–800 nm range, and a PCA fabricated on so-called low-temperature-grown (LTG) GaAs. Layers of this semiconductor of 1 µm and thicker are grown by molecular beam epitaxy (MBE) at As overpressure and at substrate temperatures in the 200–300 °C range. LTG GaAs contains a large density of non-stoichiometric As-antisite defects (As_{Ga}). The As_{Ga} defects create deep donor levels that are pinning the Fermi level position in the middle of the energy bandgap thus securing large resistivity of the material, on one hand, and acting as ultrafast non-equilibrium electron capture centers, on the other hand.

Since GaAs is not photosensitive in the spectral ranges of around 1–1.5 µm, a lot of attention is recently paid to the investigation of semiconductors having bandgaps that are narrower than GaAs energy bandgaps, and a set of material parameters appropriate for the fabrication of picosecond photoconductors. We have focused our

attention to group III bismides – semiconducting alloys with relatively narrow bandgaps that can be grown on GaAs and InP substrates. The main results of these research efforts will be presented in the second part of the article.

13.2   Mechanism of Surface THz Emission from Semiconductors

THz radiation from unbiased semiconductor surfaces illuminated by femtosecond laser pulses can be caused by several different physical mechanisms. The most trivial one is the photocurrent surge in the built-in electric field region at the illuminated surface [2]. When the energy band bending is small like in narrow-gap semiconductors or the electrons are excited with excess energies much higher than the surface potential, the photocurrent surge can be caused by different electron and hole diffusion rates, the so-called photo-Dember (PD) effect [6]. Relative roles of the current surge and PD effects depend on the excess energy of photoelectrons ε_{ex}: the first effect is dominating when electrons are excited close to the band edge, the second – at high ε_{ex} [7]. In both cases, a dynamical electric dipole is created with its axis perpendicular to the surface, therefore, when dipole field is changing radiated THz signal propagates predominantly parallel to the surface.

A simple PD effect model fails to explain several important characteristics of surface THz emission such as the line-of-sight emission from a surface illuminated along its normal [8], the generation of S-polarized THz waves, and a complex dependence of generated THz field amplitude on the azimuthal angle between the optical field and the crystal axes [9]. Phenomenologically, these features can be attributed to the second- and third-order nonlinear optical effects: the optical rectification (OR) and the electric-field-induced OR (EFIOR). However, the values of nonlinear optical susceptibilities that should be assumed to explain observed THz field intensities are several orders of magnitude higher than the corresponding material parameters.

It has been shown in [10] that a microscopic description of the effect should involve three additional physical phenomena: optical alignment of photoexcited electrons, their quasiballistic movement during the nucleation of the surface dipole, and anisotropy of the electron energy dispersion law. Firstly, optical selection rules for cubic semiconductors require that the momenta of electrons excited from the heavy hole valence subband are predominantly aligned along the refracted beam direction (see Fig. 13.1), whereas the momenta of less numerous electrons excited from the light hole valence subband are mainly parallel to the refracted light polarization [11].

Secondly, the main part of the THz pulse is generated during the first 100–200 fs after photoexcitation, that is, at the ballistic stage of photocarriers movement. If ε_{ex} is high enough, the electrons can propagate from the surface as far as several hundred nanometers, and the THz signal amplitude will provide information on the energy

Fig. 13.1 Optical
alignment of the momenta
of electrons excited from the
heavy hole subband by the
linearly p-polarized light
beam impinging on the
semiconductor surface at the
incline angle
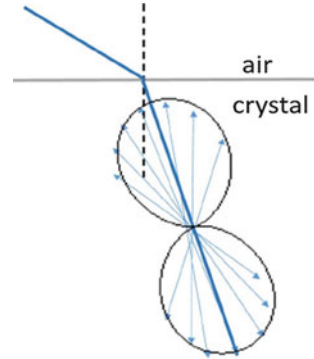
band structure even remote from the surface layers of the semiconductor structure. Finally, when optically aligned electrons move in a nonparabolic conduction band, the electrons moving in the built-in electric field toward the surface and away from it due to the electric field effect will experience different effective masses. Moreover, the resulting lateral photocurrent component will also depend on the optical field direction with respect to the crystallographic axes, because the conduction and valence bands nonparabolicity will be accompanied by their nonsphericity [12]. Such microscopical interpretation of EFIOR-like observations typical for THz generation from InAs is provided in [8, 10].

In InSb, another narrow gap semiconductor, any built-in fields are typically screened by large intrinsic electron density of that material, thus OR, rather than EFIOR type features are observed when THz surface emission is investigated [13]. These features can be also explained microscopically by a joint action of the optical alignment and the energy band nonsphericity. Figure 13.2 illustrates this explanation. It shows the cross-sections of isoenergetic surfaces of InSb conduction band parallel to a (111) crystallographic plane and the lateral momentum component distribution of the photoelectrons excited by an optical beam propagating along the [111] axis. It can be seen that these surfaces lose their spherical symmetry with increasing electron excess energy. Because of this asymmetry, the electrons excited with lateral momentum components directed to the right, along the [112] axis, will have a larger effective mass as compared to that of the electrons excited in the opposite petal of the momentum distribution. This imbalance will lead to the appearance of lateral photocurrent components for three azimuthal angles for which the optical polarization vector is perpendicular to the directions of the largest isoenergetic surface curvature.

From what is said above it is clear that the THz emission from semiconductor surfaces is essentially caused by the femtosecond optical pulse induced photocurrents which can be monitored without any metallic contacts. Moreover, these photocurrents are caused by close to monoenergetic electron bunches that move ballistically during THz pulse generation and so they can be used to investigate the band structures at energies remote from band extrema and the band line-up in heterostructures. In the following we will present THz excitation spectroscopy – a

Fig. 13.2 Cross-sections of the conduction band isoenergetic surfaces at different excess energies (grey lines) and the momentum distribution of photoelectrons excited from the heavy-hole valence band
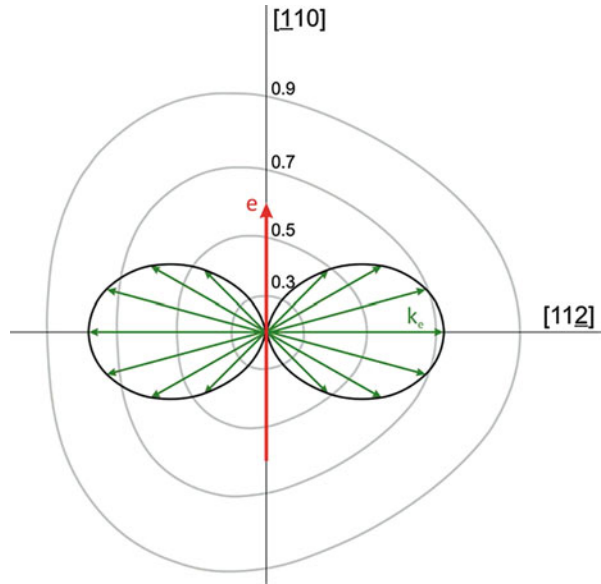
powerful technique that exploits these advantages by using variable wavelength optical pulses for photoexcitation.

13.3 Experimental Technique

Surface THz emission experiments were performed in the quasi-reflection geometry with samples illuminated at 45° to their surface normal. Two femtosecond laser systems were employed for the photoexcitation: an optical-parametric-amplifier (OPA, Orpheus, Light Conversion Ltd.) with pulse duration of 160 fs, pulse repetition rate of 200 kHz, and wavelength tunable from 650 to 2600 nm (shorter wavelengths up to 350 nm were reached using the second harmonics generation in a BBO crystal), and Ti:sapphire laser oscillator (20 fs, 76 MHz, and 800 nm). For the pulse detection in THz TDS experiments a photoconductive antenna activated by 1030 nm wavelength optical pulses from amplified laser system, fabricated from GaAsBi layer (TERAVIL. Ltd) was used; whereas photoconductors fabricated from low temperature GaAs were used in the second TDS system. Measurements were performed at two experimental geometries differing by sample excitation angles used: 45 and 0°. The first one is an ordinary configuration, which is depicted in Fig. 13.3a. The second one was arranged in such a way that the optical excitation and THz radiation were impinging the samples at 0° (Fig. 13.3b). For that reason we used a pellicle type beam-splitter, which partially reflects the optical beam (reflectance/transmittance = 45:55) but it is practically transparent to THz radiation (transmittance ≈95%). All measurements were performed at the room temperature.

Fig. 13.3 Experimental setup of THz time-domain spectroscopy system
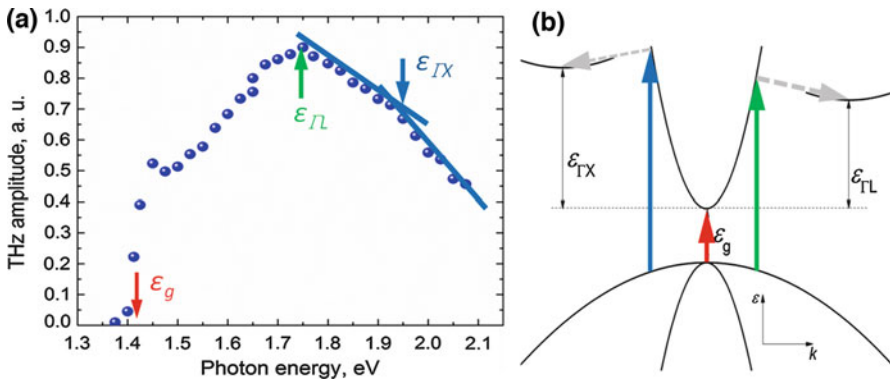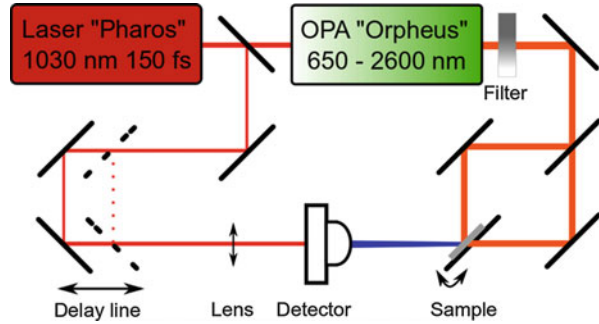
Fig. 13.4 THz excitation spectrum of GaAs (**a**) and its energy band scheme with possible electron transitions (**b**)

13.4 THz Excitation Spectra of Semiconductors

Figure 13.4a, which shows a THz excitation spectrum of GaAs, demonstrates the potential of such experiments when investigating the electron energy band structure of semiconductor crystals. Various characteristic energies of this structure that can be identified from THz excitation spectrum are indicated on a schematic representation of an energy dispersion law of GaAs shown in Fig. 13.4b. As it seen from this Figure, THz emission is present even at the smallest absorbed photon energies, $h\nu > \varepsilon_g$. When the electron excess energy is small, the THz pulses are mainly generated due to photocurrent surge in the built-in surface electric field. An increase in photon energies leads to higher electron excess energies and the carrier separation is enhanced due to optically aligned and ballistically moving away from the surface photoelectrons. Thus the initial part of measured spectral dependence evidences that both photocurrent surge related effects are resulting in generation of THz pulses of the same polarity, which means that the energy bands at the surface of a semi-insulating GaAs crystal are bended upwards. A clear maximum at $h\nu \approx 1.75$ eV followed by an additional kink at ~1.94 eV are present on the dependence shown in

Fig.13.4a; their origin is related to the onset of electron scattering to the subsidiary conduction band valleys at L and X points of the Brillouin zone, respectively. The electron scattering time to those valleys is of the order of 200 fs for Γ-L transitions and 80 fs for Γ-X transitions [11], therefore, it significantly impairs their quasi-ballistic movement and reduces the strength of the electrical dipole and the THz radiation caused by the dynamics of it.

The energy position of the subsidiary valleys can be found from simple considerations involving electron energy and momentum conservation laws. For a parabolic conduction band Γ valley, as in GaAs it gives the relation

$$\varepsilon_{\Gamma \to L, X} = \frac{m_h}{m_h + m_e} \left(h\nu - \varepsilon_g \right) - \hbar\omega_{iv} \tag{13.1}$$

where m_h is the heavy hole effective mass, m_e is the electron effective mass, and ħω_iv is the intervalley phonon energy. The intervalley energy separations $\Delta\varepsilon_{iv}$ of 0.3 eV and 0.45 eV for Γ-L and Γ-X transitions, respectively, obtained from the analysis of results shown in Fig.13.4a perfectly fit to the known values of those parameters of GaAs [12]. For a non-parabolic, Kane-type conduction band, the expression (13.1) becomes more complicated:

$$\mathcal{E}_{\Gamma \to L, \ X}(h\nu) = \frac{-1 - \frac{m_e}{m_h} + \sqrt{\left(1 + \frac{m_e}{m_h}\right)^2 + 4\frac{m_e}{m_h}\frac{h\nu - \varepsilon_g}{\varepsilon_g}}}{2\frac{m_e}{m_h}\frac{1}{\varepsilon_g}} - \hbar\omega_{iv}. \tag{13.2}$$

Therefore, THz excitation spectroscopy provides a unique possibility to directly determine the intervalley energy separation between non-equivalent conduction band valleys that was until now evaluated from the hot-electron transport and other indirect characteristics. The value of this parameter is important for designing various semiconductor devices: from high power and high frequency diodes and transistors to quantum confinement based light emitters.

In a series of research papers [12–16] our group was performing THz excitation spectroscopy experiments on various semiconductor crystals. Some of these spectra normalized to their maxima are presented on Fig. 13.5. Their shape is similar differing only in THz emission onset energies, which correlate with the energy bandgaps of different crystals. All spectral dependences have sharp maxima corresponding to photon energies for which the photoexcited electron excess energy becomes larger than the intervalley separation in the conduction bands. In a series of research papers [12–16] our group was performing THz excitation spectroscopy experiments on various semiconductor crystals. Some of these spectra normalized to their maxima are presented on Fig. 13.5. In$_{0.84}$Ga$_{0.16}$N is an exception, because a thin layer of this wide bandgap material is grown on a GaN substrate, and the sudden reduction of THz pulse amplitude at $h\nu > 3.3$ eV is caused by electron retardation by the built-in electric field at the interface with substrate. An additional maximum of InP spectrum appears due to the action of the photo-current surge at low electron

Fig. 13.5 THz excitation spectra of several group A3B5 semiconductors normalized to their maximum amplitudes
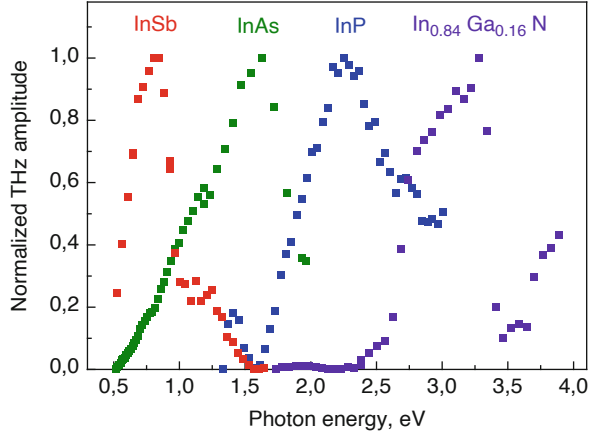
Table 13.1 Parameters of THz excitation spectra measured on binary A3B5 semiconducting crystals

Material	ε_g, eV	ε_0, eV	ε_{max}, eV	$\Delta\varepsilon_{iv}$, eV	E_{THz} (1 μm)	E_{THz} (1.5 μm)	References
InSb	0.18	<0.5	0.8	0.51	0.3	1.5	[13]
InAs	0.35	0.5	1.5	1.08	1	1	[12]
GaSb	0.6	0.72	0.72	0.11	0.05	0.26	[17]
InN	0.8	1.0	>3.1	?	–	–	[15]
InP	1.34	1.34	2.3	0.75	–	–	[14]
GaAs	1.42	1.42	1.8	0.3			[12]

excess energies and it is caused by an upward bending of the bands at a semi-insulating InP crystal surface.

Table 13.1 summarizes the use of THz excitation spectroscopy for the determination of conduction band structure details in A3B5 crystals. In this Table ε_0 marks the photon energy at which THz emission sets-on, ε_{max} – is the photon energy corresponding to the maximum of radiated THz pulse amplitude. The THz pulse amplitudes emitted when semiconductors are excited by optical pulses with the wavelengths from technologically important 1 μm and 1.55 μm spectral ranges are also indicated. These amplitudes are normalized to the amplitudes obtained when using p-type InAs – the most efficient THz surface emitter at the moment [12]. The results shown in Table 13.1 are mainly obtained on bulk crystalline samples. The GaSb and InN are exceptions for which epitaxial layers were investigated instead of bulk samples. One could expect that the most efficient THz emitters should be semiconductors with the narrowest bandgap and the largest electron mobility. In such materials the electrons would be photoexcited with a higher excess energies, they would move ballistically faster and, due to a smaller electron scattering rate, over longer distances.

According to such a consideration, the best surface emitter should be InSb, however, experimental results clearly evidence the dominance of InAs practically

Fig. 13.6 Peak-to-peak amplitudes of THz pulses measured as a function of 1.55 μm femtosecond laser beam fluency
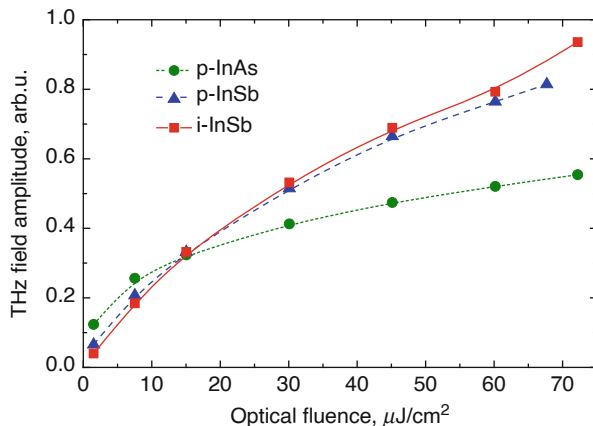
at all spectral regions, for which femtosecond lasers are available. The main advantages of InAs over InSb as a material for THz emitters are the twice higher energy distance to the high effective mass valleys of the conduction band and the more than one order of magnitude lower intrinsic carrier concentration. Higher $\Delta\varepsilon_{iv}$ allows to excite electrons in InAs to energy levels where they can propagate with high group velocities and their movement is more influenced by the effects of nonparabolicity and non-sphericity of the conduction band. These conditions are essential for anisotropic photocurrents with strong lateral compo-nents – an EFIOR-like effect that is mainly responsible for the THz emission from InAs [8, 10]. In p-type InAs, where the surface electric field has the same polarity as the PD field, amplitudes of emitted THz pulses are more than 2 times higher than those in n-type InAs.

In intrinsic or n-doped InSb all the built-in electric fields are effectively screened by a large density, high mobility equilibrium electrons, therefore, EFIOR-like contribution is weak, and the prevailing mechanism of THz emission is the lateral photocurrents arising due to the anisotropy of isoenergetic surfaces (OR-like effect, see Fig. 13.2.). This problem has been addressed in Ref. [18], where the epitaxial layers of p-type InSb were studied as THz emitters acti-vated by 1.55 μm wavelength femtosecond laser pulses and their performance was compared with the p-InAs and intrinsic InSb. The results of this investigation are presented in Fig. 13.6. The THz pulses radiated by the p-InAs are the strongest in a rather narrow range at the lowest excitation levels, but their amplitudes start to saturate relatively early, when the photoexcited carrier density reaches approximately $5 \cdot 10^{17}$ cm^{-3}. At higher optical fluencies, both of the InSb samples radiate THz pulses that are about two times stronger than those radiated by the p-InAs.

The lateral photocurrents can be enhanced and the THz emission efficiency can be improved if one exploits internal electric fields in semiconductor structures consisting of differently doped layers. Such an experiment was performed in [19] where the THz emission from GaInAs p-i-n diodes was investigated. All p-i-n structures were grown by MBE on an n-type InP substrate (carrier concentra-tion $\sim 1.5 \times 10^{18}$ cm^{-3}); 50 nm n-type GaInAs (carrier

Fig. 13.7 THz pulses
generated by the p-InAs
crystal and sample GaInAs-
750 excited at 1030 nm
wavelength, 10 mW average
optical power [19]
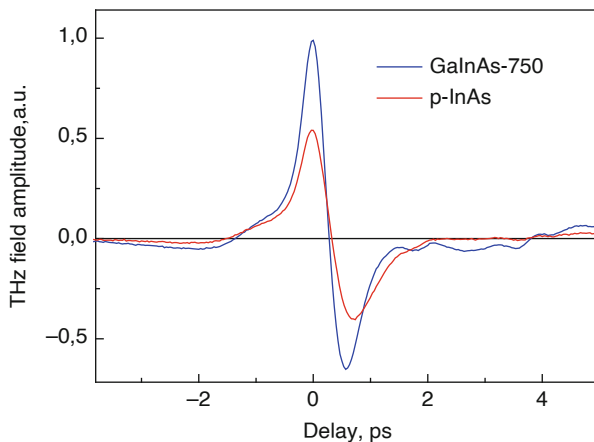
concentration $\sim 1.5 \times 10^{18}$ cm^{-3}), unintentionally doped GaInAs, and 50 nm
thickness p-type GaInAs (carrier concentration $\sim 8 \times 10^{17}$ cm^{-3}) layers. The
width of the unintentionally doped region was different: 200 nm (GaInAs-200),
400 nm (GaInAs-400), and 750 nm (GaInAs-750). The first two were grown on the
(100) oriented substrates, whereas the third structure (GaInAs-750) on the (111)
oriented substrate. The samples were excited either at incline angles or perpendicular
to their surface; the THz radiation was monitored either in the transmission or
quasireflection directions. In the case of signal registration in the transmission
direction the structure was photoexcited from the substrate side because the THz
pulses cannot penetrate a highly conductive InP substrate and are reflected and
absorbed by it. The THz pulse radiated by the GaInAs p-i-n diode with the thickest
i-region is compared in Fig. 13.7 with the signal emitted from the p-type InAs crystal
($p = 2 \times 10^{17}$ cm^{-3}) both photoexcited at exactly the same conditions using the Yb:
KGW 76 MHz oscillator. The THz transients were detected in reflection and
transmission experimental geometries, but the THz pulse amplitudes emitted from
p-i-n structure in the same transmission geometry were only slightly, by ~25%,
smaller than in the reflection geometry. It is seen that the peak-to-peak amplitude of
the pulse generated by the p-i-n structure is nearly 2 times higher than that obtained
from the laser excited surface of the p-InAs single crystal.

   This ratio can be further improved by applying reverse dc bias to the diode. The
performance of 2 THz emitting GaInAs p-i-n structures when excited with tunable
wavelength femtosecond pulses generated by OPA is illustrated and compared with
the THz excitation spectrum of the p-type InAs crystal in Fig. 13.8. All these
dependences are measured in the reflection geometry with a constant average optical
power of 2.5 mW incident on the samples and the THz excitation spectra are
normalized to the same number of photons. The GaInAs p-i-n junction containing
the 200 nm wide i-region provides signal amplitudes similar to those of p-InAs over
the spectral range from 1 to 1.7 μm, whilst the sample GaInAs-400 emits THz pulses
with approximately 50% higher amplitudes than those emitted from the p-type InAs
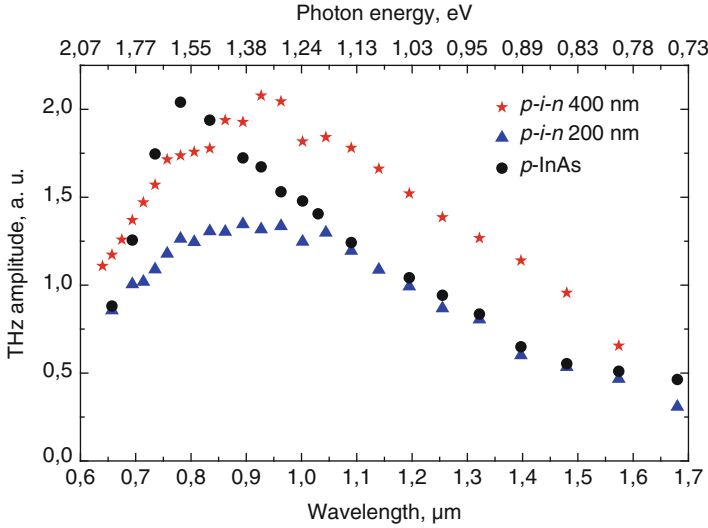
Fig. 13.8 THz excitation spectra for samples GaInAs-200 and GaInAs-400 compared with a similar dependence measured on the p-type InAs crystal

Fig. 13.9 Azimuthal angle dependences for the sample GaInAs-750 excited with 1 µm wavelength pulses from OPA measured in the line-of-sight geometry. Optical beam impinging along the surface normal from the structure side (1) and from the substrate side (2)
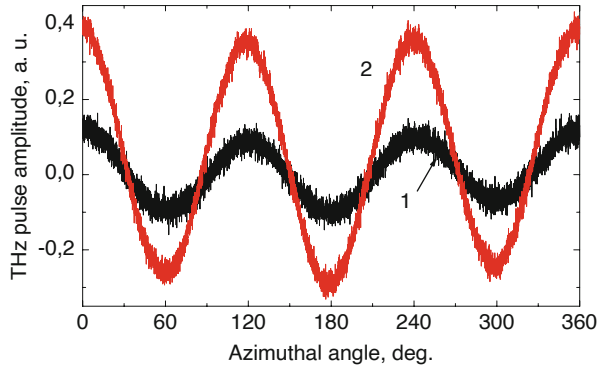
over a wide 0.9–1.5 µm laser wavelength range. Figure 13.8 shows that the p-i-n emitters radiate substantial THz signals even for the laser wavelengths close to the absorption edge of the GaInAs (~1.67 µm) where the excitation is almost homogeneous over the active region width. It is known that the THz emission due to the PD effect sets on only when the photoexcited electrons reach rather high excess energies, which points out to the possible effect of the photocurrent surge and electron and hole separation in the built-in electric field of the i-layer of the p-i-n structure.

At shorter wavelengths the lateral photocurrent components become more important. Interesting effects were observed in GaInAs-750 sample grown on a [111] substrate. The THz pulses from this sample in the line-of-sight geometry with laser beams impinging along the normal to the growth surface (traces 1 and 2 on Fig. 13.9)

from two opposite sides. In this experimental geometry the THz signal reaching the detector is solely caused by the anisotropic lateral photoconductivity effect. It is interesting to note that the azimuthal angle dependent THz radiation component is stronger when the sample is illuminated from the substrate side. In this case the majority of photoexcited electrons are moving in the direction towards the top of the structure and they are effectively decelerated by the built-in electric field in the i-region. This will increase their effective time-of-flight across the electric field, increase their lateral displacement, and, therefore, enhance the strength of the dynamic dipole which causes THz emission. This observation helps to understand a rather unexpected difference in THz emission efficiencies from n- and p-type InAs crystal surfaces. The Fermi level at the InAs surface is pinned at As_{In} donor level that is about 0.18-eV above the conduction band minimum. Therefore, the surface field and the field caused by PD effect are of the same polarity in n-type InAs crystals and of the opposite polarity in p-type crystals, which results in higher THz pulse amplitudes generated from p-InAs crystal surfaces.

The research on the surface THz emitters is rapidly progressing; they are already used in TDS systems activated by long wavelength femtosecond laser pulses. A THz-TDS system activated by 1.55 μm wave-length pulses from an Er-doped fiber laser with the p-type InAs crystal as an emitter and the GaInAsBi photoconductive antenna as a detector achieved comparable performance with standard TDS systems that are using a Ti:sapphire laser and the low-temperature grown (LTG) GaAs PCAs [20].

13.5   Optoelectronic THz Frequency Range Components from Dilute Bismides

Alternative to LTG GaAs material photosensitive at fiber laser wavelengths shall be a narrower bandgap semi-conductor with a fairly high dark resistivity and short carrier lifetimes. Higher electron mobilities typical for the narrow-gap semiconductors and higher electron excess energies are expected to yield higher optical-to-THz power conversion efficiencies. PCAs activated by long wavelength optical pulses can be fabricated from the LTG GaInAs. For 1 μm wavelength TDS systems the GaInAs can be grown on GaAs substrates, but the PCA performance is greatly reduced by low electron mobility in this material [22]. The $Ga_{0.53}In_{0.47}As$ lattice-matched to InP substrates, has a bandgap of ~0.74 eV required for PCAs sensitive to 1.5 μm wavelength radiation, however, the low-temperature grown layers of this material become highly n-type conductive as the As_{Ga} defect band becomes resonant with the conduction band [23].The resulting high dark conductivity is not acceptable for THz PCAs. Due to this reason, alternative techniques have been developed to simultaneously achieve high resistivity and ultrafast behaviour of GaInAs. The Fe doping of MOVPE grown layers [24] as well as the heavy ion bombardment [25]

Fig. 13.10 Energy bandgap as a function of material composition in three compounds: GaAsBi (points), GaAsSb and GaInAs. Numbers on the abscise axis indicate percent of Bi, Sb, and In, respectively
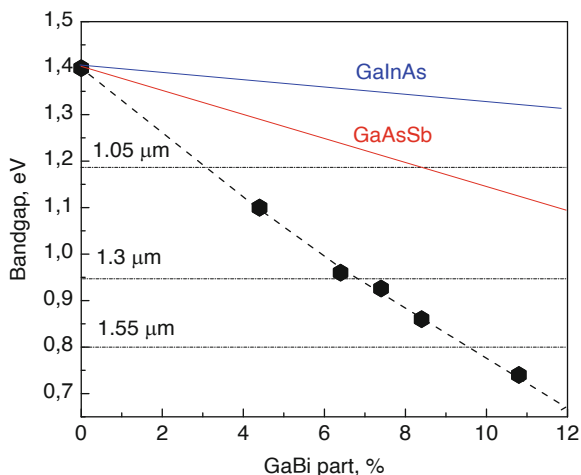
have both been applied, but failing to achieve material characteristics equivalent to LTG GaAs.

In [26] we have proposed to fabricate pulsed THz emitters and detectors from group III element bismides. Introduction of Bi into the crystalline lattice of A3B5 semiconductor compounds results in a strong reduction of the energy bandgap accompanied by a relatively small change in the lattice constant. First, the THz-TDS system activated by a Ti:sapphire laser (photon energy of 1.5 eV) having PCAs for both emitter and detector fabricated from the ternary GaAsBi layer grown on a semi-insulating GaAs substrate at 280 °C temperature was investigated and frequency bandwidths of the emitted THz transients broader than 3 THz were demonstrated. The physical characteristics of GaAsBi relevant to the applications in terahertz optoelectronics were studied in more detail in [27]. GaAsBi layers with up to 8.4% Bi were of p-type conductivity with carrier densities ranging from 3×10^{14} to 2×10^{15} cm^{-3} and resistivities exceeding 60 Ω cm. Energy bandgap of the gallium bismide alloys as determined from spectral measurements of the optical absorption, photoconductivity and photoluminescence show a decrease with increasing Bi content at an average rate of 80 meV/%Bi, which is much faster than in GaInAs or GaAsSb alloys with a similar percentage of In or Sb, respectively (Fig. 13.10).

It is seen from Fig. 13.10 that GaAsBi with ≥4%Bi has energy gaps lower than the photon energies of lasers generating in 1 μm wavelength range; 1.55 μm range laser pulses are efficiently absorbed in a material with more than 10% of Bi. Moreover, the electron mobility in GaAsBi is relatively large, in the range from 2000 cm^2/Vs to 2800 cm^2/Vs [28, 29], even in the layers with picosecond electron lifetimes. This set of material parameters indicates that the GaAsBi material could be a prospective platform for the development of THz optoelectronic devices activated by long-wavelength femtosecond optical pulses.
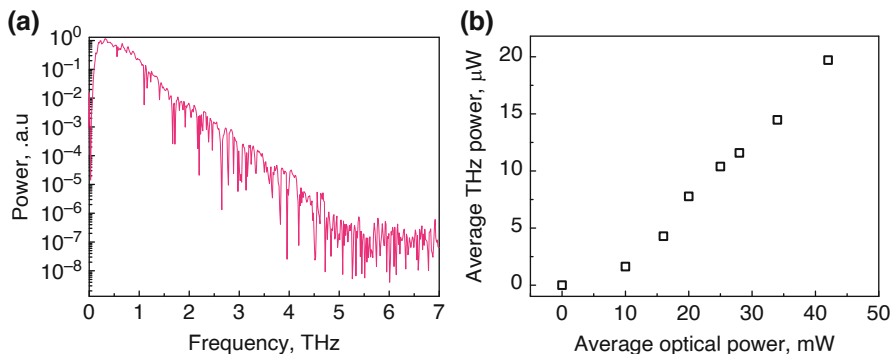
Fig. 13.11 (**a**) The Fourier spectrum of the THz radiation transient generated and detected by photoconductive components made from the GaBiAs layers that are activated by 70 fs, 1030 nm laser pulses. (**b**) is the average THz output power dependence on the optical pump power at the bias voltage of 60 V

First THz TDS systems based on 1 μm range femtosecond lasers and the GaAsBi PCAs were demonstrated in [30]. In one case, a femtosecond Yb:KGW oscillator (Light Conversion Ltd.) generating 70 fs, 1030 nm pulses at a repetition rate of 76 MHz was used for both the excitation and the sampling of THz radiation. The Fourier spectrum obtained from the THz transients generated and detected by the photoconductive components made from the GaAsBi layers is shown in Fig. 13.11a. The average laser power used for the excitation and detection was 30 mW and 20 mW, respectively. A Golay cell (Tydex) was employed to measure the dependence of an average THz emission power on the bias voltage at different excitation powers (Fig. 13.11b). The data presented in Fig. 13.11b reveal that the characteristics of this THz-TDS system are close to that of a Ti:sapphire laser based system: the optical-to-THz power conversion efficiency of GaAsBi based system is comparable with the best large-aperture THz emitters made from GaAs and excited by Ti: sapphire laser pulses [31].

Another set of experiments was performed in Ref. [30] by using the same pair of PCA components and a home-built positive dispersion Yb-doped fiber oscillator based on the dual-output scheme introduced by Chong et al. [32]. The optical pulse repetition rate was 45 MHz, the average optical power used to excitate the GaAsBi THz emitter and detector was fixed at 8 mW. The THz-TDS system based on the fiber oscillator revealed a slightly worse performance as compared to the case of Yb: KGW laser and the same optoelectronic THz components (signal-to-noise ratio was 50 dB, spectral bandwidth was ~3 THz), which was explained by a substantially shorter pulse duration and a higher pulse peak power of Yb:KGW laser.

Bismide PCAs for THz pulse emission and detection using 1 μm wavelength lasers are already available commercially (TERAVIL Ltd.); such antennas for 1.55 μm and longer wavelengths are still under development.

GaAsBi on the GaAs substrates can be grown by MBE and MOCVD techniques [33, 34]. It was found [35] that the bandgap of GaAsBi decreases with the addition of

Bi up to seven times faster in comparison to increasing the InAs content in GaInAs; consequently, the lattice mismatch between GaAsBi alloy and GaAs substrate is approximately four times smaller than GaInAs with a similar bandgap. However, for the Bi content larger than ~10% at which absorption edge of GaAsBi reaches 1.5 μm wavelength a large number of Bi-related point and cluster defects appears and the material becomes highly p-doped [36]. Moreover, the GaAsBi layer surface becomes rough and often contains numerous bismuth droplets which prevents the fabrication of satisfactory metallic contacts that are necessary for PCAs. In [20] the photoconductive THz detectors activated by long-wavelength femtosecond laser pulses fabricated from the epitaxial layers of quaternary dilute bismide compound (GaIn) (AsBi) grown on GaAs substrates were investigated. The rationale for selecting this material for PCAs activated by infrared laser pulses is as follows. The deep As_{Ga} donor level is located approximately in the middle of the 1.42 eV wide energy bandgap of GaAs. Alloying GaAs with InAs shifts down the conduction band edge with a rate of – 15 meV/%In [37]. On the other hand, Bi-introduction affects both conduction and valence band edge energies. According to C. A. Broderick et al., [38], the rates of change of these edges for low quantities of Bi in GaAs are equal to – 28 meV/%Bi and + 53 meV/%Bi, respectively.

By appropriately selecting In and Bi content it is possible to realize the situation at which both conduction and valence bands move towards each other symmetrically. For a certain In and Bi content ratio in $Ga_{1-x}In_xAs_{1-y}Bi_y$ x = 1.66y, the As_{Ga} or other deep levels responsible for high resistivity and short lifetimes should remain in the middle of the bandgap making the material properties optimal for ultrafast photoconducting applications.

The GaInAsBi layers were grown on a semi-insulating (100) GaAs substrate in the molecular beam epitaxy reac-tor SVT-A. The substrate temperature during all growth runs was 240 °C, the III to V group element ratio was ~1.1. The growth rate of the GaInAsBi layer was ~0.5 μm/h and the thickness of the layers was 1–1.5 μm. The two samples with smooth and droplet-free surfaces were selected for further investigation. Their main parameters are summarized in Table 13.2.

The energy bandgap of GaInAsBi layers as well as the electron trapping times and their mobility (material characteristics essential for PCA-based THz component performance) were investigated by the optical pump-THz probe technique. In this experiment, a femtosecond laser pulse excites electron–hole pairs in the sample, which induces additional free-electron absorption of THz radiation pulses synchronized with the sample photo-excitation. It has been found that the carrier lifetimes in both samples are shorter than 1 ps, which is comparable to the temporal resolution of the experiment. The PCAs with the shape of coplanar Hertzian dipoles with a

Table 13.2 The main parameters of the investigated GaInAsBi samples [20]

Sample	In, %	Bi, %	$p \times 10^{15}$, cm^{-3}	Hall mobility, cm^2/ V s	Resistivity, Ω cm	Energy bandgap, eV
A	12	10	1.3	10	400	0.68
B	19	9.5	5.6	11	110	0.6

Fig. 13.12 Bismide THz detector sensitivity as a function of the central wavelength in femtosecond optical pulses
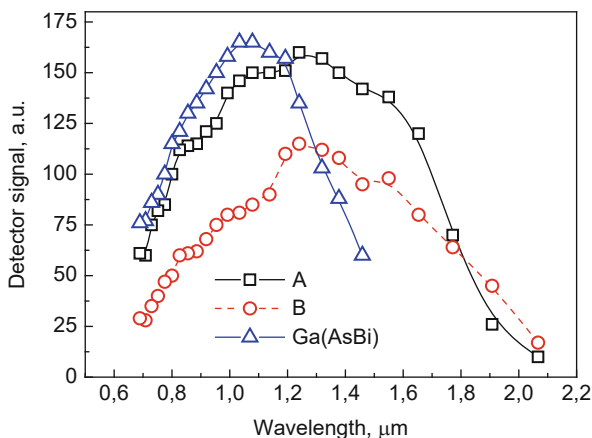
photoconducting gap of 10–15 μm between the Ti–Au electrodes were fabricated on both quaternary wafers. The spectral photoresponse of PCAs was investigated using an experimental set-up based on the OPA system described above. In the THz TDS arrangement activated by this laser system, a p-type InAs was used as a surface emitter illuminated by a part (∼310 mW) of the Yb:KGW laser beam and delayed by different times with respect to the optical beam (1 mW) from the OPA activating the investigated PCA which was used to detect the radiated THz signals. Figure 13.12 presents the dependence of the THz pulse amplitude on photon energy of the optical pulses which activates the THz detectors. Spectral characteristics of detectors made from both GaInAsBi layers are compared with each other and with the spectrum of the detector made from a ternary GaAsBi layer.

It can be seen from the Fig. 13.12 that the THz detectors made from the quaternary bismide layers can be activated by optical pulses of significantly longer wavelengths; the sensitivity of the detector from sample A at 1.5 μm wavelength is comparable to the sensitivity of GaAsBi detector in a 1 μm wavelength range. More than this, the sensitivity of devices fabricated from GaInAsBi layers B and A at 1.9 μm was only 2 and 3 times, respectively, lower than at 1.5 μm.

In the later work [39] the GaInAsBi layers with 12.5% In and 8.5% Bi and better electrical characteristics were grown and used to fabricating both the emitter and the detector PCAs. The layer used for an emitter was 1.4 μm thick, whereas the layer for a THz detectors was 0.84 μm thick and it was grown on a seven period AlAs/GaAs Bragg reflector (maximum reflectance at 1.53 μm) in order to increase the laser pulse absorption and to eliminate the effect of spurious optical reflections from the back side of the GaAs substrate. Electrical characteristics of the layers were determined from the Hall-effect measurements. Both layers had a p-type conductivity, the resistivity was equal to 820 Ω·cm, the hole concentration was $8 \cdot 10^{13}$ cm^{-3}, and the hole mobility was 90 cm^2/V·s. The performance of photoconductive THz components manufactured from GaInAsBi epitaxial layers was investigated in a free-space THz TDS system based on femtosecond Er-doped fiber laser (Toptica)

Fig. 13.13 THz transient (**a**) and its Fourier spectrum (**b**) for TDS system based on femtosecond Er:fiber laser and photoconductive components from GaInAsBi epitaxial layers
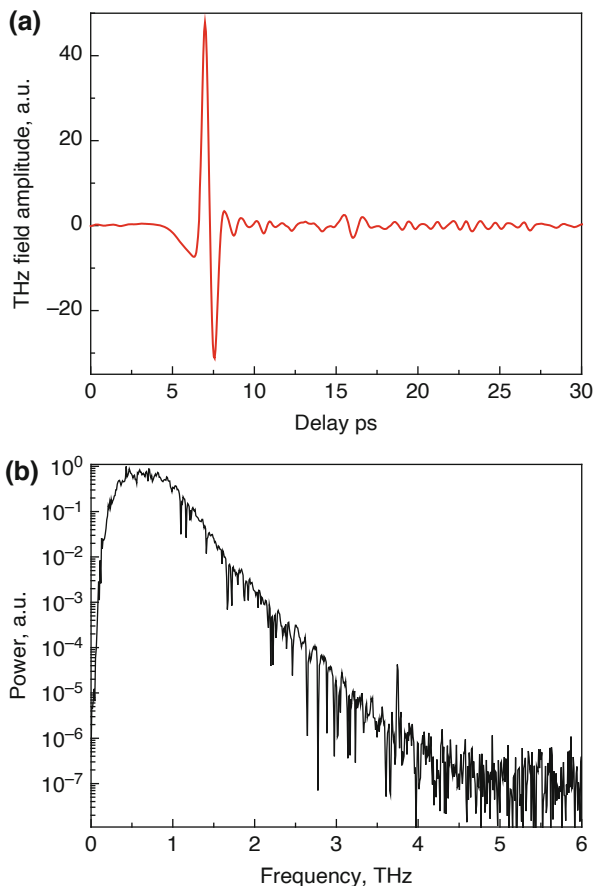
generating 1.55 µm wavelength, 100 fs duration, and 80 MHz repetition rate optical pulses. The generated THz radiation pulse and its Fourier spectrum are shown in Fig. 13.13.

A wide use of the bismide based optoelectronic THz components can be envisaged in future systems activated by 2 µm and longer wavelength femtosecond lasers, because by increasing the wavelength and decreasing photon energy of optical pulses leads to enhanced optical-to-THz conversion efficiencies. For the first time the THz pulse emission from GaInAsBi epitaxial layer grown on InP substrate employing such long wavelength optical pulses was demonstrated in [21]. Figure 13.14a shows the surface THz excitation spectrum of this layer compared with the spectrum of a PCA fabricated from it. A large aperture photoconductive emitter has 400 µm wide Ti/Au contacts with a 480 µm wide photosensitive gap. The photoconductor was mounted on a substrate lens made from a high resistivity silicon, the incoming laser beam was focused to the part of the gap close to the anode contact, and the light spot diameter was 100 µm. The energy bandgap of the material
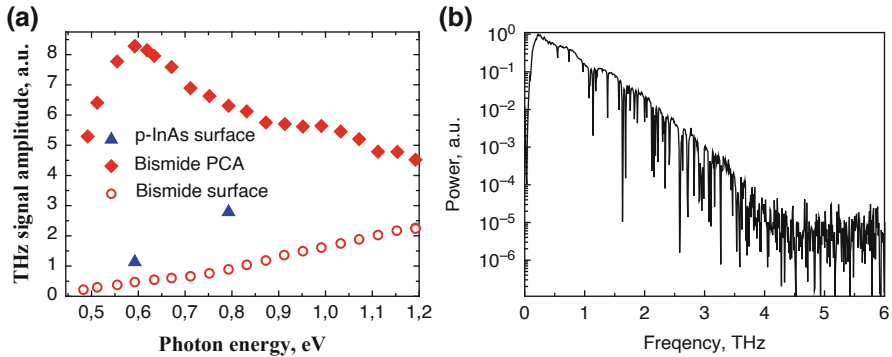
Fig. 13.14 (**a**) THz excitation spectra of the GaInAsBi epitaxial layer with 53%In and 6%Bi (layer i401, empty points) and PCA fabricated from that layer (full points) biased cw at 50 V voltage. Signal emitted from p-type InAs surface is shown for comparison. (**b**) Fourier spectrum emitted by PCA fabricated from this layer excited by 1.55 μm wavelength pulses and biased to 50 V [21]

is 0.4 eV, the THz emission is observed even at photon energies lower than 0.5 eV ($\lambda < 2.5$ μm). The Fourier spectrum of the THz pulse radiated by this emitter when photoexcited by 1.55 μm laser pulses is shown in Fig. 13.14b. Its signal-to-noise ratio is higher than 60 dB, which is comparable to PCAs made from Be-doped GaInAs/AlInAs superlattices [23].

Before concluding we would like to mention that advanced materials [41, 42] and compact sources for the THz region such as quantum cascade lasers and superlattice multipliers [43–53] are also being investigated by other teams and can potentially deliver complementary devices to those discussed in this paper.

13.6   Conclusions

By replacing bulky and expensive femtosecond Ti:sapphire lasers in the THz-TDS systems by more compact and cost effective fibre lasers could significantly expand the use of these unique spectroscopic techniques. The main research challenge in this field is to find appropriate semiconductor materials from which the optoelectronic THz emitters and detectors activated by 1 μm, 1.5 μm, or even 2 μm wavelength femtosecond optical pulses could be fabricated. Such materials should have relatively narrow energy bandgaps, which contradicts with the requirement of having a high dark resistivity that is, *e.g.*, of a critical importance for photoconductive THz emitters. For THz detector materials, on the other hand, the subpicosecond carrier lifetimes are necessary, which can mainly be achieved at the cost of their reduced mobilities. We had approached these challenges by working on two directions.

In the first research direction, the THz pulse emission from the surfaces of various semiconducting crystals illuminated by femtosecond laser pulses was investigated and compared. For the surface THz emitters such material limitations as a low

resistivity or a narrow bandgap that are critical for their PCA counterparts are unessential. The efficient surface THz emitters were established for all three spectral ranges of the fibre lasers mentioned above; their investigation has led to the determination of the microscopic phenomena behind the physical effect of the surface emission. The possibility of using a technically more convenient line-of-sight geometry of the emitter branch was also demonstrated. Though the absolute THz power radiated by surface emitters is still a few orders of magnitude lower than that radiated by the PCAs, they are competitive when one compares the frequency bandwidths and the signal-to-noise ratios. More progress could be expected when using specially designed multilayer structures or by placing the emitting material in an external magnetic field [40].

In the second direction, a novel group of semiconducting alloys – the ternary and quaternary bismides, were used as the substrates for the photoconductive THz emitters and detectors activated by the long wavelength laser pulses. The epitaxial layers of these alloys can be grown on the semi-insulating GaAs or InP that makes the fabricated PCAs compatible with the existing THz-TDS designs. The THz emitters and detectors activated by 1 μm wavelength femtosecond optical pulses were fabricated from the GaAsBi layers grown on GaAs substrates. For such devices activated by 1.5 μm range laser beams the quaternary GaInAsBi alloy with a particular combination of indium and bismuth contents was established, whereas the THz emitters and detectors for 2 μm spectral range were fabricated from the layers of this alloy grown on InP substrates.

References

1. Auston DH, Cheung KP, Valdmanis JA, Kleinman DA (1984) Cherenkov radiation from femtosecond optical pulses in electro-optic media. Phys Rev Lett 53:1555
2. Zhang XC, Hu BB, Darrow JT, Auston DH (1990) Generation of femtosecond electromagnetic pulses from semiconductor surfaces. Appl Phys Lett 56:1011
3. Carey JJ, Bailey RT, Pugh D, Sherwood JN, Cruickshank FR, Wynne K (2002) Terahertz pulse generation in an organic crystal by optical rectification and resonant excitation of molecular charge transfer. Appl Phys Lett 81:4335
4. Beaurepaire E, Turner GM, Harrel SM, Beard MC, Bigot JY, Schmuttenmaer A (2004) Coherent terahertz emission from ferromagnetic films excited by femtosecond laser pulses. Appl Phys Lett 84:3465
5. Ponseca CS Jr, Arlauskas A, Yu H, Wang F, Nevinskas I, Duda E, Vaičaitis V, Eriksson J, Bergqvist J, Liu XK, Kemerink M, Krotkus A, Inganas O, Gao F (2019) Pulsed terahertz emission from solution-processed lead iodide perovskite films. ACS Photonics 6:1175
6. Dekorsy T, Auer H, Waschke C, Baker HJ, Roskos HG, Kurz H, Wagner V, Grosse P (1995) Phys Rev Lett 74:738
7. Reklaitis A (2011) Crossover between surface field and photo-Dember effect induced terahertz emission. J Appl Phys 109:083108
8. Cicėnas P, Geižutis A, Malevich VL, Krotkus A (2015) Terahertz radiation from an InAs surface due to lateral pho-tocurrent transients. Opt Lett 40:5164

9. Reid M, Cravetchi IV, Fedosejevs R (2005) Terahertz radiation and second-harmonic generation from InAs: Bulk versus surface electric-field-induced contributions. Phys Rev B 72:035201

10. Malevich VL, Ziazulia PA, Adomavičius R, Krotkus A, Malevich YV (2012) Terahertz emission from cubic semiconductor induced by a transient anisotropic photocurrent. J Appl Phys 112:073115

11. Becker PC, Fragnito HL, Brito Cruz CH, Shah J, Fork RL, Cunningham JE, Henry JE, Shank CV (1988) Femtosecond intervalley scattering in GaAs. Appl Phys Lett 53:2089

12. Arlauskas A, Krotkus A (2012) THz excitation spectra of AIIIBV semiconductors. Semicond Sci Technol 27:115015

13. Arlauskas A, Subačius L, Krotkus A, Malevich VL (2017) Terahertz emission from InSb illuminated by femto-second laser pulses. J Phys D Appl Phys 50:055101

14. Norkus R, Arlauskas A, Krotkus A (2018) Terahertz excitation spectra of InP single crystals. Semicond Sci Technol 33:075010

15. Norkus R, Aleksiejūnas R, Kadys A, Kolenda M, Tamulaitis G, Krotkus A (2019) Spectral dependence of THz emission from InN and InGaN layers. Sci Rep 9:7077

16. Pačebutas V, Stanionytė S, Arlauskas A, Norkus R, Butkutė R, Geižutis A, Čechavičius B, Krotkus A (2018) Terahertz excitation spectra of GaAsBi alloys. J Phys D Appl Phys 51:474001

17. Nevinskas I, Vizbaras K, Vizbaras A, Trinkūnas A, Krotkus A (2016) Magnetic field enhanced terahertz pulse emission from a femtosecond laser excited GaSb epitaxial layer. Electron Lett 52:1627

18. Nevinskas I, Vizbaras K, Trinkūnas A, Butkutė R, Krotkus A (2017) Terahertz pulse generation from (111)-cut InSb and InAs crystals when illuminated by 1.55-μm femtosecond laser pulses. Opt Lett 42:2615

19. Nevinskas I, Stanionytė S, Pačebutas V, Krotkus A (2015) Terahertz emission from GaInAs p-i-n diodes photoex-cited by femtosecond laser pulses. Lith J Phys 55:274

20. Pačebutas V, Urbanowicz A, Cicėnas P, Stanionytė S, Bičiūnas A, Nevinskas I, Krotkus A (2015) Growth and characterization of quaternary (GaIn)(AsBi) layers for optoelectronic terahertz detector applications. Semicond Sci Technol 30:094012

21. Pačebutas V, Stanionytė S, Norkus R, Bičiūnas A, Urbanowicz A, Krotkus A (2019) Terahertz pulse emission from GaInAsBi. J Appl Phys 125:174507

22. Gupta S, Whitaker JF, Mourou GA (1992) Ultrafast carrier dynamics in III-V semiconductors grown by molecular beam epitaxy at very low substrate temperatures. IEEE J Quantum Electron 28:2464

23. Sartorius B, Roehle H, Künzel H, Böttcher J, Schlak M, Stanze D, Venghaus D, Schell M (2008) All-fiber terahertz time-domain spectrometer operating at 1.5 μm telecom wavelengths. Opt Express 16:9565

24. Wood CD, Hatem O, Cunningham JE, Linfield EH, Davies AG, Cannard PJ, Robertson MJ, Moodie DG (2010) Terahertz emission from metal-organic chemical vapor deposition grown Fe:InGaAs using 830 nm to 1.55 μm excitation. Appl Phys Lett 96:194104

25. Suzuki M, Tonouchi M (2005) Fe-implanted InGaAs THz emitters for 1.56 μm wavelength excitation. Appl Phys Lett 86:051104

26. Bertulis K, Krotkus A, Aleksejenko G, Pačebutas V, Adomavičius R, Molis G, Marcinkevičius S (2006) GaAsBi: a material for optoelectronic terahertz devices. Appl Phys Lett 88:201112

27. Pačebutas V, Bertulis K, Dapkus L, Aleksejenko G, Krotkus A, Yu KM, Walukiewicz W (2007) Characterization of low-temperature molecular-beam-epitaxy grown GaBiAs layers. Semicond Sci Technol 22:819

28. Cook DG, Hegmann FA, Young EC, Tiedje T (2006) Electron mobility in dilute GaAs bismide and nitride alloys measured by time-resolved terahertz spectroscopy. Appl Phys Lett 89:122103

29. Pačebutas V, Bertulis K, Aleksejenko G, Krotkus A (2009) Molecular-beam-epitaxy grown GaBiAs for terahertz optoelectronic applications. J Mater Sci Mater Electron 20:S363

30. Pačebutas V, Bičiūnas A, Balakauskas S, Krotkus A, Andriukaitis G, Lorenc D, Pugžlys A, Baltuška A (2010) Terahertz time-domain-spectroscopy system based on femtosecond Yb:fiber laser and GaBiAs photoconducting components. Appl Phys Lett 97:031111

31. Planken PCM, van Rijmenam CEWM, Schouten RN (2005) Opto-electronic pulsed THz systems. Semicond Sci Technol 20:S121
32. Chong A, Renniger W, Wise FW (2008) Properties of normal dispersion femtosecond fiber lasers. J Opt Soc Am B 25:140
33. Yoshimoto M, Murata S, Chayahara A, Horima Y, Saraie J, Oe K (2003) Metastable GaAsBi alloy grown by molecular beam epitaxy. Jpn J Appl Phys 42:L1235
34. Tixier S, Adamcyk M, Tiedje T, Francoeur S, Mascarenhas A, Wei P, Schietekatte P (2003) Molecular beam epitaxy growth of GaAsBi. Appl Phys Lett 82:2245
35. Francoeur S, Seong MJ, Mascarenhas A, Tixier S, Adamcyk M, Tiedje T (2003) Band gap of GaAsBi, 0<x<3.8%. Appl Phys Lett 82:3874
36. Pettinari G, Patane A, Polimeni A, Capizzi M, Lu X, Tiedje T (2012) Bi-induced p-type conductivity in nominally undoped Ga(AsBi). Appl Phys Lett 100:092109
37. Vurgaftman I, Meyer JR, Ram-Mohan LR (2001) Band parameters for III–V compound semi-conductors and their alloys. J Appl Phys 89:5815
38. Broderic CA, Usman M, Sweeney SJ, O'Reilly EP (2012) Band engineering in dilute nitride and bismide semiconductor lasers. Semicond Phys Technol 27:094011
39. Urbanowicz A, Pačebutas V, Geižutis A, Stanionytė S, Krotkus A (2016) Terahertz time-domain-spectroscopy system based on 1.55 μm fiber laser and photoconductive antennas from dilute bismides. AIP Adv 6:025218
40. Alberi K, Dubon OD, Walukiewicz W, Yu KM, Bertulis K, Krotkus A (2007) Valence band anticrossing in GaAsBi. Appl Phys Lett 91:051909
41. Beard MC, Turner GM, Schmuttenmaer CA (2001) Subpicosecond carrier dynamics in low-temperature grown GaAs as measured by time-resolved terahertz spectroscopy. J Appl Phys 90:5915
42. Nevinskas I, Kadlec F, Kadlec C, Butkutė R, Krotkus A (2019) THz pulse emission from an epitaxial n-InAs in a magnetic field. J Phys D Appl Phys 52:365301
43. Oriaku CI, Pereira MF (2017) Analytical solutions for semiconductor luminescence including Coulomb correlations with applications to dilute bismides. J Opt Soc Am B 34:321
44. Pereira MF (2018) Analytical expressions for numerical characterization of semiconductors per comparison with luminescence. Materials 11:2
45. Pereira MF (2016) The linewidth enhancement factor of intersubband lasers: from a two-level limit to gain with-out in-version conditions. Appl Phys Lett 109:222102
46. Pereira MF, Zubelli PJ, Winge D, Wacker A, Rondrigues SA, Anfertvev V, Vaks V (2017) Theory and measurements of harmonic generation in semiconductor superlattices with appli-cations in the 100 GHz to 1 THz range. Phys Rev B 96:045306
47. Pereira MF, Anfertev V, Zubelli JP, Vaks V (2017) Terahertz generation by gigahertz multi-plication in superlattices. J Nanophoton 11(4):046022
48. Apostolakis A, Pereira MF (2019) Controlling the harmonic conversion efficiency in semicon-ductor superlattices by interface roughness design. AIP Adv 9:015022
49. Apostolakis A, Pereira MF (2019) Numerical studies of superlattice multipliers performance. Quantum Sensing Nano Electron Photonics XVI:109262
50. Apostolakis A, Pereira MF (2019) Potential and limits of superlattice multipliers coupled to different input power sources. J Nanophotonics 13:036017
51. Winge DO, Franckié M, Verdozzi C, Wacker A (2016) Simple electron-electron scattering in non-equilibrium Green's function simulations. J Phys Conf Ser 696:012013
52. Pereira MF, Shulika O (2014) Terahertz and mid infrared radiation: detection of explosives and CBRN (using te-rahertz), NATO science for peace and security series-b: physics and biophys-ics. Springer, Dordrecht
53. Pereira MF, Shulika O (2011) Terahertz and mid infrared radiation: generation, detection and applications, NATO science for peace and security series-B: physics and biophysics. Springer, Dordrecht

Chapter 14
Soft Chemical Ionization Mass Spectrometric Analyses of Hazardous Gases and Decomposition Products of Explosives in Air

Kseniya Dryahina and Patrik Spanel

Abstract The need for rapid and accurate measurement of trace concentrations of compounds present in ambient humid air has led to construction of specialised mass spectrometers based on the Selected Ion Flow Tube Mass Spectrometry, SIFT-MS, its drift-tube variant, SIFDT-MS, and Proton Transfer Mass Spectrometry, PTR-MS. It is currently possible to analyse vapours of volatile organic compounds, VOC, and other gases including ammonia, hydrogen sulphide and hydrogen cyanide present in concentrations even below a part per billion by volume, ppbv. The reagent ions are formed in electrical discharges and their ion-molecule reactions with sampled analyte molecules take place at pressures of 1–2 mbar. As an example of analytical use, SIFT-MS coupled with the Laser Induced Breakdown, LIB, technique was used to analyse stable gaseous products from the decomposition of pure explosive compounds HMX, RDX, PETN and TNT and from 38 types of commercial explosive and propellant mixtures. Decomposition products analysed included NH_3, HCN, HCHO, NO, NO_2, HONO, HNO_3, C_2H_5OH, CH_3CN, DMNB, C_2H_6CO, C_2H_2 and nitroglycerine. For four selected explosives, it was found that the end products of the microscopic LIB laboratory tests correspond well to the composition of fumes from realistic explosions of 0.5 kg charges.

14.1 Introduction

The techniques currently available for analyses of trace gases and volatile organic compound (VOC) vapours in air and breath can be categorised thus:

K. Dryahina (✉) · P. Spanel
Department of Chemistry of Ions in Gaseous Phase, J. Heyrovský Institute of Physical Chemistry of the CAS, Prague, Czech Republic
e-mail: kseniya.dryahina@jh-inst.cas.cz; patrik.spanel@jh-inst.cas.cz

- Spectroscopy (including infrared and terahertz)
- Sensors (including electrochemical, nanoparticle, quartz microbalances)
- Ionization - mass spectrometry (MS) [1], and ion mobility spectrometry (IMS) [2, 3]

MS methods offer superior identification of VOCs and can attain excellent limits of detection, whilst IMS devices often do not need vacuum pumps and can be miniaturised.

The background and state-of-the art of trace gas analysis in breath and environmental monitoring has been reviewed in detail [4–6]. The techniques based on chemical ionization in flow or drift tubes are Selected Ion Flow Tube Mass Spectrometry (SIFT-MS), its drift-tube variant (SIFDT-MS) and Proton Transfer Mass Spectrometry (PTR-MS). They are all based on chemical ionisation by externally generated reagent ions and achieve reliable quantification in defined reaction times. Other relevant and presently available techniques are Secondary Electrospray Ionisation Mass Spectrometry (SESI-MS) [7], which has exceptional sensitivity [8], and the Ion Mobility Spectrometry (IMS) family of techniques that allow selection of ions in handheld instruments [9].

SIFT-MS is used for real-time detection of fumigants, toxic industrial compounds and other hazardous substances at the point of container inspection. Industry-leading accuracy, speed, and reliability for critical safety testing of trapped air in shipping containers is achieved. Mass spectrometric methods based on soft chemical ionisation have been tested for the rapid and simple identification of unknown explosives by controlled decomposition of their trace amounts and subsequent characterization of appropriate spectra of their combustion products. The chemical composition of the headspace and combustion products of the explosives have been analysed by SIFT-MS.

An understanding of the complex processes involved in the decomposition of energetic materials is essential for the development of reliable models for the performance, stability and hazard analysis of explosives. Identification of the decomposition products is of prime importance in identifying toxic, hazardous and environmentally polluting species. Energetic and explosive materials are substances or mixtures that chemically react releasing large amounts of rapidly liberated heat and gases. Today, approximately 150 different formulas are used for the military, commercial, and illicit production of explosives [10, 11]. Energetic materials and explosives may be inorganic or organic in nature and can be divided into two broad categories (low-energy explosives and high-energy explosives) based on how readily a reaction is initiated and its intensity.

Most trace explosive detection techniques, such as IMS and gas chromatography (GC), rely on vapour detection. Unfortunately, at room temperature, the vapour pressures of many common explosives are extremely small (ppbv or less), and attempts to conceal the explosives by sealing them in packaging materials can decrease the vapour concentrations by as many as three orders of magnitude [12]. An alternative optical technique for the detection of explosives is laser-induced breakdown spectroscopy (LIBS) [13]. The ability of LIBS to provide a remote, rapid

multi-element microanalysis of bulk samples (solid, liquid, gas and aerosol) in the parts-per-million by volume, ppmv, range with little or no sample preparation has been widely demonstrated and it is the greatest advantage of LIBS compared with other analytical approaches. LIBS holds particular promise for the detection and identification of explosives because of its intrinsic capability for minimally destructive, in situ, real-time detection and analysis of chemical species. More recently, the capability of LIBS to identify compounds has been realised with the advent of high-resolution broadband spectrometers. A promising method for the analysis of the stable decomposition products of energetic materials is a combination of LIB with SIFT-MS. [12, 14–16]

14.2 Quantitative Mass Spectrometry Techniques for Trace Gas Analysis

14.2.1 Selected Ion Flow Tube Mass Spectrometry (SIFT-MS)

Selected ion flow tube mass spectrometry (SIFT-MS) is a quantitative mass spectrometry technique for trace gas analysis which involves the chemical ionization of trace volatile compounds by selected positive reagent ions during a well-defined time period along a flow tube [17–19]. Absolute concentrations of trace compounds present in air, exhaled breath or the headspace of samples can be calculated in real time from the ratio of the reagent and analyte ion signal ratios, without the need for sample preparation or calibration with standard mixtures. H_3O^+, NO^+ and $O_2^{+\bullet}$ are the most suitable reagent ions, because they do not react rapidly with the major components of air and breath viz. N_2, O_2, H_2O, CO_2 and Ar, but they do react rapidly with most VOCs forming characteristic analyte ions that identify the various neutral molecules, M, in the air sample being analysed. However, when humid air or breath is analysed, hydrated ions of the kind $H_3O^+(H_2O)_{1,2,3}$, and $NO^+(H_2O)_{1,2}$ can form from the simple ions and these hydrates can also act as reagent ions leading to hydrated analyte ions of the kind $MH^+(H_2O)_{1,2,3}$. Then it is important to recognise that all the reagent and characteristic analyte ion species must be included to obtain correct analysis of each M [17–19].

A simple example is the reaction of acetone with H_3O^+ reagent ions in SIFT-MS. It proceeds rapidly by the process of proton transfer producing protonated acetone:

$$H_3O^+ + CH_3COCH_3 \rightarrow CH_3COCH_3H^+ + H_2O \tag{14.1}$$

When the concentration of acetone, [M], is small, the fractional reduction in the large reagent ion count rate is immeasurably small, but the much smaller count rates of the analyte ions can still be determined accurately. It is easy to show that the number density of the analyte ions $[MH^+]$ are related to the number density of the
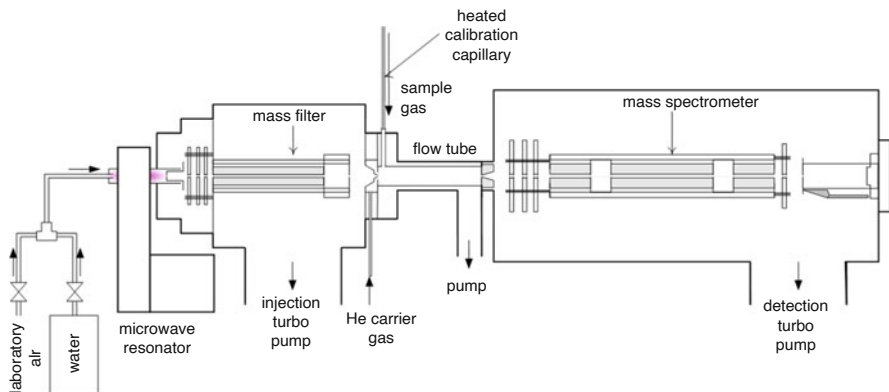
Fig. 14.1 Schematics of the *Profile* 3 SIFT-MS instrument. (Reproduced from Ref. [14] with permission from The Royal Society of Chemistry)

reagent ions [H$_3$O$^+$] as [MH$^+$] = [H$_3$O$^+$]k[M]tD_e. where k is the rate coefficient for the reaction of the H$_3$O$^+$ ions with the trace gas analyte molecules present at a number density [M] and t is the reaction time. D_e is a differential diffusion enhancement coefficient that accounts for the fact that the reagent ions and the analyte ions diffuse at different rates to the walls of the flow tube and this influences their relative number densities at the downstream sampling orifice (see Fig. 14.1), and this differential diffusion must be accounted for to obtain an accurate quantification of M. [18, 20–22] Also, mass discrimination against larger *m/z* ions in the analytical quadrupole mass spectrometer [20, 22] and the formation of hydrated reagent and analyte ions [18, 22] must be accounted for. Thus, the concentrations of trace gases in humid component mixtures such as exhaled breath can readily be calculated from the observed count rates of each analyte ion species. Of great significance is that the analyses only involve the ratio of the characteristic analyte ion count rates to the reagent ion count rates and so any drift in the reagent ion count rate does not invalidate the analyses.

The detection sensitivity of a SIFT-MS instrument depends on the count rates of the reagent ions that can be realised. For the current *Profile 3* instruments [20] these are up to 3 million counts-per-second, c/s, and the sensitivity for most VOCs is typically 10 c/s per ppbv corresponding to a practical detection limit of 1 ppbv per second of integration time. Detection limits in the sub-ppbv range have been validated for aromatic hydrocarbons [23] using longer integration times. The absolute accuracy of SIFT-MS has been validated to be better than 10% [20, 22, 24] for several compounds without the need for external standards, as long as the sample and carrier gas flow rates and flow tube temperature are accurately known and mass discrimination and diffusion effects are accounted for.

SIFT-MS instruments can be operated in two modes: They are (i) the full scan (FS) mode in which a complete mass spectrum of reagent and analyte ions is obtained by sweeping the analytical quadrupole mass spectrometer over a selected *m/z*, range for a chosen time whilst a sample of air or breath is introduced into the

carrier gas. The resulting mass spectrum is interpreted by relating the analyte ions to the trace gases present in the sample using the acquired knowledge of the ion chemistry. The concentrations of the individual trace gases can be calculated using the in-built kinetics library. (ii) the multiple ion monitoring (MIM) mode in which the count rates of the reagent ions and their hydrates, such as $H_3O^+(H_2O)_n$, and a number of characteristic analyte ions appropriate to the number of trace compounds to be analysed are monitored as air or breath displaces the ambient air at the entrance to the sampling capillary (see Fig. 14.1). This reagent ion and analyte ion monitoring is achieved by rapidly switching the downstream mass spectrometer between the several *m/z* values of the reagent and analyte ions, dwelling on each *m/z* for a predetermined short time interval. This real-time monitoring is possible because of the fast time response of SIFT-MS, which is typically less than 20 ms. The humidity of the sampled air (for example, exhaled breath consists of 6% water vapour) is routinely obtained from the data and is an indicator of sample quality and control [25].

14.2.2   Proton Transfer Reactions Mass Spectrometry (PTR-MS)

Proton transfer reactions mass spectrometry (PTR-MS) is essentially a flow-drift tube chemical ionisation (CI) analytical technique [26–28]. Ions are generated in a hollow cathode discharge and injected into a flow-drift tube buffered with the sample gas to be analysed, usually air. The ions experience an electric field coaxial with the flow tube and gain energy reaching a drift speed in the field direction and arrive at a downstream orifice where they are sampled into a differentially pumped mass spectrometer system and analysed in an analogous way to that in SIFT-MS. The reagent ions mostly used to date are H_3O^+ so, as explained previously; the primary reaction process utilized for analysis is proton transfer exemplified by reaction (14.1). Because a mass filter is not used to select reagent ions, higher currents of reagent ions can be injected, and the axial electric field results in less diffusive loss of the reagent ions to the walls of the flow-drift tube. Diffusive loss is also reduced by usage of air (the sample to be analysed) as the buffer/carrier gas rather than the lighter helium gas as used in SIFT-MS. the pressures used in the PTR-MS drift tube being different than that used in SIFT-MS flow tube. The net result is that greater count rates of the reagent H_3O^+ ions are available which leads to greater analytical sensitivity. Thus, detection limits can be in the parts-per-trillion by volume, pptv, to the sub-ppbv regime [29, 30]. Since the reagent ion energies are elevated above thermal, the formation of cluster ions of the kind $H_3O^+(H_2O)_{1,2,3}$ are suppressed in comparison with SIFT-MS, although the actual count rates depend sensitively on the ratio of electric field strength to the buffer gas number density, E/N. A very good review of PTR-MS has been given recently [27].

The kinetics of the analytical ion-molecule reactions and the reaction time can be sensitive to E/N; thus accurate quantification is not simply achieved. A canonical value $(2 \times 10^{-9} \, \mathrm{cm^3 s^{-1}})$ for the collisional reaction rate coefficients, k_c, is often used to estimate trace gas concentrations from PTR-MS data. Quantification is directly dependent on k, which can vary widely for ion-molecule reactions in the thermal energy regime (over the range $1–5 \times 10^{-9} \, \mathrm{cm^3 s^{-1}}$), so a commensurate uncertainty can be introduced into PTR-MS quantification. However, such uncertainties can be minimised using calibration techniques. It is for these reasons that PTR-MS has been used only sporadically for breath analysis [31] where greater accuracy is needed; rather, it has mostly been used for air analysis [28] and environmental studies [32, 33]. A further problem is that following proton transfer from H_3O^+ to M, some MH^+ nascent analyte ions can undergo spontaneous unimolecular dissociation or collision induced dissociation, and this must be recognised to avoid false compound identifications; see for example [34, 35]. Unimolecular dissociation of MH^+ analyte ions can occur even under the thermal energy conditions of SIFT-MS [36–38], but collision induced dissociation is exacerbated in PTR-MS where the ion-molecule interaction energies are suprathermal. Further, in conventional PTR-MS it is also impossible to separate isobaric compounds when only H_3O^+ reagent ions are used, because they simply result in MH^+ ions with the same *m/z* or fragments of these. This problem is alleviated in SIFT-MS that exploits NO^+ and $O_2^{+\bullet}$ reagent ions also. Other reagent ions can be used by changing the discharge gas composition in PTR-SRI-MS instruments [29] and high resolution analytical time-of-flight, TOF, mass spectrometers that can separate nominally isobaric compounds. [39–41]

14.2.3 Selected Ion Flow Drift-Tube Mass Spectrometry (SIFDT-MS)

The selected ion flow drift tube mass spectrometric analytical technique (SIFDT-MS) [42–44] extends the SIFT-MS by the inclusion of a static but variable *E*-field along the axis of the flow tube reactor in which the analytical ion-molecule chemistry occurs (see Fig. 14.2). The ion axial speed is increased in proportion to *E/N*. The residence/reaction time, *t*, measured by Hadamard transform multiplexing, is proportionally reduced. To ensure a proper understanding of the physics and ion chemistry underlying SIFDT-MS, ion diffusive loss to the walls of the flow-drift tube and the mobility of injected H_3O^+ ions have been studied as a function of *E/N* [44]. The production of hydrated reagent and analyte ion also has been experimentally investigated [44].

The analytical performance of SIFDT-MS has been demonstrated by the quantification of acetone and isoprene in exhaled breath. [44] A major advance compared to SIFT-MS is that the speed of ions through the reaction zone can be achieved using the adjustable *E*-field, which allows the suppression of ion diffusion losses even at
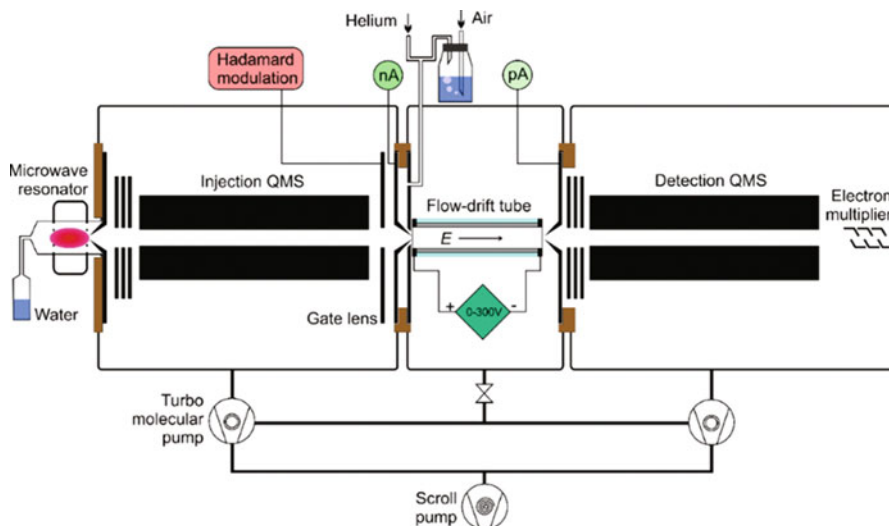
Fig. 14.2 Schematic drawing of the SIFDT apparatus. Note that the flow speed of the helium carrier gas is reduced by a restrictive aperture between the flow-drift tube compartment and the scroll pump. (Reprinted with permission from Ref. [44]. Copyright (2015) American Chemical Society)

very low carrier gas flow speeds. This corresponds to helium carrier gas and sample gas flow rates more than 7 times lower than those used in *Profile 3* SIFT-MS instruments. Thus, a less powerful vacuum pump can be used to maintain the gas flow along the ion-chemical reactor and a smaller helium carrier gas pressure reservoir is needed, which facilitates production of smaller and more versatile transportable instruments. Furthermore, smaller sample flow rates can be used for analysis, which is a distinct advantage when liquid headspace is to be analysed, which results in the less formation of ion hydrates. The simplicity of construction of the SIFDT-MS instrument is due to the use of a resistive glass flow-drift tube element and by adopting the Hadamard transform multiplexing for direct reaction time measurement, which is another improvement on SIFT-MS in which the reaction times are fixed and calculated indirectly from the carrier gas pressure and flow rate. The presence of the *E*-field results in an increase of the kinetic and internal energies of the ions that influences hydrated ion formation. Initial studies have confirmed that variation of *E/N* modifies the count rates of hydrated analyte ions relatively to the primary analyte ions without significantly modifying the bimolecular ion chemistry [42], thus promising more accurate analyses. However, it is worthy of note that increasing *E/N* to higher values (>20 Td) can promote controlled collisional disso-ciation of ions, and this might ultimately allow isobaric ions to be distinguished, a technique well known in MS-MS methods.

14.3 Decomposition Products of Explosives

To study degradation products of explosives material, SIFT-MS has been coupled with LIB. Thus, a small amount of a sample was irradiated by a sequence of 10 laser pulses each of 150 mJ using an ArF excimer laser and the stable gaseous products from the reaction zone were analysed simultaneously using SIFT-MS (see Fig. 14.3). More than 40 types of commercially produced explosives and propellants were studied in this experimental set-up and a spectral database was obtained. The concentrations of the decomposition products were determined for pure explosive compounds like HMX, RDX, PETN and TNT and for 38 types of commercially produced explosives and propellants.

Four typical representatives of industrial explosives were chosen also for the analyses of fumes from realistic explosions:

- EMSIT 1 is the underground blasting explosive of emulsion type based on ammonium and sodium nitrates;
- Ostravit C is a semi-plastic permissible gas-proof explosive contains nitro esters, mixture of nitroglycerine and ethylene glycol dinitrate;
- Perunit 28E is an explosive of a classical dynamite type; is a mixture of ammonium nitrate, nitrocellulose, and nitroglyceroglycol;
- Permonex V19 is the underground blasting powder explosive based on ammonium nitrate and TNT.

Analyses involving these explosives were carried out in four different ways:

- volatile compounds released into the **headspace** of explosives were sampled from 40 mL vials with small amount of explosive (5 g) without initiating breakdown or explosion.
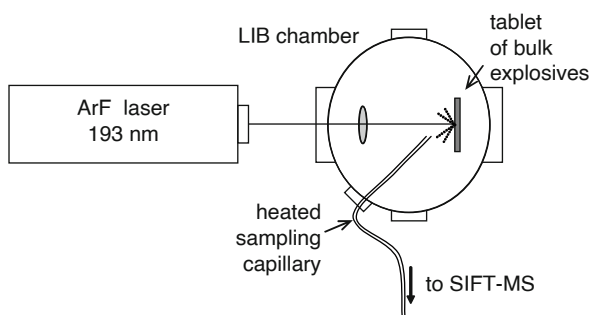
Fig. 14.3 Schematic diagram of the experimental apparatus. An ArF excimer laser (193 nm, 20 ns, and 150 mJ) was used to create pulses of radiation that were focused by a 15 cm quartz lens onto the surface of a rotating target placed in a vacuum chamber filled with Ar at a pressure of 1 atm. The stable gaseous products originating from the plasma generated by ten repeated laser pulses were extracted via a heated calibrated PEEK capillary. (Reproduced from Ref. [14] with permission from The Royal Society of Chemistry)

- fumes after **detonation** of 500 g of each explosive in a test tunnel collected into 2 L glass vessels.
- headspace above 1 kg of **sand** collected after explosion of 50 g of explosives in a steel barrel containing 10 kg of clean dry sand.
- fumes from the reaction zone of the **LIB** chamber in real time by SIFT-MS; a sequence of 10 laser pulses, 150 mJ each (ArF excimer laser) was used to simulate the explosion or combustion on a microscopic laboratory scale. The experimental set-up is shown in Fig. 14.3

SIFT-MS spectra were collected in the full scan mode over the range of m/z 10–240 which fully covers the generated volatiles at room temperature. The spectra obtained for Perunit 28E explosive are shown in Fig. 14.4. The composition of the end products of laser generated plasma plumes corresponds well to the composition of fumes collected after explosion of a much larger (500 g) charges.

HCN is a typical analyte of the explosion and it is not present in the headspace of any of the explosives. It is not surprising that it is present in the LIB samples and in the fumes after explosion in a test tunnel. However, we did not expect to see such a relatively large amount of HCN in sand samples. In order to confirm that HCN is generated in the LIB plume chemistry, the MIM mode of the SIFT-MS instrument was used to record time profiles of the concentrations of HCN during and after repeated LIB events. The plot of the real time variation of concentration of HCN in response to two separate laser pulses is shown in Fig. 14.5. HCN is generated immediately after the laser pulse and its concentration then slowly decreases over several seconds due to its diffusion into the volume of the experimental chamber.

The exponential time constant for the decay of 15 s corresponds to a characteristic diffusion length of 3–4 cm considering a diffusion coefficient 0.2 cm^2 s^{-1}. Part of HCN is produced by the reaction of excited CN radicals with water vapor molecules H$_2$O [14]. The activation energy of this reaction is 4.7 kcal mol^{-1} [14] and this reaction is thus easily energetically accessible at T > 4000 K. The concentrations obtained using the same experimental apparatus in the absence of any explosive samples are also given. Note that the levels of ethanol, NO, NO$_2$, HONO, and HCN were significantly elevated in all of the LIB experiments [12].

The concentrations of the decomposition products (NH$_3$, HCN, HCHO, NO, NO$_2$, HONO, HNO$_3$, C$_2$H$_5$OH, CH$_3$CN, DMNB, C$_2$H$_6$CO, C$_2$H$_2$ and nitroglycerine) were determined for pure explosive compounds HMX, RDX, PETN and TNT [14, 16] and for commercially produced explosives and propellants [12, 15]. The mean absolute concentrations of these stable products obtained during the first 10 s after the LIB event for the several explosives are given in Table 14.1 in units of ppbv, equivalent to nmol mol^{-1}. Trace amounts of DMNB were present due to its use as a volatile marker deliberately added into some explosives in the manufacturing process.
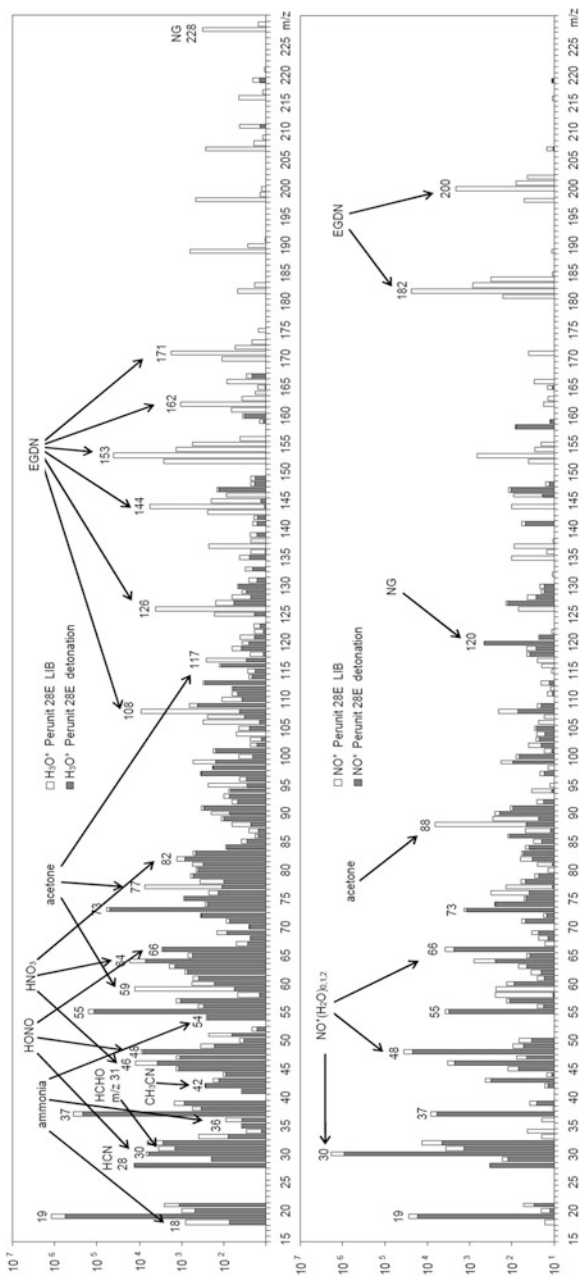
Fig. 14.4 Comparison of SIFT-MS spectra of the fumes after detonation in a test tunnel with the spectra of the fumes obtained on a microscopic scale by the LIB method is presented for Perunit 28E
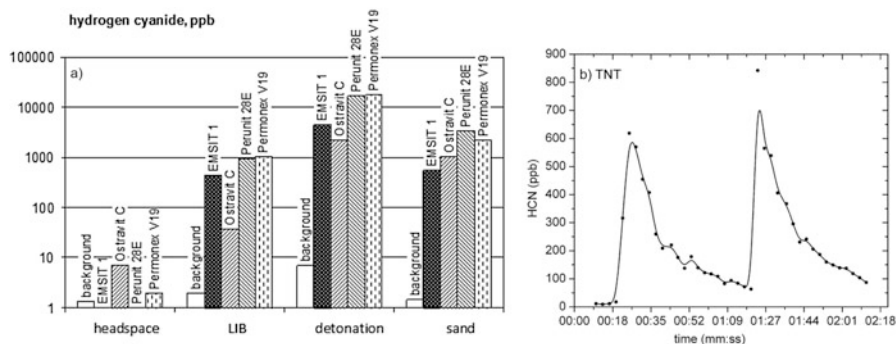
Fig. 14.5 (**a**) HCN concentration in ppb unit quantified in the headspace and fumes after detonation in test tunnel (detonation) and after combustion on a microscopic laboratory scale (LIB), headspace above sand collected after explosion. (**b**) Time dependence of the HCN concentration obtained by SIFT-MS after irradiation of a TNT sample by two sequential laser pulses. (Reproduced from Ref. [14] with permission from The Royal Society of Chemistry)

14.4   Conclusions

The combined experiments using LIB and SIFT-MS have allowed the analyses of the volatile decomposition products of commercial explosive mixtures, and it has been demonstrated that the methodology presented in this paper can be used for safe and non-destructive studies of characteristic explosion products without the need for the initiation of hazardous quantities of explosives in the form of test charges. It is also interesting to note that according to preliminary experiments, the compositions of the end products of the laser-generated plasma plumes correspond well to the composition of the fumes collected after the explosion of much larger (0.5 kg) charges. Therefore, we suggest that the results of the present study are relevant to the analysis of gaseous residues of explosions and the combustion products of real explosives and propellants.

Before concluding we would like to mention that materials [45, 46] and compact devices such as quantum cascade lasers and superlattice multipliers [47–52] are under development for the GHz-THz-MIR range, where the substances analysed here have well defined absorption signatures. These devices can deliver complementary sensors that can be combined with those here. A joint effort can potentially increase the efficiency for detection of hazardous gases and decomposition products of explosives in air.

Table 14.1 Mean concentrations in parts per billion by volume (ppbv) of the compounds identified by SIFT-MS in the atmosphere inside the experimental chamber after the initiation of the explosive samples using laser pulses

Sample	Acetylene	Acetonitrile	Ammonia	DMNB	Formaldehyde	Hydrogen cyanide	Nitric acid	Nitric oxide	Nitrous acid	Nitrogen dioxide	Nitroglycerine
TNT	28	4	46	32	46	533	75	339	45	171	4
RDX	3	8	56	9	87	746	58	856	48	90	0
HMX	0	0	10	17	11	18	22	462	38	163	6
PETN	13	10	19	18	285	91	21	1129	41	221	0
EMSIT 1	127	8	502	11	437	448	159	2144	932	2831	20
Ostravit C	9	0	1872	30	498	84	524	2218	1275	5786	242
Perunit 28E	46	8	287	21	1508	801	17,832	19,694	3094	64,513	355
Permonex V19	0	0	19	0	4	12	6	112	8	69	0
Guanidinium nitrate	0	1	21	8	39	11	30	553	25	18	2
Nitrosourea	0	0	8	0	23	6	16	572	8	30	2
Urea nitrate	0	0	14	4	38	9	33	255	17	30	1
Pickric acid	0	0	17	3	30	8	15	548	6	34	2
Tetryl	6	1	29	3	38	57	24	907	15	62	3
Ammonium nitrate	0	1	37	2	44	5	14	861	16	59	1
Semtex 10	0	3	15	72	117	116	75	479	29	28	6
Semtex 1A	103	3	70	62	132	101	62	767	31	87	0
PETN+wax	29	3	45	11	82	47	27	1009	23	89	1
Nitrocelullose A	0	0	47	3	113	32	36	580	50	64	0
Nitrocelullose B	2	0	40	2	89	15	44	565	85	43	2
Lovex S011	0	0	30	6	121	3	46	343	19	37	2
Lovex S040	0	0	24	10	150	23	52	765	34	146	3

Data from Refs. [15, 16]

References

1. Pu F et al (2019) Direct sampling mass spectrometry for clinical analysis. Analyst 144:1034–1051
2. Covington JA et al (2015) The application of FAIMS gas analysis in medical diagnostics. Analyst 14:6775–6781
3. Baumbach JI (2009) Ion mobility spectrometry coupled with multi-capillary columns for metabolic profiling of human breath. J Breath Res 3:034001
4. Davies SJ et al (2014) Breath analysis of ammonia, volatile organic compounds and deuterated water vapor in chronic kidney disease and during dialysis. Bioanalysis 6:843–857
5. Španěl P, Smith D (2011) Volatile compounds in health and disease. Curr Opin Clin Nutr Metab Care 14:455–460
6. Finamore P et al (2019) Breath analysis in respiratory diseases: state-of-the-art and future perspectives. Expert Rev Mol Diagn 19:47–61
7. Garcia-Gomez D et al (2016) Secondary electrospray ionization coupled to high-resolution mass spectrometry reveals tryptophan pathway metabolites in exhaled human breath. Chem Commun 52:8526–8528
8. Ke MF et al (2019) Generating supercharged protein ions for breath analysis by extractive electrospray ionization mass spectrometry. Anal Chem 91:3215–3220
9. Anttalainen O et al (2018) Differential mobility spectrometers with tuneable separation voltage - theoretical models and experimental findings. Trac-Trends Anal Chem 105:413–423
10. Matyáš R, Pachman J (2013) Primary explosives. Springer, Berlin/Heidelberg
11. Politzer P, Murray JS (2003) Energetic materials. Part 2. Detonation, combustion. Elsevier Science, Amsterdam
12. Civiš M et al (2011) Laser ablation of FOX-7: proposed mechanism of decomposition. Anal Chem 83:1069–1077
13. Cremers DA, Radziemski LJ (2013) Handbook of laser-induced breakdown spectroscopy, 2nd edn. Blackwell Science Publishing, Oxford
14. Sovová K et al (2010) A study of the composition of the products of laser-induced breakdown of hexogen, octogen, pentrite and trinitrotoluene using selected ion flow tube mass spectrometry and UV-Vis spectrometry. Analyst:1106–1114
15. Civis S et al (2016) Selected ion flow tube mass spectrometry analyses of laser decomposition products of a range of explosives and ballistic propellants. Anal Methods 8:1145–1150
16. Lehký L, Kyncl M (2008) Projekt report. FT-TA4/124: research of new methods of detection of explosives
17. Španěl P, Smith D (1996) Selected ion flow tube: a technique for quantitative trace gas analysis of air and breath. Med Biol Eng Comput 34:409–419
18. Španěl P et al (2006) A general method for the calculation of absolute trace gas concentrations in air and breath from selected ion flow tube mass spectrometry data. Int J Mass Spectrom 249:230–239
19. Smith D, Španěl P (2005) Selected ion flow tube mass spectrometry (SIFT-MS) for on-line trace gas analysis. Mass Spectrom Rev 24:661–700
20. Smith D et al (2009) Ionic diffusion and mass discrimination effects in the new generation of short flow tube SIFT-MS instruments. Int J Mass Spectrom 281:15–23
21. Dryahina K, Španěl P (2005) A convenient method for calculation of ionic diffusion coefficients for accurate selected ion flow tube mass spectrometry, SIFT-MS. Int J Mass Spectrom 244:148–154
22. Španěl P, Smith D (2001) Quantitative selected ion flow tube mass spectrometry: the influence of ionic diffusion and mass discrimination. J Am Soc Mass Spectrom 12:863–872
23. Dryahina K et al (2018) Quantification of volatile compounds released by roasted coffee by selected ion flow tube mass spectrometry. Rapid Commun Mass Spectrom 32:739–750
24. Španěl P et al (1997) Validation of the SIFT technique for trace gas analysis of breath using the syringe injection technique. Ann Occup Hyg 41:373–382

25. Španěl P, Smith D (2001) On-line measurement of the absolute humidity of air, breath and liquid headspace samples by selected ion flow tube mass spectrometry. Rapid Commun Mass Spectrom 15:563–569

26. Lindinger W et al (1998) On-line monitoring of volatile organic compounds at pptv levels by means of proton-transfer-reaction mass spectrometry (PTR-MS) medical applications, food control and environmental research. Int J Mass Spectrom Ion Process 173:191–241

27. Blake RS et al (2009) Proton-transfer reaction mass spectrometry. Chem Rev 109:861–896

28. J d G, Warneke C (2007) Measurements of volatile organic compounds in the earth's atmosphere using proton-transfer-reaction mass spectrometry. Mass Spectrom Rev 26:223–257

29. Jordan A et al (2009) An online ultra-high sensitivity proton-transfer-reaction mass-spectrometer combined with switchable reagent ion capability (PTR+ SRI- MS). Int J Mass Spectrom 286:32–38

30. Lindinger W, Jordan A (1998) Proton-transfer-reaction mass spectrometry (PTR-MS): on-line monitoring of volatile organic compounds at pptv levels. Chem Soc Rev 27:347–375

31. Karl T et al (2001) Human breath isoprene and its relation to blood cholesterol levels: new measurements and modeling. J Appl Physiol 91:762

32. De Gouw J et al (2003) Validation of proton transfer reaction-mass spectrometry (PTR-MS) measurements of gas-phase organic compounds in the atmosphere during the New England Air Quality Study (NEAQS) in 2002. J Geophys Res-Atmos 108(4682)

33. Hewitt C et al (2003) The application of proton transfer reaction-mass spectrometry (PTR-MS) to the monitoring and analysis of volatile organic compounds in the atmosphere. J Environ Monit 5:1–7

34. Taipale R et al (2008) Technical note: quantitative long-term measurements of VOC concentrations by PTR-MS-measurement, calibration, and volume mixing ratio calculation methods. Atmos. Chem Phys 8:6681–6698

35. Schripp T et al (2010) Interferences in the determination of formaldehyde via PTR-MS: what do we learn from m/z 31? Int J Mass Spectrom 289:170–172

36. Schoon N et al (2007) A selected ion flow tube study of the reactions of H_3O^+, NO^+ and O_2^+ with a series of C_5, C_6 and C_8 unsaturated biogenic alcohols. Int J Mass Spectrom 263:127–136

37. Španěl P et al (2004) Quantification of hydrogen cyanide in humid air by selected ion flow tube mass spectrometry. Rapid Commun Mass Spectrom 18:1869–1873

38. Dhooghe F et al (2009) Flowing afterglow selected ion flow tube (FA-SIFT) study of ion/molecule reactions in support of the detection of biogenic alcohols by medium-pressure chemical ionization mass spectrometry techniques. Int J Mass Spectrom 285:31–41

39. Blake RS et al (2006) Chemical ionization reaction time-of-flight mass spectrometry: multi-reagent analysis for determination of trace gas composition. Int J Mass Spectrom 254:85–93

40. Wyche K et al (2005) Differentiation of isobaric compounds using chemical ionization reaction mass spectrometry. Rapid Commun Mass Spectrom 19:3356–3362

41. Blake R et al (2004) Demonstration of proton-transfer reaction time-of-flight mass spectrometry for real-time analysis of trace volatile organic compounds. Anal Chem 76:3841–3845

42. Spesyvyi A et al (2017) Ion chemistry at elevated ion-molecule interaction energies in a selected ion flow-drift tube: reactions of H_3O^+, NO^+ and O_2^+ with saturated aliphatic ketones. Phys Chem Chem Phys 19:31714–31723

43. Spesyvyi A et al (2016) In-tube collision-induced dissociation for selected ion flow-drift tube mass spectrometry, SIFDT-MS: a case study of NO+ reactions with isomeric monoterpenes. Rapid Commun Mass Spectrom 30:2009–2016

44. Spesyvyi A et al (2015) Selected ion flow-drift tube mass spectrometry: quantification of volatile compounds in air and breath. Anal Chem 87:12151–12160

45. Oriaku CI, Pereira MF (2017) Analytical solutions for semiconductor luminescence including coulomb correlations with applications to dilute bismides. J Opt Soc Am B 34:321–328

46. Pereira MF (2017) Analytical expressions for numerical characterization of semiconductors per comparison with luminescence. Materials (Basel) 11:2

47. Pereira MF (2016) The linewidth enhancement factor of intersubband lasers: from a two-level limit to gain without inversion conditions. Appl Phys Lett 109:222102
48. Pereira MF et al (2017) Terahertz generation by gigahertz multiplication in superlattices. J Nanophoton 11(046022)
49. Apostolakis A, Pereira MF (2019) Controlling the harmonic conversion efficiency in semiconductor superlattices by interface roughness design. AIP Adv 9:015022
50. Apostolakis A, Pereira M (2019) Potential and limits of superlattice multipliers coupled to different input power sources. J Nanophoton 13:036017
51. Apostolakis A, Pereira MF (2020) Superlattice nonlinearities for gigahertz-terahertz generation in harmonic multipliers. Nano 9(12):3941–3952. https://doi.org/10.1515/nanoph-2020-0155
52. Pereira MF, Anfertev V, Shevchenko Y, Vaks V (2020) Giant controllable gigahertz to terahertz nonlinearities in superlattices. Sci Rep 10:15950

Chapter 15
On the Prospect of Application of Point-Contact Sensors to Solving the Global Security Problems: An Analytical Review

G. Kamarchuk, A. Pospelov, A. Savytskyi, V. Gudimenko, V. Vakula, A. Herus, D. Harbuz, L. Kamarchuk, and M. F. Pereira

Abstract In recent years, the problem of CBRN materials and explosives has attracted much attention because the threat they pose is high and tends to increase. Effective protection of critical infrastructure against CBRNE threats can be achieved by developing breakthrough technologies to create a new generation of portable, multifunctional, autonomous, energy-efficient, and low-cost devices. One of the advanced approaches to creating new innovative tools to successfully control CBRNE agents can be based on high-tech solutions involving point-contact sensors. Research and development of point-contact sensors is an emerging trend in modern sensorics. To better understand the mechanisms of point-contact sensors operation and their potential to solve the global security problems we pay attention to some of the original properties of Yanson point contacts. They are totally different from those

G. Kamarchuk (✉) · A. Savytskyi · V. Gudimenko · V. Vakula · A. Herus
Department of Spectroscopy of Molecular Systems and Nanostructured Materials, B. Verkin Institute for Low Temperature Physics and Engineering of the National Academy of Sciences of Ukraine, Kharkiv, Ukraine
e-mail: kamarchuk@ilt.kharkov.ua

A. Pospelov · D. Harbuz
Department of Physical Chemistry, National Technical University "Kharkiv Polytechnic Institute", Kharkiv, Ukraine

L. Kamarchuk
Pediatrics Department, SI "Institute for Children and Adolescents Health Care" of NAMS of Ukraine, Kharkiv, Ukraine

Department of Fundamental Medicine, V. Karazin Kharkiv National University, Kharkiv, Ukraine

M. F. Pereira
Department of Condensed Matter Theory, Institute of Physics CAS, Prague, Czech Republic

Department of Physics, Khalifa University of Science and Technology, Abu Dhabi, UAE
e-mail: pereira@fzu.cz

203

of traditional sensors based on the principle of electric conduction change and, among others, exploit use of tunnelling mechanisms. Special attention is paid to the potential use of point-contact sensors in the development of combined devices and technologies, involving such competing schemes as THz techniques, to detect terror threats and CBRNE agents.

15.1   Introduction

In recent years, the problem of dangerous chemical, biological, radiological, and nuclear materials and explosives (CBRNE) has attracted much attention because the threat they pose is high and tends to increase [1, 2]. Effective protection of critical infrastructure against CBRNE can be achieved by developing breakthrough technologies to create a new generation of portable, multifunctional, autonomous, energy-efficient, and low-cost devices. It should be emphasized that the problems caused by CBRNE agents can be solved by involving multidisciplinary knowledge and bringing together highly skilled experts from different areas of research. These efforts can yield new valuable information which could be used to lay the foundation for the development of new unique combined devices and technologies to detect terror threats and CBRNE agents. Recent studies have demonstrated the high effectiveness of point-contact sensors and THz technologies [3, 4]. At this point, before delving deeper into point-contact sensor technique, we would like to make some competing detection schemes: recent simulations tools for that are now available to support the development of customized and efficient semiconductor sources operating in the mid infrared with good quality emission linewidth. Furthermore, recent progress in the GHz-THz points towards the possibility of combining in a single box source and detectors operating from the GHz to the NIR, allowing the detection of a very wide range of absorption signatures of the majority of gases of relevance for both atmospheric control and CBRNE detection [4–9].

Research and development of point-contact sensors is an emerging trend in the modern sensorics [3]. The process of knowledge accumulation, which resulted in the observation of point-contact gas-sensitive effect [10, 11] followed by the development of point-contact sensors [12], had been launched by Igor Yanson's discovery of point-contact spectra of electron-phonon interaction [13] which gave birth to point contact spectroscopy (PCS) and made it a powerful research tool in solid state physics.

A Yanson point contact is usually defined as a contact of small size between two bulk metallic electrodes which contact with each other over a small area [14]. They are characterized by direct conduction, i.e. they do not contain tunnelling barriers and their size is smaller than (or close to) the mean free paths of charge carriers [15]. This allows Yanson point contacts to be put into the category of nano-objects with characteristic dimensions ranging from the size of one atom to a few nanometers.

Point-contact sensors are based on Yanson point contacts. To avoid confusion with terms, it should be noted that in contrast to many theoretical contact models proposed by various authors (see, for example [16–18]), a Yanson point contact is a real object which is produced using the Yanson PCS technology [3], meets the Yanson PCS criteria [14], and possesses a number of physical properties [10, 13, 19–21] which are not typical of conventional electric contacts.

Nonequilibrium electrons provide broad possibilities for Yanson point contacts to be employed in spectroscopy and detection of gases. When the current flows, electrons travelling through the contact get accelerated in the electric field concentrated in the contact and gain an additional energy eV, where e is the electron charge and V is the voltage applied to the contact [15]. This results in a nonequilibrium electronic distribution with the excess energy with an order of magnitude of eV, playing an important role in the spectral and gas-sensitive properties of Yanson point contacts.

Conventional point-contact sensors typically operate in nonthermal regimes. At room temperature, we can talk about a ballistic current regime in dendrite point contacts evidenced by the quantization of their conductance and a linear relation between the square root of the relative point contact conductance and the point contact diameter [21]. Other types of point-contact sensors are also characterized by nonthermal regimes of current, such as diffusion or intermediate regimes. In nonthermal regimes, Yanson point contacts display another important property – the ability of a point contact to withstand high current densities and voltage bias in the contact without its structure being destroyed. For example, point heterocontacts Au/SWNT, with their size ranging from several units to a few tens of Å [22], don't get damaged with voltage bias increasing up to 5 V. This means that the excess energy of electrons contributing to the nonequilibrium distribution function in such Yanson point contacts can reach the value of 5 eV at room temperature.

These properties are crucial for the gas-sensitive effect to be observed and point-contact sensors to operate for the following reasons.

1. The point-contact gas-sensitive effect manifests itself at room temperatures as a change of the point contact electric conductivity by 2–3 orders of magnitude when exposed to gases of concentration of a few ppm units and less, which exhibit either donor or acceptor properties with respect to electron transfer between the gas molecules and the gas-sensitive material of the samples as well as give rise to a shift in the density of electron states within the point-contact area [3]. An ordinary small electric point contact cannot operate as a gas-sensitive element since current flows through it in the thermal regime. Behaviour of such contacts corresponds to the dirty limit of current flow and can be described in the framework of the Maxwell model [23]. As a result of current flow, the contact gets heated and starts radiating thermal energy, which prevents adsorption of gas molecules on the contact surface.
2. In a nonequilibrium state, in order to create optimal conditions for sensor operation, the current flowing through a point-contact-based sensitive element is usually chosen to be about 1 mA. The high sensitivity of the point-contact

sensor is due to the significant change in its conductance caused by the gas, which can even result in a sharp growth of the current flowing through the contact. Taking into account the short response times of point-contact sensors, for example, their almost immediate reaction to nitrogen oxides [10], one can easily imagine a snowballing process of current increase in the contact. In the case of a conventional electric contact, even if we assume it can function as a gas-sensitive element, such a large and virtually instantaneous change in the current intensity will immediately destroy the contact. So an ordinary electric contact cannot be used as a sensitive element, being unable to withstand the extreme current conditions realized in the process of interaction with a gaseous medium. In contrast to conventional electric contacts, Yanson point contacts can survive huge current densities under the conditions needed for the point-contact gas-sensitive effect to be observed. Current density in point-contact sensors can be as high as 10^7 A/cm^2 without affecting their structure [10]. Conventional electric contacts are not suited for such current regimes since they behave as ordinary uniform bulk conductors, which start melting at current densities of the order of magnitude of 10^2 A/cm^2.

3. The possibility of separating nonequilibrium and thermal effects is another key feature of Yanson point contacts [15]. It creates the necessary conditions for "injecting" the excess energy into the electronic subsystem without destroying the contact. As a result, in Yanson point contacts nonequilibrium electrons can exist with excess energies comparable to the energies of atom vibrations in a crystalline lattice or to the adsorption (desorption) energies of the gas molecules adsorbed on the surface of the conduction channel. This lays the foundations for the realization of phonon spectroscopy (Yanson PCS) [13] and operation of point-contact sensors (point-contact gas-sensitive effect) [10]. At low temperatures Yanson PCS is possible because all the excess energy of electrons in a nonequilibrium state, which they gain as the current flows through the contact, is consumed to excite lattice vibrations and emit phonons with long mean free paths. In the case of the point-contact gas-sensitive effect at room temperature, the excess energy is transferred to the adsorbed atoms, which causes their desorption and leads to very short relaxation times of point-contact sensors.

4. Another property which is very important for point-contact sensors is the electric potential distribution in the contact [15]. The current state of a point contact is characterized by an electron distribution which is essentially different from that of a homogeneous conductor. The electric field concentrates in the constriction area and covers the space of the order of the point-contact diameter d due to the potential distribution. A current flowing in a contact channel of diameter d (Fig. 15.1) provides a voltage bias which drops over a distance equal to the channel length. This means that the *resistance of this small area determines the resistance of the entire "bulk electrode - point contact - bulk electrode" system*. As a consequence, the interaction of the bulk electrodes forming the point contact and current-feeding wires with the surrounding gas yields a negligible contribution to the point contact resistance and is not registered. The reaction between the gas and the point contact constriction area determined by the point-contact

Fig. 15.1 Distribution of the potential φ along the z-axis of the point contact. $d = 2a$ – contact diameter, V – voltage, e – electron charge
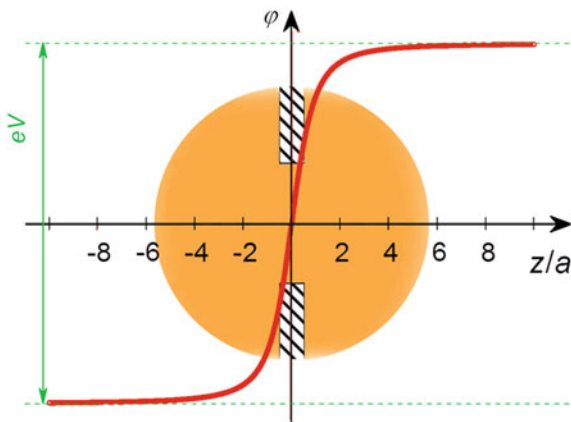
conductive cross-section only contributes to the noticeable resistance variation of the whole structure. Therefore, when the contact interacts with the gas medium, the specific potential distribution in the contact is responsible for the formation of the sensor response signal only by the area of the point contact [3]. This property of Yansosn point contacts allows one to avoid the problem of taking into account the contribution of the current-feeding wires to the response signal, which arises in the case of sensor devices with the operation principle based on conductivity change. The specific potential distribution in the point contact (see Fig. 15.1) eliminates any contribution of conducting wires to the response signal of a point-contact sensor. This feature is among the fundamental factors which are responsible for the high reliability of the results provided by ultrasensitive point-contact sensor devices [3].

5. When the conduction channel of Yanson point contact is immersed into a liquid, the potential distribution is crucial for the observation of another specific effect which reveals the quantum properties of Yanson point contacts and can be used to develop a new principle of selective detection in gaseous and liquid media. This effect is known as the cyclic switchover effect [21]. Due to the peculiar potential distribution, as the current flows through the *electrode – point-contact – electrode* system, the electric field is concentrated in the contact area. This allows the potential drop in the atom-sized area of the conduction channel of a point contact to reach values comparable to those of the electrode system decomposition, that is, in other words, the energies needed for an electrochemical reaction to start [24]. As a result, a Yanson point contact becomes the basis for the realization of an atom-sized *gapless electrode system* [21, 25]. This new type of electrochemical electrode system has no analogue. Realization of the gapless electrode system paves the way to direct study of electrochemical processes at the atomic level (see, for example, [21]) and development of a new generation of breakthrough sensor technologies based on using quantum systems to detect energy states (see Sect. 15.4).

The unique properties of Yanson point contacts provide new, previously unknown, possibilities of developing various areas of sensor technology and creating new approaches and principles of detection based on point-contact sensors. Below we consider some of them, as well as a number of results which illustrate the prospects of using point-contact sensors to solve the global security problems.

15.2 Detection of Marker Components

Terrorism poses a major danger to the global civilization [26]. Among the various threats, we highlight explosives and the so-called CBRN terrorism using chemical, biological, radiological, and nuclear agents. The leading role in the prevention of this kind of terrorism is played by sensor devices, whose sensitivity and fast response make it possible to detect minute concentrations of dangerous gaseous products in the atmosphere. These devices also need to be small so that they can be reliably camouflaged indoors and outdoors. Another significant feature of sensing elements is the possibility of prompt detection and concentration characterization of affected areas, which is especially important in the case of ecological terrorism concerning air and water environment. Nanostructured point-contact sensing elements fully meet these requirements [3].

The discovery of the gas sensitivity of Yanson point contacts [10] opened a new dimension in the development of high-precision nanostructured sensor devices. Fundamental low-temperature studies of the fine structure of solids using Yanson point-contact spectroscopy [19] entailed development of applications for point contacts in analytical techniques [11, 27–29]. One of the first studies in this area showed a significant change in the resistance of the system as a response to the interaction of analyzed molecules with the point-contact nanostructure, which is conduction channel of a Yanson point contact [10], the character of the conductivity changes depends on both the nature of the channel material and the nature of the gas agent. Point-contact sensors demonstrated excellent performance, in particular, immediate response, short recovery time and ultra high sensitivity evidenced, for example, by a 1000%-strong response after 1-s exposure to 0.1 ppm NO_x.

When solving the problems of detection selectivity, we took into consideration the fact that the channel surface can undergo a natural chemical transformation or be modified intentionally. Depending on the original material and the conditions of preliminary exposition, the channel surface can be a metal, a semiconductor or a structure with a mixed type of conduction. The key property which characterizes the nature of the analyzed gas agent is its activity with respect to electrons, in other words, the balance between its donor and acceptor properties. Numerous studies have shown that for all combinations of physicochemical properties of the gas and the substrate the change in resistance of the conduction channel of a point contact is caused by the influence of the molecules of the analyzed agent on the concentration of charge carriers in the nanostructured system. The considerable magnitude levels of the resistance response are due to the commensurateness between the channel and

the analyte molecules. This fact is also a fundamental reason for the extremely high sensitivity of sensor devices based on Yanson point contacts [3].

An important role in the point-contact sensorics is played by the original material of the conduction channel. A Yanson point contact can be made from almost any conductive material. The choice of the material is mostly determined by the nature of the target analyte and the service conditions of sensor device. The techniques used to produce point-contact structures are rather simple [3, 14, 19] and in many cases do not require high-precision processing. Very often copper is used as the material for point contacts. This choice is favoured by both the low cost of copper and the large number of technological methods and techniques regarding its use in fundamental studies. Quite a few studies in this area were performed with heterocontacts – nanostructures of heterogeneous nature. For example, some interesting results for both fundamental science and practical applications were obtained with heterocontacts between carbon single walled nanotubes (SWNT) and a gold wire [11]. Point heterocontacts Au/SWNT exhibit very high sensitivity to ammonia and nitric oxides vapours with fast response and relaxation times (Fig. 15.2). These samples have a very low limit of detection which is three orders of magnitude lower than this parameter for sensor analogues based on carbon nanotubes. Broad prospects can be opened up by sensor studies of heterocontacts "synergetic alloys – copper" [30].

Fig. 15.2 Resistance change in response to 150 s pulse for Au-SWNT point contact for different concentrations of NH_3
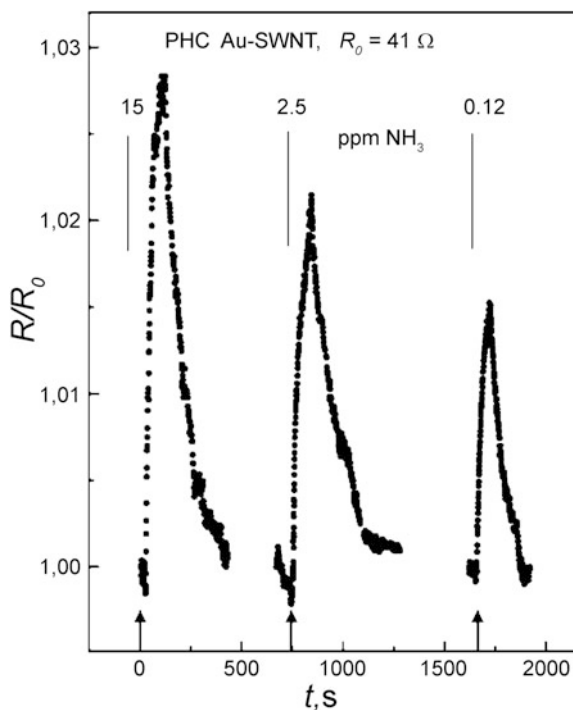
Another significant factor influencing the choice of the material is its manufacturability. The authors have modified one of the basic methods for producing point contacts and developed a new technology for controlled synthesis of this nanostructure. A Yanson point contact with its characteristic properties is formed in the contact area between the tip of a dendrite growing in an electrolyte with applied electric field and the surface of the counter electrode [21, 24]. Using the cyclic switchover effect, it was shown [21, 24] that the dendrite growth has a quantized nature shaped by the quantum shell effect [31, 32]. The cyclic switchover effect combined with the quantum structural and electronic characteristics point contacts manifested during theirs electrochemical synthesis allowed us to develop a new method for manufacturing nanoobjects of the size down to that of a single atom [21]. Such an approach could be helpful for industrial manufacture of point-contact sensors with extremely small sizes which demonstrate a drastic improvement of their metrological parameters. In this way it is possible to efficiently produce point contacts using electrochemically active materials. The list of such materials is quite long and puts no limits to the process of the device adaptation to the peculiar conditions of the environment it is going to be used in.

Among the most important technical characteristics of sensors used to fight terror threats and their consequences are high reliability, sensitivity and operation speed materialized qualitatively and quantitatively in the response signal. Since the processes leading to the formation of response to the action of the analyte are determined by the efficiency of influence of the target molecules on charge transfer in the point contact, the question about sensitivity of the channel surface to these molecules is of crucial importance. The energy spectrum characterizing the interaction between the analyte and the conduction channel of a Yanson point contact lies between the energy level which corresponds to virtually nonexistent specificity and is determined by the forces of dispersion interaction (below 1 kJ/mole) and the binding energy of the chemical compound which is being formed (over 50 kJ/mole). The levels to be preferred within this range are those of intermediate energies corresponding to physical adsorption. While a weak interaction makes it more difficult to obtain a stable reproducible response, formation of a chemical compound will lead to an irreversible loss of the sensing element, thus reducing to 1 the number of measurements which can be made with one sensing element. The latter scenario is, in principle, acceptable, since the technologies of Yanson point-contact spectroscopy offer all necessary means for a prompt creation of a new Yanson point contact to be used in further measurements. Any type of chemical sensors undergoes changes caused by irreversible processes in superficial layers of sensitive element under their interaction with the analyzed gases. This effect leads to a drift in sensor parameters and a reduction of the reproducibility of the results as a consequence of the limited durability of sensor operation. This decreases the lifetime of the sensing element and results in the need of its frequent replacement. Therefore, for correct measurements only a fresh, active surface should be used every time during repeated tests in gas media. These problems can be solved by using the Chubov displacement technique [3, 33] successfully applied in Yanson point-contact spectroscopy. It allows an easy and fast creation of many different point contacts in a wide resistance range and

selection of the necessary sample for further use. This technique also provides realization of the concept of using a point contact as a disposable sensing element which can be quickly replaced with another.

The reversible physical adsorption of the analyte on the surface of the conduction channel of a point contact allows one to permanently monitor with a high degree of sensitivity and reliability the state of the atmosphere surrounding the device. As the analyte concentration changes, the reversibility can easily manifest itself, which is directly related to the intensity of the response signal. An increase in the intensity of current flowing through the contact saturates energetically the surface layer of the conduction channel and shifts the adsorption balance towards desorption of molecules. This approach is applied to 'refresh' the gas-sensitive surface.

A detailed analysis of the available published data [3] and thorough studies of the gas sensitivity of point-contact nanosensors allow us to make the following conclusion. Point-contact sensors are capable of detecting with an extremely high sensitivity almost all types of gases, both donor and acceptor ones, chemically active and inert. The set of specific features sensor devices possess to effectively fight against the threats of ecological terrorism and its consequences makes them unique and having no alternatives for the time being.

15.3   Spectral-Type Sensor Analysis

Information reported in this section illustrates the unique fundamental properties of Yanson point contacts which underlie the distinct difference in the behaviour of point-contact sensing elements and conventional sensors based on the registration of change in their electric conduction, for example, using the tunnelling mechanisms. One of the original properties of point-contact sensors can be sketched in the complex curves of response [3, 12, 34] to the action of complex gas media which are similar to point-contact spectra obtained in Yanson point-contact spectroscopy [14, 19]. Prior to the discovery of the point-contact gas-sensitive effect [10], such a behavioural pattern of the response curves had been unknown in sensor engineering. The reason is that point contacts are nanostructured objects of quantum nature. Hence their capability of registering fine structural changes caused by the absorption of external agents. The temporal characteristics of the signal registered by the sensor device contain information about the absorption energy levels of the components of the gas medium [3]. The complex gas medium affects the temporal dependence of the point-contact electric conductance, which thus looks like a point-contact spectrum obtained in Yanson point-contact spectroscopy [14]. This finding makes it possible to develop a new efficient approach to analyzing complex molecular systems by means of unique point-contact sensor devices. This approach is based on the implementation of spectral principles of analysis via an integral characterization of the system without identifying separate components in the analyzed medium. The obtained complex non-monotonic dependences make the response

curves of point-contact sensors much more informative than those of conventional and nanostructured chemical sensors.

These properties of point-contact sensors allow one to analyze complex gas mixtures in a simple and reliable way. Analysis of complex gas media is quite a difficult task for conventional sensors based on the principle of identifying single gas components. The main technological solution to this is offered by "electronic nose" devices. Implementation of multisensory technologies of the "electronic nose" type is one of the promising trends for sensor application in the analysis of gas mixtures. Unlike the conventional approach to the development of sensors, mostly focused on improving selectivity to specific compounds, the electronic nose technologies deal with multiple arrays of relatively nonselective sensors [35]. Development of this technique has become possible due to the enhancement of computing power enabling real-time processing of multiparameter information. Point-contact sensors excel considerably the "electronic noses" as far as their capabilities are concerned. This is due to the fact that point-contact sensor devices allow a spectroscopic approach to analyzing complex gas media [3]. As a result, point-contact sensors directly register the full profile of a complex gas medium [12] while an "electronic nose", which has a limited number of sensitive elements, can only get information about substances whose number does not exceed the number of sensors in the device. With the help of computing machines it reproduces the profile of a gas medium using discrete points provided by each element. The informative value of the obtained curve is quite limited, which can cause substantial errors in the subsequent analysis of a complex gas medium consisting of hundreds and more components. The curve does not reflect the contributions of all the components of the complex gas medium and the various interactions occurring in it, thus worsening the reliability of the obtained data and narrowing the possibility of making predictions. Using point-contact sensors allows us to trace with a high resolution in the multidimensional time-concentration space the state of the interactions inside the system, while an "electronic nose" cannot do this since it only registers the presence of a limited number of components.

This new point-contact sensor technique can be applied to solve the global security problems by analyzing complex mixtures of the breath gas.

15.3.1　Detection of the Virulent Strains of Helicobacter pylori Infection

The problem of spread of infectious diseases has always posed a serious threat to human life. It comes as no surprise that biologically active substances are among the most dangerous weapons used in terror attacks. One of such sources is *Helicobacter pylori* (*H. pylori*) infection. The problem of detection and eradication of *Helicobacter pylori* (*H. pylori*) infection is of great importance due to the worldwide bacterium prevalence and its role in the pathogenesis of a number of severe gastric

and extragastric diseases [36–38]. The bacterium colonizes gastric mucosa initiating a cascade of inflammatory reactions manifesting themselves with dyspepsia and later transforming into chronic atrophic gastritis and, subsequently, gastric cancer [39, 40]. The reported global tendency of worldwide non-decreasing prevalence of *H. pylori* could be co-influenced by the functional limitations of urea breath tests (UBT) currently preferred for noninvasive recognition of *H pylori* in a clinical setting. Namely, the UBT can demonstrate false-positive or false-negative results. Not all strains of the *H. pylori* are aggressive and require antibiotic treatment. False positive results of breath tests in combination with inability of rapid and precise differentiation of pathogenic strains of the infection lead to overuse of antibiotic treatment, polypragmasia and growing antibiotic resistance in the population, resulting in an increasing burden of chronic diseases and malignancies associated with this bacterium. In this view, development of new diagnostic tests for differentiated recognition of *H. pylori* virulent strains is required for the efficient management of *H. pylori*-related morbidities.

A selective analysis of the gas mixture exhaled by a human provides solution to many social problems connected with uncontrollable spread of infections, poor diagnosis of dangerous diseases, and various kinds of terror threats. In the recent years, the importance of these problems has increased with growing flows of migrants. Point-contact sensors can become a basis for the development of innovative technologies aimed at averting global threats which arise from spread of infections across the world. For example, the recently obtained state-of-the-art results [12] have already become a prerequisite for the development of an advanced low-cost breakthrough technology for detecting *Helicobacter pylori* and its carcinogenic strains. The importance of this work comes from the fact that *Helicobacter pylori* is the most widespread infection in the world. The infection rate of human population amounts to 100% in many developing countries. Such rates can lead to a global spread of the infection as a result of mass migration from developing countries caused by armed conflicts, poverty, unemployment, and other social problems. Taking into account that the carcinogenic strains of *Helicobacter pylori* cause many dangerous diseases, the spread of the infection can lead to an uncontrollable growth of such diseases as peptic ulcer disease, gastric cancer, and gastric MALT lymphoma. This may become a very dangerous global process, since stomach cancer, for instance, is already ranked second in the top lethal cancer diseases after lung cancer. The high danger of *Helicobacter pylori* is also due to the fact that the diseases mentioned above, as well as some other diseases related to the bacterium persistence, appear a long time (up to 20 years) after the infection. Therefore, a logical solution to the global problems caused by this bacterium is to promptly detect and eradicate it. This needs efficient and low-cost noninvasive screening tests, which would allow a quick and reliable diagnosis of the carcinogenic strains of *Helicobacter pylori* in the real-time mode [12]. Presently, none of the existing methods for detecting *Helicobacter pylori* can pretend to be used as a screening method because of the rather high cost of the examination. Moreover, none of the known tests is able to detect the carcinogenic strains of the bacterium in the real-time mode. At the moment tests used for the detection of the virulence factors are

Fig. 15.3 Response curves
of the TCNQ compound-
based point-contact
nanosensors to the action of
breath gas of different
patients: 1 – patient with
non-ulcer dyspepsia,
H. pylori-, CagA-; 2 –
patient with ulcer dyspepsia,
H. pylori+, CagA+. *V* –
voltage, *t* – time, t_1 – time of
exposure, t_2 – time of
relaxation
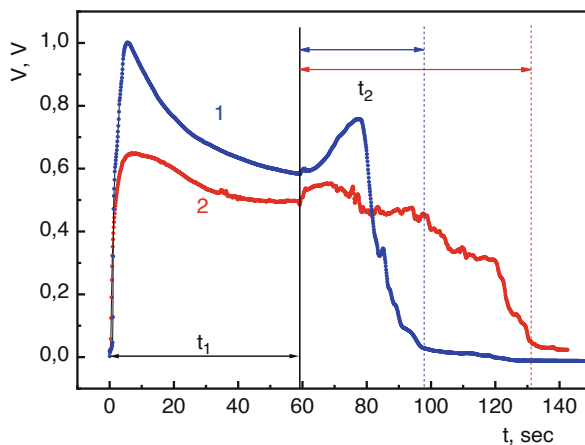
complex, time-consuming, and costly; the procedure is mostly invasive and requires
biopsy sampling with further growth of pure cultures in bacteriological laboratory,
and, finally, genome analysis itself. Therefore, this multistep diagnostic process is
currently used mainly for scientific purposes, not in practical healthcare.

Thanks to the unique properties of point-contact sensors we have succeeded in
creating a method of noninvasive detection of carcinogenic strains of *Helicobacter
pylori* in the real-time mode [12]. The performed studies have shown that the states
of the human body infected with different strains of *H. pylori* generate sensor
response curves characterized by different parameters (see Fig. 15.3). The metabo-
lism products of carcinogenic strains of *H. pylori* have a dominant influence on the
electric conductance of the sensors and affect the behaviour of the response curves.
As different strains of *H. pylori* have various biochemical properties, and therefore,
volatile products of their vital activity emitted to the breath gas also vary, point-
contact sensors are able to distinguish them through point-contact breath spectra and
relaxation times in the framework of the spectroscopic approach to breath analysis.
Therefore, it is possible to differentiate between the strains of *H. pylori* with different
carcinogenic potential using point-contact sensors based on TCNQ compounds. This
indicates the possibility of developing real-time breath tests to detect cytotoxic
strains of *Helicobacter pylori* infection. The point-contact-sensor-based real-time
breath test can potentially become the core of a screening technology which, thanks
to its simplicity and low cost, will be affordable and thus suitable for screening
examination of wide sections of population even in countries of low socio-economic
development. This will provide solution to the problem of spread of *Helicobacter
pylori* and avert the elevated occurrence of the diseases caused by the bacterium.

15.3.2 Sensor Profiling of Breath Gas as a Tool to Thwart Terror Attacks

In their complex work, security services rely heavily on undercover activity and use of various technological devices. None of these devices, except for polygraphs, offers the possibility of analyzing the human emotional state. It is well known, however, that the results obtained with a polygraph are often unreliable [41].

The emotional state of a person intending to commit a certain illegal act undergoes changes. Under the influence of an emotional distress, the hormonal composition of the blood and the activity of the vegetative system of the human body also change. This in turn leads to changes in the composition of the breath gas. The ability to determine emotional deviations of the suspicious person can help the law enforcement forces to prevent terrorist attacks. One of the promising tools to develop suitable technologies is point-contact sensors. Using the point-contact sensor spectral approach to analyze complex gas media, one can easily detect deviations in the breath profile which depend on the emotional state of a human. Here we demonstrate the possibility of observing with point-contact sensors the differences between the breath gas composition of a person before and after an emotional impact and finding correlations between the parameters of the sensor response signal for different people.

In this research, the point-contact sensor matrix is based on the organic conductor TCNQ. The original method of synthesis of TCNQ derivatives, peculiarities of their morphology, sensor effects in the created materials, and performance of the point-contact sensor multistructure based on a TCNQ compound are discussed in detail in Refs. [3, 12, 34, 42]. TCNQ compounds are attractive as sensor materials due to their structural properties and electrical conductance. The conductance of conventional conductors is usually isotropic, i.e. not depending on crystallographic directions. The adsorption of an external agent on the surface of such conductors does not cause essential change in their electric conductance. However, anisotropy may give rise to significantly more pronounced effects. Organic conductors based on TCNQ are representatives of such systems with highly anisotropic crystal lattice and electrical conductivity. The electrical anisotropy entails a strong dependence of their conductance on the distribution of electronic density of states, which, in turn, varies substantially during the adsorption of gases on the material surface [34].

The unique basic properties of Yanson point contacts in combination with the specific morphology and sensor effects of TCNQ-based materials enhance considerably the performance of point-contact sensor multistructures with respect to those of the existing homogeneous and nanostructured sensor samples. As a result, point-contact nanosensor arrays represent a new type of sensors with an excellent performance allowing realization of a new approach to analysis of gas media. This leads to point-contact sensor analysis of complex gas media by detecting the energy profile of the analyzed gas mixture. Point-contact sensors allow obtaining comprehensive information about the energy state of the investigated system. Such a possibility creates the basis for the implementation of this approach [34]. The approach is based

on the principles of spectral analysis using integral characteristics of a system without determining separate components of the analyzed medium. The complex non-monotonic dependence of the response curves of point-contact sensors makes them much more informative compared to those of conventional and nanostructured chemical sensors. This new technique has been successfully applied to medical diagnosis by analyzing complex mixtures of breath gas [12] (see Sects. 15.3 and 15.3.1).

To study emotional states of a person, a portable measuring complex was used, which had demonstrated its high efficiency in the study of carcinogenic strains of *Helicobacter pylori* [12]. This device allows recording and analyzing response curves of point-contact sensors under the action of breath gas in real-time mode, which is the most important condition for obtaining reliable information on the peculiarities of human metabolism.

We have obtained and studied the response curves of point-contact sensors in the breath-gas media of 30 volunteers before and after an emotional impact. The study was conducted in accordance with the methodology developed earlier and described in detail in Refs. [34]. The emotional impact was induced by videos which the volunteers found "funny" or "comic". The registration procedure of the sensor response curve is fast enough and takes about 3–4 min. The short recovery time of point-contact sensors allows performing a real-time breath analysis and provides a possibility of making several cycles of breath test for the same volunteer within a short period of time. Thus, to observe the reproducibility of results and obtain a rich data set for further treatment the researcher made 3–5 breath tests for each volunteer.

Under the influence of various external factors, the human body experiences both physiological changes (such as an increased heart rate, sweating or a change in the size eye pupils) and modification of the hormonal composition of the blood.

We have found out that the response curves of point-contact sensors under the action of breath gas of a human in the state of emotional excitement are significantly different from the corresponding curves for the same volunteer at the state of rest (Fig. 15.4). Whereas initial curves generally correlate well with response curves of healthy people in the studies aimed to identify carcinogenic strains of *Helicobacter pylori*, the response curves recorded after an emotional impact are significantly different from any curves that we have previously observed in various studies. The nature of the changes is, for the most part, a decrease in the relaxation time and the blurring of the exposure peak. Given the number of considered curves, it can be stated that such changes are specific and correlate with the processes occurring in the human body in the state of emotional arousal.

Observing the changes in the response curves over time, we found that those caused by an emotional impact remained stable. The curves restore their original shape during an hour after the end of the emotional impact. At the same time, the period of time after the start of the emotional impact, during which the changes in the response curve begin to appear, is no more than 10 min. Such a considerable time of relaxation to the initial state makes it possible to reliably record the deviations in the human emotional states.

Fig. 15.4 Typical variation of response curves of TCNQ-based point-contact sensors under the influence of breath gas of a volunteer depending on his/her emotional state. 1 – Curve recorded before the emotional impact; 2 – Curve recorded after the emotional impact
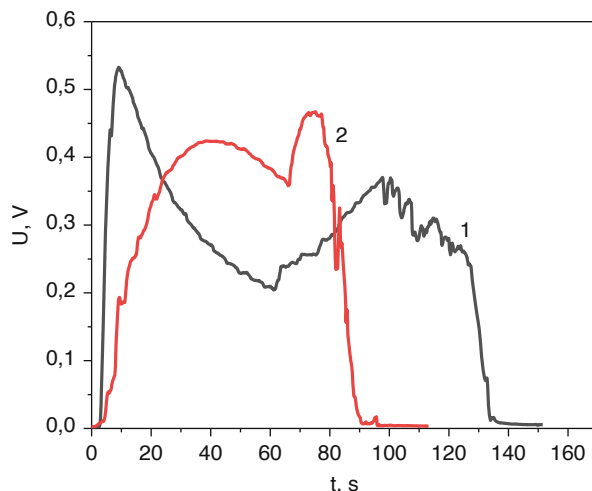
These results allow us to believe that point-contact sensors based on TCNQ compounds are a promising tool for express analysis of human emotional states, with potential for security applications. The demonstrated possibility of using them in real-time mode along with their low cost and compact size facilitates the task of implementing such devices. Despite the voluminous list of tasks to be solved for the promotion of point-contact sensors as a tool for express analysis of human emotional states, their sensitivity, high response speed, the long period of verification of emotional states and the principle of analysis directly based on metabolic states of the human body make such sensors promising devices with high reliability of analysis that can essentially improve the effectiveness of the polygraph technique.

15.3.3 Selective Quantum Sensors for Impact Monitoring of Environment and Defence Against CBRNE Agents

When a point contact is immersed in a liquid, a nanostructured gapless electrode system (GES) is formed on its conduction channel. This is a new type of electrochemical electrode system created for the first time with dendrite Yanson point contacts. It differs fundamentally [21, 24] from the existing electrochemical systems. In contrast to the traditional electrochemical electrode system consisting of two or more electrodes separated by electrolyte and thus having no direct channel of electron conduction, the GES is a monolithic conductor immersed in electrolyte with applied electric field with a potential uniformly distributed along its longitudinal axis. The GES manifests itself both with point contact properties [14, 19] and electrochemical system characteristics [28, 29]. Thus, the GES specific surface properties are accompanied by the original characteristics of the point contact

conduction channel. The ability of this object to concentrate electric field and to keep the object's identity under a super high current density is combined with oppositely directed electrochemical activity at the ends of the point contact conductivity channel. The electric field concentration and the monotonic change of the potential along the point contact channel create conditions when the reductive processes can proceed on the side of the negative pole of the electric energy source and the oxidative ones can occur on the side of the positive pole. To realize these processes it is necessary that the potential difference across the point contact channel is higher than the decomposition voltage of the electrode system, which in this case consists of electrodes formed at the opposite ends of the point contact conduction channel [24]. The spatial approach to the control of the electrode processes at a distance of the order of magnitude of a few nm, realized in the GES, is practically unattainable with the already known thin-layered electrochemical cells [44]. This fact allows observing new nanodimensional phenomena using the GES.

One of these phenomena is the cyclic switchover effect [21]. The cyclic switchover effect consists in alternating phases of formation and dissolution of point contacts we discovered in the process of synthesis of dendrite point contacts. It is a cooperative effect resulting from the quantum properties of Yanson point contacts and unique electrochemical nature of their conduction channels. The processes of formation and dissolution of the conduction channel of dendrite Yanson point contacts are shaped by the quantum shell effect [21, 31] and clearly reveal the quantum properties of the contacts. As a result, the cyclic switchover effect is an efficient tool to register the whole variety of quantum states of the system in the dynamic mode. When the cyclic switchover effect takes place, a strong nonlinear dependence of conductance G of point contacts on electrolyte concentration is observed (see Fig. 15.5 in Ref. [21]). The change in the electrolyte composition
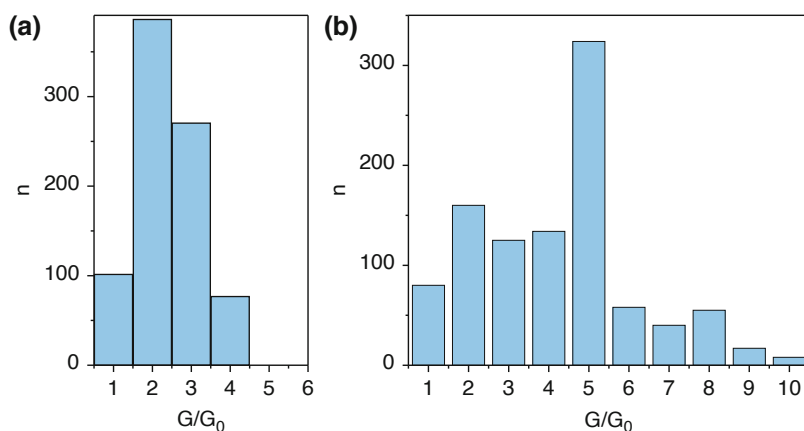

Fig. 15.5 Conductance histograms of dendrite copper point contacts grown in the drop of bi-distilled water under gas action. a – dendrite point contacts in argon medium; b – dendrite point contacts in an argon (99.99%) + methane (0.01%) medium; G – conductance, G_0 – conductance quantum, n – number of counts

leads to a change in the electric synthesis process and can be used for analytical purposes by recording and analysing the conductance of the nanostructures created during the self-oscillatory process of dendrite point-contact growth and dissolution. This means, for example, that if the dendrite point-contact electrode system immersed into a drop of electrolyte is put in contact with a gas medium, one can detect the gas molecules during the nanostructure synthesis. Indeed, solvated gas molecules diffuse into the crystallization zone and affect the electrochemical synthesis of the dendrite point-contact structure. This leads to the appearance of new quantum metastable states in the growing dendrite point-contact structure. As a consequence, the characteristics of the switchover and shell effects change. In this case, the conductivity histogram is a fingerprint of the process of point-contact interaction with the gas analyte. Another gas agent will lead to another conductivity histogram; i.e. each histogram corresponds to a peculiar gas. Thus, every gas is characterized by the unique conductance histogram obtained for a self-oscillating dendrite point-contact structure. This implies absolute selectivity of the method of gas detection proposed here.

The detection process is as follows. Consider a system for creating a dendrite point contact using the 'needle-anvil' method, in which the needle tip is in a drop of electrolyte or bidistilled water on the anvil surface. A detailed description of the technology for producing dendrite point contacts can be found in Refs. [3, 21, 24]. When a current flows through the needle-electrolyte-anvil system, dendrites start growing in the electrode-active areas of the needle surface characterized by the highest density of electric field lines. If the current continues to flow, a cyclic process develops in the system after some hundred milliseconds to several minutes: point contact resistance varies with time as it passes through the stages of growth, reduction, and stabilization. These stages, which are repeated many times, account for the cyclic changes in the physical and chemical properties of the object. The recurrence of the cyclic changes is automatic with no external influence. The variations of the interelectrode voltage during the self-oscillations of resistance show up as clearly visible steps in the dependence $R(t)$ and are attributed to electron conductance quantization of dendrite point contacts and electronic shell effect [21].

A quantum point-contact sensor device is characterized by an ultrahigh resolution and is able to register at a molecular level the complex interactions occurring in multicomponent gas and liquid media. This allows one to successfully use it for the defence against CBRNE agents and solve a number of global ecological and social problems that threaten the survival of mankind. One of those problems is the problem of climate change which can worsen the food situation in the world and incite armed conflicts aimed at redistribution of resources. To avert this, an efficient control of the earth's climate needs to be organized. A successful control and prediction of climate change is only possible under the condition of quick and continuous assessment of the concentration of greenhouse gases in the atmosphere. The quantum selective point-contact detector of gas and liquid media is a portable device which can become a basic element of a simple and inexpensive technology for controlling these problems. The already obtained results suggest good prospects for the proposed method of high-precision detection of carbon dioxide [43]. There

are all necessary preconditions for the creation of highly efficient quantum point-contact detectors of methane, nitrogen oxide, aqueous vapour and all other gases important for the control over the climate change. It should be noted that the quantum detector under consideration provides a complex analysis of not only the main greenhouse gases, but also their precursors. This means a higher reliability and credibility of registration of the ecological trends and a significantly enhanced predictive capability of monitoring.

The simplicity of construction of point-contact sensor device and its low cost will allow a global multi-position impact monitoring of the environment to quickly detect areas of chemical pollution in potentially dangerous regions of intense anthropogenic influence. The high reliability and sensitivity of detection are guaranteed by the continuous quantitative and qualitative control of the atmosphere.

Before proceeding to concluding remarks, we would like to mention that the devices discussed here can be used in connection with other sensors based on GHz-THz-MIR spectroscopy, notably based on superlattices and quantum-cascade structures [45–52], with potential for creating networks of detectors covering a large area, delivering a cost-effective solution.

Here are other materials also being investigated for spectroscopy and devices in the THz range, notably based on superlattices and quantum-cascade structures [4–9, 45–52].

15.4   Conclusions

We have discussed the physical properties of Yanson point contacts which give rise to the point-contact gas-sensitive effect and make it possible to develop a new generation of nanosensors. The original fundamental properties of Yanson point contacts are responsible for the behaviour of point-contact sensing elements which is totally different from that of traditional sensors based on the principle of electric conduction change and, among others, exploit the tunnelling mechanisms. The nature of Yanson point contacts opens up new possibilities never known before of developing various areas in sensor technology and creating new approaches and detection principles based on point-contact sensors.

As can be seen from the presented data, point-contact sensing elements are the building blocks of nanosensors with excellent performance to be used in new approaches to analyse gas media. Point-contact sensors are capable of detecting with an extremely high sensitivity almost all types of gases, both donor and acceptor gases, chemically active and inert. The obtained data demonstrate that performance of point-contact sensors provides them with a great competitive advantage compared to other types of sensors [3]. Moreover, the characteristics of point-contact sensors excel essentially those of their competitors.

One of the original properties of point-contact sensors can be illustrated in their rich response [3, 12, 34] which is measured during the action of complex gas media and is similar to the point-contact spectra obtained in Yanson point-contact

spectroscopy [14, 19]. This finding makes it possible to develop a novel and effective approach to analyzing complex molecular systems with the unique point-contact sensor devices. This approach is based on the spectral principles of analysis using integral characteristics of a system without determining separate components of the analyzed medium.

The new approach to detecting complex molecular systems using point-contact sensors has proved to be successful in analyzing human breath gas, which made it possible to develop the basic technologies for detecting carcinogenic strains of *Helicobacter pylori*. The importance of this study comes from the fact that *Helicobacter pylori* is the most widespread infection in the world. The infection rate of human population amounts to 100% in many developing countries. Such rates can lead to a global spread of the infection as a result of mass migration from developing countries caused by armed conflicts, poverty, unemployment and other social problems. Taking into account that the carcinogenic strains of *Helicobacter pylori* cause many dangerous diseases, the spread of the infection can lead to an uncontrollable growth of such diseases as peptic ulcer disease, gastric cancer, and gastric MALT lymphoma. This may become a very dangerous global process, since stomach cancer, for example, is already ranked second in the top lethal cancer diseases after lung cancer. The point-contact-sensor-based real-time breath test can become the core of a screening technology which, thanks to its simplicity and low cost, will be affordable and thus suitable for screening examination of wide sections of population even in countries of low socio-economic development. This will provide solution to the problem of *Helicobacter pylori* spread and avert the elevated occurrence of diseases caused by the bacterium.

Another example of the successful implementation of the new approach to analyzing complex molecular systems using point-contact sensors is detection of human emotional states. The emotional state of a person who intends to commit a certain illegal act undergoes some changes. Under the influence of an emotional distress, the hormonal composition of the blood and the activity of the vegetative system of the human body also change. This, in turn, leads to a change in the composition of breath gas. The ability to determine emotional deviations of a suspicious person can help the law enforcement forces to prevent terror attacks. The obtained results demonstrate that point-contact sensors can be considered a promising tool for express analysis of human emotional states and can thus be applied to develop a novel technology for thwarting terror attacks at earlier stages of their organization.

The search for innovative principles of detection and their comprehensive validation can give a fresh impetus to the development of a new generation of sensor devices. In this regard, the new method for selectively detecting gases and liquid media which uses the quantum properties of Yanson point contact seems to be quite promising. The method and the technology proposed are based on the characterization of the energy of interaction of point-contact structures with gas and liquid media through quantum parameters of the point-contact conductance. The quantum nature of the electric properties of point contacts makes it possible to use them for recording minute variations of superficial states of point-contact conduction channel caused by

adsorption of an external agent. The registration procedure is performed with the highest possible resolution of one conductance quantum which is equal to addition of one atom to the point-contact channel. As a result, quantum point-contact sensors operate with the highest sensitivity and at the cutting edge of detection limit of sensor devices. A quantum point-contact sensor device has an ultrahigh resolution and is able to register at a molecular level the complex interactions in multicomponent gas and liquid media. This allows one to successfully use it for the defence against CBRNE agents and solve a number of global ecological and social problems that threaten the survival of mankind.

Point-contact sensors represent a promising technology to be used to create unique combined devices and technologies to detect terror threats and CBRNE agents. In this connection, we would like to emphasize the great opportunities which can be offered by the development of multipurpose technologies using point heterocontact nanosensors and advanced THz-Mid Infrared (TERA-MIR) sensing devices based on solid-state heterostructures which employ micron or submicron scale engineering. The heterostructure approach has proven to be a useful tool to design highly efficient devices based on the principles of TERA-MIR spectroscopy combined with those of Yanson point-contact spectroscopy and point-contact gas-sensitive effect.

Thus, point-contact detectors can be a basic element of a simple and inexpensive technology for a successful control over CBRNE agents, defence against terrorism, providing solutions to a variety of social problems connected with uncontrollable spread of infections, prognosis of the climate change and environmental monitoring, be used to perform a global multi-position impact monitoring of the environment to quickly detect areas of chemical pollution in potentially dangerous regions of intense anthropogenic influence.

References

1. European Union: European Commission (5.5.2014). Communication from the Commission to the European parliament, the Council, the European economic and social Committee and the Committee of the regions on a new EU approach to the detection and mitigation of CBRN-E risks. COM(2014) 247 final, Brussels.
2. European Union: Europol (2018) European Union terrorism situation and trend report 2018. European Union Agency for Law Enforcement Cooperation, The Hague
3. Kamarchuk GV, Pospelov AP, Kamarchuk LV, Kushch IG (2015) Point-contact sensors and their medical applications for breath analysis: a review. In: Karachevtsev VA (ed) Nanobiophysics: fundamentals and applications. Pan Stanford Publishing, Singapore
4. Pereira MF, Shulika O (eds) (2011) Terahertz and mid infrared radiation: generation, detection and applications (NATO science for peace and security series B: physics and biophysics). Springer, Dordrecht
5. Oriaku CI, Pereira MF (2017) Analytical solutions for semiconductor luminescence including Coulomb correlations with applications to dilute bismides. J Opt Soc Am B 34:321
6. Pereira MF (2018) Analytical expressions for numerical characterization of semiconductors per comparison with luminescence. Materials 11:2

7. Pereira MF (2016) The linewidth enhancement factor of intersubband lasers: from a two-level limit to gain without in-version conditions. Appl Phys Lett 109:222102

8. Pereira MF, Zubelli PJ, Winge D, Wacker A, Rondrigues SA, Anfertev V, Vaks V (2017) Theory and measurements of harmonic generation in semiconductor superlattices with applications in the 100 GHz to 1 THz range. Phys Rev B 96:045306

9. Pereira MF, Anfertev V, Zubelli JP, Vaks V (2017) Terahertz generation by gigahertz multiplication in superlattices. J Nanophotonics 11:046022

10. Kamarchuk GV, Pospelov OP, Yeremenko AV, Faulques E, Yanson IK (2006) Point-contact sensors: new prospects for a nanoscale sensitive technique. Europhys Lett 76:575

11. Kamarchuk GV, Kolobov IG, Khotkevich AV, Yanson IK, Pospelov AP, Levitsky IA, Euler WB (2008) New chemical sensors based on point heterocontact between single wall carbon nanotubes and gold wires. Sensors Actuators B Chem 134:1022

12. Kushch I, Korenev N, Kamarchuk L, Pospelov A, Kravchenko A, Bajenov L, Kabulov M, Amann A, Kamarchuk G (2015) On the importance of developing a new generation of breath tests for Helicobacter pylori detection. J Breath Res 9:047109

13. Yanson IK (1974) Nonlinear effects in the electric conductivity of point junctions and electron-phonon interaction in normal metals. J Exp Theor Phys 39:506

14. Khotkevich AV, Yanson IK (1995) Atlas of point contact spectra of electron-phonon interactions in metals. Kluwer Academic Publishers, Boston/Dordrecht/London

15. Kulik IO, Omelyanchuk AN, Shekhter RI (1977) Electrical conductivity of point microcontacts and the spectroscopy of phonons and impurities in normal metals. Sov J Low Temp Phys 3:740

16. Sharvin YV (1965) A possible method for studying Fermi surfaces. J Exp Theor Phys 21:655

17. Kulik IO, Yanson IK (1978) Microcontact spectroscopy of phonons in the dirty limit. Sov J Low Temp Phys 4:596

18. Kulik IO, Shekhter RI, Shkorbatov AG (1981) Point-contact spectroscopy of electron-phonon coupling in metals with a small electron mean free path. J Exp Theor Phys 54:1130

19. Naidyuk YG, Yanson IK (2005) Point-contact spectroscopy. Springer, New York

20. Krans, J.M., Ruitenbeek, J.M. van, Fisun, V.V., Yanson, I.K., de Jongh, L.J. (1995). The signature of conductance quantization in metallic point contacts. Nature (London, U.K.), 375, 767

21. Pospelov AP, Pilipenko AI, Kamarchuk GV, Fisun VV, Yanson IK, Faulques E (2015) A new method for controlling the quantized growth of dendritic nanoscale point contacts via switchover and shell effects. J Phys Chem C 119:632

22. Savitsky AV, Pospelov OP, Kamarchuk GV (2010) Doslidzhennia elektrychnoi providnosti heterokontaktiv Au-SWNT v hazovomu seredovyshchi (Investigation of electrical conductivity of heterocontacts Au-SWNT in a gas environment). J Kharkiv National University V.N. Karazin. Series Physics 915:40

23. Maxwell JC (1904) A treatise of electricity and magnetism. Clarendon, Oxford

24. Kamarchuk GV, Pospelov AP, Savitsky AV, Koval LV (2014) Nonlinear cyclical transport phenomena in copper point contacts. Low Temp Phys 40:937

25. Pospelov AP, Kamarchuk GV, Alexandrov YL, Zaika AS, Yeremenko AV, Faulques E (2004) New development of impedance spectroscopy. In: Faulques EC, Perry DL, Yeremenko AV (eds) Spectroscopy of emerging materials (NATO science series). Kluwer Academic Publishers, Boston/Dordrecht/London

26. Richards A (2015) Conceptualizing terrorism. Oxford University Press, New York

27. Kamarchuk GV, Pospelov AP, Yeremenko AV, Faulques E, Yanson IK (2007) New nanosensors for monitoring gas media. Sensor Electron Microsyst Technol (3):46

28. Pilipenko AI, Pospelov AP, Kamarchuk GV, Bondarenko IS, Shablo AA, Bondarenko SI (2011) Point-contact sensory nanostructure modeling. Funct Mater 18:324

29. Pospelov AP, Kamarchuk GV, Savytskyi AV, Sakhnenko MD, Ved MV, Vakula VL (2017) Macroscopic simulation of atom-sized structures of functional materials: phenomenology of the elongated electrode system. Funct Mater 24:463

30. Pospelov A, Kamarchuk G, Sakhnenko N, Gudimenko V, Ved M (2018) Ternarnyi splav Co-Mo-W yak chutlyvyi material nanostrukturnoho hazovoho sensora (Ternary alloy Co-Mo-W as a sensitive material of a nanostructured gas sensor). Bull Natl Tech Univ "Kharkiv Polytechnic Institute" Ser Chem Chem Technol Environ 50:1269

31. Yanson AI, Yanson IK, van Ruitenbeek JM (1999) Observation of shell structure in sodium nanowires. Nature (London, U.K.) 400:144

32. Yanson AI, Yanson IK, van Ruitenbeek JM (2000) Supershell structure in alkali metal nanowires. Phys Rev Lett 84:5832

33. Chubov PN, Yanson IK, Akimenko AI (1982) Electron-phonon interaction in aluminum point contacts. Sov J Low Temp Phys 8:32

34. Kushch IG, Korenev NM, Kamarchuk LV, Pospelov AP, Alexandrov YL, Kamarchuk GV (2011) Sensors for breath analysis: an advanced approach to express diagnostics and monitoring of human diseases. In: Mikhalovsky S, Khajibaev A (eds) Biodefence (NATO science for peace and security series a: chemistry and biology). Springer, Dordrecht

35. Zohora SE, Khan AM, Srivastava AK, Hundewal N (2013) Chemical sensors employed in electronic noses: a review. Int J Soft Comput Eng 3:405

36. Malfertheiner P, Megraud F, O'Morain CA, Atherton J, Axon AT, Bazzoli F, Gensini GF, Gisbert JP, Graham DY, Rokkas T, El-Omar EM, Kuipers EJ (2012) Management of Helicobacter pylori infection – the Maastricht IV/ Florence consensus report. Gut 61:646

37. Garza-González E, Perez-Perez GI, Maldonado-Garza HJ, Bosques-Padilla FJ (2014) A review of Helicobacter pylori diagnosis, treatment, and methods to detect eradication. World J Gastroenterol 20:1438

38. Cizginer S, Ordulu Z, Kadayifci A (2014) Approach to Helicobacter pylori infection in geriatric population. World J Gastrointest Pharmacol Ther 5:139

39. Graham DY (2000) Helicobacter pylori infection is the primary cause of gastric cancer. J Gastroenterol 35:90

40. Ferreccio C, Rollán A, Harris PR, Serrano C, Gederlini A, Margozzini P, Gonzalez C, Aguilera X, Venegas A, Jara A (2007) Gastric cancer is related to early Helicobacter pylori infection in a high-prevalence country. Cancer Epidemiol Biomark Prev 16:662

41. National Research Council (2003) The polygraph and lie detection. The National Academies Press, Washington, DC

42. Kamarchuk GV, Pospelov AP, Harbuz DA, Gudimenko VA, Kamarchuk LV, Zaika AS, Pletnev AM, Kravchenko AV (2017) Nanostrukturnye tochechno-kontaktnye sensory dlya diagnostiki kantserogennykh shtammov bakterii Helicobacter pylori (Nanostructural point-contact sensors for diagnostics of carcinogenic strains of Helicobacter pylori). Biophys Bull 2:66

43. Kamarchuk GV, Pospelov AP, Savytskyi AV, Herus AO, Doronin YS, Vakula VL, Faulques E (2019) Conductance quantization as a new selective sensing mechanism in dendritic point contacts. SN Appl Sci 1:244

44. Damaskin BB, Petriy OA, Tsirlina GA (2006) Elektrokhimiya (Electrochemistry). Kolos, Moscow

45. Apostolakis A, Pereira MF (2019) Controlling the harmonic conversion efficiency in semiconductor superlattices by interface roughness design. AIP Adv 9:015022

46. Apostolakis A, Pereira MF (2019) Numerical studies of superlattice multipliers performance. Quantum Sens Nano Electron Photon XVI:109262

47. Apostolakis A, Pereira MF (2019) Potential and limits of superlattice multipliers coupled to different input power sources. J Nanophoton 13:036017

48. Pereira MF, Faragai IA (2014) Coupling of THz radiation with intervalence band transitions in microcavities. Opt Express 22:3439

49. Winge DO, Franckié M, Verdozzi C, Wacker A (2016) Simple electron-electron scattering in non-equilibrium Green's function simulations. J Phys Conf Ser 696:012013

50. Pereira MF, Shulika O (2014) Terahertz and mid infrared radiation: detection of explosives and CBRN (using te-rahertz). NATO science for peace and security series-B: physics and biophysics. Springer, Dordrecht
51. Apostolakis A, Pereira MF (2020) Superlattice nonlinearities for Gigahertz-Terahertz generation in harmonic multipliers. Nanophotonics 9(12):3941–3952. https://doi.org/10.1515/nanoph-2020-0155
52. Pereira MF, Anfertev V, Shevchenko Y, Vaks V (2020) Giant controllable gigahertz to terahertz nonlinearities in superlattices. Sci Rep 10:15950

Chapter 16
Development of Gas Sensor Systems in the Infrared Region

**Juliana Carvalho, Sully Quintero, Marbey M. Mosso,
Luiz Carlos Guedes Valente, and Marcos Sebastião De Paula Gomes**

Abstract The focus of this work is the development of gas detection system with acetylene (C_2H_2) and carbon dioxide (C_2O). The system operates in the near infrared region (NIR) including an amplified spontaneous emission source (ASE) and microstructured optical fibers in series with optical gas cells. A scanning system based on laser ring and fiber Bragg grating (FBG) is designed for the 1950 nm wavelength. A system able to reflect Bragg wavelength is verified within the absorption lines according to high-resolution transmission molecular absorption database (HITRAN).

16.1 Introduction

There are several of hazardous gases in the atmosphere, mostly produced by the burning of fossil fuels, industrial activities and flames. Some techniques can detect chemical, biological, radiological or nuclear warfare (CBRN) explosives, steam plumes that they generated [1].

J. Carvalho (✉)
Instituto de Telecomunicações, Universidade de Aveiro, Aveiro, Portugal

S. Quintero · M. M. Mosso
Departmento de Engenharia Mecânica, Pontifícia Universidade Católica do Rio de Janeiro, Rio de Janeiro, Brazil
e-mail: sully@puc-rio.br

L. C. G. Valente
Ouro Negro SA, Rio de Janeiro, Brazil
e-mail: luiz.guedes@ouronegro.com.br

M. S. D. P. Gomes
Petrobras Research and Development Center (CENPES), Rio de Janeiro, Brazil
e-mail: mspgomes@puc-rio.br

Since the optical molecules of some gases have absorptions associated with their various vibrational modes, which are unique and depend on the geometry and masses of the atoms that make them up, an electromagnetic radiation can be absorbed when its frequency is identical to that of molecular vibration. The major atmospheric gases have infrared absorption on electromagnetic spectrum. Absorption of visible and near infrared (NIR) radiation in the gaseous atmosphere is primarily due to water vapor (H_2O), ozone (O_3), and carbon dioxide (CO_2) [2]. Still on gas class, acetylene (C_2H_2) is a hydrocarbon of interest from a variety of viewpoints in atmospheric and pollution studies with infrared absorption bands also. In this context, the objective of study in this work is the measurements and detection of C_2H_2 and carbon dioxide (CO_2), which also contribute to our planet global warming and are responsible for at least 30% of this damage.

Infrared light transmission can be performed through optical fibers made with pure or doped silica, and these waveguide is playing an increasingly important role in environmental and safety monitoring, as well as chemical and biological sensing [3]. Photonic crystal fibres (PCF) has, in this way, extended the range of possibilities and new applications in optical fibers, both by improving well-established properties and introducing new features such as low-loss guidance in a hollow core [4].

This paper presents a new study methodology employing micro structured optical fibers as gas sensors and system components such as light sources, fiber Bragg grating, couplers and gas cells [5–7]. Besides this introduction, Sect. 16.2 describes the procedure and measurements of microstructure optical fibers. Section 16.3 presents a scanning system based on laser ring and FBG developed and the results obtained. Finally, Sect. 16.4 presents final considerations and conclusions.

16.2 Study and Characterization of Microstructured Optical Fibers

Externally, a microstructured optical fiber is very similar with a conventional optical fiber. However, this difference is found in his cross section, which has microscopic holes in the perpendicular plane to the axis thereof, extending along the entire length of the fiber producing a refractive-index difference between glass and air. These air holes form a periodic microstructure, with a low index of refraction in around a core that can be solid or hollow, being the presence, distribution and size of these holes are responsible for confinement and for the light conduction. Using different architectures it is possible to define and control special optical properties such as: dispersion, birefringence, and non-linearity. These special properties led to the development of several applications in the areas of communications optics, non-linear optics, and sensing.

The complex structure of PCF makes its electromagnetic analysis challenging [4, 8–10]. The PCF holes propagate the light wave and at the same time the fiber capillary has the possibility to confine the gas in analysis. With aim of developing an

optical gas sensor, the application process consists of guide inside a microstructured optical fiber an infrared light source and gas (CO_2 or C_2H_2) together, an experimental proposal for performing measurements from the observing this interaction, taking results of gas concentration by light-absorption spectroscopy [11–13].

The light absorption is a measurement described by Beer-Lambert law (Eq. 16.1) [14], which relates the attenuation of signal with the properties of the material through which the light is propagating.

$$I(l) = I_0 e^{-\alpha l} \tag{16.1}$$

Where I is the transmitted light through the gas cell, I_0 the incident light, α is the absorption coefficient and l the optical path length, being the measurement of the absorbed light level in the sample is effectively proportional to the density of molecules present in this sample.

16.2.1 Microstructure Sizing by Microscopy and Near Field Measurement

The PCF structures are currently produced in many laboratories worldwide using a variety of different techniques for photonics and telecommunications applications. In cooperative works with Acreo Swedish ICT, this laboratory fabricated the microstructured fibers to be tested in this work as gas detectors. To perform the tests of this fiber, two steps were executed: the first one it was taking dimensions measurements with a microscope and the second stage was obtaining with a charge-coupled device (CDD) camera near field images (600 nm). The measurements were taken from two different fibers FOM1 and FOM2. In Fig. 16.1a, the FOM1 structure consist of seven equilateral triangles and one semicircle; FOM2 eight cylinders. Both microstructure fibers have central holes cores (40 and 39 μm). The pictures in Fig. 16.1b show the optical signal propagation. The light source for observe the signal propagated is a HeNe laser in 633 nm and 1 mW. For conclusive

ACREO FOM1   ACREO FOM2   ACREO FOM1   ACREO FOM2
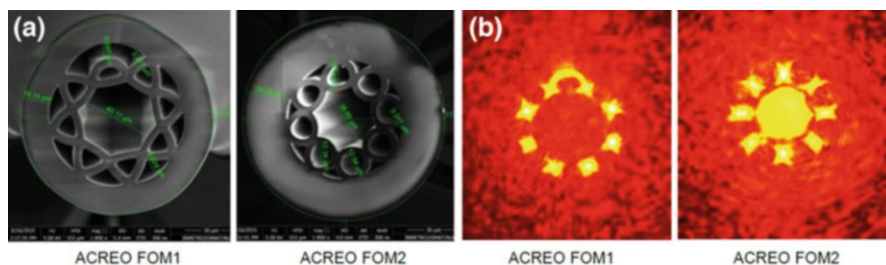
Fig. 16.1 Acreo microstructured optical fibers (FOM1 and FOM2). (**a**) Dimensions measurements with a microscope. (**b**) Near field images with a CDD camera

interpretation, the evaluation of these results show that in this first fiber (FOM1) the light propagation is in fiber cladding holes where there is less gas concentration through it. On the other hand, in second fiber (FOM2) the light is propagating along the fiber core and holes, where there is more gas concentration. So, this one is chosen to be tested as a sensor possibility.

16.2.2 *Light Coupling Test with Gas C_2H_2 and CO_2*

The C_2H_2 gas has absorption lines around 1500 nm wavelength, so the system was pumped near the range of 1500 and 1570 nm (Fig. 16.2), where green line is the high-resolution transmission molecular absorption database (HITRAN [15]) reference, and in this range the transmittance percentage is 0%, indicating that there is light absorption. The red line represents the amplified spontaneous emission (ASE) source spectrum. Power level is −48 dBm in 1530 nm, where the signal is more intensity. This analysis concludes that there is light absorption in the presence of C_2H_2 and FOM2 can be applied as a sensor for detection of this gas.

In the case of CO_2 which has absorption line around with wavelength around 2000 nm, during the gas injection tests it was not possible to obtain promising results with this microstructured optical fiber, since these one have range operation between 750 and 1700 nm.

To activate this realization, a commercial alternative of PCF was studied and evaluated. The research carried out presented the HC-2000 Thorlabs – hollow core PCF, 2000 nm, Ø 14.5 μm core [16]. This optical fiber was purchased and applied to the system operating in NIR with an ASE source, and initial tests were realized for optic length of 1 m. Figure 16.3 presents the experimental results, where during the tests it was found that between 2.000 and 2.025 μm wavelengths (grey region on graphic), the lines are more intense due to higher gas absorption, which shows that there is a possibility to develop a CO_2 gas sensor with HC-2000 optical fiber.

Fig. 16.2 C_2H_2 absorption lines for a microstructured optical fiber. ASE source in 1520 to 1570 nm
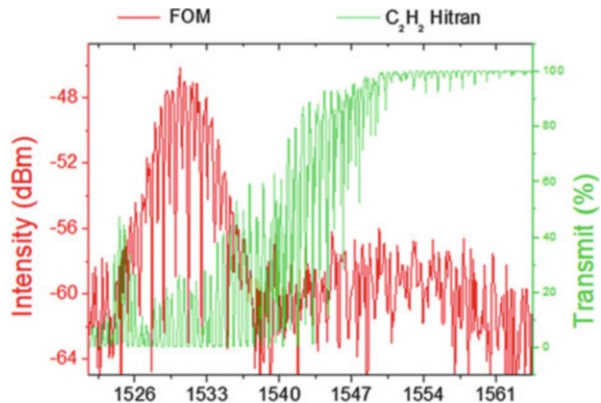
Fig. 16.3 HC-2000 results with CO_2 and ASE at 2000 nm – gas concentration 1300 ppm. Black line is the light wave propagation along the fiber and the red line indicates when is there is light signal and gas pumped interacting through the PCF core
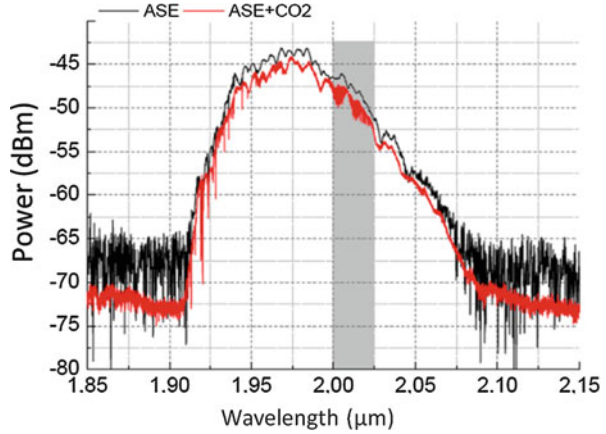
Fig. 16.4 ASE through gas cells individually and when configured in series – increase optical path length. According to Fig. 16.3 above, black line is only the ASE source. The magenta line represents the standard cell. Blue and red lines are flow and open cell respectively. The last one, green curve, is when the cells are configured in series
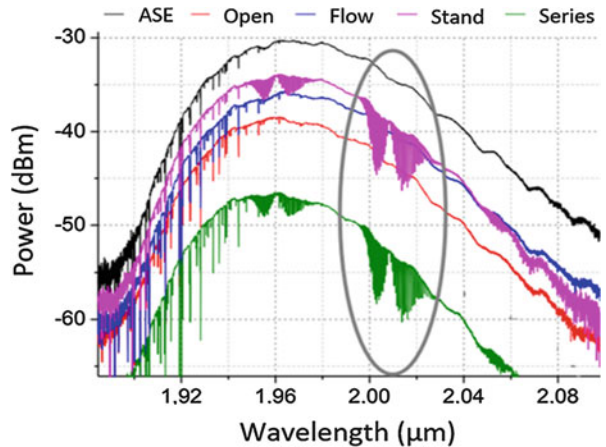
This experimental step calibrates the system and characterizes the PCF as a gas detector. Then, to increase optical path length, optical gas cells were grouped and arranged composing the second test environment: an open, flow and standard. Each cell has an individual insertion loss, so consequently the power system decrease 13 dB due this connection (Fig. 16.4). The magenta line in this graphic represents the standard cell [17], which is a closed cell where the CO_2 concentration inside it is constant and equal to 33%. Blue and red lines are flow and open cell respectively, where the gas passes through them. The last one, green curve, is when the cells are configured in series. As previously observed, the absorptions lines are more intense at the same wavelengths. The grey ellipse indicated shows the gas concentration and consequently absorption region between 2 and 2.02 μm.

16.3 Scanning System Based on Laser Ring

Fiber laser ring have many attractive features including narrow line widths for system diagnostics and coherent applications, as interrogation units for distributed fiber Bragg grating (FBG) based sensor networks [18, 19]. The objective here is the development of a scanning system based on laser ring designed for the 2000 nm wavelength from ASE source. In this step, is realized the study and application of a FBG in a scheme using optical devices: directional coupler 50% $\times$ 50%, optical gas cell, attenuators and microstructured optical fibers. The system reflected Bragg wavelength is 1950 nm and it is verified within the absorption lines of CO_2, according to HITRAN parameters. These results are obtained with an optical spectrum analyzer (OSA Thorlabs 203B 1000–2600 nm) delivering high precision and can be customized to a large number of targets with different absorption signatures. Figure 16.5 show the laser ring operation where the Bragg reflected wavelength is blue line with −45 dBm power level and, when the loopback is done, this value is increased to −25 dBm with full width at half maximum (fwhm) precision of 0.1 nm, shown in magenta line.

According to tests results, the scanning system is prepared to operate as a laser source in 1.955 μm for applications in CO_2 detection and sensor projects, since is possible to verify in Fig. 16.6 the transmittance lines within laser ring transmission signal.

The same results in optical domain can be obtained in electrical domain when a photodetector device in this bandwidth is inserted in the end of the system and the OSA is substituted for an oscilloscope. The experimental scenario is shown on Fig. 16.7, where are presented the components arrangement: CO_2 gas cylinder, a plastic box with gas cells and the PCF (HC-2000), photodetector (Thorlabs PDA10D 1.2–2.6 μm), electrical filter and oscilloscope.

The graphic shown in Fig. 16.8 below presents the results of the optical-electric conversion system acquired with the oscilloscope. The measured initial signal, black

Fig. 16.5 Results of the scanning system based on laser ring with FBG. Black line is the broadband ASE source and when this signal pass through a coupler, it is decreased 3 dB (red line). The Bragg reflected wavelength is blue one. The loopback is shown in magenta line
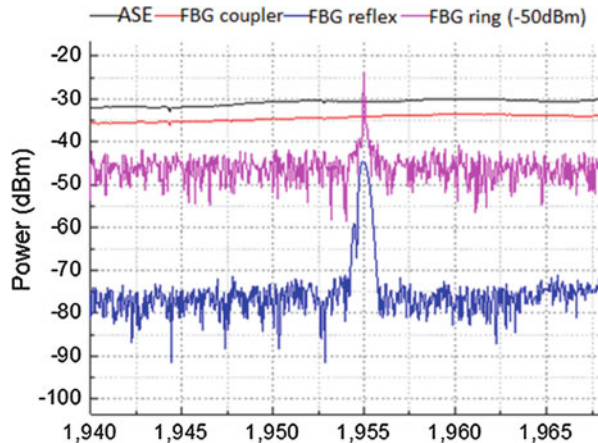
Fig. 16.6 Study of FBG in a system using optical devices and microstructured optical fibers. Bragg reflected wavelength has fwhm of 0.5 nm, indicated for blue line. The black line is the CO_2 lines absorptions HITRAN transmittance reference
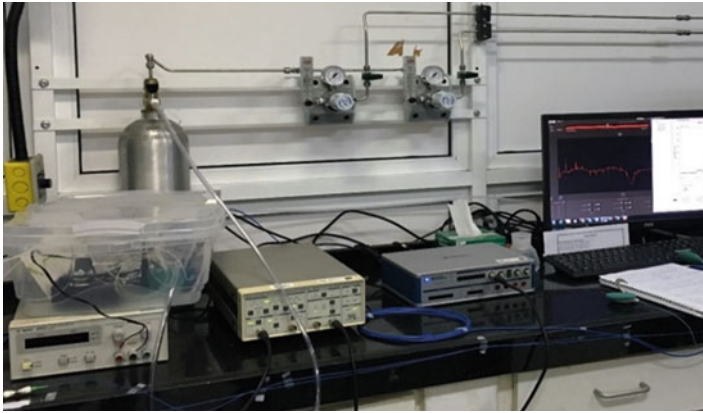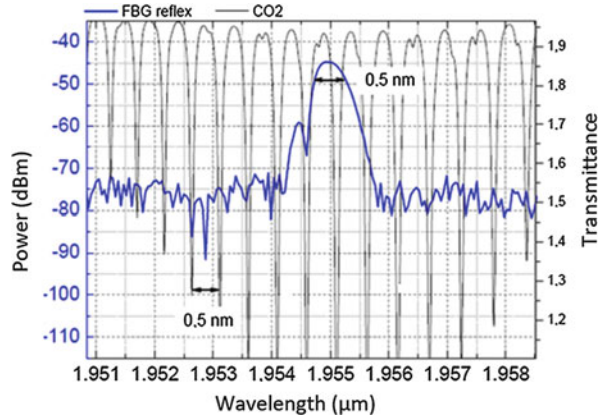
Fig. 16.7 Test bench of CO_2 detection system

Fig. 16.8 Oscilloscope results. The valleys in the blue curve indicate the points of CO_2 lines absorption
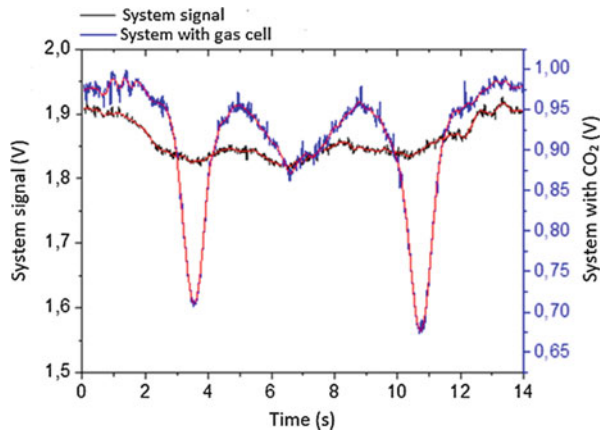
line, is the system before gas cells connection. The voltage level is 1.85 V for power input -24 dBm before optical-electric conversion. In the second step, the standard gas cell is connected to the system and the blue line shows valleys in 0.7 V, that indicate when there is gas light absorption. Two valleys mean two absorption lines.

Therefore, the obtained results show the system sensitivity for detection of CO_2 absorption lines. If the FBG were built for another wavelength corresponding to other gases absorption lines, the detection would be possible within system parameters.

Before concluding, we would like to note that recent simulations tools for the are now available to support the development of customized and efficient semiconductor sources operating in the mid infrared with good quality emission linewidth [20–22]. New compact sources, coupled with a new generation of mid infrared optical fibers will allow the extension of the inexpensive detection method described in this paper to the mid infrared. Furthermore, recent progress in the GHz-THz [23–32] points towards the possibility of combining in a single box source and detectors operating from the GHz to the NIR, allowing the detection of a very wide range of absorption signatures of the majority of gases of relevance for both atmospheric control and CBRN detection.

16.4   Conclusions

In this work, the importance of developing gas detection systems using optical waveguides is evidenced with the study of possible optical fibers to be applied as gas sensor, having emphasis in PCF. By Acreo cooperation, two microstructured optical fiber were fabricated and then tested in this effort. One of them behaves as a suitable to realize measurement of the absorption level of C_2H_2 with a laser source at 1550 nm. Particularly, the development focus of microstructured optical fibers application prioritizes the operating range in wavelengths used for telecommunications systems which corresponds to the range of 750–1700 nm. Thus, they do not always present gas absorption desired wavelengths, as was shown in FOM2 analyses with CO_2. For this step, gas cells and a commercial HC-2000 PCF were applied in the environment system, presenting satisfactory results and showing the possibility to develop CO_2 detection with this mentioned optical fiber. Final topic, a scanning system based on laser ring was designed with a FBG in 1950 nm. This system presents sensibility to CO_2 lines absorption as shown in Figs. 16.5 and 16.8, and the same results presented in optical domain can be also verify in electrical domain.

References

1. Gomes MSP (2013) Desenvolvimento de Sensores Ópticos para Monitoramento de CO_2. Petrobrás, Rio de Janeiro
2. Jane Hodgkinson RPT (2013) Optical gas sensing: a review. Meas Sci Technol 24(1):012004
3. Jin W, Ho HL, Cao YC, Ju J, Qi LF (2013) Gas detection with micro- and nano-engineered optical fibers. Elsevier 19(6, Part B):741–759
4. Russell PSJ (2006) Photonic-crystal fibers. J Lightwave Technol 24(12):4729–4749
5. de Matos CJS (2008) Fibras de cristal fotônico: novas plataformas para estudos de óptica não-linear, sensoriamento e dispositivos fotônicos. Universidade Presbiteriana Mackenzie
6. Hensley CJ, Broaddus DH, Schaffer CB, Gaeta AL (2007) Photonic band-gap fiber gas cell fabricated using femtosecond micromachining. Opt Express 15(11):6690–6695
7. Fetzer GJ, Pittner AS, Ryder WL, Brown DA (2002) Tunable diode laser absorption spectroscopy in coiled hollow optical waveguides. Appl Opt 41(18):3613–3621
8. Fávero FC (2012) Sensores a Fibra Óptica Microestruturadas, Pontifícia Universidade Católica do Rio de. Janeiro, Rio de Janeiro
9. Song YW, Havstad SA, Starodubov D, Xie Y, Willner AE, Feinberg J (2011) 40-nm-wide tunable fiber ring laser with single-mode operation using a highly stretchable FBG. IEEE Photon Technol Lett 13(11):1167–1169
10. Agrawal GP (2002) Fiber-optic communication systems. Wiley, Hoboken
11. Fields JN, Asawa CK, Ramer OG, Barnoski MK (1980) Fiber optic pressure sensor. J Acoust Soc Am 67:816
12. Allen MG (1998) Diode laser absorption sensors for gas-dynamic and combustion. Meas Sci Technol 9:545
13. Waechter H, Litman J, Cheung AH, Barnes JA, Loock H-P (2010) Chemical sensing using fiber cavity ring-down spectroscopy. Sensors 10(3):1716–1742
14. Echer E, Souza MP, Schuch NJ (2010) A Lei de Beer Aplicada na Atmosfera Terrestre. Rev Bras Ensino Fís 23(3):276–283
15. HITRAN. http://hitran.org/
16. HC-2000 Thorlabs – PCF, 2000 nm, Ø14.5 μm core. https://www.thorlabs.com/thorproduct.cfm?partnumber=HC-2000
17. Wavelength References. http://www.wavelengthreferences.com/products/single-mode-flowcells
18. Moreira MF (2004) Desenvolvimento e caracterização de um sistema laser de cristal líquido colestérico acoplado à fibra óptica. Pontifícia Universidade Católica do Rio de Janeiro, Rio de Janeiro
19. Adler F, Thorpe MJ, Cossel KC, Ye J (2010) Cavity-enhanced direct frequency comb spectroscopy: technology and applications. Rev Anal Chem 3:175–205
20. Oriaku CI, Pereira MF (2017) Analytical solutions for semiconductor luminescence including coulomb correlations with applications to dilute bismides. J Opt Soc Am B 34:321
21. Pereira MF (2018) Analytical expressions for numerical characterization of semiconductors per comparison with luminescence. Materials 11:2
22. Pereira MF (2016) The linewidth enhancement factor of intersubband lasers: from a two-level limit to gain without in-version conditions. Appl Phys Lett 109:222102
23. Pereira MF, Zubelli PJ, Winge D, Wacker A, Rondrigues SA, Anfertvev V, Vaks V (2017) Theory and measurements of harmonic generation in semiconductor superlattices with applications in the 100 GHz to 1 THz range. Phys Rev B 96:045306
24. Pereira MF, Anfertev V, Zubelli JP, Vaks V (2017) Terahertz generation by gigahertz multiplication in superlattices. J Nanophotonic 11(4):046022
25. Apostolakis A, Pereira MF (2019) Controlling the harmonic conversion efficiency in semiconductor superlattices by interface roughness design. AIP Adv 9:015022
26. Apostolakis A, Pereir MF (2019) Numerical studies of superlattice multipliers performance. Quan Sens Nano Electron Photon XVI:109262

27. Apostolakis A, Pereira MF (2019) Potential and limits of superlattice multipliers coupled to different input power sources. J Nanophotonics 13:036017
28. Winge DO, Franckié M, Verdozzi C, Wacker A (2016) Simple electron-electron scattering in non-equilibrium Green's function simulations. J Phys Conf Ser 696:012013
29. Pereira MF, Shulika O (2014) Terahertz and mid infrared radiation: detection of explosives and CBRN (using terahertz), NATO science for peace and security series-B: physics and biophysics. Springer, Dordrecht
30. Pereira MF, Shulika O (2011) Terahertz and mid infrared radiation: generation, detection and applications, NATO science for peace and security series-B: physics and biophysics. Springer, Dordrecht
31. Apostolakis A, Pereira MF (2020) Superlattice nonlinearities for gigahertz-terahertz generation in harmonic multipliers. Nano 9(12):3941–3952. https://doi.org/10.1515/nanoph-2020-0155
32. Pereira MF, Anfertev V, Shevchenko Y, Vaks V (2020) Giant controllable gigahertz to terahertz nonlinearities in superlattices. Sci Rep 10:15950
33. Xu Y, Cottenden A, Jones NB (2006) A theoretical evaluation of fibre-optic evanescent wave absorption in spectroscopy and sensors. Opt Lasers Eng 44(2):93–101
34. Pissadakis S, Selleri S Optofluidics, sensors and actuators in microstructured optical fibers 1st Ed. Elsevier 312

Chapter 17
Raman Cooperative UV Generation with Possible Applications in Microbiology

Marina Turcan and Tatiana Paslari

Abstract The goal of the present work is the study and use of the cooperative effects of bacteria located in the evanescent field of biomaterials during Raman interaction of the light in UV region. A model is proposed based upon existing experiments, which takes into account the local symmetry of biomolecules. In this paper is presented the quantum correlations which can be obtained in the processes of Raman scattering in two photon lasing. An interesting behavior of Stokes and anti-Stokes generated field in the Raman processes can be observed for the small number of pump field in nonlinear media. The photons statistic is proposed for the diagnosis of the new collective processes. The set of functions was presented, which describes the probability of simultaneous existence of $(2j + 1)$ Dicke states in the scattering process.

Metamaterials with periodical structures like quartz or glass small granules irradiated by ultraviolet-C (UV-C) to act against microbial contamination of translucent liquids and gases are studied. Investigations of the modifications of individual metamaterial elements when UV evanescent waves are dispersed in the optical contact zone, as a function of granule geometry, were performed. Different situations were investigated, when quartz (SiO_2), glass, or black (plastic) materials with dimensions of about 0.5–3 mm are separately placed into a quartz tube of about 2.7 cm diameter and 90 cm length, named "core tube". Quartz granules transmit within the (240–400 nm) region of the Hg lamp and ensure an effective decontamination of translucent liquids and gases. Our approach is based upon the increased transfer of UV radiation via evanescent waves in case of unordered metamaterials present in contaminated fluids. We made a series of estimations of the decontamination rate of this type of metamaterials vs. ordered metamaterials consisting of

M. Turcan (✉)
Quantum Optics and Kinetic Processes Laboratory, Institute of Applied Physics, Chisinau, Republic of Moldova

T. Paslari
Faculty of Physics and Engineering of Moldova State University, Chisinau, Republic of Moldova

spherical elements. Experiments have convincingly demonstrated that both quartz and glass metamaterials can effectively annihilate Coliform (including Escherichia coli) or Enterococcus bacteria. Control experiments were performed in the absence of metamaterials and/or UV-C irradiation.

17.1   Introduction

The penetration depth is typically less than that of microwave radiation. For this reason, we use UVC radiation for disinfection and treatment. The Terahertz radiation has limited penetration and cannot penetrate liquid water or metal, but UV radiation can penetrate liquid and can decontaminate it. In the same time, some frequencies of terahertz radiation can penetrate several millimeters of tissue with low water content (e.g., fatty tissue) and reflect back. In Medicine, unlike X-rays, terahertz radiation is not ionizing radiation and its low photon energies, in general, do not damage living tissues and DNA. Terahertz radiation can also detect differences in water content and density of tissue. Such methods could allow effective detection of epithelial cancer with an imaging system that is safe, non-invasive, and painless. The first images generated using terahertz radiation date from the 1960s; however, in 1995 images generated using terahertz time-domain spectroscopy generated a great deal of interest. Some frequencies of terahertz radiation can be used for 3D imaging of teeth and may be more accurate than conventional X-ray imaging in dentistry. Fourier-transform infrared spectroscopy (FTIR) is a technique used to obtain an infrared spectrum of absorption or emission of a solid, liquid or gas. Raman spectroscopy can analyse buried material or particles of foreign material smaller than 1 μm which cannot be measured by FTIR. Raman spectroscopy is one of the vibrational spectroscopic techniques used to provide information on molecular vibrations and crystal structures. When foreign material is discovered on the surface of manufactured goods or inside a transparent film, a spectrum can be taken for identification. Because Raman spectroscopy is also sensitive in lower frequency regions of the spectrum, identification of inorganic material is also possible. Crystal polymorphism of a material occurs when the chemical formula is the same but the crystal structure of the material is different. Raman spectroscopy allows for analysis of crystal polymorphism, with similar but slight differences in position and intensity ratios of particular peaks between polymorphs, sufficient for identification. Both polymerization and damage to the molecular structure are accelerated via irradiation by UV rays. By recording the Raman spectrum over time, one can follow changes in the molecular structure of the sample. For example, in a polymer the C=C bond can be formed by the irradiation of ultraviolet rays, thus changes can be tracked by focusing on the change in the corresponding peak intensity. An ultraviolet curable resin is a polymer which is composed of monomers and then hardened by the monomers crosslinking with each other due to the absorption of ultraviolet rays. If one compares the Raman spectrum after irradiation and before UV irradiation, the peak intensity windles with irradiation; thus you can see that the cure is progressing.

Raman spectroscopy is now used in a variety of fields. But in spite of this, the level of awareness of Raman spectroscopy is not as high as that of the analytical methods that everyone knows. In order to introduce the diverse characteristics of Raman spectroscopy, specific examples are incorporated in this chapter. The paper is organized as follows. The introduction, a short description and advantages of the methods in second section, theoretical and experimental approach. The installations with UV-radiation for decontamination in the case of CBRN, for daily conditions, are presented in the end of this chapter.

Raman spectroscopy is a powerful technique that can distinguish between healthy and unhealthy cells and cancerous and non-malignant cells. It has been successfully utilized to determine qualitatively and quantitatively the molecular compositions of solid, liquid, and gases samples. The nonlinear theory of the excitation of vibration modes of bio-molecule of viruses and bacteria is proposed, taking into consideration the bimodal coherent states in coherent Raman excitation of biomolecules. According to N. Blombergen [1], the coherent nonlinear Raman spectroscopy observed in 1963 will yield many new results in the next half-century. In [2], the authors summarized the most important advantages of vibrational spectroscopy based on nonlinear coherent anti-Stokes generation mechanism, which is five orders of magnitude stronger relative to spontaneous offers signals that are over Raman scattering. In several circumstances, this nonlinear technique avoids interference with a one-photon excited fluorescence background that often plagues conventional Raman measurements. This technique with the name coherent anti-Stokes Raman spectroscopy (CARS), and [2] reported the method as an attractive tool for rapid vibrational spectroscopy. For dappling the Ultrashort pulsed (USP) lasers in Coherent Raman Scattering (CRS) or CARS in the decontamination procedure of viruses and bacteria in many cases it is necessary to know and use the proposed models, not only the relative dimensions of viruses and bacteria but the symmetry and topology of theirs [3, 4]. Most natural viruses depend upon the existence of spherical capsids: protective shells of various sizes composed of protein subunits. So far, general evolutionary pressures shaping capsid design have remained elusive, even though an understanding of such properties may help in rationally impeding the virus life cycle and designing efficient nano-assemblies. Raman microscopy is a promising technology for visualizing the distribution of molecules in cells. A challenge for live-cell imaging using Raman microscopy has been long imaging times owing to the weak Raman signal. The protocol for constructing and using a Raman microscope equipped with both a slit-scanning excitation and detection system and a laser steering and nanoparticle-tracking system was done already by authors from [5]. Below we compare a part of types of the technics Raman that are more applicable in different domains in especially in medicine and physics. For this reason, we explain how to interact photons with molecules in Raman process. When a photon of light interacts with a molecule, it can induce a short-lived transition to a virtual energy state. This temporary increase in energy means that the molecule is in a higher or virtual energy state. The molecule can relax back to the initial ground state in a single step by releasing the same amount of energy as that of the incoming photon--this process's known as Rayleigh (or elastic) scattering [6]. As
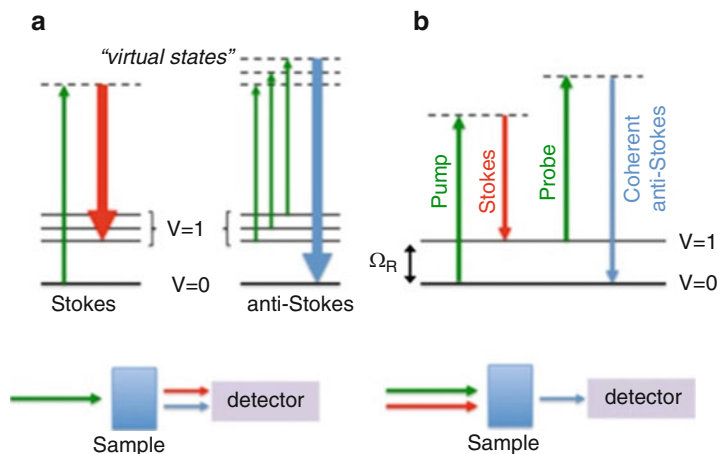
Fig. 17.1 Principle of Raman scattering mechanisms of (**a**) spontaneous Raman and (**b**) narrow-band CARS shown by Jablonski diagram (energy level diagram). Arrows represent photons (longer length denotes higher photon energy), V is the vibrational level, ΩR is the resonant vibrational frequency of a given vibrational mode [9]

the energy of a photon is proportional to its frequency, and since no energy is transferred to the molecule, Rayleigh scattered light does not yield any information about the molecules under investigation. However, relaxation can also occur in an inelastic manner — when a molecule releases a different quantity of energy to that of the incident photon. This phenomenon is known as Raman scattering; due to nuclear motion, energy can be transferred to or from the incident photon. There are two types of Raman scattering—Stokes and anti-Stokes scattering see Fig. 17.1. In the case of Stokes scattering, energy can be transferred to the molecule from the incident photon via nuclear motion within the molecule, resulting in a scattered photon of reduced energy and hence reduced frequency. Conversely, in a smaller proportion of molecules energy is transferred to the photon as, due to the distribution of thermal energy, these molecules are initially in a higher energy state. This is anti-Stokes scattering [7]. In biomedical research, Stokes scattering is most commonly observed and the signal is inherently weak.

If we get into the CARS case and compare with another effect stimulated Raman scattering (SRS) we have advantage at the detection. Nonlinear coherent Raman effects such as coherent anti-Stokes Raman scattering (CARS) and stimulated Raman scattering (SRS) enhance the weak Raman signal by means of nonlinear excitation. When the energy difference between two laser beams exciting a sample matches a molecular vibration, resonance occurs that enhances the intensity of light generated at the anti-Stokes frequency (CARS signal) or induces a change in the excitation beam intensity (SRS signal). The CARS or SRS signal is usually several orders of magnitude stronger than spontaneous Raman. This has enabled video-rate imaging to be achieved [5]. Another advantage is that these techniques allow detection of the Raman band even from strong fluorescent samples, because the

detection of CARS or SRS is not affected by fluorescence. The CARS signal is emitted at a higher frequency, which does not overlap with one-photon fluorescence, whereas SRS is detected at the excitation field frequency by radio-frequency lock-in detection. And thus far, these techniques have been demonstrated only for strong Raman bands from chemical species with high concentrations. For example, CH2-stretching vibrations, which are typically found in high concentrations in cells as lipids, produce strong CARS and SRS signals. In SERS, a metallic nano-structure interacts with incident photons, which generates an enhanced electric field in the vicinity of the metal surface. When a target molecule exists near the surface of a metallic nanostructure, Raman scattering is markedly enhanced. SERS has been widely used in biomedical applications because of its high-sensitivity detection and molecular selectivity [8].

Raman spectroscopy can distinguish between healthy and unhealthy cells and cancerous and nonmalignant cells [9]. Thus, Raman spectroscopy is a powerful technique for label-free identification and characterization with potential for translation to biomedical and clinical applications. The Raman spectrum provides a measure of the vibrational mode density of molecules that can be translated to biochemical content. In the spontaneous Raman process, (see Fig. 17.1a), a narrow band laser illuminates the sample and a portion of the incident photons is scattered by interactions with molecular vibrations, resulting in a shift to higher (anti-Stokes) or lower frequency (Stokes) photons. In the CARS process, two laser beams with different wavelengths (816 nm – pump/probe beams and 1064 nm – Stokes beam) coherently excite a particular vibrational mode, see Fig. 17.1b. For CARS, the laser source consists of two time-locked pulse trains of different wavelengths (pump + Stokes) such that the difference in photon energy corresponds to the vibrational mode to be imaged. The anti-Stokes photon is detected indicating the strength of the signal at a given vibrational mode.

17.2 Description of the Theory in the Raman Process

In this paper, we consider a propagating of the pulse along the nano-fiber in the two-photon Raman resonance with the excited atomic subsystem trapped in the evanescent field of this fiber [10]. During the pulse propagation in the fiber wave mod the new pulse is generated due to the scattering conversion of the photons in anti-Stokes (or Stokes) mode becomes possible in the process of relaxation (excitation) of the atoms trapped in the evanescent zone of the fiber. By comparing the pulse propagation through the fiber optics with atomic propagation through the cavity, studied in micro-maser models [11, 12], we propose to study the cooperative photon conversion in the dynamical regime of photon conversion between the two pulses belonging to two modes of nano-fiber during the pulse propagation. As the pump pulse is regarded as the "moving cavity" along the static atomic line, we can replace the propagation atomic flux through the cavity studied in micro-maser models [11, 12], with atomic system trapped in the evanescent zone of fiber optics and the
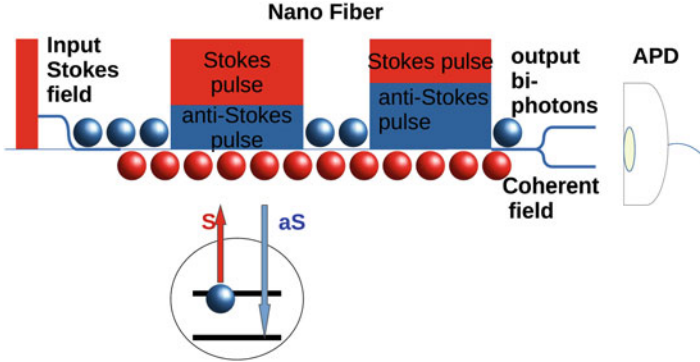
Fig. 17.2 Propagation of Stokes pulse through nano-fiber and its conversion in anti-Stokes pulse. The red part of the pulse is the Stokes component and the blue part corresponds to anti-Stokes one [7]

cavity standing waves in which is generated the photons by the pulse propagation [13], of the light into two fiber modes (see Fig. 17.2 from Ref. [7]). Due to the scattering interaction of this pulse with the tree level system trapped in the near field zone of fiber it is possible the cooperative conversion of the photons from the pump field into the new pulse mode (Stokes or anti-Stokes) as the function of the preparation of the atomic subsystem concentrated in the evanescent field. In this way, we propose to change the standing waves of the cavities with the cooperative conversion of the photons into anti-Stokes mode during the pulse propagation. This effect helps us to obtain in the output field of nano-fiber the new correlated pulse of the photons generated in the two entangled state modes of the fiber (See Fig. 17.2). The conversion takes place during the time propagation of the short pump pulse through the fiber and the conversion rate depends on the interaction time of the atoms with the photons from nano-fiber [13, 14]. The phase and amplitude of the bi - boson field coherently created in the two fiber modes is discussed in the language of induced Bose condensate.

The anti-Stokes photons are created simultaneously in the same propagation pump pulse during the cooperative scattering process. As a model we consider that n-photons from the pump field which may be converted into the anti-Stokes photon field, so that after cooperative times of the conversion the pump and anti-Stokes modes forms the new coherent state as a superposition between both modes. This conversion is similar to the Dicke super-radiance [15], but the cooperation appears between the photons belonging to two propagation modes of nano-fiber. The coherence proprieties of this bimodal field may be detected in the output field of fiber using the correlation schemes like Hanbury-Brown and Twiss (HBT) [16] or balanced homodyne detector [17].

The Hamiltonian which describes the interaction of the atoms with Stokes and anti-Stokes modes of the cavity electromagnetic field (EMF) can be represented through the atomic and field operators

$$H = \hbar(\omega_a + \omega_b)^{n_{ph}}/2 + \hbar(\omega_b - \omega_a)\widehat{J}_z + \sum_{j=1}^{N}\hbar\omega_0\widehat{R}_z^j + i\sum_{j=1}^{N}G_j(k_a,k_b)$$

$$\times\left\{\widehat{R}_j^-\widehat{J}^+ - \widehat{J}^-\widehat{R}_j^+\right\} \tag{17.1}$$

in which the last term represents the interaction Hamiltonian part, $\widehat{R}_{zj} = \left(|e\rangle_l\langle e|_l - |g\rangle_j\langle g|_j\right)/2$ is the population inversion of atom j; $\widehat{R}_j^+ = i|e\rangle_j\langle g|_j e^{-i(k_b-k_a)x_j}$ and $\widehat{R}_j^- = -i|g\rangle_j\langle e|_j e^{i(k_a-k_b)x_j}$ represent the operatoms, which describe the excitation and lowering operators between the $|g>$ -ground and $|e>$ -excited states of atomic subsystem, respectively (see Fig. 17.3) [7]. The operator $\widehat{a}\,(\widehat{a}^+)$ is the creation (annihilation) of Stokes photons and $\widehat{b}\left(\widehat{b}^+\right)$ is the creation (annihilation) of anti-Stokes field operators. The interaction constant $G(k_a, k_b) \approx 2d_{ei}d_{gi}g_ag_s/(\hbar\delta)$ describes the effective nonlinear coupling of the atom with fiber modes k_a and k_b with the energies $\hbar\omega_a$, $\hbar\omega_b$ and polarizations $e_{\lambda s}$ $e_{\lambda a}$, respectively. In order to describe the collective processes, we introduced in Hamiltonian (17.1) the collective operators for bimodal field $\widehat{J}^+ = \widehat{a}\widehat{b}^+$, $\widehat{J}^- = \widehat{b}\widehat{a}^+$, $\widehat{J}_z = \left(\widehat{a}^+\widehat{a} - \widehat{b}^+\widehat{b}\right)/2$ which are represented in Fig. 17.3.

The operator of annihilation (generation) for Stokes mode is $\widehat{a}^+(\widehat{a})$ and for anti-Stokes mode is $\widehat{b}^+\left(\widehat{b}\right)$ belong to SU(2) symmetry, see Fig. 17.2 was described in Ref. [7]. In the figure on the right are highlighted the critical points that describe the stationary solutions in the case of the semi-classical approximation for the hyper Raman laser. The working point of the hyper-Raman laser when the Bloch vector stops below
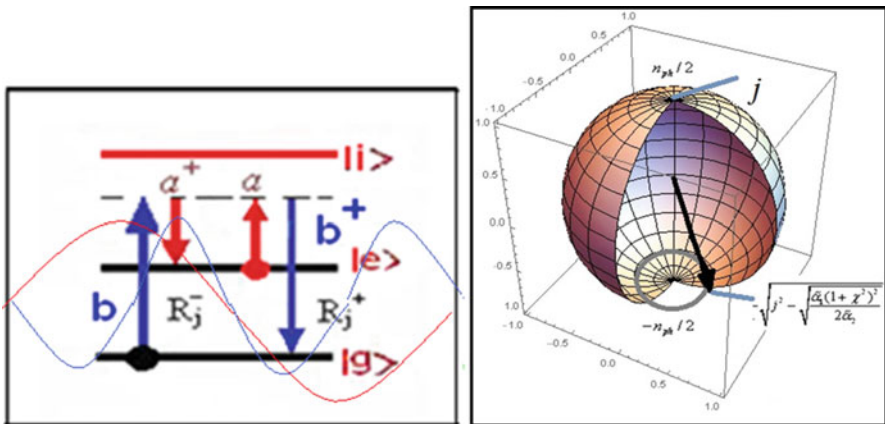

Fig. 17.3 The left figure shows the collective excitation of atom with absorption of Stokes photon and generation of anti-Stokes quanta and vice versa. The geometric representation of the symmetry of such generation field in phase space of bimodal cavity is shown in the right figure

the equator is presented here: $\left\langle \widehat{J}_z \right\rangle_1 = -\sqrt{j^2 - \sqrt{\left[\widetilde{\alpha}_1(1+\chi^2)^2\right]/2\widetilde{\alpha}_2}}, \left\langle \widehat{J}_z \right\rangle_2 = j$.
The coefficients are: $\widetilde{\alpha}_1$ emission rate of the conversion of Stokes photons in anti-Stokes, N is the mean number of atoms in the cavity, $\widetilde{\alpha}_2$ is the diffusion coefficient connected with the decreases the cavity field during the interaction with cavity field, $\chi = (\widetilde{\omega} - \omega_0)\gamma^{-1}$ is the detuning from resonance. All Raman process takes place on the surface of this sphere. This reduction to SU (2) symmetry helps us to solve exactly the super radiant conversion between the Stokes and anti-Stokes photon using the conservation law of Bloch vector.

During the propagation we can use the generalized operator equations for the field components in nano-fiber:

$$\frac{d}{dx}\left\langle \widehat{O}(x) \right\rangle = i\widetilde{\omega}\left\langle \left[\widehat{J}_z(x), \widehat{O}(x)\right] \right\rangle$$
$$+ \frac{1}{\hbar}\sum_{l=1}^{N}\left\{\left\langle \left[\widehat{J}^-(x), \widehat{O}(x)\right]\widehat{R}_l^+(x)\right\rangle + H.c.\right\} \qquad (17.2)$$

where the direction of propagation is $x = ct$, c is the photon velocity in the nano-fiber and t is the time of propagation. The bi-boson operators is introduced for the descriptions of these quantum proprieties of this field. This representation describes the cooperation and entangled states of the photons from the pump and anti-Stokes pulses. As in Dicke super radiance the cooperative effect appears between indistinguishable atoms, we decide to export this collective effect between undistinguished photons of Stokes and pump modes during the conversion. Dicke super-radiance is the emission of excited atom system of N atom with intensity of light proportional to the square number of atoms. This effect is attractive because the atoms become indistinguishable, when the dimension of the system is less than the emission of wavelength [13, 14]. In process of spontaneous emission the cooperative effect appears between indistinguishable atoms so that the system generates a pulse of photons proportional to square number of atoms. The similar effect can be proposed in the scattering processes between two cavity modes [13, 14]. In this case instead of atoms we have photons. If the photons are scattered in another mode of cavity we may consider like another state of a cavity. In other words, we can associate the photons in distributed between two cavity modes as an ensemble of two level system. Really, if the photons initially are prepared in the Stokes mode (red light all photons are in the red state) it can super radiantly converted into anti-Stokes mode (blue light). If we have the conversion of photons from red to blue light modes appear the problem what kind super radiances are generated in this process? The answer is: that the rate of living atoms in the ground state firstly increased achieving the maximum value after that it decrease like in super radiance. This rate is proportional to square number of photons prepared in anti-Stokes mode [13, 14], see Fig. 17.4 from [7]. According to Fig. 17.4 this is a difficult effect. The state of light can be measured testing the number of atoms in the ground and excited state like in the Walther micro maser experiment [11]. We want to change this procedure
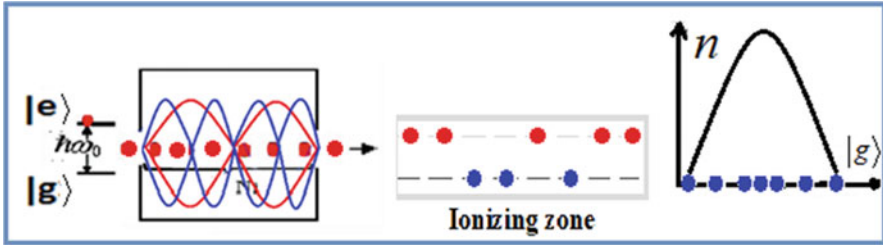
Fig. 17.4 The atomic pump of the scattering process with the transformation of n-Stokes photon field and the number of atoms in the ground state [7] are presented like in the Walther micro maser experiment [11]

of measurements, replacing the two mode cavity with electromagnetic pulse in the fiber. Nano-fiber is the system, which considers that the diameter of evanescent zone is larger than fiber diameter. The experimental group used a resonant laser for probing the atoms via the evanescent field [12].

In this case the atomic flux used in the micro cavity can be replaced by trapped atoms along the nano-fiber as is presented in Fig. 17.2 from Ref. [7]. We replace the atomic flux with trapped atoms (or doped fiber), and standing waves with two pulses propagated along the fibre like in Fig. 17.2 see Ref. [7]. This is equivalent with the studying of moving cavity in the reference system connected with moving atoms through the cavity. If we will pass on this reference system the cavity will move in the opposite direction with velocity – V. In case of Dicke super-radiance the excited ensemble of N two level atoms pass to ground state occurs due to the interaction of vacuum EMF. During the atomic super radiance the system emits a pulse of correlated photons. The detection of super-radiance is possible if we study the photon pulse shape and photon correlations.

In case of cooperative conversion of photons we observe that the n photons prepare in the pump mode are converted into the anti-Stokes photons. The cooperative correlation between the pump and anti-Stokes photons take place through the excited state of trapped atoms. In other words the rule of vacuum fields in Dicke super radiance is replaced by "atomic ensemble" in the excited state. The coherence proprieties of this field depend on the ratio between the propagation time τ_p through the fiber and τ_c cooperative conversion time τ_p/τ_c. When $\tau_p/\tau_c < 1$, the number of photons from pump field partially was converted in the anti-Stokes photons. The opposite case $\tau_p/\tau_c > 1$ can be regarded as a total conversion of pump photons to anti-Stokes photons. According to the theory of super radiance we associated the delay time with τ_p, time of the formation of super radiance pulse $\tau_p = (\tau_0/n)\ln(n)$, where τ_0 is the scattering time. As the similar delay time appears in the process of photon conversion on the pump field into anti-Stokes one, we may consider it large in comparison with super-radiance pulse duration. To avoid this discrepancy between the pulse propagation and the delay time of super radiance of cooperative process, it is better to initiate the anti- Stokes pulse to external small pulse. In this situation, the cooperative conversion process can start immediately with the entrance the pump pulse in fiber.

17.3 Quantum Solution of Master Equation

The Heisenberg equation, is obtained, for mean value of field operator $\widehat{O}(t)$ expressed through the solution of the atomic operators $\widehat{R}_j^+(t)$, $\widehat{R}_j^-(t)$ and $\widehat{R}_{zj}(t)$ represented in Born-Markov approximation [14]. The Master equation for arbitrary field operator, in the second order of interaction constant G are represented in the following way

$$
\frac{d}{dt}\left\langle \widehat{O}(t) \right\rangle = i\chi\gamma_\perp \left\langle \left[\widehat{J}_z(t), \widehat{O}(t)\right] \right\rangle + \widetilde{\alpha}_1 \left\{ \left\langle \widehat{V}^-(t)\widehat{O}(t)\widehat{V}^+(t) - \widehat{V}^-(t)\widehat{V}^+(t)\widehat{O}(t) \right\rangle + H.c. \right\}
$$

$$
-\widetilde{\alpha}_2 \left\{ \frac{(1-\chi^2)}{(1+\chi^2)^2} \left[\left\langle \widehat{V}^-(t)\widehat{V}^+(t)\widehat{V}^-(t)\left[\widehat{O}(t), \widehat{V}^+(t)\right] \right\rangle. + H.c.\right] \right.
$$

$$
+ \frac{1}{1+\chi^2}\left[\left\langle \widehat{V}^-(t)\widehat{V}^-(t)\left[\widehat{O}(t), \widehat{V}^+(t)\right]\widehat{V}^+(t) \right\rangle + H.c. \right]
$$

$$
+ i\frac{2\chi}{(1+\chi^2)^2}\left[\left\langle \widehat{V}^-(t)\widehat{V}^+(t)\widehat{V}^-(t)\left[\widehat{O}(t), \widehat{V}^+(t)\right] \right\rangle - H.c.\right] \right\}. \tag{17.3}
$$

Where for $n = 1$, $\widetilde{\omega} = \omega_d - \omega_b \approx \omega_0$, $V^\pm = J^\pm$, we have Raman process and $n = 2$, $\widetilde{\omega} = \omega_d - \omega_b \approx \omega_0$, $V^\pm = (J^\pm)^2$, we have hyper-Raman process. The coefficients in Master equations in the resonance case are: $\widetilde{\alpha}_1 = G^2 N/\hbar^2$ emission rate of the conversion of Stokes photons in anti-Stokes, N is the mean number of atoms in the cavity, $\widetilde{\alpha}_2 = 2G^4 N/\left[\hbar^4\gamma^3\right]$ is the diffusion coefficient connected with the decreases the cavity field during the interaction with cavity field, $\chi = (\widetilde{\omega} - \omega_0)\gamma^{-1}$ is the detuning from resonance. In this equation, the new constants are represented through the interaction parameter, $K_l^2(k_a k_b)$, detuning, $\widetilde{\omega} - \omega_0$, number of atoms, N, polarization damping rates $\gamma_\perp$ and are defined below. $\widetilde{\alpha}_1 = NK_l^2(k_a k_b)/\left[\hbar^2\gamma_\perp(\chi^2 + 1)\right]$ is the analytical expression of emission rate of anti-Stokes photons, $\widetilde{\alpha}_2 = 2K_j^4(k_a, k_b)N/\left[\hbar^4\gamma_{II}\gamma_\perp^2\right]$ describes the diffusion coefficient in the generation process of anti-Stokes photons. Here the parameter $\chi = (\widetilde{\omega} - \omega_0)\gamma_\perp^{-1}$ depends on the detuning between the transition frequency ω_0 and $\widetilde{\omega} = \omega_a - \omega_s$. The first term of Eq. (17.3) describes the rate of collective transformation of anti-Stokes photons into Stokes photons. The terms, proportional to the diffusion coefficient in the generation process of anti-Stokes photons $\widetilde{\alpha}_2$, correspond to nonlinear attenuation processes of the generation, which, has the tendency to stabilization of scattering process. The scheme of atomic transitions between the atomic levels with collective amplification of Stokes (anti-Stokes) field number is represented above. The experimental parameters were discussed in more detail in [17, 18] for the cases of H2 and CS2 Raman lasers.

In semi-classical approach, it is neglected the quantum fluctuations of the conversion operator of Stokes photons in anti-Stockes $\widehat{J}_z(t)$. Let us consider instead of the $\widehat{O}(t)$ operator the operator $\widehat{J}_z(t)$. In this case we can use the following de-correlation method for field operators

$$
\left\langle \widehat{\widetilde{J}}^- \widehat{\widetilde{J}}^+ \widehat{\widetilde{J}}^- \widehat{\widetilde{J}}^+ \right\rangle \approx \left\langle \widehat{\widetilde{J}}^- \widehat{\widetilde{J}}^+ \right\rangle \left\langle \widehat{\widetilde{J}}^- \widehat{\widetilde{J}}^+ \right\rangle, \quad \left\langle \widehat{\widetilde{J}}^- \widehat{\widetilde{J}}^- \widehat{\widetilde{J}}^+ \widehat{\widetilde{J}}^+ \right\rangle
$$

$$
\approx \left\langle \widehat{\widetilde{J}}^- \left(\widehat{\widetilde{J}}^+ \widehat{\widetilde{J}}^- - 2\widehat{J}_z \right) \widehat{\widetilde{J}}^+ \right\rangle
$$

$$
= \left\langle \widehat{\widetilde{J}}^- \widehat{\widetilde{J}}^+ \right\rangle \left\langle \widehat{\widetilde{J}}^- \widehat{\widetilde{J}}_z \right\rangle - 2\left\langle \widehat{J}_z \right\rangle \left\langle \widehat{\widetilde{J}}^- \widehat{\widetilde{J}}^+ \right\rangle \tag{17.4}
$$

Following this method and the conservation law $j(\,j+1) = \widehat{J}_z^2 + \widehat{J}_z + \widehat{\widetilde{J}}^- \widehat{\widetilde{J}}^+$, we obtain for Raman case Eq. (17.5). For $\omega_d - \omega_b = \omega_0$; *Raman process* $\widehat{O}(t) = \widehat{J}_z(t)$

$$
\frac{d}{dt} \left\langle \widehat{J}_z(t) \right\rangle = \left[j(\,j+1) - \left\langle \widehat{J}_z(t)^2 \right\rangle - \left\langle \widehat{J}_z(t) \right\rangle \right]
$$

$$
\times \left\{ 2\widetilde{\alpha}_1 - \frac{4\widetilde{\alpha}_2}{1+\chi^2} \left\{ \frac{1}{1+\chi^2} \left[j(\,j-1) - \left\langle \widehat{J}_z(t) \right\rangle^2 - \left\langle \widehat{J}_z(t) \right\rangle \right] - \left\langle \widehat{J}_z(t) \right\rangle \right\} \right\}. \tag{17.5}
$$

This equation pass into the Dicke super-radiant equation when the second order parameter $\widetilde{\alpha}_2$ is neglected in comparison with the first order $\widetilde{\alpha}_1$. Here $2j = n_{ph}$ is the number of the photons in Stokes modes at the initial time $t = 0$. We found the equation for the hyper Raman process too [14]. The steady state points on the Bloch sphere (see Fig.17.3 right) for the Eq. (17.4) can be found from the expression (17.5) for the Eq. (17.4) can be found if we equalled to zero left part. For $j \gg 1$, they correspond to the following values of mean value of the conversion operator: $\left\langle \widehat{J}_z \right\rangle_1 = -\sqrt{\,j^2 - (1+\chi^2)^2/b}$, $\langle J_z \rangle_2 = n_{ph}/2$. First point exists, when $j^2 > (1+\chi^2)^2/b$, where $b = 2\widetilde{\alpha}_2/\widetilde{\alpha}_1$ represent critical point. This point corresponds to the stabilization of the coherent states between the Stokes and anti-Stokes photons. When the above inequality is violated, $j^2_{critic} \leq (1+\chi^2)^2/b$, the laser condition for conversion of Stokes photons in anti-Stokes is absent. In this case the Bloch vector passed from ground state $-n_{ph}/2$ to upper state $n_{ph}/2$ like in the Dicke super radiance (see Fig. 17.5). In Fig. 17.5 we have the transformation of Stokes photons in anti-Stokes photons.

Passing from the field operator $\widehat{O}(t)$ in the Heisenberg picture to the density matrix W(t) in the Schrödinger representation Sp{W(t),O(0)} = Sp{W(0),O(t)}, we obtain the following master equation from Eq. (17.3), following the generalized equation for the bimodal cavity field operator $\widehat{O}(t)$

Fig. 17.5 The dependence
of emission rate and
inversion as function of the
relative time 2t
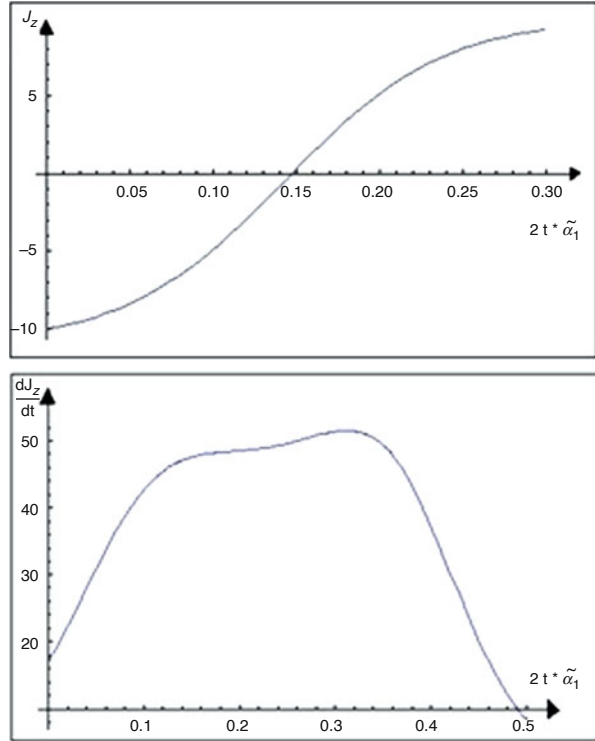
$$\frac{dW(t)}{dt} = -i\chi\gamma_\perp\left[\hat{J}_z, W(t)\right] + \tilde{\alpha}_1\left\{2\hat{J}^{+2}W(t)\hat{J}^{-2} - W(t)\hat{J}^{-2}\hat{J}^{+2} - \hat{J}^{-2}\hat{J}^{+2}W(t)\right\}$$

$$-\tilde{\alpha}_2\{\frac{1-\chi^2}{(1+\chi^2)^2}\left[\hat{J}^{+2}W(t)\hat{J}^{-2}\hat{J}^{+2}\hat{J}^{-2} - W(t)\hat{J}^{-2}\hat{J}^{+2}\hat{J}^{-2}\hat{J}^{+2} + \hat{J}^{+2}\hat{J}^{-2}\hat{J}^{+2}W(t)\hat{J}^{-2} - \hat{J}^{-2}\hat{J}^{+2}\hat{J}^{-2}\hat{J}^{+2}W(t)\right]$$

$$+\frac{1}{1+\chi^2}\left[\hat{J}^{+2}\hat{J}^{2+}W(t)\hat{J}^{2-}\hat{J}^{-2} - \hat{J}^{2+}W(t)\hat{J}^{2-}\hat{J}^{-2}\hat{J}^{+2} + \hat{J}^{+2}\hat{J}^{+2}W(t)\hat{J}^{-2}\hat{J}^{-2} - \hat{J}^{-2}\hat{J}^{+2}\hat{J}^{+2}W(t)\hat{J}^{-2}\right]$$

$$+i\frac{2\chi}{(1+\chi^2)^2}\left[\hat{J}^{+2}W(t)\hat{J}^{-2}\hat{J}^{+2}\hat{J}^{-2} - W(t)\hat{J}^{-2}\hat{J}^{+2}\hat{J}^{-2}\hat{J}^{+2} - \hat{J}^{-2}\hat{J}^{-2}\hat{J}^{-2}W(t)\hat{J}^{-2} + \hat{J}^{-2}\hat{J}^{+2}\hat{J}^{-2}\hat{J}^{+2}W(t)\right]\}\}.$$

$$(17.6)$$

This equation describes the collective transformation of Stokes photons in anti-Stokes fields and is similar to super-radiant master equations, which are traditionally studied in these studies [15, 17]. Let us find a quantum solution for the master Eq. (17.6). As it is proposed in papers [15, 17], we can expand the density matrix [14] over the coherent states of generalized of the angular moment states. As results from the Q and P-diagonal representation of density matrices, [13] when the right side of master equation has a relatively bi-quadrate form for the operators J^+ and J^-, the solution of master equation can be represented through diagonal bracket operator angular momentum states $W(t) = \sum_{m=-j}^{+j}P_m(t)|m,j\rangle\langle m,j|$.

Here, the Hilbert's vectors $|m,j\rangle$ belongs to the set of angular momentum states and obeys to SU(2) symmetry $(J^+)^2|m,j\rangle = \sqrt{(j-m-1)(j-m)(j+m+2)(j+m+1)}|m+2,j\rangle$ and $J^-|m,j\rangle = \sqrt{(j-m+1)(j+m)}|m-1,j\rangle$, P_m is the population probability of the state $|m, j\rangle$. By introducing the solution in Eq. (17.6), it is easy to obtain the following system of equations for the probabilities $\{P_m\}$

$$\frac{dP_m(t)}{dt} = 2\tilde{\alpha}_1\{P_{m-1}(t)(j-m+2)(j-m+1)(j+m)(j+m-1) - P_m(t)(j-m)(j+m+1)\}$$
$$-2\tilde{\alpha}_2\{\frac{1-\chi^2}{(1+\chi^2)^2}\left[P_{m-1}(t)(j-m+1)^2(j+m)^2 - P_m(t)(j-m)^2(j+m+1)^2\right]$$
$$+\frac{1}{1+\chi^2}(j-m+1)(j+m)[P_{m-2}(t)(j-m+2)(j+m-1) - P_{m-1}(t)(j+m+1)(j-m)]\}; \quad -j \leq m \leq j;$$

$$(17.7)$$

The set of functions $\{P_m(t)\}$ describes the probability of simultaneous existence of $(2j + 1)$ Dicke states in the scattering process [15]. The initial condition for the system of Eqs. (17.7) is $P_{-j} = 1$, $P_{-j+1} = P_{-j+2} = \ldots = P_j = 0$. The numerical behaviors of the system of Eqs. (17.7) is graphically represented in Fig.17.6, for following parameters of the system $\tilde{\alpha}_2/\tilde{\alpha}_1 = 0.005$ and $2j = 10$.

It was noticed, that the quantum fluctuations play an important role in the process of generation of Stokes or anti-Stokes photons. As results from the figures presented above, the transformation of $2j + 1 = 11$ Stokes photons into 11 anti-Stokes photons, take places in a very interesting way. This distribution can be regarded as the probabilistic repartitions between Stokes and anti-Stokes photons: (0,10); (1,9); (2,8); (3,7); (4,6); …(6,4); (7,3); (8,2); (9,1); (10,0). In the brackets, the first number (n, m) represents the Stokes photons and the second number - the anti-Stokes photons. The sum of these probabilities is equal to unity: $\sum_{m=-j}^{+j} P_m(t) = 1$.

The modern investigations connected with the manipulation of quantum fluctuations of the generated light and there application in transmission and detection of information with high degree of security play an important role in the modern defense problems. The UV radiation is largely absorbed by matter, and the purification of water or other biological liquid needs small volumes. In order to exclude this question, i.e., decontamination of small volumes, an efficient method was proposed, based on evanescent field technique created around silica metamaterials. When UV light is propagated through an optical fiber, significant quantity of radiation is spread outside of the fiber as an evanescent field that interacts with surrounding medium. Optical techniques play an important role for localization of nanometric and submicronic particles. Such methods, based on optical metamaterials (e.g., photonic crystals, optical fibres or cavities) where the penetration of evanescent field in the contaminated zone is primordial, can be used as an efficient decontamination procedure for viruses and microorganisms [19]. We provide a detailed theoretical description of the interaction of UV radiation with viruses, explaining the physical mechanism [20]. The experimental results that confirm the efficiency of the decontamination method for yeast, other results was published in

Fig. 17.6 The time dependence of probabilities $\{P_m(t)\}$ for following values of the relative parameter $\widetilde{\alpha}_2 = 0.005\widetilde{\alpha}_1$ and number of photons 2j = 4 (**a**) and 2j = 10 (**b**)
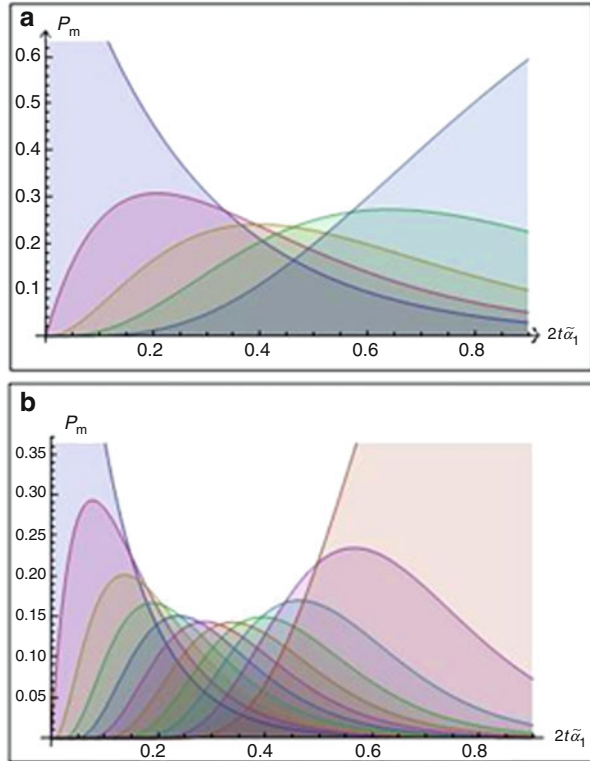
our previous paper [19]. A comparative analysis of the decontamination rate for these three types of metamaterials is made [20]. Before we proceed to concluding remarks, we would like to mention that there are other materials also being investigated for spectroscopy delivering devices that can also access vibrational and rotational levels, notably based on superlattices and quantum-cascade structures [21–33].

17.4　Conclusions

We propose new method of the Raman Cooperative Generation with possible applications in medicine and microbiology. The paper contains a fundamental aspect but at the same time and applicative character of its results. An important aspect of the fundamental part of the paper is that we propose the development of the vibrational model of microorganism inactivation for a deeper understanding of the non-thermal selective action mechanisms on microorganisms taking into account both the duration, frequency and intensity of radiation pulses. So the development of metamaterial contact techniques with organic tissue opens up new possibilities for

the prevention, monitoring in different environments. They will provide a selective interaction with the pathogen biomolecules having a negligible destructive action on human tissue component. The quantum correlations that can be obtained in the processes of Raman scattering in two-photon generation were presented. The photons statistic is proposed for the diagnosis of the new collective processes in biological systems. The set of functions was presented, which describes the probability of the simultaneous existence of $(2j + 1)$ Dicke states in the scattering process.

References

1. Bloembergen N, Shen YR (1963) Quantum-theoretical comparison of nonlinear susceptibilities in parametric media, lasers and Raman lasers. Phys Rev A 133:37
2. Begley RF, Harvey AB, Byer RL (1974) Coherent anti-stokes Raman spectroscopy. Appl Phys Lett 25:387
3. Qiang T, Chang C (2012) Diagnostic applications of Raman spectroscopy. Nanomedicine 8:545
4. Mannige RV, Brooks CL (2010) Periodic table of virus capsids: implications for natural selection and design. PLoS One 5(3):e9423
5. Almar FP, Jun A, Hiroyuki Y, Kosuke D, Mikiko S, Satoshi K, Katsumasa F (2013) Raman and SERS microscopy for molecular imaging of live cells. Nat Protoc 8(4):677
6. Katherine JI, Ember MA, Hoeve SL, McAughtrie MS, Bergholt BJ, Dwyer MM, Stevens KF, Stuart JF, Colin JC (2017) Raman spectroscopy and regenerative medicine: a review. NPJ Regen Med 2:12, 13
7. Turcan M, Enaki NA (2015) Cooperative generation of entanglement states by Raman conversion of photons in nano-fibers. Rom Rep Phys 67(4):1334
8. Yonzon CR, Haynes CL, Zhang X, Walsh JT, Van D (2004) A glucose biosensor based on surface-enhanced Raman scattering: improved partition layer, temporal stability, reversibility, and resistance to serum protein interference. Anal Chem 76:78
9. Potcoava MC, Futia GL, Aughenbaugh J, Schlaepfer IR, Gibson EA (2014) Raman and coherent anti-stokes Raman scattering microscopy studies of changes in lipid content and composition in hormone-treated breast and prostate cancer cells. J Biomed Opt 19(11):111605
10. Yuen SY, Lax B, Wolff PA (1976) Two-photon coherent states of the radiation field. Phys Rev A 13(6):2226
11. Weidinger M, Varcoe BTH, Heerlein R, Walther H (1999) Trapping states in the micromaser. Phys Rev Lett 82:3795
12. Brune M, Raimond JM, Haroche S (1987) Theory of the Rydberg-atom two-photon 'micromaser'. Phys Rev A 35:154
13. Turcan M, Enaki NA (2012) Cooperative scattering effect between stokes and anti-stokes field stimulated by a stream of atoms. Opt Commun 285(5):686
14. Enaki NA, Turcan M (2013) Cooperative quantum correlations between stokes and anti-stokes modes in four-wave mixing. Phys Scr T153:014021
15. Dicke RH (1954) Coherence in spontaneous radiation processes. Phys Rev 93:99
16. Hanbury BR, Twiss RQ (1956) The question of correlation between photons in coherent light rays. Nature 178:1046
17. Simon C et al (2010) Quantum memories a review based on the European integrated project "Qubit Applications (QAP)". Eur Phys J D 58:1–22

18. Inouye S, Chikkatur AP, Stamper-Kurn DM, Stenger J, Pritchard DE, Ketterle W (1999) Superradiant Rayleigh scattering from a Bose-Einstein condensate. Science 285:571–574

19. Enaki N, Bazgan S, Ciobanu N, Turcan M, Paslari T, Ristoscu C, Vaseashta A, Mihailescu IN (2017) Improvement in ultraviolet based decontamination rate using metamaterials. J Appl Surf Sci 417:40

20. Enaki N, Profir A, Bizgan S, Paslari T, Ristoscu C, Mihailescu CN, Badiceanu M, Mihailescu IN (2018) Chapter 13: Metamaterials for antimicrobial biofilm applications: photonic crystals of microspheres and optical fibers for decontamination of liquids and gases. In: Tiwari A (ed) Handbook of antimicrobial coatings. Elsevier, pp 257–282. ISBN: 978-0-12-811982-2

21. Oriaku CI, Pereira MF (2017) Analytical solutions for semiconductor luminescence including Coulomb correlations with applications to dilute bismides. J Opt Soc Am B 34:321

22. Pereira MF (2018) Analytical expressions for numerical characterization of semiconductors per comparison with luminescence. Materials 11:2

23. Pereira MF (2016) The linewidth enhancement factor of intersubband lasers: from a two-level limit to gain with-out in-version conditions. Appl Phys Lett 109:222102

24. Pereira MF, Zubelli PJ, Winge D, E J, Wacker A, Rondrigues SA, Anfertvev V, Vaks V (2017) Theory and measurements of harmonic generation in semiconductor superlattices with applications in the 100 GHz to 1 THz range. Phys Rev B 96:045306

25. Pereira MF, Anfertev V, Zubelli JP, Vaks V (2017) Terahertz generation by gigahertz multiplication in superlattices. J. Nanophotonics 11(4):046022

26. Apostolakis A, Pereira MF (2019) Controlling the harmonic conversion efficiency in semiconductor superlattices by interface roughness design. AIP Adv 9:015022

27. Apostolakis A, Pereira MF (2019) Numerical studies of superlattice multipliers performance. Quantum Sens Nano Electron Photonics XVI:109262

28. Apostolakis A, Pereira MF (2019) Potential and limits of superlattice multipliers coupled to different input power sources. J Nanophotonics 13:036017

29. Winge DO, Franckié M, Verdozzi C, Wacker A (2016) Simple electron-electron scattering in non-equilibrium Green's function simulations. J Phys Conf Ser 696:012013

30. Pereira MF, Shulika O (2014) Terahertz and mid infrared radiation: detection of explosives and CBRN (using terahertz), NATO science for peace and security series-B: physics and biophysics. Springer, Dordrecht

31. Pereira MF, Shulika O (2011) Terahertz and mid infrared radiation: generation, detection and applications, NATO science for peace and security series-B: physics and biophysics. Springer, Dordrecht

32. Apostolakis A, Pereira MF (2020) Superlattice nonlinearities for gigahertz-terahertz generation in harmonic multipliers. Nano 9(12):3941–3952. https://doi.org/10.1515/nanoph-2020-0155

33. Pereira MF, Anfertev V, Shevchenko Y, Vaks V (2020) Giant controllable gigahertz to terahertz nonlinearities in superlattices. Sci Rep 10:15950

Chapter 18
THz Spectroscopy of Advanced Materials

Can Koral, Gianpaolo Papari, and Antonello Andreone

Abstract Materials research is an essential component of modern terahertz systems: novel, broadband, low loss and tunable devices all heavily rely on new materials, ranging from graphene to transition metal dichalcogenides and doped semiconductors. At the same time, terahertz spectroscopy provide a powerful tool for the characterisation of a broad range of materials, including composite polymers and biomolecules. In this review, we will present our recent progress on the use of time domain spectroscopy to extract microscopic information in an otherwise inaccessible portion of the electromagnetic spectrum.

18.1 Introduction

Due to its unique properties, the THz spectral regime is still out of reach of optical laser wavelengths, while at the same time standard high frequency electronics starts to fail. There is therefore an ever-expanding need for devices and systems operating at the THz frequencies that are efficient, tunable and broadband. Development of new and advanced materials can drive the rapid evolution of critical technologies like revolutionized information and telecommunication systems, highly efficient photovoltaic technologies and high colour contrast light emitting devices, among others. It is not farfetched that this demand would continually rise in the foreseeable future.

When used as a probe, the THz radiation can provide simultaneous and straightforward measure of the materials most fundamental properties, i.e. charge population

C. Koral
National Institute for Nuclear Physics, Naples Unit, Naples, Italy
e-mail: can.koral@na.infn.it

G. Papari · A. Andreone (✉)
Department of Physics, University of Naples "Federico II", Naples, Italy
e-mail: gianpaolo.papari@unina.it; andreone@unina.it

dynamics, mobility, and the interplay between the two, which are not accessible to other optical or electrical techniques.

In this chapter, we will review our recent progress on the understanding of the electrodynamic parameters of some selected materials, potentially of interest for a number of different applications in the THz range, ranging from opto-electronics and bio-electronics to sensing.

18.1.1 ZnO Nanopowders

The large bandgap (3.3 eV) [1], visible light transparency, availability and multiple techniques for thin film deposition (chemical vapour deposition, sputtering, molecular beam epitaxy, etc.) make zinc oxide (ZnO) a versatile semiconductor extensively used in different technological applications [2, 3 and references therein]. Solar cells [4–10], piezoelectric actuators [11, 12] and thin film transistors are just a few examples of technological returns of ZnO. Different kind of doping have been applied to ZnO, aiming at improving conducting properties but preserving its transparency [8, 9, 13, 14]. Successful results have been reported in the attempt to dope ZnO with fluorine (F), since an additional electron with respect to oxygen is naively considered a "shallow donor" [2, 8, 9, 15]. Nevertheless, the mechanism through which F atoms can provide free carriers is still controversial [2, 16, 17]. Indeed, some authors predict an increase of extra delocalized electrons as well as overall carrier mobility due to F-doping [18, 19]. On the other hand, a decrease of conductivity of F-doped ZnO is expected by other studies [12].

Indeed, fluorine atoms are supposed to occupy oxygen vacancies that are the most favourable defects in ZnO_2. However, F atoms are theoretically expected to widen the distance between neighbouring Zn atoms, producing a deep localized state [2]. Density functional theory has been employed to account for the effect of fluorine doping on ZnO:F transport properties [16]. F atoms can work as either donor or acceptor according to the case they get full of oxygen vacancies or remain interstitials. The resulting activation energies have been estimated to be too high (~0.7 eV) for effectively providing any kind of carrier at room temperature, and the increase of free charge density could be ascribed to the effect of surface passivation operated by fluorine.

18.1.2 Graphene-Like Layers in Eumelanin

Graphene represents the first achievement of a fully two-dimensional material. A single sheet of carbon atoms is technologically versatile for its high ease of integrability [20–23] and fruitful electrodynamic properties in THz region, where it has been considered for the development of sensors [24, 25], filters [26], spatial light modulators [27–29], mantle cloaks [30]. Hybridized with organic based electronics

[31, 32], it has been extensively used for the production of novel biocompatible devices [33–36]. Within this frame the possibility to reproducibly fabricate graphene based nanowires and interfaces becomes quite relevant although only few attempts have been provided so far [37].

Recently, a reliable way for the realization of graphene micro-circuitry turned out to be the exploitation of graphene-like (GL) layers [38]. A GL layer is a platelet composed of a few layers of graphene having width of few nanometers. As a consequence of the manufacturing process, GL samples are born as water suspension, inherently predisposed to be molded in many shapes, and suitable for wiring organic electronics structures by spraying and/or ink-jet printing techniques either on rigid or flexible supports. An entire set of optical devices, including metamaterials, filters, absorbers, modulators, cloaks etc. can be newly proposed through the employment of the moldable GL compound. Analogously to some use of carbon nanotubes [39], a GL layer allows further interesting applications, to create new and cost-effective materials with tailored electrodynamic properties, for instance trough the mixture with specific insulating components.

Within the scenario of bio-electronics, eumelanin, a proved biocompatible material [40], can be exploited as an insulating sheath and host for GL layers in bioorganic environments.

18.1.3 Transition Metal Dichalcogenides

Transition metal dichalcogenides (TMDs) are characterized by a layered structure, responsible for their peculiar intrinsic 2-D electronic properties. Each crystal plane is based on the chemical configuration MX_2, where M is a metal and X is a chalcogen [41, 42]. Adjacent layers are held together by van der Waals forces, which inhibits free charge mobility across MX_2 planes. TMDs in thin-film form offer a large variety of compounds with adjustable band gaps [43, 44] and present a good transparency in the THz band that might pave the way to the development of a promising class of novel devices for THz optoelectronics [44]. Different from other tunable band gap systems like graphene, TMDs can also exploit an additional external parameter to control their own electro-optic properties as the magnetic field because of the spin-dependent band gap [45]. Furthermore, it has been shown [41, 46, 47] that the energy band structure of TMDs presents an interesting and unique dependence on the layer number, and a band gap transition from indirect to direct one for monolayer samples. Consequently, there is a consistent and growing demand in thin-film characterization, for the possible development of novel fast electronic [48, 49] and/or electro-optical systems [50, 51].

18.2 Sample Preparation and Structural Characterization

18.2.1 ZnO Nanopowders

Bare and F-doped ZnO powders were prepared by the hydrothermal route. Typically, a solution containing a 1:1 molar ratio of triethylamine (TEA) and zinc acetate di-hydrate (ZAD) was prepared, mixing TEA (0.84 mL) and ZAD (1.32 g) into ethanol (36.0 mL) under constant stirring. After complete dissolution of ZAD, water (4.0 mL) was added drop-wise, producing a whitish suspension. Afterwards, different amounts of ammonium hydrogen fluoride (NH_4FHF) were used to realize the following atomic F concentrations: 1 at%, 3 at%, and 5 at%. The obtained suspensions were sealed within a Teflon recipient (the liquid volume corresponding to 75% of the whole), placed into a circulating oven and kept at 120 °C overnight. After cooling down to room temperature, powders were recuperated by centrifugation and repeatedly washed (three times with distilled water). Prepared samples will be named thereafter F1, F3, F5, respectively. F0 indicates the undoped sample.

For the THz measurements, pellets of ZnO:F/KBr in the ratio 1:10 were opportunely realised. Samples roughly 330 μm thick were obtained by pressing a mixture of 90% of KBr powder with the 10% of ZnO:F. KBr was chosen because sufficiently transparent up to about 2.5 THz, behaving therefore as an optimal host for THz spectroscopy. This procedure gives the advantage to precisely control within a few microns the thickness of each sample that is a crucial parameter for THz spectroscopy.

18.2.2 GL and EUGL Pellets

GL layers were obtained applying a two-step oxidation/chemical reduction strategy described in a previous work [38]. A brief description of the applied method is as follows: 500 mg of Carbon Black (CB) powder was oxidized with nitric acid (67%, 10 mL) at 100 °C under stirring and reflux for 90 h. The oxidized carbonaceous material, labeled as GL-ox, was recovered by centrifugation and washed with distilled water until acid traces were successfully removed. After the oxidation step, 60 mg of GL-ox was dispersed in distilled water (60 mL) and treated with hydrazine hydrate (1.35 mL) of at 100 °C under reflux. After 24 h the suspension was cooled at room temperature and the excess of hydrazine was neutralized with an diluted nitric acid (4 M) allowing the precipitation of a black solid: the GL layers. GL layers were recovered by centrifugation (3000 rpm, 30 min), washed with distilled water and recovered again by centrifugation. This last purification step was repeated twice. The material was in part stored as aqueous suspension (mass concentration 1 mg mL-1, pH 3.5) and in part dried at 100 °C and stored. Analytical grade chemicals were purchased from Sigma Aldrich and used without any further

purification. CB (N110 type, furnace black, 15–20 nm primary particles diameter, specific BET area 139 m^2 g^{-1}) was purchased from Sid Richardson Carbon Co.

Eumelanin was synthetized under biomimetic conditions through 5,6-dihydroxindole (DHI) and 2-carboxy-5,6-dihydroxindole (DHICA) oxidative co-polymerization [52]. DHI and DHICA were prepared according to a procedure previously described [53]. A mixture (3:1 in weight) of DHI/DHICA was dissolved in methanol (20 mg/mL) by ultrasonic agitation and the resulting suspension was kept for 10 min under magnetic stirring. The pH was adjusted to 8 with ammonia solution (28% in water) allowing indoles to auto-oxidize and polymerize. After 1 h, the reaction was quenched by adding acetic acid solution (1 M) until pH 4 is established. The material was then dried at 100 °C and stored as EU.

The hybrid material EUGL was prepared according to the procedure previously described [40]. Briefly, a proper amount of GL layers in aqueous suspension (1 mg mL^{-1}) was added to the mixture of eumelanin precursors (DHI/DHICA) dissolved in methanol before the addition of ammonia solution to induce the EU precursors oxidation and polymerization. The work-up of the reaction was the same as described for the preparation of pure eumelanin. The suspension was dried in an oven at 100 °C and stored. After drying the EUGL hybrid resulted insoluble in water.

Solid dispersions were prepared by mixing and grinding the samples with KBr (host) in different mass ratios (see [54] for details). The solid dispersions were compressed at 10 tons for 10 min into thin disks (13 mm in diameter) having thickness values ranging between 0.038 and 0.045 cm.

18.2.2.1   WSe$_2$ and MoSe$_2$ Films

TMD films have been deposited using a process known as thermally assisted conversion (TAC). TAC has the capability of depositing a continuous large-scale film with multiple layers [55]. The appropriate transition metal (Mo, W) films were deposited using a sputter coater (PECS, Gatan) at <2 Å/s to form a smooth conformal coating 10 nm thick on a c-axis SiO$_2$ substrate. In order to convert the metal films with their respective diselenides, they were exposed to selenium vapor at an elevated temperature in a home-built hot-wall chemical vapor deposition reactor with a process that has been described in more detail previously [43]. Specifically, metal films were converted to selenide in the reactor with chamber temperature at 600 °C under a flow of about 150 sscm of argon with the Se powder source held upstream at 219 °C for 2 h. Previous characterization indicated that the final thickness of selenide (MoSe$_2$, WSe$_2$) was 20 nm, which was double the initial metal thickness. To protect the films from oxidants in the atmosphere, they were encapsulated with 5 nm of Al$_2$O$_3$ using atomic layer deposition carried out over 46 cycles at 80 °C and a pressure of 2.2 Torr.

Using a shadow mask, samples were deposited on one half of SiO$_2$ c-axis substrates having a total area of 2 cm × 1 cm. The second half was intentionally left bare, so that one could retrieve the thin-film parameters employing the exact film thickness and refractive index $\widetilde{n}_s$ of the specific substrate on which each sample was

deposited. As it will be shown in detail in the next paragraphs, this was the only effective procedure to minimize the error introduced by the unavoidably slight difference in substrate parameters [56].

18.3   Experimental

THz spectroscopy measurements were carried out using a Time-Domain system based on a fs fiber system (Menlo Systems™). Generation and detection of THz signal is accomplished through the use of two photoconductive antennas based on GaBiAs semiconductor technology and excited by a laser pulse having 1560 nm wavelength and a repetition rate of 80 MHz. THz signal is collimated and then focalized on the sample using TPX (Polymethylpentene) lenses. The size of the Gaussian profile of the focused THz pulse, estimated with the standard knife-edge technique, is of the order of 2 mm. Temporal sampling rate is fixed at about 0.1 ps, whereas the whole acquisition interval ranges between 100 and 200 ps, giving a frequency resolution of about 5 GHz in the optimised conditions. The free space signal has a bandwidth extension up to about 4 THz, roughly halved in case of samples showing a high level of absorption. Samples are placed on an aluminum plate provided with circular holes 8 mm in diameter, as sketched in Fig. 18.1.

The holder is mounted on a two-dimensional motor stage, which enables to acquire measurements through free space, reference, and samples during the same run, with an enhanced accuracy on phase and amplitude for each single acquisition. In order to reduce or eliminate the effect of H_2O absorption in the frequency spectra, all measurements are performed in a purging box filled with N_2 and a humidity level lower than 0.1%.

18.4   Theoretical Background

Electrodynamic properties of powders, pellets and films have been studied by applying a standard approach based on the computation of the complex Transfer Function (TF) $\widetilde{T}(\omega)$ ($\omega = 2\pi f$), experimentally obtained through the ratio between the signal transmitted through the pellet $\widetilde{E}_s(\omega)$ and the signal collected in free space $\widetilde{E}_r(\omega)$.

In the case of bulk (optically thick) samples, the modulus of transmission can be expressed as

$$T(\omega) = \frac{E_S(\omega)}{E_R(\omega)} = \widetilde{t}_{as}\widetilde{t}_{sa}\ exp\left[-i(\widetilde{n}_s - \widetilde{n}_{air})\frac{\omega d}{c}\right] \cdot FP(\omega) \tag{18.1a}$$
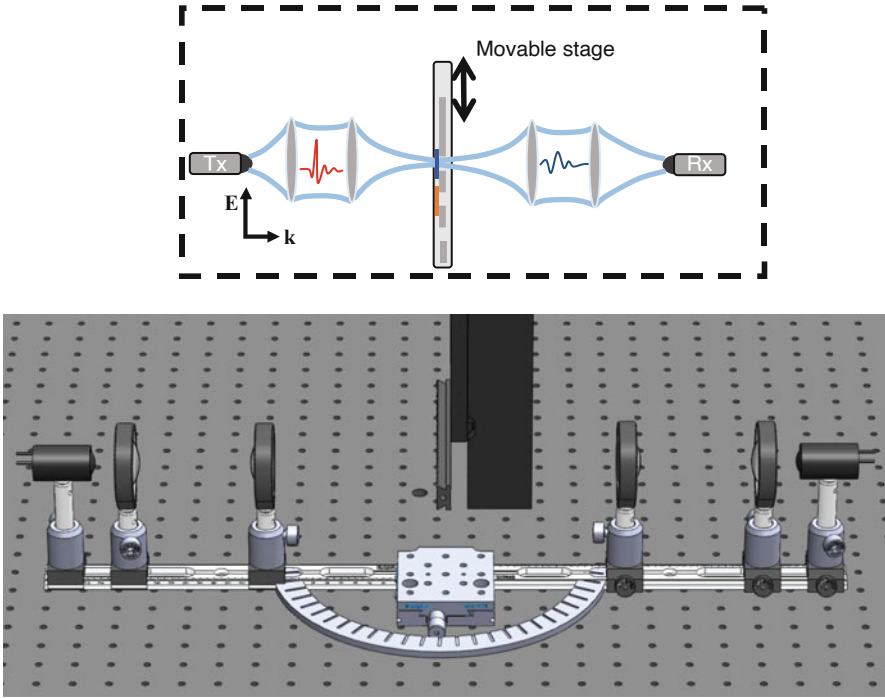
where

Fig. 18.1 Upper part: a sketch of the measurement scheme. Lower part: a pictorial representation of the optical setup. The THz radiation is collimated and then focalized, the holder can be moved so that the reference and different samples can be measured in the same experimental run

$$FP(\omega) = \cfrac{1}{1 - \left(\cfrac{\widetilde{n} - \widetilde{n}_{air}}{\widetilde{n}_s + \widetilde{n}_{air}}\right)^2 \exp\left(-i2\widetilde{n}_s \frac{\omega d}{c}\right)} \tag{18.1b}$$

$\widetilde{t}_{as}$ and $\widetilde{t}_{sa}$ are the Fresnel coefficients at the boundaries air-sample and sample-air respectively, $\widetilde{n}_s$ is the complex refractive index of the sample, $\widetilde{n}_{air}$ the refractive index of air, d the sample thickness and c is the speed of light. The factor FP accounts for the oscillations due to the Fabry-Perot effect. A commercial software (Teralyzer™) has been used to achieve $\widetilde{n}_s = n_s + ik_s$ for each single sample. This routine is based on *the total variation technique* [57–60] that defines the refractive index n_s, the extinction coefficient k_s, and the effective optical thickness d_{eff}, related to the minimum amplitude of FP oscillations. The effective optimal thickness is achieved with a precision of 2 μm.

The complex dielectric function $\widetilde{\varepsilon}_s/\varepsilon_0 = \varepsilon_r + i\varepsilon_i$ is easily obtained through the relations $\varepsilon_r = n_s^2 - k_s^2$ and $\varepsilon_i = 2n_s k_s$ [61], with ε_0 as vacuum permittivity.

In order to extract the intrinsic value of the dielectric function of samples under test, we employed the mean field theory (Landau–Lifshitz–Looyenga model [62]). Briefly, we used the following formula

$$\widetilde{\varepsilon}_g\left(\eta_g\right) = \left(\widetilde{\varepsilon}_s^{1/3} - \left(1 - \eta_g\right) \cdot \widetilde{\varepsilon}_h^{1/3}\right)^3 / \eta_g \qquad (18.2)$$

relating the guest substance permittivity $\widetilde{\varepsilon}_g$ to the permittivity of both the host substance $\widetilde{\varepsilon}_h$ (KBr) and sample (mixture) substance $\widetilde{\varepsilon}_s$. The coefficients $\eta_{g,\,h}$ represent the concentrations in volume of guest and host substance and are related to the experimental concentrations in weight α_g, through the equation:

$$\eta_g = \left(1 + \frac{\rho_g}{\rho_h}\frac{1 - \alpha_g}{\alpha_g}\right)^{-1} \qquad (18.3)$$

with ρ_g and ρ_h mass density of the guest and host substance respectively.

For thin films deposited on a substrate having a refractive index $\widetilde{n}_{substr}$, it can be easily shown [68] that also this parameter has to be used in Eq. (18.1b), so that

$$FP(\omega) = \frac{1}{1 - \left(\frac{\widetilde{n} - \widetilde{n}_{air}}{\widetilde{n}_s + \widetilde{n}_{air}}\right)\left(\frac{\widetilde{n}_s - \widetilde{n}_{substr}}{\widetilde{n}_s + \widetilde{n}_{substr}}\right)\exp\left(-i2\widetilde{n}_s\frac{\omega d}{c}\right)}$$

Permittivity and conductivity parameters in the following have been fitted using a conventional Drude-Smith model [63]. Complex permittivity can be written as

$$\widetilde{\varepsilon}(\omega) = \varepsilon_\infty - \left\{\frac{\omega_p^2}{\omega^2 + i\omega\omega_\tau}\left(1 + c_1\frac{\omega_\tau}{\omega_\tau - i\omega}\right)\right\} \qquad (18.4)$$

where ε_∞ is the asymptotic value of ε_r, $\omega_p^2 = ne^2/\varepsilon_0 m^*$ is the plasma frequency, n and m^* are the carrier density and effective mass respectively, and $\omega_\tau = 1/\tau$ is the relaxation frequency. The coefficient c_1 ranges between -1 and 0 and accounts for the portion of localized/backscattered electrons. THz conductivity can be simply obtained through the expression

$$\widetilde{\sigma}(\omega) = -i[\widetilde{\varepsilon}(\omega) - \varepsilon_\infty]\varepsilon_0\omega \qquad (18.5)$$

and from here the dc conductivity σ_{dc}, using

$$\sigma_{dc} = (1 + c_1)\omega_p^2\varepsilon_0/\omega_\tau \qquad (18.6)$$

18.5   THz Spectroscopy

18.5.1   ZnO

An expanded view on the measured time dependent THz signals is shown in Fig. 18.2, left panel, where the reference (free space), ZnO:F1/KBr, ZnO:F3/KBr and ZnO:F5/KBr sample curves are reported as solid lines with different colors. The average delay between the reference and the ZnO:F/KBr samples is mostly due to the contribution of the KBr which occupies the 90 wt.% of each pellet mixture. Instead, the effect of losses is more pronounced by comparing the transmission moduli $\left|\widetilde{T}(\omega)\right|$ as reported in Fig. 18.2, right panel. The average transmission amplitude undergoes a robust enhancement of about 50% passing from ZnO:F0 (not shown) to ZnO:F1. Increasing the doping level, $\left|\widetilde{T}(\omega)\right|$ in doped samples decreases, remaining anyway more transparent than pure ZnO. All samples display significant Fabry-Perot oscillations, whose periodicity [64] $\Delta f = \frac{c}{2n_p d} \approx 0.2\ THz$ yields a refractive index for a pellet $n_p \approx 2.3$, in agreement with the value achievable by temporal delay of THz signals $n_p = c\frac{\delta t}{d} + 1$ for $d \cong 330\ \mu m$ and $\delta t \cong 1.4\ ps$.

Following the theoretical approach described in the previous section, we have extracted the intrinsic $\widetilde{\varepsilon}$ for all samples. The real part of permittivity tends to increase passing from $\varepsilon_r \cong 10$ for ZnO:F0 (not shown) to $\varepsilon_r \cong 14$ for ZnO:F5 at 1 THz. Instead, ε_i describes more complicate dynamics as the doping increases. At 1 THz, the bare sample has $\varepsilon_i \cong 18$ whereas for ZnO:F1 the value drops at $\varepsilon_i \cong 10.5$, losing about 42% of its value. As the doping is further increased ε_i gets closer to the value of bare ZnO, although ZnO:F5 still has $\varepsilon_i \cong 15$. The sample conductivity can be easily gained through $\sigma(\omega) = \varepsilon_0 \omega \varepsilon_i(\omega)$, whose dependence on fluorine doping clearly follows the same dynamics as in ε_i. In Fig. 18.3, left and right panel respectively, the real part of the dielectric function ε_r and the THz conductivity σ are reported as a function of frequency in the left and right panel respectively.
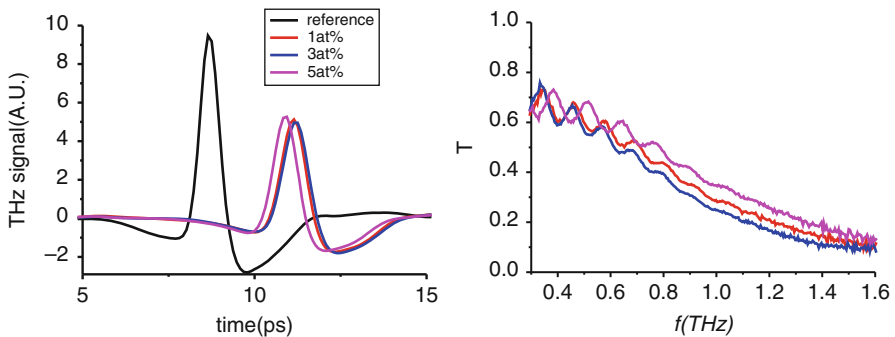

Fig. 18.2 Left: Electric field signals versus time transmitted in free space (black curve) and through the ZnO:F/KBr samples under test. Right: Corresponding transmission versus frequency. Samples having 1 at%, 3 at% and 5 at% fluorine are represented by the red, blue and magenta solid lines respectively
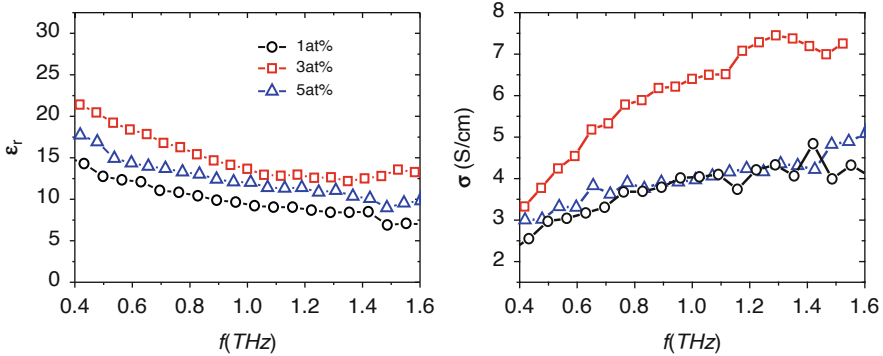
Fig. 18.3 Left: relative permittivity (ε_r) vs f. Right: conductivity (σ) vs f. Experimental data for the ZnO:F samples are plotted via circles, squares, and triangles corresponding to fluorine percentage of 1 at.%, 3 at.% and 5 at.% respectively

Table 18.1 Parameters used for the best fit of the ZnO:F powders complex permittivity according to the Drude-Smith model. The uncertainty of tabled parameters is of the order of 2% (taken from [66])

Sample	ω_p (THz)	ω_τ (THz)	C_1	σ_{dc} (S/cm)	ε_∞
F0	49	10	−0.70	6.4	10
F1	49	13	−0.85	2.4	9.5
F3	50	13	−0.83	2.9	11
F5	50	11	−0.8	4.0	12

Taking as a reference the extracted direct conductivity, we can quantify the decrease of ZnO:F transport properties, noting that at 1 THz we find: $\sigma_{dc}(ZnO:F1) \times 2.7 \cong \sigma_{dc}(ZnO:F0)$ and $\sigma_{dc}(ZnO:F5) \times 1.6 \cong \sigma_{dc}$.

THz and *dc* conductivity of the bare sample are in agreement with similar measurements performed on zinc oxide thin films [13, 65]. Instead, THz conductivity of ZnO:F1 undergoes a relevant decrease passing from about 10 S/cm, in the absence of doping, to about 6 S/cm. In order to find more quantitative information on the intrinsic conductivity we have fitted for all samples $\widetilde{\varepsilon}$ with the Drude-Smith model (Eq. 18.4). The extracted parameters, which are affected by an uncertainty of about 2%, are summarized in Table 18.1.

According to the Drude-Smith model, specifically developed to account for the rate of backscattering processes in granular systems, the conductivity decreases because of the simultaneous increase of $|c_1|$ and relaxation time ω_τ (Eq. 18.6). Indeed, both parameters increase by more than 20% in ZnO:F1 and ZnO:F3. In ZnO:F5, instead, this increase is of the order of 10% only, in spite of a relevant decrease of its conductivity in comparison with the bare sample. The lowering of conductivity can be better accounted for by looking at the change in morphology of ZnO:F powders, as shown by SEM analysis. The growth of $|c_1|$ is coherent with a system in which the number of grain boundaries involved into the relaxation process

increases. Since the relative variation of relaxation time $\omega_\tau = 1/\tau$ follows the variation in $|c_1|$, we can infer that the Mattheissen's rule [67] $1/\tau = 1/\tau_i + 1/\tau_{gb}$ holds. Here τ_i accounts for the relaxation process inside a single grain and τ_{gb} relates to the average scattering time at grain boundaries. As fluorine doping is increased, the change in morphology suggests that τ_{gb} decreases, so that ω_τ basically follows the change in ω_{gb}.

The consequences of an effective doping mechanism would reflect into a strong enhancement of ω_p because of the growth of carrier density. Instead, we observe a slight upshift of about 2%, hardly explainable in terms of an effective doping mechanism. On the other hand, the real part of permittivity tends to grow as a function of doping, and the reference value ε_∞ in ZnO:F5, is about 20% larger than the bare value. This is the signature of some localized (polarizable) charge provided by the doping process. The enhancement of ε_∞ is reasonably ascribable to the enhancement of luminescence centers observed in PL measurements too.

We can therefore summarize the most significant information extracted using THz spectroscopy from ZnO:F samples, as a function of the doping increase:

σ_{dc} first decreases and then increases again, however never restoring the value of the bare sample;
both $|c_1|$ and ω_τ reasonably increase for the rise of scattering rate at grain boundaries;
ω_p remains basically constant, and ε_∞ tends to increase.

It is remarkable to note that the above Drude-Smith parameters keep their significance and trends within the highest uncertainty inherited from $\widetilde{\varepsilon}$.

We infer therefore that the fluorine doping slightly affects the polarization charge of ZnO:F powders but does not enhance the carrier density. ZnO:F samples instead show a granular morphology at nanoscale, compatible with the growth of the grain boundary scattering rate and the decrease of σ_{dc}. The increase of the fraction of smaller particles with the amount of doping precursor can explain this effect.

18.5.2 GL and EUGL

Again, the time dependent evolution of the electric field transmitted through different samples is recorded and compared with the reference (air) signal. From here, meaningful information on the electrodynamic parameters of the samples under text can be derived from the frequency transmission $T(\omega)$ in the range 0.1–2 THz. Results for GL/KBr mixtures are reported in Fig. 18.4 for various volume concentrations. Increasing the content of GL in KBr, THz losses increase accordingly, so that the amplitude scales down and is frequency limited by the lower Signal-to-Noise Ratio (SNR). Therefore, in pure KBr $T(\omega)$ extends to 2 THz, whereas for maximum GL layers concentration (approximately 10%) a significant signal is observed up to 1 THz only.
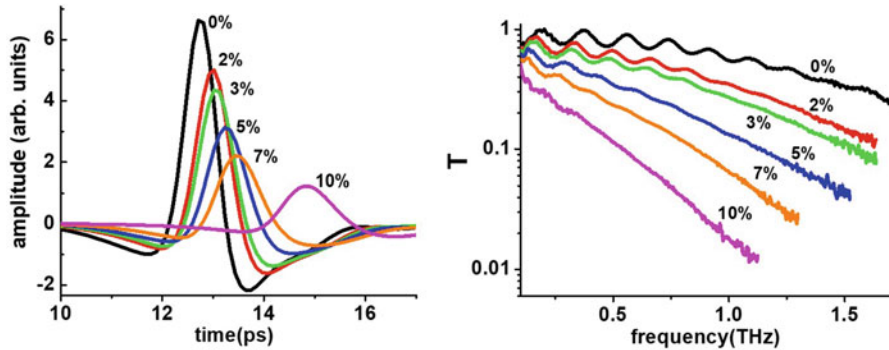
Fig. 18.4 Left: Time dependent evolution of the transmitted THz signal as a function of different GL concentration. Black: 0% (pure KBr); red: 2%; green: 3%; blue: 5%; orange: 7%; magenta: 10%. Percentages refer to the concentration of GL in the KBr matrix. Right: T as a function of frequency for the same samples

We first use THz spectroscopy to capture changes in the electrodynamic parameters obtained through chemical transformations of compounds GL and EUGL layers are based on.

Then, the technique is applied to highlight the differences in the electrodynamic behavior of simple mixtures of eumelanin and graphene-like layers (EU + GL) and the hybrid obtained through their polymerization (EUGL) (for details, refer to [54]).

Polymerization induces EU to incorporate GL layers into nanodrops having an average diameter of few tenths of nanometers [38]. This has incisively affected the percolation path when compared to the case of a simple mixture between EU and GL layers. If the polymerization helps also the onset of new chemical bonds that may degrade GL conductivity, it remains an issue that has not been addressed yet.

Using the retrieval procedure, we can finally extract the complex permittivity and the effective thickness of pure KBr and mixed samples of GL and EUGL layers. Once $\widetilde{\varepsilon}_h$, the complex permittivity of the host substance (KBr), and $\widetilde{\varepsilon}_s (\alpha_g)$ have been retrieved, $\widetilde{\varepsilon}_g$ (α_g) is obtained employing Eqs. (18.2) and (18.3). At 1 THz we find $\varepsilon_r(KBr) \cong 5$ and $\sigma_r(KBr) \cong 0.4$ *S/cm*, in substantial agreement with results reported in [68].

A summary of the results on the real and imaginary parts of the dielectric function as a function of frequency and the conductivity for two representative GL and EUGL samples are reported in Fig. 18.5.

In the GL sample, both ε_r and ε_i strongly decrease in the frequency range 0.3–1.5 THz. In comparison, the hybrid EUGL displays similar frequency dependence for ε_r, with smaller values but at the highest frequencies. The behavior of ε_i instead is quite different, with nearly flat frequency dependence and absolute values reduced by a factor 5 or more.

Quantitative insights on the complex dielectric function $\widetilde{\varepsilon}$ of both GL and EUGL compounds can be retrieved using a simple Drude-Smith model through Eqs. (18.4) and (18.5). We found reasonable parameters by fitting *simultaneously* the families of
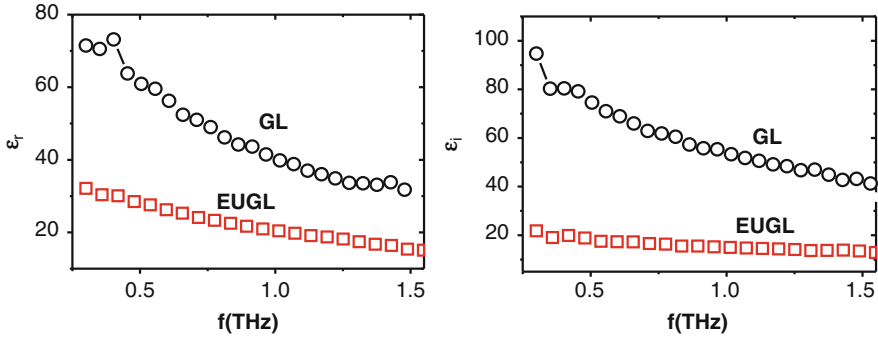
Fig. 18.5 In the panels the real (left) and imaginary (right) components of the permittivity as a function of frequency for two different samples (graphene-like, GL: black circles; hybrid graphene-like + eumelanin, EUGL: red squares) are shown

Table 18.2 List of parameters used for fitting ε_r and σ data through Drude-Smith model for the GL and EUGL mixtures. The last two columns account for the total uncertainty relative to $\tilde{\varepsilon}$ and σ_r obtained through data dispersion (taken from [54])

Sample	ω_p (THz)	ω_τ (THz)	C_1	σ_{dc} (S/cm)	ε_∞	$\delta\varepsilon$	$\delta\sigma$
GL	82.9	1.6	−0.75	15	32	15%	10%
EUGL	50.2	1.8	−0.85	2.9	18	13%	10%

curves $\varepsilon_r(\eta_g)$ and $\varepsilon_i(\eta_g)$ of both GL and EUGL samples. Drude-Smith model implies the knowledge of 4 parameters that are summarized in Table 18.2. Through Eq. (18.6) we get as direct conductivities $\sigma_{dc} =15$ S/cm and $\sigma_{dc} =2.9$ S/cm for GL and EUGL respectively. The total uncertainty relative to the complex permittivity ($\delta\varepsilon$) and conductivity ($\delta\sigma$) are worth 15%(13%) and 10%(10%) for GL (EUGL) samples. Specifically the permittivity uncertainty has been calculated by the spread of $\tilde{\varepsilon}$ as function of concentration η_g so that $\delta\varepsilon = \sqrt{\delta\varepsilon_r{}^2 + \delta\varepsilon_i{}^2}$, whereas $\delta\sigma$ just relies on the data spread detected into plotting $\sigma_r (\eta_g)$.

GL and EUGL appear sharply different in terms of σ_{dc} and ε_∞ because we find σ_{dc} (GL) $\cong 5\, \sigma_{dc}$ (EUGL), and $1.77\, \varepsilon_\infty$ (EUGL) $\cong \varepsilon_\infty$ (GL). Also ω_p values are well separated within $\delta\varepsilon$ interval whereas ω_τ values, describing the time scale of photoconduction, are comparable within the total uncertainty ($\delta\varepsilon$), because of the dependence of both on conductive properties of GL. Amplitudes of σ_{dc} are suppressed by the factor $1 + c_1$ which limits to less than 30% the fraction of carriers available for direct conduction. GL and EUGL display photoconductive properties similar to the amorphous carbon [69], that are a few times lower than the performances of carbon nanotubes compound [70] and a factor 1000 lower than performances of graphene based systems [71]. Charge densities of GL and EUGL are slightly lower than carbon nanotubes, indeed being $n = \omega_p^2 m^* \varepsilon_0/e^2$ we get n $(GL) \cong 2 \cdot 10^{18}/cm^3$ and $n(EUGL) \cong 2 \cdot 10^{17}/cm^3$ having employed $m^* = 0.87\, m_e$ the effective mass of charges in carbon amorphous samples [72].

18.5.3 TMD

In Fig. 18.6 the temporal evolution of the electric field signals transmitted across the WSe$_2$ (left panel) and MoSe$_2$ (right panel) samples is reported. Black curves represent the free space transmission, whereas red curves refer to signals passing through the bare substrate. Peak amplitude in the substrate was always around 20% lower than the free space case, and its delay of about $\delta t \approx 2$ ps described the proper change in refractive index (since the nominal thickness was 300 µm, this corresponds to $n_s \approx 2$ for the crystalline SiO$_2$). The presence of the WSe$_2$ and MoSe$_2$ thin-film induced a further reduction in the transmitted signal (blue curves) of about 30% and 10%, respectively, when compared to the bare substrate. In all cases, THz waves impinging and passing through each sample caused an etalon effect with the first reflected signal manifesting itself with a delay of almost 5 ps from the main peak.

Time dependent signals were then converted in the frequency domain using a fast Fourier transform (FFT) method to get the transmission function $\widetilde{T}(\omega) = \widetilde{E}_f(\omega)/\widetilde{E}_s(\omega)$, where the complex quantities $\widetilde{E}_f(\omega)$ and $\widetilde{E}_s(\omega)$ are the FFT curves of the sample and bare substrate, respectively.

Results are presented in Fig. 18.7 in terms of the real and imaginary part of the complex dielectric function.

The real part ε_r (left panel) displays substantially a flat dynamics, with MoSe$_2$ characterized by a very high dielectric constant (≈ 1000) and WSe$_2$ values being slightly negative. Imaginary parts ε_i of the two films are reported in the right panel, showing the expected free-charge decrease, although values for ε_i (WSe$_2$) were larger than for ε_i (MoSe$_2$) by a factor of 5 or more. The MoSe$_2$ film, therefore, showed a semiconducting behavior with the real part being strictly positive and a fast decay of ε_i versus frequency [67]. On the other hand, the WSe$_2$ sample clearly presented a weak metallic behavior in the THz region, showing a complete negative ε_r and large values for ε_i.

Fitting curves on the retrieved dielectric functions of WSe$_2$ and MoSe$_2$ films, obtained via the DS model, are reported as continuous black lines in the same
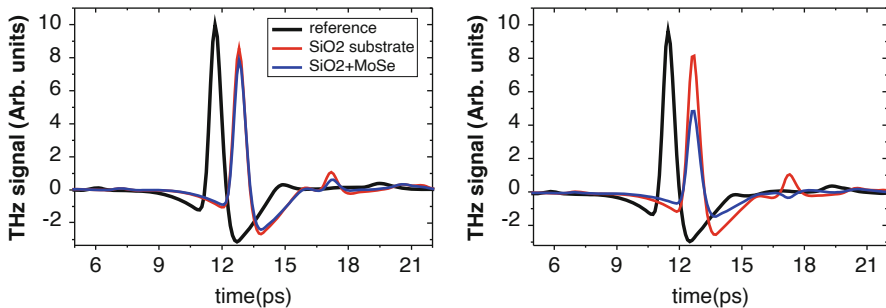

Fig. 18.6 Left: Black, red and blue solid lines represent the time dependent THz signals referred to free space, SiO$_2$ substrate and WSe$_2$ film + substrate respectively. Right: Similarly, with the blue curve showing the measurement on the MoSe$_2$ film + substrate
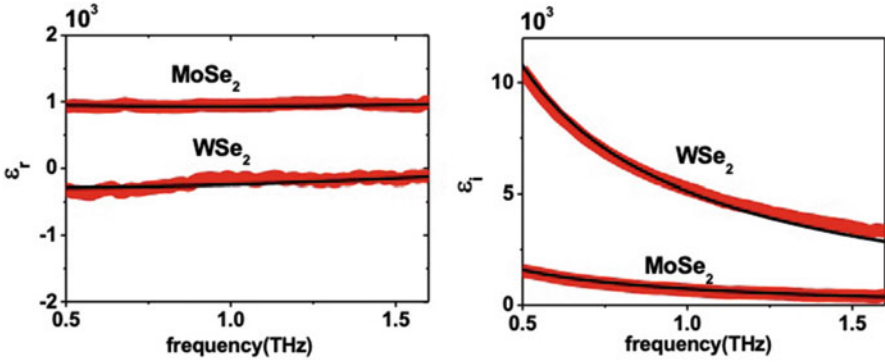
Fig. 18.7 Left and right graphs show the real (ε_r) and imaginary (ε_i) parts respectively of dielectric function of TMD's films as a function of frequency, extracted by using the Transfer Function model. Black lines corresponds to the Drude-Smith model fits whose parameters are reported in Table 18.3

Table 18.3 Best fit parameters for the dielectric functions of WSe_2 and $MoSe_2$ films using the Drude-Smith model. Parameter accuracy is of the order of 5% (taken from [75])

Sample	ω_p (THz)	ω_τ (THz)	C_1	σ_{dc} (S/cm)	ε_∞
WSe_2	850	16	−0.22	3000	1200
$MoSe_2$	270	9.5	−0.35	444	1220

figures. The used fitting parameters are reported in Table 18.3, with an uncertainty of about 5%. The higher conductivity of WSe_2 with respect to $MoSe_2$ mainly resulted in larger values of ω_p and smaller values of c_1, as expected.

Nevertheless, the frequency response of the dielectric function and the values retrieved for the d.c. conductivity using the DS model was in clear contrast to what is observed in single crystal samples [73]. The observed metallic behavior may be ascribed to the presence of conductive channels in grain boundaries. A high density of metallic grain boundaries can in fact spontaneously form in slightly Se-deficient Mo thin films grown by molecular-beam epitaxy [74]. We speculate that the same mechanism may apply to WSe_2 samples. This would also explain the larger values of conductivity in the latter case.

Before we proceed to concluding remarks, we would like to mention that there are other materials also being investigated for spectroscopy and devices in the THz range, notably based on superlattices and quantum-cascade structures [76–88].

18.6   Conclusions

Our results on fluorine doped ZnO powders prepared through hydrothermal synthesis show that F atoms do not work as donors but rather affect the morphology of ZnO crystals only, promoting the onset of a granular phase. Electron paramagnetic resonance (EPR) and photoluminescence (PL) measurements [66] proved the effective F doping of ZnO structures, showing that, increasing the doping level up to 5%, F atoms mainly occupy oxygen vacancies, inherently present in the bare ZnO. The increase of luminescence centers revealed via PL data well corresponds to the rise of asymptotic permittivity detected by THz spectroscopy. THz TDS measurements confirm that ZnO:F powders do not show an increment in free carrier charge. Indeed, the doping precursor exerts a relevant leaching on ZnO mesocrystals, leading to an increase of the fraction of smaller nanoparticles and, consequently, of scattering rate at grain boundaries, that ultimately affects conductivity. Our outcomes are in accordance with theoretical calculations asserting it is not possible to provide free carriers in ZnO through F doping at room temperature. Experimental verification of free charge enhancement in ZnO thin films can be reasonably related to a different role played by F atoms, which can work as passivation layer preserving the intrinsic conductivity of zinc oxide.

We have also performed a detailed THz investigation on the high frequency electrodynamics in graphene-like and eumelanin-graphene-like layers. Samples have been hosted in KBr powder with different concentrations. Intrinsic values of $\widetilde{\varepsilon}$ have been achieved through a Landau-Lifshitz approach. Above the percolation concentration, all data converge inside specific areas in $\widetilde{\varepsilon}$ vs frequency space, allowing to get with a reasonable precision information – using a simple Drude-Smith model - on the electrodynamic parameters of both hybrids in this frequency range. Measured values of conductivity are encouraging and open the possibility to employ GL and EUGL compounds for the development of bio-compatible circuitry and devices working up to the THz range.

Finally, we have retrieved the dielectric function of conducting $MoSe_2$ and WSe_2 TMDs. Thin films have been created via a thermally assisted conversion process, which produced samples with good homogeneity. We have extracted the electrodynamic parameters of thin films deposited on 300 μm thick substrates, which introduce a relatively strong FP effect in transmission data. By applying a rigorous protocol based on the TF model and a self-consistent moving average procedure, we have minimized the periodic FP oscillations and fitted $\widetilde{\varepsilon}$ with the Drude–Smith function. The relatively high conductivity observed in both compounds may be ascribed to a high density of line defects presenting a metallic character. The relatively high transparence along with the conducting features are encouraging in view of a possible use of TMD-based thin-films for applications as tunable metadevices in the THz region. The observed conducting nature can represent a promising alternative for the realization of new devices with higher currents and lower contact resistance.

References

1. Mang A, Reimann K, Rübenacke S (1995) Band gaps, crystal-field splitting, spin-orbit coupling, and exciton binding energies in ZnO under hydrostatic pressure. Solid State Commun 94:251
2. Janotti A, Van de Walle CG (2009) Fundamentals of zinc oxide as a semiconductor. Rep Prog Phys 72:126501
3. Ozgur U, Alivov YI, Liu C, Teke A, Reshchikov MA, Dogan S, Avrutin V, Cho SJ, Morkoc HA (2005) Comprehensive review of ZnO materials and devices. J Appl Phys 98:1
4. Azarang M, Shuhaimi A, Yousefi R, Sookhakian M (2014) Effects of graphene oxide concentration on optical properties of ZnO/RGO nanocomposites and their application to photocurrent generation. J Appl Phys 116:084307
5. Saáedi A, Yousefi R, Jamali-Sheini F, Zak AK, Cheraghizade M, Mahmoudian MR, Baghchesara MA, Dezaki AS (2016) XPS studies and photocurrent applications of alkali-metals-doped ZnO nanoparticles under visible illumination conditions. Physica E Low Dimens Syst Nanostruct 79:113
6. Dezfuly RF, Yousefi R, Jamali-Sheini F (2016) Photocurrent applications of $Zn_{(1-x)}Cd_xO/rGO$ Nanocomposites. Ceram. Int 42:7455
7. Kharatzadeh A, Jamali-Sheini F, Yousefi R (2016) Excellent Photocatalytic performance of $Zn_{(1-x)}Mg_xO/rGO$ Nanocomposites under natural sunlight irradiation and their photovoltaic and UV detector applications. Mater Des 107:47
8. Gordon RG (1997) Deposition of transparent conducting oxides for solar cells. AIP conference proceedings, pp 39–48
9. Liang H, Gordon RG (2007) Atmospheric pressure chemical vapor deposition of transparent conducting films of fluorine doped zinc oxide and their application to amorphous silicon solar cells. J Mater Sci 42:6388
10. Tari O, Aronne A, Addonizio ML, Daliento S, Fanelli E, Pernice P (2012) Sol–gel synthesis of ZnO transparent and conductive films: A critical approach. Sol Energy Mater Sol Cells 105:179
11. Li T, Li YT, Qin WW, Zhang PP, Chen XQ, Hu XF, Zhang W (2015) Piezoelectric size effects in a zinc oxide micropillar. Nanoscale Res Lett 10:394
12. Zhang Y, Liu C, Liu J, Xiong J, Liu J, Zhang K, Liu Y, Peng M, Yu A, Zhang A, Zhang Y, Wang Z, Zhai J, Wang ZL (2016) Lattice strain induced remarkable enhancement in piezoelectric performance of ZnO-based flexible nanogenerators. ACS Appl Mater Interfaces 8:1381–1387
13. Benramache S, Belahssen O, Temam HB (2014) Effect of band gap energy on the electrical conductivity in doped ZnO thin film. J Semicond 35:73001
14. Addonizio ML, Aronne A, Daliento S, Tari O, Fanelli E, Pernice P (2014) Sol–gel synthesis of ZnO transparent conductive films: the role of pH. Appl Surf Sci 305:194
15. Liu L, Mei Z, Hou Y, Liang H, Azarov A, Venkatachalapathy V, Kuznetsov A, Du X (2015) Fluorine doping: A feasible solution to enhancing the conductivity of high-resistance wide bandgap Mg0.51Zn0.49O active components. Sci Rep 5:15516

16. Liu B, Gu M, Liu X, Huang S, Ni C (2010) First-principles study of fluorine-doped zinc oxide. Appl Phys Lett 97:1
17. Zhang SB, Wei S-H, Zunger A (2001) Intrinsic N-type versus P-type doping asymmetry and the defect physics of ZnO. Phys Rev B 63:75205
18. Choi Y-J, Park H-H (2014) A simple approach to the fabrication of fluorine-doped zinc oxide thin films by atomic layer deposition at low temperatures and an investigation into the growth mode. J Mater Chem C 2:98
19. Lee HB, Ginting RT, Tan ST, Tan CH, Alshanableh A, Oleiwi HF, Yap CC, Jumali MHH, Yahaya M (2016) Controlled defects of fluorine-incorporated ZnO nanorods for photovoltaic enhancement. Sci Rep 6:32645
20. Liang G, Hu X, Yu X, Shen Y, Li HL, Davies AG, Linfield EH, Hou Kun Liang HK, Zhang Y, Yu SF, Wang QJ (2015) Integrated terahertz graphene modulator with 100% modulation depth. ACS Photonics 2:1559
21. Docherty CJ, Johnston MB (2012) Terahertz properties of graphene. J Infrared Milli Terahz Waves 33:797
22. Chen Z, Ren W, Gao L, Liu B, Pei S, Cheng H-M (2011) Three-dimensional flexible and conductive interconnected graphene networks grown by chemical vapour deposition. Nat Mater 10:424
23. Schwierz F (2010) Graphene transistors. Nat Nano 5:487
24. Sun J, Muruganathan M, Mizuta H (2016) Room temperature detection of individual molecular physisorption using suspended bilayer graphene. Sci Adv 2:e150151
25. Vicarelli L, Vitiello MS, Coquillat D, Lombardo A, Ferrari AC, Knap W, Polini M, Pellegrini V, Tredicucci A (2012) Graphene field-effect transistors as room-temperature terahertz detectors. Nat Mater 11:865
26. Danaeifar M, Granpayeh N, Mohammadi A, Setayesh A (2013) Graphene-based tunable terahertz and infrared band-pass filter. Appl Opt 52:E68
27. Sensale-Rodriguez B, Yan R, Kelly MM, Fang T, Tahy K, Hwang WS, Jena D, Liu L, Xing HG (2012) Broadband graphene terahertz modulators enabled by intraband transitions. Nat Commun 3:780
28. Lee SH, Choi M, Kim T-T, Lee S, Liu M, Yin X, Choi HK, Lee SS, Choi C-G, Choi S-Y, Zhang X, Min B (2012) Switching terahertz waves with gate-controlled active graphene metamaterials. Nat Mater 11:936
29. Kakenov N, Takan T, Ozkan VA, Balcı O, Polat EO, Altan H, Kocabas C (2015) Graphene-enabled electrically controlled terahertz spatial light modulators. Opt Lett 40:1984
30. Chen P-Y, Alú, A. (2011) Atomically thin surface cloak using graphene monolayers. ACS Nano 7:5855
31. Yoo D, Kim J, Kim JH (2014) Direct synthesis of highly conductive poly(3,4-ethylenedi-oxythiophene):poly(4-styrenesulfonate) (PEDOT:PSS)/graphene composites and their applications in energy harvesting systems. Nano Res 7:717
32. Park JW, Jang J (2015) Fabrication of graphene/free-standing nanofibrillar PEDOT/P (VDF-HFP) hybrid device for wearable and sensitive electronic skin application. Carbon 87:275
33. Cohen-Karni T, Qing Q, Li Q, Fang Y, Lieber CM (2010) Graphene and nanowire transistors for cellular interfaces and electrical recording. Nano Lett 10:1098
34. Liu Q, Guo B, Rao Z, Zhang B, Gong JR (2013) Strong two-photon-induced fluorescence from Photostable, biocompatible nitrogen-doped Graphene quantum dots for cellular and deep-tissue imaging. Nano Lett 13:2436
35. He Q, Wu S, Gao S, Cao X, Yin Z, Li H, Chen P, Zhang H (2011) Transparent, flexible, all-reduced graphene oxide thin film transistors. ACS Nano 5:5038
36. Liu Y, Yu D, Zeng C, Miao Z, Dai L (2010) Biocompatible graphene oxide-based glucose biosensors. Langmuir 26:6158

37. Tosic D, Markovic Z, Jovanovic S, Prekodravac J, Budimir M, Kepic D, Holclajtner-Antunovic I, Dramicanin M, Todorovic-Markovic B (2016) Rapid thermal annealing of nickel-carbon nanowires for graphene nanoribbons formation. Synth Met 218:43

38. Alfè M, Gargiulo V, Di Capua R, Chiarella F, Rouzaud J-N, Vergara A, Ciajolo A (2012) Wet chemical method for making graphene-like films from carbon black. ACS Appl Mater Interfaces 4:4491

39. Casini R, Papari G, Andreone A, Marrazzo D, Patti A, Russo P (2015) Dispersion of carbon nanotubes in melt compounded polypropylene based composites investigated by THz spectroscopy. Opt Express 23:18182

40. Gargiulo V, Alfè M, Di Capua R, Togna AR, Cammisotto V, Fiorito S, Musto A, Navarra A, Parisi S, Pezzella A (2015) Supplementing p-systems: eumelanin and graphene-like integration towards highly conductive materials for the mammalian cell culture bio-interface. J Mater Chem B 3:5070

41. Wang QH, Kalantar-Zadeh K, Kis A, Coleman JN, Strano MS (2012) Electronics and optoelectronics of two-dimensional transition metal dichalcogenides. Nat Nanotechnol 7:699

42. Jariwala D, Sangwan VK, Lauhon LJ, Marks TJ, Hersam MC (2014) Emerging device applications for semiconducting two-dimensional transition metal dichalcogenides. ACS Nano 8:1102–1120

43. Gatensby R, Hallam T, Lee K, McEvoy N, Duesberg GS (2016) Investigations of vapour-phase deposited transition metal dichalcogenide films for future electronic applications. Solid State Electron 125:39

44. Chen Y, Xi J, Dumcenco DO, Liu Z, Wang D, Shuai Z, Huang Y, Xie L (2013) Tunable band gap in atomically thin transition-metal Dichalcogenide alloys. ACS Nano 7:4610

45. Xu X (2014) Spin and pseudospins in transition metal dichalcogenides. Nat Phys 10:343

46. Guo HY, Lu N, Wang L, Wu XJ, Zeng XC (2014) Tuning electronic and magnetic properties of early transition-metal dichalcogenides via tensile strain. J Phys Chem C 118:7242

47. Li Y, Tongay S, Yue Q, Kang J, Wu J, Li J (2013) Metal to semiconductor transition in metallic transition metal dichalcogenides. J Appl Phys 114:174307

48. Docherty CJ, Parkinson P, Joyce HJ, Chiu M-H, Chen C-H, Lee M-Y, Li L-J, Herz LM, Johnston MB (2014) Ultrafast transient terahertz conductivity of monolayer MoS_2 and WSe_2 grown by chemical vapor deposition. ACS Nano 8:11147

49. Lui CH, Frenzel AJ, Pilon DV, Lee YH, Ling X, Akselrod GM, Kong J, Gedik N (2014) Trion-induced negative photoconductivity in monolayer MoS_2. Phys Rev Lett 113:166801

50. Tian H, Chin ML, Najmaei S, Guo Q, Xia F, Wang H, Dubey M (2016) Optoelectronic devices based on two-dimensional transition metal dichalcogenides. Nano Res 1:1543–1560

51. Sun Z, Martinez A, Wang F (2016) Optical modulators with 2D layered materials. Nat Photonics 10:227

52. D'Ischia M, Wakamatsu K, Napolitano A, Briganti S, Garcia-Borron JC, Kovacs D, Meredith P, Pezzella A, Picardo M, Sarna T, Simon JD, Ito S (2013) Melanins and melanogenesis: methods, standards, protocols. Pigment Cell Melanoma Res 26:616–633

53. Edge R, D'Ischia M, Land EJ, Napolitano A, Navaratnam S, Panzella L, Pezzella A, Ramsden CA, Riley PA (2006) Dopaquinone redox exchange with dihydroxyindole and dihydroxyindole carboxylic acid. Pigment Cell Res 19:443

54. Papari GP, Gargiulo V, Alfè M, Di Capua R, Pezzella A, Andreone A (2017) THz spectroscopy on graphene-like materials for bio-compatible devices. J Appl Phys 121:145107

55. Gatensby R, McEvoy N, Lee K, Hallam T, Berner NC, Rezvani E, Winters S, O'Brien M, Duesberg GS (2014) Controlled synthesis of transition metal dichalcogenide thin films for electronic applications. Appl Surf Sci 297:139

56. Walther M, Cooke DG, Sherstan C, Hajar M, Freeman MR, Hegmann FA (2007) Terahertz conductivity of thin gold films at the metal-insulator percolation transition. Phys Rev B 76:125408

57. Pupeza I, Wilk R, Koch M (2007) Highly accurate optical material parameter determination with THz time-domain spectroscopy. Opt Express 15:4335

58. Scheller M, Jansen C, Koch M (2009) Analyzing Sub-100-Mm samples with transmission terahertz time domain spectroscopy. Opt Commun 282:1304
59. Dorney TD, Baraniuk RG, Mittleman DM (2001) Material parameter estimation with terahertz time-domain spectroscopy. J Opt Soc Am A 18:1562
60. Duvillaret L, Garet F, Coutaz J-LL (1996) A reliable method for extraction of material parameters in terahertz time-domain spectroscopy. IEEE J Sel Top Quantum Electron 2:739
61. Angrisani L, Cavallo G, Liccardo A, Papari G, Andreone A (2016) THz Measurement Systems. In: Cocco L (ed) New Trends and Developments in metrology. InTech, London
62. Banhegyi G (1988) Numerical analysis of complex dielectric mixture formulae. Colloid Polym Sci 266:11
63. Smith NV (2001) Classical generalization of the Drude formula for the optical conductivity. Phys Rev B 64:155106
64. Withayachumnankul W, Naftaly M (2014) Fundamentals of measurement in terahertz time-domain spectroscopy. J Infrared Millimeter Terahertz Waves 35:610
65. Baxter JB, Schmuttenmaer CA (2006) Conductivity of ZnO nanowires, nanoparticles, and thin films using time-resolved THz spectroscopy. J Phys Chem B 110:25229–25239
66. Papari GP, Silvestri B, Vitiello G, de Stefano L, Rea I, Luciani G, Aronne A, Andreone A (2017) Morphological, structural, and charge transfer properties of F-doped ZnO: A spectro-scopic investigation. J Phys Chem C 121:16012
67. Titova LV, Cocker TL, Cooke DG, Wang X, Meldrum A, Hegmann FA (2011) Ultrafast Percolative transport dynamics in silicon nanocrystal films. Phys Rev B 83:1
68. Fabian D, Brunner J, Schneider A, Gunter P (2009) A terahertz time-domain spectrometer for simultaneous transmission and reflection measurements at normal incidence. Opt Express 17:20685
69. Wang H, Guo JQ, Zhou YS (2013) Understanding terahertz optical properties of amorphous carbon thin films. Carbon 64:67
70. Nemilentsau AM, Shuba MV, D'yachkov PN, Slepyan GYA, Kuzhir PP, Maksimenko SA (2010) Electromagnetic response of the composites containing chemically modified carbon nanotubes. J Phys Conf Ser 248:012003
71. Dadrasnia E, Lamela H, Kuppam MB, Garet F, Coutaz J-L (2014) Determination of the DC electrical conductivity of multiwalled carbon nanotube films and Graphene layers from noncontact time-domain terahertz measurements. Advances in Condensed Matter Physics 2014:370619
72. Titantah JT, Lamoen D (2004) Determination of the electron effective band mass in amorphous carbon from density functional theory calculations. Phys Rev B 70:033101
73. Kam K-K (1982) Electrical properties of WSe_2, WS_2, $MoSe_2$, MoS_2, and their use as photoanodes in a semiconductor liquid junction solar cell. PhD thesis, Iowa State University, Ames, IA, USA
74. Ma Y, Kolekar S, Diaz HC, Aprojanz J, Miccoli I, Tegenkamp C, Batzill M (2017) Metallic twin grain boundaries embedded in MoSe 2 monolayers grown by molecular beam epitaxy. ACS Nano 11:5130
75. Papari GP, Koral C, Hallam T, Duesberg GS, Andreone A (2018) Terahertz spectroscopy of amorphous WSe2 and MoSe2 thin films. Materials 11:1613
76. Pereira MF, Winge D, Wacker A, Zubelli JP, Rodrigues AS, Anfertev V, Vaks V (2017) Theory and measurements of harmonic generation in semiconductor Superlattices with applications in the 100 GHz to 1 THz range. Phys Rev B 96:045306
77. Pereira MF (2018) Analytical expressions for numerical characterization of semiconductors per comparison with luminescence. Materials 11:1–15
78. Apostolakis A, Pereira MF (2019) Controlling the harmonic conversion efficiency in semicon-ductor superlattices by interface roughness design. AIP Adv 9:015022
79. Apostolakis A, Pereira MF (2019) Numerical studies of superlattice multipliers performance. Quantum Sens Nano Electron Photonics XVI:109262

80. Apostolakis A, Pereira MF (2019) Potential and limits of superlattice multipliers coupled to different input power sources. J. Nanophotonics 13:036017
81. Pereira MF (2016) The linewidth enhancement factor of intersubband lasers: from a two-level limit to gain without inversion conditions. Appl Phys Lett 109:222102
82. Pereira MF, Faragai IA (2014) Coupling of THz radiation with intervalence band transitions in microcavities. Opt Express 22:3439
83. Pereira MF, Anfertev V, Zubelli JP, Vaks V (2017) THz generation by GHz multiplication in superlattices. J Nanophotonics 11:046022
84. Winge DO, Franckié M, Verdozzi C, Wacker A (2016) Simple electron-electron scattering in non-equilibrium Green's function simulations. J Phys Conf Ser 696:012013
85. Pereira MF, Shulika O (2014) Terahertz and mid infrared radiation: detection of explosives and CBRN (using terahertz), NATO science for peace and security series-B: physics and biophysics. Springer, Dordrecht
86. Pereira MF, Shulika O (2011) Terahertz and mid infrared radiation: generation, detection and applications, NATO science for peace and security series-B: physics and biophysics. Springer, Dordrecht
87. Apostolakis A, Pereira MF (2020) Superlattice nonlinearities for gigahertz-terahertz generation in harmonic multipliers. Nano 9(12):3941–3952. https://doi.org/10.1515/nanoph-2020-0155
88. Pereira MF, Anfertev V, Shevchenko Y, Vaks V (2020) Giant controllable gigahertz to terahertz nonlinearities in superlattices. Sci Rep 10:15950

Chapter 19
Development of Stand-Off Imaging Systems Using Low Cost Plasma Detectors That Work in the GHz to THz Range

Demiral Akbar, Hakan Altan, João Pedro Pavia, Marco A. Ribeiro, A. Behzat Sahin, and Cemre Kusoglu Sarikaya

Abstract Technologies used to detect mm-wave/Terahertz (THz) radiation range from those that are based on temperature changes, direct/indirect transitions or those that detect through the applied electric field. However, many commercially available detectors have limitations in terms of speed and responsivity and are quite expensive. For these reasons, commercially available indicator lamps which are called glow discharge detectors (GDDs) can be a good alternative since they are low cost and can detect microwave to mm-wave radiation with high sensitivity. These detectors have shown a good response in the mm wave region of the spectrum below ~100GHz, and here we show that their sensitivity even extends far into the THz region. To allow for such a broad frequency sensitivity we studied the detection mechanism behind the glow discharge, and find that it is as a non-local thermal equilibrium plasma whereby it can be simulated using a kinetic approach. The validity of such an approach is shown by obtaining plasma discharge parameters which agree well with experimental observations. The sensitivity of these lamps to frequencies which range from

D. Akbar
Department of Mechanical Engineering, OSTIM Technical University, Ankara, Turkey
e-mail: demiral.akbar@ostimteknik.edu.tr

H. Altan (✉) · C. K. Sarikaya
Department of Physics, Middle East Technical University, Ankara, Turkey
e-mail: haltan@metu.edu.tr; ckusoglu@metu.edu.tr

J. P. Pavia · M. A. Ribeiro
Deptartment of Information Science and Technology, ISCTE-University Institute of Lisbon, Lisbon, Portugal
e-mail: Joao_Pedro_Pavia@iscte-iul.pt; Marco.Ribeiro@iscte-iul.pt

A. B. Sahin
Deptartment of Electrical and Electronics Engineering, Ankara Yıldırım Beyazıt University, Ankara, Turkey
e-mail: absahin@ybu.edu.tr

gigahertz to terahertz region allowed us to investigate the possibility of using these lamps in array configurations for low-cost active imaging purposes.

19.1   Introduction

The mm-wave (MMW)/Terahertz region has spawned a multitude of imaging techniques and systems in the past decade due to the inherent possibility it offers and that is to detect and image concealed objects or hazardous materials at stand-off distances. Typically, the drawbacks have been that detection and/or mm-wave generation technologies are quite expensive and systems that have been commercially developed are not robust enough to deploy in various environments, i.e. indoors as well as outdoors. One research area, first started in the 1950s, was to use a glow discharge to detect microwave to millimeter wave radiation through monitoring the changes in the discharge current [1]. Many studies since then have been performed to better understand the mechanisms that are the reasons for the change in the discharge current, but definite results beyond qualitative descriptions of the interaction based on analytical models has never been reached [2–5]. This area has become relevant again in the international arena due to the high interest in developing MMW/THz technologies. The applicability of these devices for the detection of MMW was first demonstrated by Farhat and Kopeika [6]. What makes this detection possible is the wave penetration through the plasma since the plasma frequency (in the sub-GHz to GHz range [7, 8]) is smaller than the radiation frequency. These studies since then have continued and recent investigations have shown that commercially available indicator lamps filled with a gas like Neon have been found to be very good MMW detectors performing as well as Golay cells or direct Schottky diode detectors [9]. Known as Glow Discharge Detectors (GDD), such devices cost less than 1 euro each, which is orders of magnitude less than for conventional mm-wave/THz detectors whose use in commercial THz imaging systems can cost hundreds of thousands of dollars. The price reduction can be very significant when considering FPAs of large numbers of detectors and could make fast FPA MMW/THz imagers financially feasible for widespread use. Other advantages include, linear polarization sensitivity, large dynamic range, room temperature operation, and relatively fast response compatible with video frame rates for moving targets. Our efforts have also shown that the responsivity at the low-end of the MMW spectrum (towards 30 GHz) is much better than that in the higher end (towards 300 GHz) for certain types of commercially available indicator lamps. In one study a better responsivity at 100 GHz was measured compared to 250 GHz, indicating that responsivity decreases as the radiation frequency increases [10]. These studies have shown that these GDDs can be efficient detectors of radiation for frequencies from a few GHz to hundreds of GHz. For higher resolution imaging with conventional optical systems one needs to go to high frequencies. The limited response of these devices at higher frequencies have spawned heterodyne detection methods to overcome issues with noise [11]. These applications have

shown that GDDs based on commercially available indicator lamps can detect radiation at much higher frequencies (low THz frequency range) than had been previously thought. While commercial indicator lamps have proven to be useful in detecting microwave to low frequency THz radiation, their design is inherently aimed at emission of light and not detection of MMW. There is room for improvement in developing a GDD for this purpose and for this reason home-built devices based on GDD technology is being investigated by various other research groups in the world [12, 13]. Commercially available neon indicator lamps, namely GDDs have been our primary research interest since they are proven to be cost-effective, low noise, fast response mm- wave/Terahertz (THz) detectors [9, 10]. Previously, we have investigated various GDDs in terms of their speed, frequency response and polarization dependence based on their orientation with respect to the incident light [14]. Our efforts have also shown that electrode geometry leads to internal antenna properties that significantly affect detection sensitivity [15]. These studies so far have focused on detection of the radiation but not on the underlying physical principles behind the detection or investigate the limits of the detection in terms of frequency response. In this study we give a brief overview of the theory behind the detection mechanism and continue to investigate the dynamics of the discharge plasma based on kinetic theory to describe the interaction of the electrons in the plasma with the surrounding ions and atoms. We find that the kinetic approach explains the discharge parameters obtained experimentally quite well. Furthermore, we study the response of commercially available indicator lamps and see that when corrected for the absorption of the glass protecting the discharge the response of the device does not diminish as rapidly in the THz frequency range. These studies suggest that the detection mechanism of the discharge towards far-infrared radiation is quite not well understood and numerical models are needed such as the one proposed here to explain the detection.

19.2 Detection Mechanism

In order to understand the detection mechanism of GDDs, it is necessary to understand what is involved in the mm wave-plasma interaction. First, it is known that THz waves can penetrate through the plasma because the plasma frequency in the discharge tube (sub-GHz to GHz range) is smaller than the THz frequency [7]. In addition, the mm wave radiation and the plasma are thought to interact in two ways: Cascade ionization and diffusion current [16]. Here, low energetic electrons are made to oscillate by the incoming radiation, and are able to diffuse out of the Faraday dark space and out of the negative glow region, these interactions are given by the following relations for diffusion:

$$\Delta J \approx \frac{e^2 \eta_o M \nabla n P_D}{3km^2(\omega^2 + \nu^2)} \qquad (19.1)$$

and enhanced ionization:

$$\Delta J = \frac{J_o \omega_o^2 (E_o d)^2}{2\omega V_i^2} \qquad (19.2)$$

where $\omega_p = \sqrt{n_e e^2/m\epsilon_o}, \omega_o = \sqrt{n_i e^2/m\epsilon_o}$ is the plasma frequencies for electrons and ions respectively, ω is the far-infrared radiation frequency, e is the electronic charge, k is the Boltzmann constant, ν is the electron-neutral collision frequency, M is the neutral mass, m is the electron mass, η_o is the intrinsic impedance of free space, n is the average current carrier density as a function of position, P_D is the radiation power on the detector, ΔJ is the change in current density, V_i is the ionization potential of the gas, d is the length of the cathode fall, n_i is the hole density and, ω_0 is the so-called hole-plasma frequency. While this gives a broad understanding of the method of interaction the physical phenomena resulting from this interaction have not been studied in detail, thus how the radiation interacts with the plasma is still not known exactly. Previous experiments performed by our group has shown that the mm wave radiation is detected as a change in the plasma current for commercially available discharge lamps.

GDDs are basically Neon lamps, cylindrical glass tubes containing two electrodes and a low- pressure noble gas which can be either pure or a mixture of noble gases. The dominant gas is Neon resulting in an orange glow. Some commercially available Neon lamps have a phosphorescent coating inside the glass which results in a green glow. A sufficient potential difference between the electrodes causes the ionization of the gas and thus the formation of electrons and ions. As the negatively charged particles move toward the anode, the positively charged ions move toward the cathode, causing secondary electron emission in the cathode, which plays an important role in the sustainability of the generated plasma. The light is the result of excitation of the gas atoms by the electrons in the plasma. The excited gas atoms fall to a lower energy level by emitting photons in a color that is characteristic of the gas.

The breakdown of the gas for an applied voltage results in a current, which is controlled using a load resistor. Typically, the load resistances are approximately 10s of kilo ohms that result in a low current allowing the lamp to operate at long lifetimes on the order of thousands of hours. However, detection of mm-wave radiation is greater when the lamp is operated in the abnormal glow region or when the current through the lamp increases with increasing bias. This is typically observed for loads that are much lower allowing for currents through the lamps to be approximately 10s of milliamps (mA). This level of current is representative of the non-local thermal equilibrium where the temperature of the electrons are much greater than the other particles inside the plasma. In order to understand the behavior of such plasma particles adequately, a kinetic approach rather than one based on a fluid approach is required. This approach can be realized through the Boltzmann equation:

$$\left[\frac{\partial}{\partial t} + \boldsymbol{v}\,\boldsymbol{\nabla}_r + \boldsymbol{a}\,\boldsymbol{\nabla}_v\right] f(\boldsymbol{r}, \boldsymbol{v}, t) = \left(\frac{\partial f}{\partial t}\right)_{coll.} \tag{19.3}$$

where, v, r and a are the velocity, position and acceleration of the plasma particles, respectively. Since the direct solution of this equation is highly complicated mathematically, particle simulation methods that give the same results [17, 18] can be used to explain the kinetic behavior of particles. Previously developed Particle in Cell/Monte Carlo Collision (PIC/MCC) method is used here since neon lamps acting as GDDs are known to be low pressure non-LTE plasma lamps [19].

19.2.1 Parallel 1d3v PIC/MCC Simulation of GDD

The kinetic approach is of great importance in non-LTE plasmas. In order to understand the detection mechanism and compare with experimental results simulations focused on lamps which had a pure gas content. Previous studies done by our group members analyzed the discharge emission lines of various types of commercially available lamps. Of the ones tested, Neon lamps designated as N520A supplied by International Light Technologies, LLC were chosen since they had a pure Neon gas content confirmed by measuring emission line spectra and had no phosphor coating inside (GDDs with phosphor coating is known to have better sensitivity). The parameters with govern the discharge is applied bias and load resistance. Abnormal glow region is characterized by an increase in discharge current with increase in bias, and to ensure that the GDD operated in this region the behavior of the discharge was observed for a varying applied bias for a constant load. The current-voltage characteristic of the GDD with the code N520A obtained experimentally is shown in Fig. 19.1.

To simulate the behavior all parameters specific to the discharge must be determined. For this particular GDD which is simulated using the Particle in Cell/Monte Carlo Collision (PIC/MCC) method, the positions of particles are analyzed in one dimension and their velocities in three dimensions (referred to as 1d3v). The PIC/MCC code [19] is written in Fortran 90 language. In order to achieve performance improvement, this code is parallelized by using the Open MPI library. Before GDD simulation, the code has been shown to be successful in providing experimental results by simulating plasmas generated in our laboratory where all parameters were controlled [20]. Since the N520A is enclosed in a glass ampule, the pressure inside is unknown. Therefore, the current-voltage characteristic of the GDD (Fig. 19.1) served as a guide to help us determine the pressure inside.

As shown in Fig. 19.1, the current of 1.18 ± 0.11 mA is obtained with a voltage of 130 Volts. This applied voltage corresponds to the GDD voltage of 74.5 V due to the 47 kΩ resistance connected in series. To simulate this circuit, the applied voltage between the electrodes is reduced as the current increases in the simulation as $\mathbf{V_{GDD} = V_0 - IR}$, where $\mathbf{V_0}$ is the applied voltage which equals to 130 V. As a
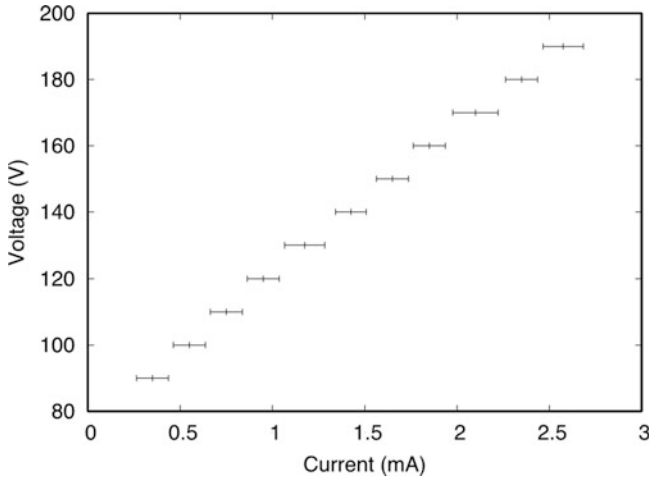
Fig. 19.1 The current-voltage characteristic of the GDD with the code N520A

Table 19.1 The parameters used in the PIC/MCC simulation of GDD

Inter-electrode distance (mm)	1.3
Super particle weighting (10^8)	5.2
Time step (10^{-11} s)	1
Number of grid points	600
Secondary electron emission coefficient (γ)	0.35
Reflection coefficient (r)	0.2
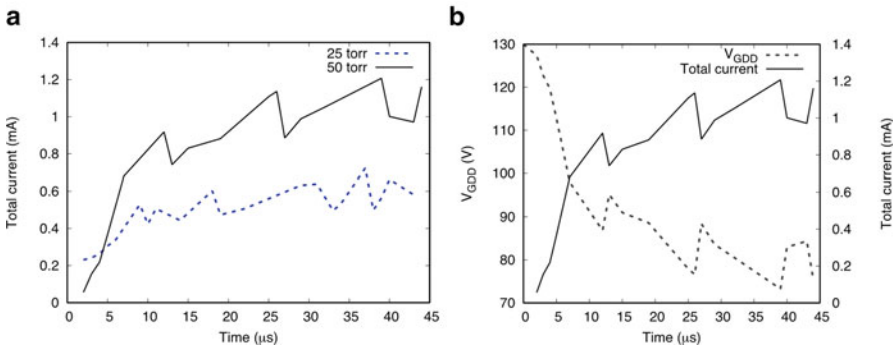
Fig. 19.2 (**a**) The change of the total current over time obtained for 25 and 50 torr pressure, (**b**) The change of the GDD potential and the total current over time for 50 torr pressure

result of this arrangement, the plasma in the aforementioned GDD is simulated for 25 and 50 torr pressures. For details of the simulation model, refer to the study in Ref. [20] (Table 19.1).

Figure 19.2a shows the change of the total current which includes ion, electron and displacement current over time obtained for 25 and 50 torr pressure. As can be

understood, it takes 45 μs to obtain converged values for both pressures. When these values are considered, it is seen that the total current obtained from the simulation is around 0.6 mA for 25 torr pressure and around 1.1 mA for 50 torr. In this case, it is concluded that the GDD (N520A) has around 50 torr pressure since this pressure provides a value of the current compatible with the experimentally obtained value. In addition, the stability of the GDD voltage around 75 Volts in the simulation (Fig. 19.2b) supports this compatibility. Similar pressures have been reported in experimental studies done previously to detect MMW radiation for discharge geometries similar to N520A [21]. Accurate determination of the unknown pressure shows that the kinetic approach gives us an accurate description of the discharge parameters. This is the first step towards to achieving a better understanding of the interaction of THz/mm waves with plasma in GDDs.

19.3   Low and High Frequency Response of the GDD

To understand the detection mechanism and its dependence on the radiation frequency a specialized amplifier circuit which allowed for a high gain while reducing noise due to the bias voltage was developed. The circuit allowed for a ten times better response at a modulation frequency of 50 kHz compared to the signal obtained using lock-in detection methods. The gain factor for lower MMW frequencies was about 100, while the gain factor for the terahertz range was more than 2000. A specialized filter was used to filter out the noise around the modulation frequency of 50 kHz. This was crucial in observing the responsivity of the GDD over a broad frequency range from 84GHz to 125GHz and 252 to 375GHz, the limits of our tunable MMW source (Modified YIG oscilator driven VDI Inc.WR9.0 Broadband Source with Tripler Extension). The source power was calibrated using a Golay Cell (Tydex GC-1P) and this data was used to calculate the response of the GDD over the MMW-THz frequency range. Of the various types of GDDs used to detect the radiation, the phosphor coated N523 (supplied by International Light Technologies, LLC) responded the best over the entire frequency range. To accurately describe the response of the GDD the loss due to the glass shell casing needs to be addressed. The loss of power due to the glass wall in the GDD is taken into account by using the experimentally obtained absorption coefficient curve of the glass (Fig. 19.3).

The corrected response for N523 GDD for the frequency range as given by our source is shown in Figs. 19.4 and 19.5.

The obtained results in the low frequency end agree well with literature values which report responsivity on the order of ~100 V/W for similar Neon indicator lamps [22]. The responsivity of the GDD increases towards the low-end limit of the MMW region (~30 GHz) limited only by its physical size.
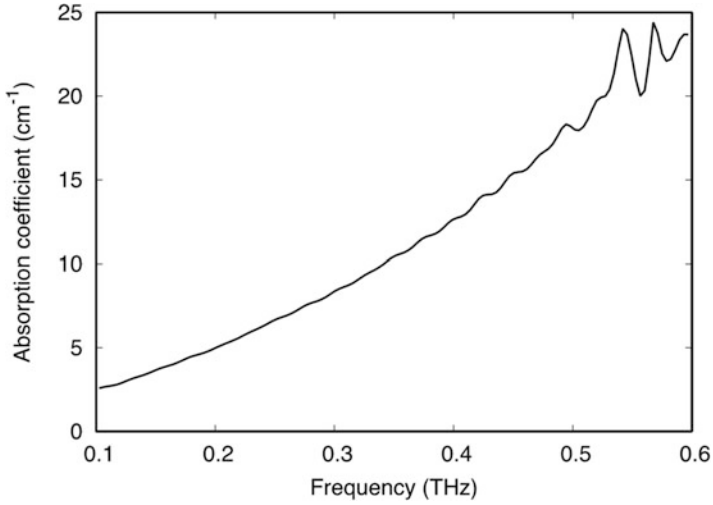
Fig. 19.3 Absorption Coefficient of the Glass Wall Typically Used in a Commercial GDD
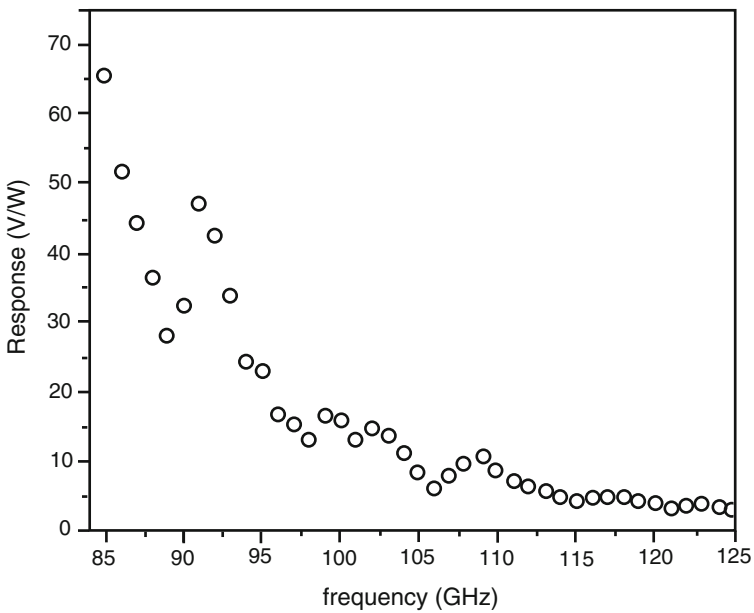

Fig. 19.4 Response corrected for the loss due to the 0.5 mm thick glass shell for GDD (N523) in the MMW range
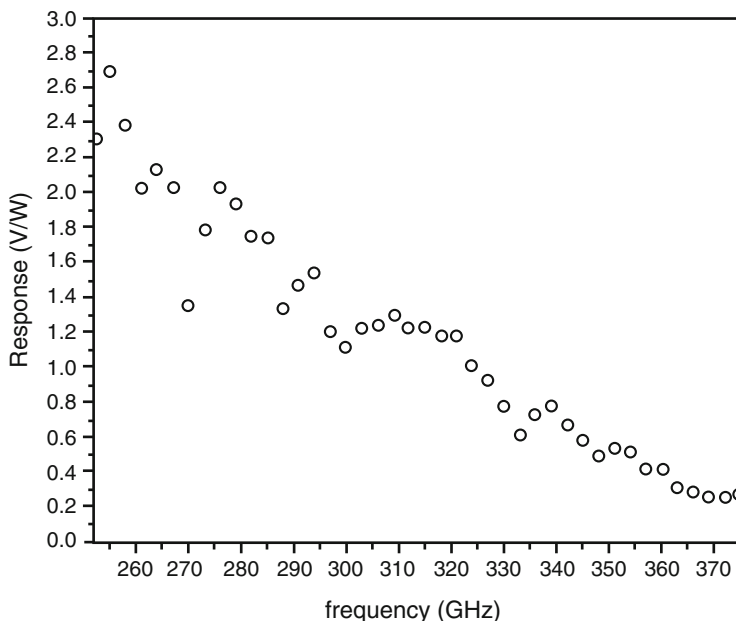
Fig. 19.5 Response corrected for the loss due to the 0.5 mm thick glass shell for GDD (N523) in the THz range

19.4 Conclusion

Glow Discharge Detectors (GDDs) based on commercially available Neon indicator lamps provide a cost-effective, sensitive, room temperature operating means to detect radiation from GHz to THz frequency range. The lower cost of higher power sources especially in the GHz frequency range coupled with the fact that these detectors can be easily assembled in array configurations opens up the possibility of developing active imaging systems with sufficient dynamic range to image scenes. Here two types of commercially available indicator lamp were studied, one with phosphor coating and one without with similar geometrical dimensions. It was found that a numerical model based on a kinetic approach which utilized Boltzmann equation simulated the non-local thermal equilibrium conditions associated with the plasma inside the GDD quite well allowing us to accurately predict experimental discharge parameters. The response of GDD was studied from the MMW to THz range. The response decreased rapidly, and after 100GHz the decay slowed down which suggests that these types of lamps could detect even higher frequencies in the THz range. The working simulation of the discharge parameters coupled with a broad understanding of the detection limits will aid in the future full simulation of the interaction of the GHz to THz frequency radiation with the plasma discharge.

References

1. Burroughs G, Bronwell A (1952) High-Sensitivity Gas Tube Detector. Teleteknik II:62–63
2. Lampert MA, White AD (1953) Microwave techniques for studying discharges in gases. Electr Commun 30:124–128
3. Udelson BJ (1957) Effect of microwave signals incident upon different regions of a dc hydrogen glow discharge. J Appl Phys 28:380–381
4. Lobov GD (1960) Gas discharge detector of microwave oscillations. Radiotech Electron 5:152–165
5. Severin PJW (1965) The interaction of microwaves with the cathode fall and negative glow in a glow discharge. Phillips Research Laboratories, Eindhoven
6. Farhat NH, Kopeika NS (1972) A low-cost millimeter wave glow-discharge detector. Proceedings of the IEEE 60:759–760
7. Kopeika NS (1978) Glow discharge detection of long wavelength electromagnetic radiation: cascade ionization process internal signal gain and temporal and spectral response properties. IEEE Trans Plasma Sci 6:139–157
8. Kopeika NS, Farhat NH (1975) Video detection of millimeter waves with glow discharge tubes: part I - physical description; part II - experimental results. IEEE Trans Electron Devices 22:534–548
9. Abramovich A, Kopeika NS, Rozban D, Farber E (2007) Inexpensive detector for terahertz imaging. Appl Opt 46(29):7207–7211
10. Rozban D, Kopeika NS, Abramovich A, Farber E (2008) Terahertz detection mechanism of inexpensive sensitive glow discharge detector. J Appl Phys 103:093306
11. Avihai Aharon (Akram), Daniel Rozban, Natan S. Kopeika, Amir Abramovich (2013) Heterodyne detection at 300 GHz using neon indicator lamp glow discharge detector. Appl Opt 52:4077–4082
12. Hou L, Park H, Zhang X-C (Feb, 2011) Terahertz wave imaging system based on glow discharge detector. IEEE J Sel Top Quantum Electronics 17:177–182
13. Hou L, Shi W (2012) Fast terahertz continuous-wave detector based on weakly-ionized plasma. IEEE Electron Device Lett 33:1583–1585
14. Alasgarzade N, Takan T, Uzun-Kaymak IU, Sahin AB, Altan H (2015) Modualtion and frequency response of GDDs in the millimeter wav/THz region. Proc SPIE 9510C
15. Cinar K, Bozaci HM, Altan v H (2013) Characterization of a glow discharge detector with terahertz time domain spectroscopy. IEEE Sensors J 13(7):2643–2647
16. Kopeika NS (1975) On the mechanism of glow discharge detection of microwave and millimeter-wave radiation. Proc IEEE 63(6):981–982
17. Nanbu K (2000) Probability theory of electron-molecule, ion-molecule, molecule-molecule, and coulomb collisions for particle modelling of materials processing plasmas and cases. IEEE Trans Plasma Sci 28:971–990
18. Longo S (2000) Monte carlo models of electron and ion transport in non-equilibrium plasmas. Plasma Sources Sci. Technol. 9:468–476
19. Kusoglu Sarikaya C, Rafatov, Kudryavtsev AA (2016) Particle in Cell/Monte Carlo Collision analysis of the problem of identification of impurities in the gas by the plasma electron spectroscopy method. Phys Plasmas 23:063524

20. Kusoglu Sarikaya C, Akbar D, Ribeiro MA, Altan H (2018) Understanding the detection mechanism of mm wave radiation in glow discharge detectors. Proc SPIE 10800:108000E
21. Farhat NH (1974) Optimization of millimeter-wave glow-discharge detectors. Proc IEEE 62(2):279–281
22. Hou L, Park H, Zhang X (2009) Broadband detector measures IR, millimeter & THz waves. In: 2009 34th international conference on infrared, millimeter, and terahertz waves, Busan, pp 1–2